Nouvelles cibles thérapeutiques dans les gliomes infiltrants du tronc cérébral de l'enfant

Nathalene Truffaux

UNIVERSITE PARIS-SUD

ÉCOLE DOCTORALE : 418 - Cancérologie
UMR8203 CNRS « Vectorologie et Thérapeutiques Anticancéreuses »

Oncologie

THÈSE DE DOCTORAT

soutenue le 26/05/2014

par

Nathalène TRUFFAUX

NOUVELLES CIBLES THERAPEUTIQUES DANS LES GLIOMES INFILTRANTS DU TRONC CEREBRAL DE L'ENFANT

Directeur de thèse : Jacques GRILL — Pédiatre Oncologue, Institut Gustave Roussy, Villejuif

Composition du jury :

Président du jury :	Jean FEUNTEUN	Professeur et Directeur de Recherche, Université Paris Sud
Rapporteurs :	Natacha ENTZ-WERLE,	Professeur et Pédiatre Oncologue, Hôpital de Hautepierre, Strasbourg
	Yves DE KEYZER	Directeur de Recherche INSERM, Université Paris Descartes
Examinateurs :	Marie-Christine MULTON,	Manager Senior, Sanofi R&D, Vitry-sur-Seine
	Marc SANSON	Professeur et Neuro-oncologue, Hôpital de la Pitié-Salpêtrière, Paris

REMERCIEMENTS

Je remercie tout d'abord l'ensemble des membres de mon jury d'avoir accepté d'évaluer ce travail de thèse.

Mes remerciements vont ensuite au Docteur Jacques GRILL, pour sa confiance, son implication et son soutien dans la réalisation de ce travail. Au cours de ces quatre années, il m'a fait partager sa vision de clinicien et sa curiosité faisant de ce sujet passionnant une expérience formidable. Je tiens à lui témoigner mon profond respect et toute ma sympathie.

Je remercie également les membres de l'équipe, pour leur aide, leur bienveillance et leur gentillesse : Cathy, Gaétan, Ludivine, Estelle, Marie-Anne, David, Marianne, Wassim, Roxane, Carole, Hervé et le Docteur Birgit GEOERGER.
Merci à Felipe ainsi qu'aux anciens membres de l'équipe.

Je remercie le Dr. Lluis Mir de m'avoir accueillie dans son unité et ainsi que tous les membres de l'unité.

Un grand merci à Véronique Scott, pour sa gentillesse, son soutien et ses précieux conseils.
Je remercie tous les gens qui ont contribué d'une manière ou d'une autre à la réalisation de ce projet, aux membres de l'UGF et spécialement à Catherine Richon.

Je remercie mes amis de Paris et d'ailleurs.
Spécial remerciement à Audette avec qui j'ai découvert la vie parisienne…

Merci mes parents pour leur soutien et leur amour.
Merci à Diane pour son aide et son soutien et également à mes autres frère et sœurs.

Merci également à Arnaud, pour tout ce qu'il m'apporte au quotidien et ce malgré la distance.

Je tiens à remercier l'Association « l'Etoile de Martin » qui a soutenu ce financement de thèse.

Enfin mes pensées vont aux patients et à leur famille.

RESUME

Le gliome infiltrant du tronc cérébral est une tumeur rare, non opérable et inéluctablement fatale. En raison du manque de ressource biologique disponible, aucun progrès dans la compréhension de la biologie de ces tumeurs n'a été fait jusqu'à ces dernières années, laissant la radiothérapie pour seul traitement efficace, et seulement transitoirement. Enfin, grâce à la mise en place de collecte d'échantillons de gliomes infiltrant du tronc cérébral au diagnostic ou à l'autopsie, un nombre sans précédent d'analyses biologiques et génomiques a pu être mené et améliorer la connaissance de ces tumeurs. Si ces études ont montré que ces gliomes pédiatriques étaient bien différents de ceux de l'adulte, elles ont aussi fait apparaître la présence d'anomalies génétiques récurrentes spécifiques de ces tumeurs sous-tentorielles. Ainsi le *Platelet-Derived Growth Factor Receptor Alpha* (PDGFRα) est apparu comme cible prédominante dans ces tumeurs compte tenu des nombreuses anomalies génétiques constatées. La recherche d'un médicament efficace pouvant inhiber cette voie nous a conduit à évaluer l'effet du dasatinib qui est un inhibiteur multi-ciblé. Nous en rapportons ici l'efficacité *in vitro* sur de nouvelles lignées cellulaires de gliomes infiltrants du tronc cérébral établies à partir de biopsies stéréotaxiques réalisées au diagnostic. Sachant néanmoins que les thérapies ciblées restent peu efficaces en clinique quand elles sont utilisées seules, nous mettons en évidence l'intérêt de combiner le dasatinib avec un inhibiteur de MET, 2ème oncogène fréquemment amplifié dans ces tumeurs. D'autre part, une stratégie originale de criblage médicamenteux a été mise en œuvre. Celle-ci a permis de définir de manière fonctionnelle de nouveaux médicaments potentiellement efficaces dans les gliomes infiltrants du tronc cérébral, incluant les inhibiteurs d'*Histone deacetylases* (HDAC), les inhibiteurs des *Cyclin-Dependent Kinases* (CDK) ou encore les inhibiteurs du protéasome.
Enfin par la technique de séquençage génome-entier, de nouvelles anomalies génétiques jamais rencontrées dans aucun autre cancer ont été détectées. Parmi celles-ci se trouvent des mutations d'histone H3K27M dont la fréquence élevée (80%) suggère leur rôle fondamental dans la genèse de ces tumeurs. Des mutations activatrices d'ACVR1/ALK2 ont été également mises en évidence. Celles-ci représentent désormais de nouvelles cibles à explorer.
Ce travail de thèse rapporte la recherche de nouvelles cibles thérapeutiques d'une part, via une approche exploratoire par criblage médicamenteux et recherche d'anomalies génétiques par séquençage « génome-entier », et d'autre part, via une approche de validation préclinique sur le plan des thérapies ciblées de type inhibiteurs de tyrosine-kinases.

Mots clés : Gliome infiltrant du tronc cérébral, thérapie ciblée, criblage fonctionnel, dasatinib, séquençage « génome-entier », *ACVR1*

ABSTRACT

Diffuse Intrinsic Pontine Glioma (DIPG) is a rare, unresectable and universally fatal tumor. Due to the lack of available material, no improvements have been made in the knowledge of the biology of this tumor until recent years, leaving radiotherapy as the only efficient treatment, and only transiently. Recently, the effort engaged for collecting samples in this disease at the diagnosis or at the autopsy resulted in an unprecedented number of analyses consequently improving our knowledge in DIPG. Those studies bring evidences for their differences with adult gliomas, but also with other pediatric supratentorial glioma showing specific genomic alterations. Thus, *Platelet-Derived Growth Factor Receptor Alpha* (PDGFRα) appeared to be one of the major target given its frequent aberrations found in those tumors. Investigating an effective drug to inhibit this pathway led us to evaluate the effect of dasatinib, which is known as a multi-targeted inhibitor. We report here the *in* vitro efficacy of dasatinib on new cell lines of DIPG developed from stereotaxic biopsy at diagnosis**.** Because therapies are largely inefficient in the clinic when they are used as a monotherapy, we bring out our interest on combining dasatinib with an inhibitor of MET, which is the 2nd most common amplified oncogene in these tumors.

Additionally, an innovative strategy of pharmacological screening has been successfully tested. New drugs, potentially efficient in DIPG, have been fonctionnaly-defined, including *Histone deacetylase inhibitors* (HDACi), *Cyclin-Dependent Kinases inhibitors* (CDKi) and proteasome inhibitors as well.

Finally, by using whole genome sequencing (WGS), we have been able to discover new genetic abnormalities, never encountered before in other cancers. Among those, mutations of histone H3K27M with a high frequency of 80% were found, suggesting that they have a fundamental role in tumors genesis. Moreover, ACVR1/ALK2 activating mutations have been identified as well. And this gene now represents a new target to explore.

This work reports the research of new therapeutic targets through an exploratory approach using drug screening and WGS on the one hand, and on the other hand through a preclinical validation approach in terms of targeted therapies with tyrosine-kinases inhibitors.

Keywords: Diffuse Intrinsic Pontine Glioma (DIPG), targeted therapy, functional screening, dasatinib, Whole genome sequencing, *ACVR1*

LABORATOIRE D'ACCUEIL

UMR8203 sous la direction du Dr. Lluis Mir
« Vectorologie et thérapeutiques anti-cancéreuses »

<u>Equipe du Dr. Jacques Grill</u>
« Identification de cibles et nouvelles thérapies dans les tumeurs pédiatriques »

Pavillon de Recherche 2
114, rue Edouard Vaillant
94805 VILLEJUIF CEDEX

+33 1 42 11 62 09

SOMMAIRE

ABREVIATIONS

ACVR1 :	Activin A receptor type 1
ALT :	Alternative lengthening of telomeres
ATRX :	Alpha thalassemia/mental retardation syndrome X-linked
BMP :	Bone morphogenic proteins
CED :	Convection Enhanced Delivery
CGH :	Comparative genomic hybridization
DAXX :	Death domain-associated protein 6
DIPG :	Diffuse intrinsic pontine glioma
EGF(R) :	Epidermal growth factor (receptor)
FISH :	Fluorescence in situ hybridization
FOP :	Fibrodysplasie ossifiante progressive
GSEA :	Gene set enrichment analysis
HDAC :	Histone deacetylase
HGF :	Hepatocyte growth factor
IHC :	Immunohistochimistry
H3K27ac	Histone H3 acétylé en Lysine 27
H3K27me3 :	Histone H3 triméthylé en Lysine 27
MAPK :	Mitogen-activated protein kinase
MET :	MNNG HOS transforming gene
MGMT :	O6-methyl-guanine DNA methyltransferase
NSC :	Neural stem cell
OS :	Overall survival
PCA :	Composante principale analysis
PDGF(R-A/B) :	Platelet derived growth factor (receptor A / B)
PFS :	Progression free survival
PI3K(CA) :	Phosphatidyl inositol 3-kinase (catalytic subunit)
PTEN :	Phosphatase and tensin homolog
RNA-Seq :	RNA Sequencing
RTK :	Récepteur à activité tyrosine kinase
SAHA :	Suberoylanilide hydroxamic acid
SNC :	Système nerveux central
TCGA :	The cancer genome atlas
TIM :	Target Inhibition Map
TMZ :	Temozolomide
VEGF(R) :	Vascular endothelial growth factor (receptor)
WGS :	Whole genome sequencing

LISTE DES PUBLICATIONS

Publication majeure :

Truffaux N, Philippe C, Paulsson J, et al. Preclinical evaluation of dasatinib alone and in combination with cabozantinib for the treatment of Diffuse Intrinsic Pontine Glioma

⇒ Soumis à Clinical Cancer Research

Collaborations :

Grasso C*, Truffaux N*, Berlow N et al. Functionally defined therapeutic targets in Diffuse Intrinsic Pontine Glioma

⇒ Soumis à Nature Translational Medicine

Taylor R*, Mackay A*, Truffaux N, et al. Recurrent activating *ACVR1/ALK2* mutations in diffuse intrinsic pontine glioma

*Contribution équivalente

⇒ Publié dans Nature Genetics

LISTE DES ILLUSTRATIONS

LISTE DES TABLEAUX

INTRODUCTION

Partie I : Généralités sur les gliomes infiltrants du tronc cérébral

1. Introduction générale

Le gliome infiltrant du tronc cérébral, variant anatomique des gliomes de haut grade, se développe presque exclusivement chez l'enfant et le jeune adulte. Il s'agit de la troisième tumeur cérébrale en fréquence à cet âge et la première cause de mortalité par tumeur cérébrale chez l'enfant. Son caractère infiltrant et sa localisation rendent impossible toute chirurgie d'exérèse. Cette tumeur ne répond que transitoirement à la radiothérapie. Elle présente presque systématiquement une chimiorésistance et depuis la preuve d'efficacité de la radiothérapie (Coutel 1959) aucun autre traitement n'a été validé en 50 ans. Malgré la radiothérapie, la plupart des patients décèdent dans les deux ans après diagnostic. Depuis ces 20 dernières années, l'imagerie par résonnance magnétique ayant remplacé la biopsie, des signes cliniques et radiologiques évocateurs suffisent pour bien des équipes pour établir ce diagnostic (Albright et al. 1993). Cette approche est néanmoins prise en défaut dans un certain nombre de cas (Hankinson et al. 2011; Sufit et al. 2012) justifiant pour d'autres équipes une pratique plus systématique des biopsies (Roujeau et al. 2007).

Depuis une dizaine d'années, de nombreux essais cliniques combinant chimiothérapie, radiothérapie et plus récemment nouvelles thérapies ciblées impliquant les inhibiteurs de récepteurs à activité tyrosine kinase et les agents anti-angiogéniques ont été réalisés dans ces affections malheureusement sans succès. Le développement de ces nouvelles stratégies thérapeutiques chez l'enfant a été influencé par les thérapies de l'adulte en occultant leurs différences biologiques. Des études biologiques récentes réalisées surtout à partir de matériel autopsique, la première publiée en 2010 (Zarghooni et al. 2010), ont permis de découvrir des anomalies biologiques qui pourraient nous aider à mieux redéfinir les traitements à explorer.

2. Epidémiologie

Après les cancers hématologiques, les tumeurs du système nerveux central représentent les tumeurs les plus fréquentes parmi les tumeurs solides en pédiatrie (cf. **Figure 1**). Elles représentent approximativement 20% de l'ensemble des cancers de l'enfant et sont la principale cause de décès en oncologie chez l'enfant, l'adolescent et le jeune adulte (Gurney, Smith, et Buni 2013).

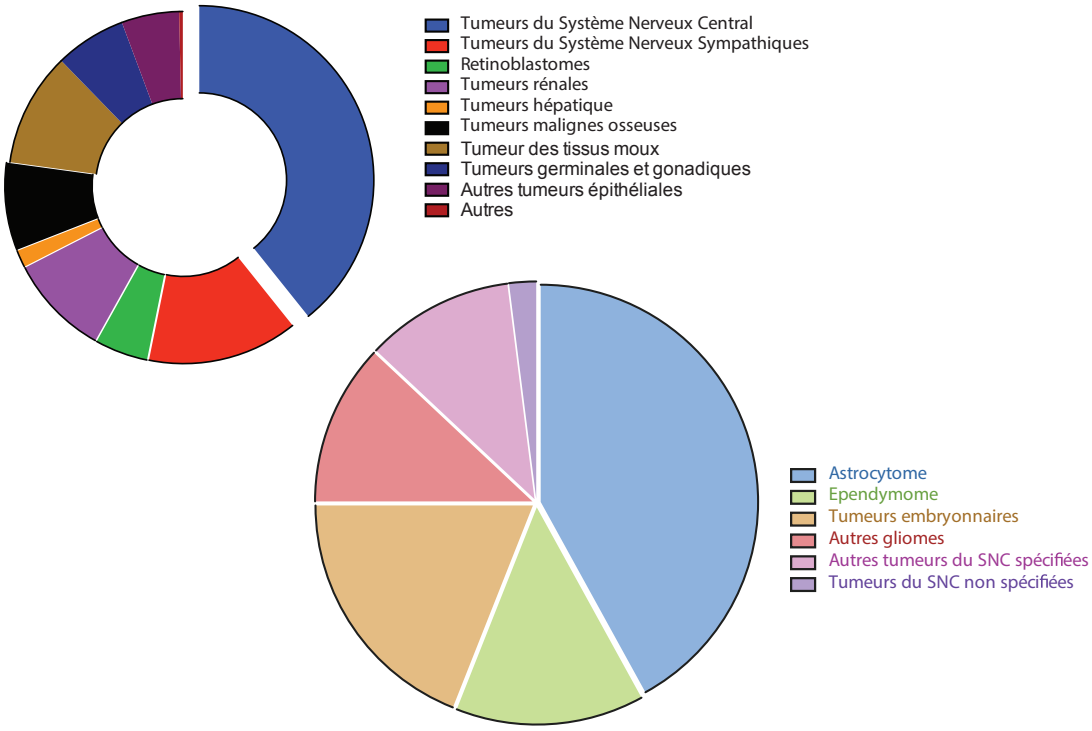

Figure 1 : Répartition par types de tumeurs solides et répartition des tumeurs cérébrales de l'enfant (0-14 an) en France. D'après (Desandes et al. 2004) et le Registre National des Tumeurs Solides de l'Enfant, 2000-2006 (http://www.chu-nancy.fr/rntse/).

Le gliome infiltrant du tronc cérébral est une des 3 tumeurs cérébrales malignes les plus fréquentes en pédiatrie après les médulloblastomes et les épendymomes. A ce jour, son incidence n'est pas bien définie par les registres en l'absence de preuve histologique mais cette tumeur survient généralement chez les enfants âgés de 5 à 10 ans (cf. **Figure 2**) (Wolff et al. 2008) et est extrêmement rare chez l'adulte. On estime qu'il y a environ 30 à 40 nouveaux cas par an en France. Il n'y a pas de différence dans la répartition selon le sexe et la localisation géographique.

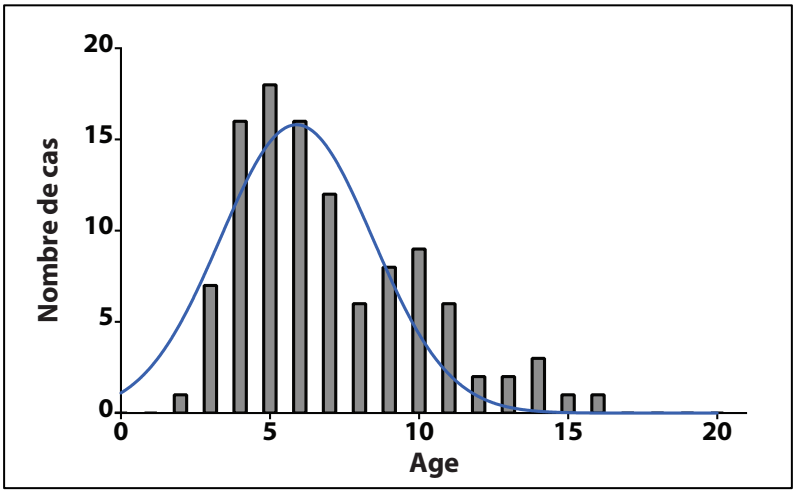

Figure 2 : Incidence des DIPG par âge. Etablit sur une cohorte de 108 enfants, d'après le registre du service de Neurochirurgie de l'Hôpital Necker-Enfants Malades (Paris) sur la période 2000-2013. Le pic d'incidence survient au milieu d'enfance.

3. Développement et anatomie du tronc cérébral

3.1. Développement du tronc cérébral

Au cours de son développement, le tube neural en croissance sous contrainte de la boite crânienne va subir un enroulement et des courbures successives de ses vésicules à l'origine des différentes structures du SNC. Le tronc cérébral dérive du mésencéphale (3ème vésicule), du métencéphale (4ème vésicule) et du myélencéphale (5ème vésicule)**(**cf**. Figure 3)**. A cette régionalisation antéro-postérieure s'ajoute une polarisation ventro-dorsale du tube neural. Sous influence de signaux d'induction, une population cellulaire appelée neuroblastes va se différencier des cellules progénitrices en division et migrer jusqu'à leur localisation définitive dans la future substance grise retrouvée dans le cortex, le cervelet et la moelle épinière. Au niveau du tronc cérébral, ces futurs neurones vont se regrouper en noyaux au niveau ventral pour former les noyaux gris du tronc cérébral et les noyaux des nerfs crâniens. Dans un second temps, un deuxième linéage cellulaire de type glial va se mettre en place et coloniser la substance grise. Ce linéage comporte plusieurs étapes de différenciation intermédiaires aboutissant à la formation d'astrocytes et d'oligodendrocytes.

L'histogenèse du SNC est divisée en plusieurs phases, dont certaines se terminent à la fin de l'adolescence (Tau et Peterson 2010). Ces dernières phases constituent donc une période de reprise d'activité mitotique et de différenciation de précurseurs neuraux dont le rôle est suspecté dans l'apparition des tumeurs. Plus particulièrement, les DIPG survenant dans une zone circonscrite du tronc cérébral et dans une période délimitée de l'enfance suggère une dérégulation de ce processus de neurogenèse postnatale. Monje et ses collaborateurs ont en effet identifié une population de précurseurs neuraux exprimant des marqueurs phénotypiques de type « Cellule Souche Neurale » (NSC) dans le tronc cérébral humain et murin dont la distribution anatomique et temporelle corrèle avec l'incidence des DIPG et mettent en évidence l'existence d'une cellule d'origine candidate (Monje et al. 2011).

Dans ces travaux, les modèles établis *in vitro* et *in vivo* à partir de prélèvements autopsiques de DIPG soulignent l'implication de la voie Sonic Hedgehog normalement impliquée dans le développement du tube neural et dans la neurogenèse tardive (Ahn & Joyner, 2005; Q. R. Lu et al., 2000). Ces observations soutiennent l'hypothèse selon laquelle la physiopathologie de cette tumeur est liée à la reprise programmée d'une neurogenèse localisée au niveau ventral du pont.

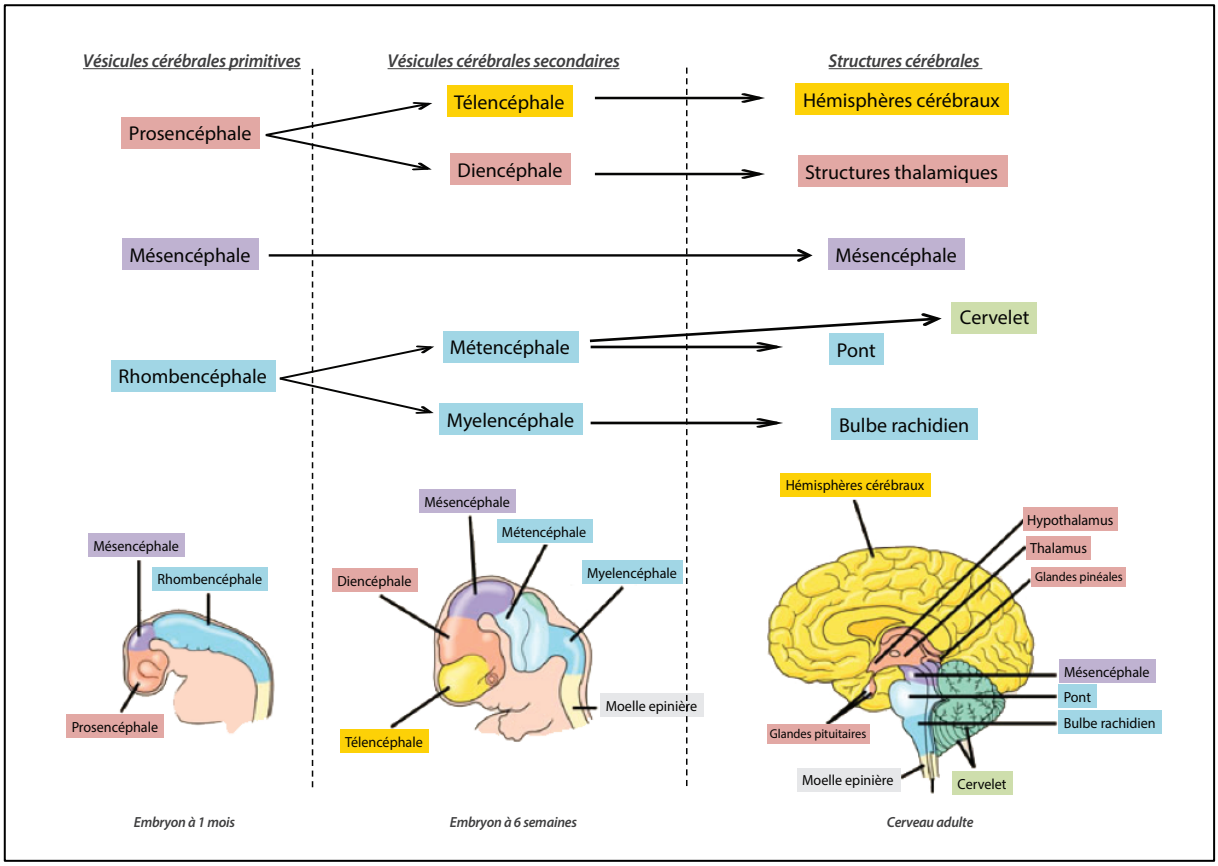

Figure 3 : Vue schématique du développement du SNC.
(Adapté du site http://www.startsateight.com/2011/05/kids-are-not-just-mini-adults-brain-development/)

3.1. Anatomie du tronc cérébral

Le tronc cérébral assure les fonctions vitales (comme la respiration et le rythme cardiaque) et commande les mouvements et les réflexes. Cette structure anatomique située dans la fosse postérieure de l'encéphale, relie les différents éléments du système nerveux : le cerveau, le cervelet et la moelle épinière. Il est aussi une région de passage des voies sensitives et motrices ainsi qu'un centre de contrôle de la douleur. Il constitue également une zone d'émergence de la majorité des nerfs crâniens (III-XII). Il est composé de 3 parties (de haut en bas) :

_ le mésencéphale ou pédoncules cérébraux,

_ le pont (de Varole) ou protubérance annulaire,

_ le bulbe rachidien ou moelle allongée.

Les gliomes infiltrants du tronc cérébral se développent classiquement au niveau ventral du pont et envahissent les structures postérieures **(**cf. **Figure 4**).

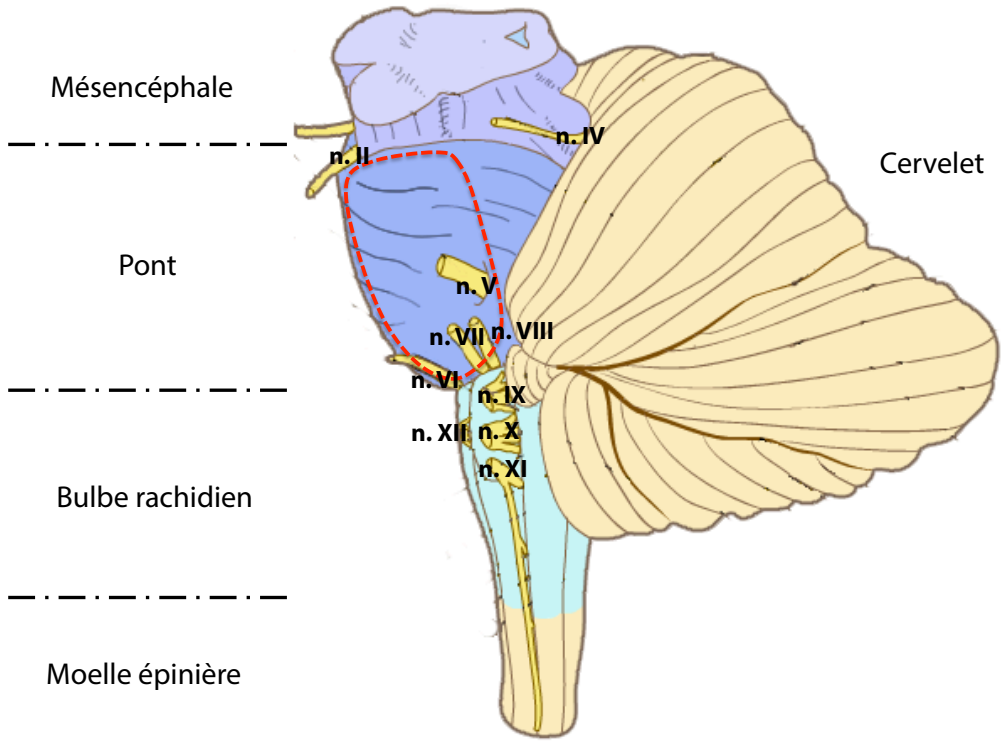

Figure 4 : Représentation schématique du tronc cérébral et des nerfs crâniens. Les gliomes infiltrants du tronc cérébral surviennent généralement dans la partie ventrale du pont (zone délimitée en pointillées rouges), alors que les tumeurs focales se développent en dehors de cette structure.

4. Classification des gliomes infiltrants du tronc cérébral

4.1. Classification des gliomes selon l'OMS

Le diagnostic et la classification histologique des gliomes reposent actuellement sur la classification de l'Organisation Mondiale de la Santé (OMS) 2007, qui les différencie selon le type cellulaire prédominant et le degré de malignité (Louis et al. 2007). Les gliomes peuvent être définis en trois groupes : les tumeurs astrocytaires (astrocytomes), les tumeurs oligodendendrocytaires (oligodendrogliomes) et les tumeurs mixtes présentant un mélange des deux populations cellulaires. Ces trois catégories sont elles-mêmes classées selon le niveau de malignité croissante :

_ les gliomes de bas grade ou bénins :

- astrocytomes pilocytiques (Grade I)
- astrocytomes diffus (Grade II)
- oligodendrogliomes (Grade II)
- oligoastrocytomes (Grade II)

_ les gliomes de haut grade ou malins :

- astrocytomes anaplasiques (Grade III)
- oligodendrogliomes anaplasiques (Grade III)
- oligoastrocytomes anaplasiques (Grade III)
- glioblastomes multiformes (Grade IV)

Bien que cette classification représente encore à ce jour l'indicateur le plus fiable pour le comportement biologique et le pronostic clinique des gliomes des adultes, celle-ci n'est pas toujours applicable aux tumeurs pédiatriques qui ont souvent des aspects histologiques particuliers. Le « grading » lui aussi peut être pris en défaut car des gliomes de bas grade peuvent montrer des index mitotiques élevés, surtout chez le jeune enfant. Cette faible valeur pronostique a été mise en évidence dans l'étude d'une vaste cohorte de 340 gliomes pédiatriques supratentoriels de type astrocytaire pour lesquelles la classification selon les critères de l'OMS ou selon des critères histologiques ne suffisait pas à les différencier en terme de survie (Gilles et al. 2000).

4.2. Particularité de la classification des gliomes infiltrants du tronc cérébral

La classification des gliomes du tronc cérébral ne s'appuie pas nécessairement sur des critères histologiques. Au cours des dernières décennies, de nombreuses classifications propres à ces tumeurs sous-tentorielles se sont succédées évoluant au gré des techniques d'imagerie. La tomodensitométrie (ou scanographie) (Berger et al. 1983; Epstein et McCleary 1986; Stroink et al. 1987) puis l'imagerie par résonnance magnétique (IRM) (Albright et al. 1993; Barkovich et al. 1990; Fischbein et al. 1996) et enfin l'association de ces deux techniques (Choux et al., 2000) ont permis de classer ces gliomes selon leur localisation anatomique ainsi que leur aspect morphologique en imagerie. Ainsi cette classification simplifiée permet de distinguer les gliomes infiltrants des lésions focales du tronc cérébral.

Les lésions focales, classées bas grade sont moins fréquentes (environ 20% des tumeurs sous-tentorielles), surviennent généralement en dehors du pont (au niveau du mésencéphale ou du bulbe rachidien) permettant ainsi un accès par chirurgie et présentent un meilleur pronostic que les lésions diffuses (Fried et al. 2012).

Les gliomes infiltrants du tronc cérébral, se développent classiquement au niveau du pont (précision terminologique anglo-saxonne de DIPG : *Diffuse Instrinsic Pontine Glioma*), montrent un aspect peu délimité en imagerie, sont classés haut grade et présentent un mauvais pronostic. Cette classification établie sur le plan morphologique et topographique est imparfaitement corrélée à des formes particulières sur le plan anatomopathologique mais les gliomes de bas grade ne sont pas infiltrants en général.

5. Comparaison moléculaire entre gliomes malins de l'adulte et ceux de l'enfant

Les gliomes malins de l'adulte et de l'enfant partagent des caractéristiques histologiques, cependant d'importantes différences ont été mises en évidence dans le mode de progression de la maladie et dans la prévalence de localisation tumorale (Paugh et al. 2010; Qaddoumi, Sultan, et Gajjar 2009).

En 2008, le glioblastome adulte bénéficiait de la phase pilote du projet « *The Cancer Genome Atlas* » (TCGA) pour être caractérisé de manière globale au niveau génomique. Les résultats de cette étude ont permis d'établir 4 sous-groupes de glioblastomes caractérisés par leur profil d'expression, leurs anomalies génétiques et leur comportement clinique (cf. **Figure 5**) (Cancer Genome Atlas Research Network 2008; Verhaak et al. 2010).

Sous-groupe	Proneural	Neural	Classique	Mésenchymal
Marqueurs exprimés	Olig2/DDL3/Sox2	MBP/MAL	EGFR/AKT2	YKL40/CD44/MET
Anomalies génétiques	TP53 IDH1 PI3K PDGFRA		Chr7 (amplification) Chr10 (perte) EGFR (amplification) CDKN2A (délétion)	NF-1 PTEN Akt
Comportement clinique	Ne répond pas à la chimiothérapie		Amélioration clinique avec traitement Témozolomide / Radiothérapie	Amélioration clinique avec traitement Témozolomide / Radiothérapie
Pronostic Survie Médiane (mois)	16,2	15,0	12,2	15,0

Figure 5 : Classification moléculaire des 4 sous-groupes de glioblastome chez l'adulte. Abréviation : Chr (Chromosome). D'après (Verhaak et al. 2010; Bartek et al. 2012).

Cet effort de caractérisation au niveau génomique a été conduit secondairement dans les gliomes de l'enfant et a révélé que les altérations génétiques observées étaient représentées avec une fréquence distincte entre les deux groupes d'âge. Ces travaux ont clairement démontré les différences génétiques entre tumeurs pédiatriques et adultes ainsi que l'hétérogénéité au sein même d'un type histologique (Rickert et al. 2001; Wong et al. 2006; Haque et al. 2007; Faury et al. 2007; Bax et al. 2010; Paugh et al. 2010; Schiffman et al. 2010; Zarghooni et al. 2010). Ces observations ont d'autant plus permis d'interpréter le manque de reproductibilité de la classification de l'OMS face à l'hétérogénéité de ces gliomes et *a fortiori* de devoir considérer leur prise en charge d'une manière plus spécifique.

Les principales altérations génétiques spécifiques par âge seront discutées dans les paragraphes suivants sans distinction topographique.

5.1. EGFR

L'EGFR (*Epidermal Growth Factor Receptor* ou Erb-1) est de loin l'oncogène le plus fréquemment impliqué dans la gliomagenèse chez l'adulte. Il code pour le récepteur transmembranaire du facteur de croissance épidermique (EGF) dont l'amplification est retrouvée dans 40 à 50% des gliomes malins de l'adulte. Dans la moitié des cas, cette amplification est associée à un réarrangement du gène (EGFRvIII) conduisant à l'expression d'une forme tronquée et constitutionnellement active de la protéine (L. Liu et al. 2005).
Bien que la surexpression de ce récepteur ait été observée de façon variable dans 10 à 80% des gliomes malins pédiatriques (Bredel et al. 1999; Gilbertson et al. 2003), l'amplification et la mutation associées sont des évènements moins fréquents dans cette population. Une série de gliomes malins pédiatriques supratentoriels a rapporté l'amplification de EGFR dans 8 des 74 cas (11%) et la délétion EGFRvIII dans 6 des 35 cas (17%) (Bax et al. 2009). D'autres auteurs ont encore confirmé ces observations (Qu et al. 2010; Paugh et al. 2010). On citera néanmoins les résultats d'une étude à ce jour jamais confirmés, portant sur une série de 11 patients atteints de DIPG dans laquelle 6 exprimaient la délétion EGFRvIII (Li et al. 2012). Hormis cette dernière, l'ensemble de ces résultats supporte la notion que l'amplification et la mutation de EGFR dans les gliomes malins de l'enfant sont nettement moins fréquentes que celles observées chez l'adulte.

5.2. PDGFR

L'activation du récepteur au PDGF (*Platelet Derived Growth Factor*) a été observée dans environ 80% des gliomes malins pédiatriques (Thorarinsdottir et al. 2008). Outre l'expression du PDGFR alpha ou beta qui a été mise en évidence dans ces tumeurs pédiatriques (Liang et al. 2008; Geoerger et al. 2009), l'amplification du gène PDGFRA s'est révélée être l'événement le plus souvent observé avec des fréquences variant entre 8 et 28% selon les études (Di Sapio et al. 2002; Wong et al. 2006; Zarghooni et al. 2010; Paugh et al. 2010; Schiffman et al. 2010; Barrow et al. 2011; Puget et al. 2012) et se rapprochant de celles observées chez l'adulte (Rao et al. 2010; Verhaak et al. 2010) Quelques rares gains/amplifications des gènes *PDGFA, PDGFB* et *PDGFRB* pourraient également contribuer à l'activation de cette voie (Bax et al. 2010; Zarghooni et al. 2010; Paugh et al. 2010).
L'absence de critère défini pour l'amplification de ce gène mais également l'échantillonnage des tissus analysés dans lesquels ces anomalies de nombre de copies touchent une population sous-clonale pourraient expliquer la disparité des résultats présentés dans ces publications. En outre, l'amplification de *PDGFRA* est plus fréquente dans les gliomes radio-induits (Paugh et al. 2010) et la plupart des études sur les DIPG étant faites sur des cas autopsiques, elles sont post-irradiation.

D'autre part, la fréquence et le type des mutations du gène *PDGFRA* observées dans les deux groupes d'âges sont différents. Typiquement, parmi les tumeurs de l'adulte amplifiées *PGFDRA*, 40% présentent également une délétion des exons 8 et 9 ($PDGFRA^{\Delta 8,9}$) (Ozawa et al. 2010), cependant la fréquence globale est d'environ 4% dans cette population (Verhaak et al. 2010; Brennan et al. 2013). Dans les tumeurs pédiatriques, cet événement particulier n'a jamais été observé mais ils sont néanmoins plus souvent mutés de façon ponctuelle, avec une fréquence estimée entre 4 et 9% (Sturm et al. 2014).

Globalement, l'identification récurrente de cette voie au cours de ces différentes études permet de considérer l'implication du PDGFR comme cible majeure dans les gliomes malins pédiatriques.

5.3. IDH1/2

L'isocitrate déshydrogénase (IDH)-1/2 est une enzyme du cycle de Krebs, qui catalyse la décarboxylation oxydative de l'isocitrate en α-cetoglutarate par réduction du $NADP^+$ en NADPH. Elle a pour rôle de protéger la cellule contre le stress oxydatif.
La mutation du gène qui entraine la substitution de l'acide aminé Arginine en position 132 altère le site de fixation de l'isocitrate, diminue ainsi l'activité normale de l'enzyme et entraine la formation d'un oncométabolite, le 2-hydroxyglutarate (2-HG) (Dang et al. 2009). Secondairement, le 2-HG est responsable une hyperméthylation de l'ADN par inhibition des déméthylases entrainant ainsi une dérégulation épigénétique et transcriptomique (Chowdhury et al. 2011; Xu et al. 2011).
Chez l'adulte, cette mutation a été très largement décrite dans 70% des gliomes de bas grade et 85% des glioblastomes secondaires et seulement dans 5% des glioblastomes primaires (Parsons et al. 2008; Balss et al. 2008; Hartmann et al. 2009; Ichimura et al. 2009; Nobusawa et al. 2009; Yan et al. 2009). Elle n'est cependant que très rarement retrouvée dans les échantillons pédiatriques avec une fréquence générale estimée à 10% principalement chez les adolescents (Balss et al. 2008; Yan et al. 2009; De Carli, Wang, et Puget 2009; Antonelli et al. 2010; Paugh et al. 2010; Schiffman et al. 2010; Setty et al. 2010; I. F. Pollack et al. 2011).

5.4. MGMT

La méthylguanine méthyltransférase (MGMT) est une enzyme importante dans le processus de réparation des lésions de l'ADN notamment causées par des agents alkylants, tel que le témozolomide (TMZ) ou les nitrosourées. Celle-ci contrecarre l'effet cytotoxique du TMZ en ôtant les groupements méthyl adduit en position O^6 sur la guanine. En absence de celle-ci, la cellule est donc plus sensible à ce traitement. La méthylation des ilots CpG situés dans le promoteur du gène est le processus par lequel son expression est inhibée. Cette modification épigénétique est observée dans environ 40% des glioblastomes de l'adulte et constitue un marqueur prédictif de réponse à ce type de traitement (Hegi et al. 2005). L'importance de la méthylation de ce promoteur dans les gliomes malins pédiatriques a été par la suite évaluée. La valeur prédictive pour la réponse au TMZ a été observée mais également une forte corrélation a été mise en évidence entre la méthylation du promoteur et la survie (Donson et al. 2007). De même cette corrélation entre la surexpression de MGMT en immunohistochimie et un pronostic défavorable a été établie sur une large cohorte de gliomes malins pédiatriques traités par chimiothérapie adjuvante à base d'agents alkylants (I. F. Pollack, Hamilton, Sobol, et al. 2006). En règle général, par comparaison avec celles de l'adulte, les tumeurs pédiatriques expriment plus fortement MGMT mais ce phénomène de

résistance ne semble pas expliquer l'absence de bénéfice observée dans le traitement de gliomes du tronc cérébral chez l'enfant dans lesquels le gène n'est pas exprimé (Chassot et al. 2012; Zarghooni et al. 2010).

5.5. PTEN

Des anomalies du gène suppresseur de tumeur PTEN ont été identifiées dans de nombreux cancers. Des mutations ou délétions du gène conduisant à une perte de fonction ou une sous-expression de la protéine induisent une dérégulation de la voie de signalisation Akt. Ces anomalies décrites dans 15 à 40% des gliomes malins de l'adulte (Smith et al. 2001) ont une valeur pronostique et prédictive dans la réponse aux traitements (Mellinghoff, Cloughesy, et Mischel 2007). Chez les enfants, ces événements plus rares (Schiffman et al. 2010) sont corrélés au grade histologique et à un mauvais pronostic (Raffel et al., 1999; I. F. Pollack et al., 2006; Mueller et al., 2012). Une autre étude a également démontré que parmi les anomalies fréquemment observées, la perte du gène était le seul facteur indépendant associé à la survie des gliomes malins pédiatriques (Korshunov et al. 2005).

5.6. Codélétion 1p/19q

L'analyse cytogénétique haute résolution par hybridation génomique comparative (CGH) a révélée des différences de profils chromosomiques notables entre les tumeurs pédiatriques et adultes. L'exemple le plus marquant concerne les oligodendrogliomes, tumeurs plus fréquentes chez l'adulte que chez l'enfant. Parmi les caractéristiques de cette tumeur, la codélétion 1p/19q correspondant à une translocation centromérique déséquilibrée t(1 ;19)(q10 ;p10) est un événement précoce retrouvé dans environ 70% des oligodendrogliomes de l'adulte et associé à un meilleur pronostic et ainsi qu'à une bonne chimiosensibilité (Cairncross et al. 1998). Cette perte simultanée est extrêmement rare chez l'enfant même si son incidence augmente avec l'âge (Raghavan et al. 2003).

5.7. Mutations somatiques de l'histone H3 et phénotype d'allongement alternatif des télomères

Encore plus récemment, grâce aux techniques de séquençage « génome entier » ou « exome entier » de gliomes malins pédiatriques, deux groupes nord-américains ont mis en évidence des mutations somatiques dans les gènes *H3F3A* et *HIST1H3B* codant pour deux isoformes de la sous-unité de l'histone H3, H3.3 et H3.1 respectivement (Schwartzentruber et al. 2012; Wu et al. 2012). De plus, la recherche de ces mutations dans une cohorte élargie de 784 gliomes pédiatriques et adultes montre que celles-ci se produisent exclusivement dans les gliomes malins pédiatriques ou du jeune adulte (âge<30 ans) (Schwartzentruber et al. 2012).

Le rôle des histones est d'organiser la chromatine pour rendre l'ADN accessible aux processus cellulaires, notamment à la réplication, à la transcription et à la réparation. Le remodelage de la chromatine est dû essentiellement à des modifications post-traductionnelles de type méthylation et/ou acétylation au niveau de résidus spécifiques situés sur les queues N-terminales des histones. Ces histones sont incorporées dans l'ADN grâce à des protéines chaperonnes, les complexes HIRA et DAXX/ATRX pour les histones de type H3.3 et le complexe CAF-1/PCNA pour les histones de type H3.1 (Hamiche et Shuaib 2012).

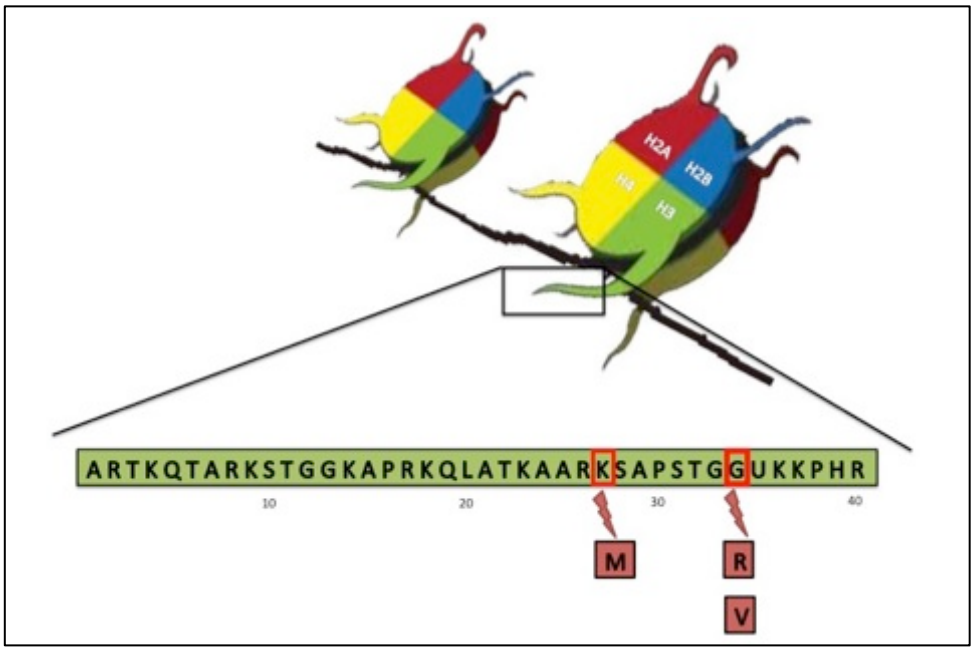

Figure 6 : Mutations de l'histone H3. Trois mutations récurrentes non-synonymes variant d'un seul nucléotide sont observées dans les gènes codant pour les isoformes H3.3 et H3.1 de l'histone H3.

Ce sont sur deux de ces résidus hautement conservés et très proches que portent les mutations (cf. **Figure 6**):

_ le résidu Lysine (K) en position 27 muté en Méthionine (M), notée K27M

_ le résidu Glycine (G) en position 36 muté en Arginine (R) ou en Valine (V), notées G34R ou G34V, respectivement.

Ces mutations ont donc pour conséquence d'abroger ces modifications post-traductionnelles affectant ainsi la régulation des gènes à proximité desquels ces histones sont chargées.

Plus largement, Schwartzentruber et ses collaborateurs ont démontré que les mutations somatiques de la voie H3.3-ATRX-DAXX sont récurrentes dans les tumeurs pédiatriques et associées au phénotype d'allongement alternatif des télomères (ALT). Décrit dans 5-10% des cancers, l'ALT est un mécanisme responsable de la maintenance des télomères indépendamment de la télomérase via des phénomènes de recombinaisons homologues non réciproques entre différents télomères.

Ces mutations mono-alléliques et mutuellement exclusives sont retrouvées spécifiquement dans les gliomes malins chez l'enfant et le jeune adulte (âge<30ans). Enfin, ces mutations sont non seulement associées à des paramètres cliniques tels que la localisation anatomique et l'âge du patient mais montrent également un profil de méthylation et d'expression spécifique à chacune d'entre elles (Sturm et al. 2012).

6. Diagnostic

Le diagnostic de gliome infiltrant du tronc cérébral se base actuellement sur un tableau clinique évocateur et sur les données recueillies en imagerie.

6.1. Signes cliniques

Cette maladie montre un pic d'incidence situé entre 5 et 10 ans et la plupart des patients présentent des signes neurologiques caractéristiques de la zone atteinte. En se développant les cellules tumorales compriment les noyaux et les tractus présents dans la protubérance annulaire. Ceci se manifeste par une triade symptomatique :

- Un déficit cérébelleux (perte de l'équilibre et de la coordination)
- Une affection des voies longues (perte sensorielle ou surtout motrice des extrémités et du tronc)
- Une paralysie des nerfs crâniens (troubles oculomoteurs et/ou de la déglutition/phonation).

Le délai entre les premiers symptômes et le diagnostic est relativement court (inférieur à deux mois) et représente un important critère diagnostique.

6.2. Imagerie

Le diagnostic est établi à partir des caractéristiques à l'imagerie. L'IRM présente une lésion intrinsèque et infiltrée, centrée sur la protubérance et rarement exophytique. Occupant classiquement plus de 50% du pont, la tumeur est hypointense en T1 et hyperintense en T2. Bien que d'autres lésions puissent également survenir au niveau du tronc cérébral, le tableau clinique, l'âge de déclaration et les caractéristiques à l'imagerie suffisent en général pour établir le diagnostic.

Il y a une nécessité de développer d'autres méthodes non invasives permettant de suivre l'évolution de la maladie. En complément de cette méthode standard, de nouvelles approches en Spectroscopie de Résonnance Magnétique (MRS), en tenseur de diffusion ou en perfusion pourraient permettre de suivre l'évolution de la maladie, que ce soit sa réponse au traitement ou bien sa progression. Quelques équipes ont commencé à explorer cette possibilité dans les gliomes infiltrants du tronc cérébral pédiatriques (Blüml et al. 2011; Sedlacik et al. 2013; Seymour et al. 2008).

6.3. Biopsie

Depuis une vingtaine d'année, l'IRM est considéré comme l'examen standard suffisant pour établir le diagnostic de cette tumeur, cependant de rares cas de tumeurs non gliales siégeant dans le tronc cérébral ont été rapportés et souligne l'intérêt de la biopsie en cas de lésion atypique (Sufit et al. 2012; Zagzag et al. 2000).
Longtemps, l'argument majeur en défaveur de la biopsie fut que le résultat histologique n'impactait en rien la décision thérapeutique et le pronostic du patient (Albright et al. 1993) ne pouvant ainsi motiver cette pratique en routine. De plus, la crainte liée au risque du geste chirurgical s'est longtemps exprimée au sein de la communauté des neurochirurgiens et des neuro-oncologues. Ce risque a finalement été réévalué par plusieurs groupes européens qui ont démontré le faible taux de morbidité et l'absence de mortalité en plus de son intérêt diagnostique (Franzini et al. 1988; Leach et al. 2008; Pincus et al. 2006; Roujeau et al. 2007; Samadani et al. 2006). Cette procédure est aujourd'hui considérée comme suffisamment sûre (Puget, Blauwblome, et Grill 2012).

Deux voies d'abord sont possibles pour réaliser ce geste : l'approche transcérébelleuse et l'approche transcérébrale transfrontale. Les patients biopsiés au sein de notre réseau le sont toujours par voie transcérébelleuse au niveau de la jonction entre le pédoncule cérébelleux moyen et le tronc cérébral lui-même.

Récemment, la systématisation de cette procédure dans un contexte d'évaluation prospective a montré son intérêt dans plusieurs essais cliniques en France (Geoerger et al. 2009; Geoerger et al. 2011) (et étude CILENT en cours, *Cilengitide in Combination With Irradiation in Children With Diffuse Intrinsic Pontine Glioma,* NCT01165333) mais également en recherche avec la réalisation d'études génomiques (Puget et al. 2012).
L'autopsie est également un autre moyen de recueillir du tissu tumoral. Plusieurs groupes en ont montré l'intérêt dans l'établissement de collections d'échantillons destinées à des analyses génomiques ou bien à l'établissement de modèles cellulaires dérivés (Broniscer et al. 2010; Caretti et al. 2012; Monje et al. 2011).

Ces dernières années, grâce à un effort dans la mise en œuvre de collecte d'échantillons de gliomes infiltrants du tronc cérébral au diagnostic ou à l'autopsie, un nombre sans précédent d'études biologiques et génomiques a pu être mené et améliorer la connaissance de ces tumeurs.
Les avancées permises dans la connaissance de la biologie de cette tumeur seront abordées dans la suite de ce rapport (cf. **INTRODUCTION Partie III**).

7. Traitement

La radiothérapie est le traitement standard des gliomes infiltrants du tronc cérébral. La dose totale délivrée est de 54 à 60 Gy sur 6 semaines en fraction de dose journalière de 180 à 200 cGy. La zone irradiée recouvre la tumeur avec une marge de 1 à 2 cm dans le tissu normal. Deux tiers des patients présentent une amélioration des symptômes neurologiques avec un contrôle de la croissance tumorale mais cette réponse est transitoire puisque l'estimation, peut être un peu pessimiste au vu de notre expérience actuelle du prolongement de survie est de 3 mois en moyenne (Langmoen et al. 1991).

8. Progression et survie

8.1. Survie générale et survie sans progression

D'après les données historiques et celles d'essais récents, la médiane de survie sans progression est de 5 à 9 mois et celle de la survie globale des patients atteints de gliomes du tronc est de 8 à 11 mois et la survie (Hargrave, Bartels, et Bouffet 2006). La plupart des patients décèdent dans les deux ans après diagnostic (cf. **Figure 7**).

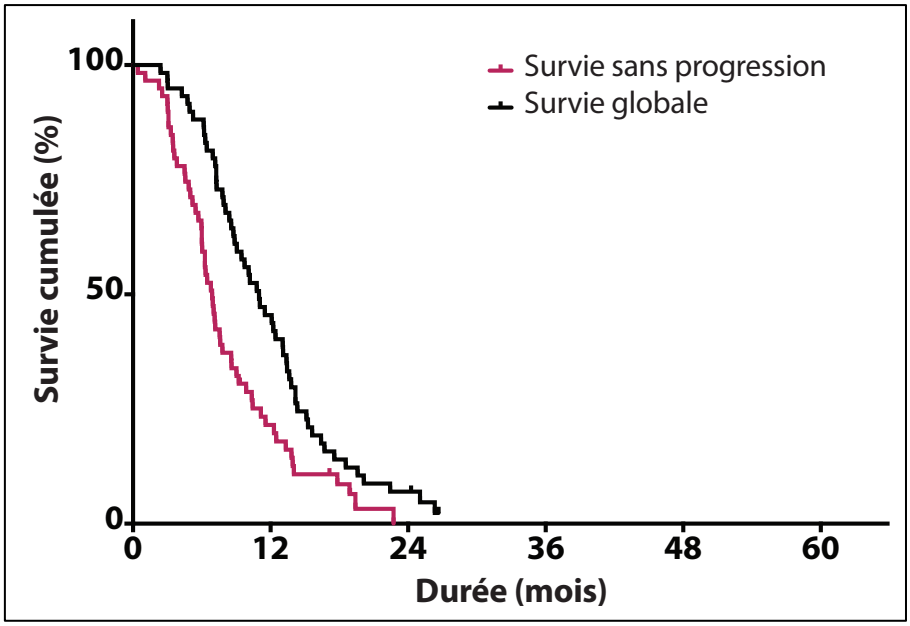

Figure 7 : Courbes de survie globale et survie sans progression des gliomes infiltrants du tronc cérébral. Etablies sur une cohorte de 60 enfants suivis à l'Institut Gustave Roussy (Villejuif) sur la période 2006-2013.

8.2. Progression tumorale

La rechute survient généralement localement 3 à 8 mois après la fin de la radiothérapie. Celle-ci se manifeste cliniquement et/ou radiologiquement et le siège de la rechute concerne le volume irradié élargi.

Certaines études ont évalué l'extension de la progression tumorale à l'autopsie et ont mis en évidence un envahissement tumoral des structures supratentorielles ainsi qu'une dissémination leptoméningée (Yoshimura et al. 2003). D'autres auteurs ont également constaté cette dissémination leptoméningée au diagnostic et une corrélation entre la présence de ces lésions et un raccourcissement de la durée de survie (Wagner et al. 2006; Sethi et al. 2010).

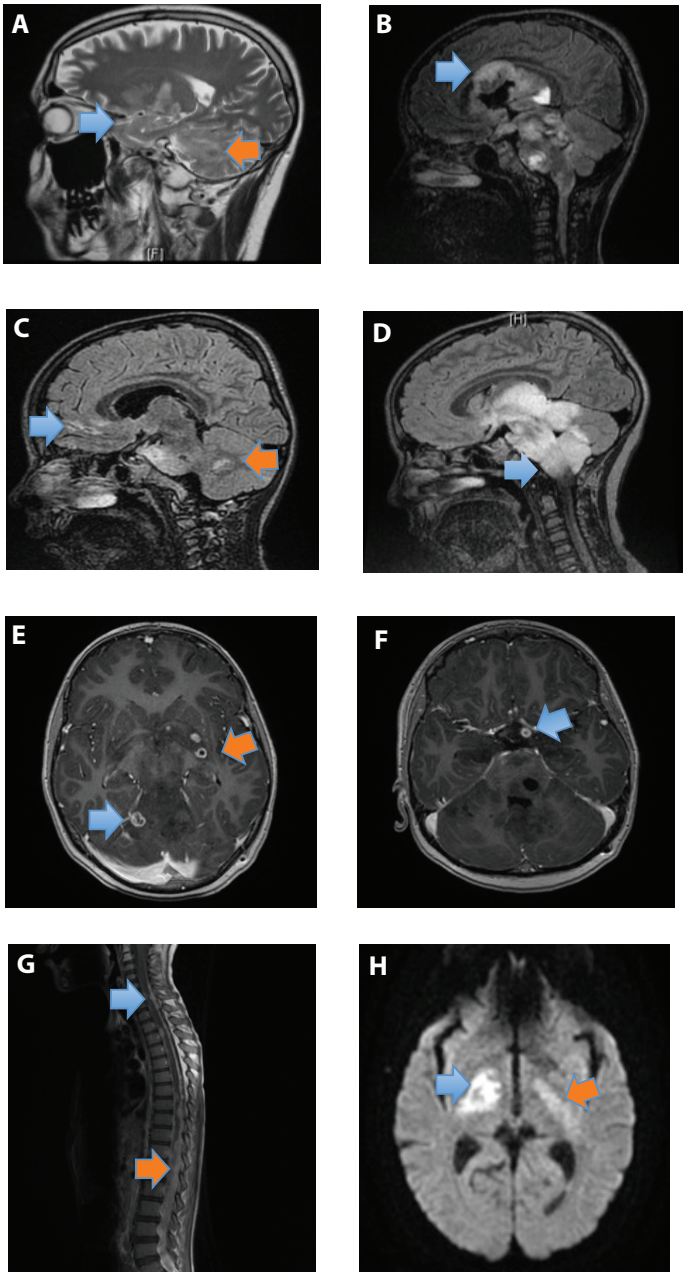

Figure 8 : Images de progression tumorale de DIPG.
(A) Séquence sagittale T2 montrant une infiltration tumorale dans le lobe temporal (bleu) et dans la substance blanche du cervelet (orange).
(B) Séquence sagittale T2 montrant une propagation intraventriculaire (bleu).
(C) Séquence FLAIR sagittale montrant une propagation leptoméningée dans le lobe frontal (bleu) et de l'infiltration de la substance blanche du cervelet (orange).
(D) Séquence FLAIR sagittale montrant la propagation centrifuge et bulbaire invasion (bleu)
(E) Séquence axiale T1 avec injection de gadolinium montrant nodules tumoraux éloignés dans la partie droite du vermis (bleu) et dans la capsule interne (orange).
(F) Séquence axiale T1 avec injection de gadolinium montrant un nodule tumoral éloigné dans le tractus optique gauche.
(G) Séquence sagittale T1 avec injection de gadolinium de la colonne vertébrale montrant une propagation leptoméningée (bleu) et des nodules dans le canal rachidien (orange).
(H) Imagerie de diffusion montrant la propagation de la tumeur dans le thalamus (bleu) et dans le pallidum (orange).

Partie II : Essais cliniques dans les gliomes infiltrants du tronc cérébral

1. Radiothérapie

La radiothérapie étant actuellement le seul traitement efficace, de nombreux essais ont cherché à l'améliorer davantage en modifiant les doses, les modalités d'administration ou bien en le combinant avec des chimiothérapies concomitantes.

Tandis que les premières études ont déterminé le seuil d'efficacité à 50 Gy (F. Lee 1975; T. H. Kim et al. 1980; Littman et al. 1980) d'autres évaluant l'efficacité de doses supérieures à 60 Gy allant jusqu'à 78 Gy en hyperfractionnement n'ont montré aucun bénéfice sur la survie (Freeman et al. 1993; Packer et al. 1994; Mandell et al. 1999). D'autres études ayant évalué l'efficacité de la radiothérapie délivrée en hypofractionnement avec pour but l'amélioration de la qualité de vie du patient en réduisant la durée de traitement à 3 semaines a rapporté des résultats comparables à ceux du fractionnement classique (Janssens et al. 2013; Negretti et al. 2011).

D'autres stratégies ont tenté en vain d'améliorer l'efficacité de la radiothérapie en la combinant avec des agents radiosensibilisants (Aquino-Parsons, Hukin, et Green 2008; Bradley et al. 2013).

2. Chimiothérapies

Un effort important a été fait pour évaluer l'utilité des chimiothérapies dans le schéma thérapeutique de ces patients. A ce jour, un large panel de molécules cytotoxiques a déjà été testé au diagnostic ou à la progression tumorale en complément de la radiothérapie et selon divers protocoles : chimiothérapies néo-adjuvantes, concomitantes et adjuvantes administrées en monothérapie, en combinaison ou encore à hautes doses avec greffe de cellules souches hématopoïétiques. Les résultats de ces études sont rapportés dans le **tableau 1**. Aucun de ces essais n'a pu conclure sur un bénéfice substantiel en terme d'allongement de survie même si certains patients ont répondu transitoirement. Pour la plupart, ces études ne sont pas randomisées et comparées au bras historique correspondant aux patients traitées par radiothérapie conventionnelle délivrée en une seule fraction de dose journalière de 1,8 à 2 Gy pour lesquels la médiane de durée de survie sans progression et de survie globale sont estimées entre 5 et 7 mois et 9 à 13 mois respectivement (Jennings et al. 2002; Frappaz et al. 2008).

3. Témozolomide

Le témozolomide qui s'inscrit dans le protocole standard des gliomes malins de l'adulte (Stupp et Roila 2008) a été largement évalué à travers plusieurs schémas de combinaisons et n'a démontré aucune efficacité dans ces tumeurs sous-tentorielles chez l'enfant (Sirachainan et al. 2008; Jalali et al. 2010; Sharp et al. 2010; Cohen et al. 2011; Chassot et al. 2012; Warren et al. 2012).

Tableau 1 : Résultats des essais cliniques de chimiothérapies dans les gliomes du tronc cérébral

Molécule	*Modalité*	*Tumeur*	*Pronostic*	*Auteurs*	*Année*
Prednisone, CCNU, Vincristine	RT (groupe A) *vs*. RT plus CT Adjuvante (groupe B)	BSB (n=74)	Survie à 5 ans : A, 17% ; B, 20%	Jenkin et al.	1987
Cisplatine, Cyclophosphamide	HRT plus CT concomitante	BSG au diagnostic (n=35)	Survie médiane : 9 mois	Kretschmar et al.	1993
Thiotepa, Etoposide	RT plus CT Haute Dose Adjuvante (avec autogreffe)	DIPG au diagnostic et recidivants (n=16)	Survie médiane : 11,4 mois	Dunkel et al.	1998
Cisplatine	Groupe A : RT plus CT concomitante Groupe B : HRT plus CT concomitante	DIPG au diagnostic (n=106; A, 66 ; B,64)	Survie médiane : A, 8,5 mois ; B, 8 mois	Mandell et al.	1999
Cisplatine	HRT plus CT concomitante	DIPG au diagnostic (n=34)	Survie médiane : 12 mois	Allen et al.	1999
Thiotepa, Busulfan	RT plus CT Haute Dose Adjuvante (avec autogreffe)	DIPG au diagnostic (n=35)	Survie médiane : 10 mois	Bouffet et al.	2000
Tamoxifène	RT plus CT concomitante	DIPG au diagnostic (n=29)	Survie médiane : 9 mois	Broniscer et al.	2000
Carboplatine	RT plus CT Néo-adjuvante et Adjuvante	DIPG au diagnostic (n=19)	Survie médiane : 11 mois	Doz et al.	2002
Groupe A : carboplatin, etoposide, vincristine Groupe B : cisplatin, cyclophosphamide, etoposide, vincristine	HRT plus CT Adjuvante	DIPG au diagnostic (n=63; A, 32 ; B,31)	Survie à 1 an : 32 % (A et B)	Jennings et al.	2002
Trophosphamide, Etoposide	RT plus CT Concomitante	DIPG au diagnostic (n=20)	Survie médiane : 8 mois	Wolff et al.	2002
Etanidazole	HRT plus CT concomitante	DIPG au diagnostic (n=18)	Survie médiane : 9 mois	Marcus et al.	2003
Témozolomide	RT plus CT Adjuvante	DIPG au diagnostic (n=36)	Survie médiane : 12 mois	Broniscer et al.	2005
Topotécan	HRT plus CT Concomitante	DIPG au diagnostic (n=32)	Survie médiane : 8,3 mois	Bernier-Chastagner et al.	2005
HIT - GBM (carboplatine, etoposide, ifosfamide / trophosphamide, vicristine)	RT plus CT Concomitante	DIPG au diagnostic (n=153)	Survie à 1 an : 40 %	Wagner et al.	2006
Thalidomide	RT plus CT Concomitante	DIPG au diagnostic (n=12)	Survie médiane : 9 mois	Turner et al.	2007
Vincristine Etoposide	RT plus CT Concomitante	DIPG au diagnostic (n=30)	Survie médiane : 10,3 mois	Korones et al.	2008
Témozolomide (Acide rétinoïque adj.)	RT plus CT Concomitante	DIPG au diagnostic (n=12)	Survie médiane : 13,5 mois	Sirachainan et al.	2008
Cisplatin, Etoposide, Vincristine, Ifosfamide	RT plus CT concomitante	DIPG au diagnostic (n=37)	Survie médiane : 9 mois	Wolff et al.	2010
Témozolomide	RT plus CT concomitante	DIPG au diagnostic (n=20)	Survie médiane : 9,2 mois	Jalali et al.	2010
Thalidomide Témozolomide	RT plus CT concomitante	DIPG au diagnostic (n=12)	Médiane de survie sans progression : 7,5 mois Survie médiane : 12 mois	Kim et al.	2010
Témozolomide	RT plus CT concomitante	DIPG au diagnostic (n=15)	Survie médiane : 9,8 mois	Sharp et al.	2010
Thalidomide Celecoxib - etoposide	RT plus CT concomitante	DIPG au diagnostic (n=8)	Survie médiane : 12,5 mois	Kavivuori et al.	2011
Témozolomide (+ O6BG*)	RT plus CT Adjuvante	Groupe A : HGG récidivants (n=25) Groupe B : BSG au diagnostic (n=16)	Médian de survie sans progression : A, 52 jours ; B, 60 jours	Warren et al.	2011
Témozolomide	RT plus CT Concomitante	DIPG au diagnostic (n=63)	Survie médiane : 9,6 mois	Cohen et al.	2011
Interferon α	RT plus CT Adjuvante	DIPG au diagnostic (n=32)	Médiane de survie sans progression : 7,8 mois	Warren et al.	2012

*adj. : adjuvant ; BSG : Gliome du tronc cérébral ; CT : Chimiothérapie ; DIPG : Gliome infiltrant du tronc cérébral ; HRT : Radiothérapie hyperfractionnnée ; RT : Radiothérapie ; * : modificateur de réponse biologique.*
D'après Warren 2012, Kebudi 2013.

4. Thérapies anti-angiogéniques

Parmi les molécules anti-angiogéniques en cours d'évaluation, la thalidomide en traitement combiné à d'autres molécules chimiothérapeutiques et concomitant à la radiothérapie semble apporter un bénéfice en terme de qualité de vie (C.-Y. Kim et al. 2010; Kivivuori et al. 2011) (cf. **Tableau 1**).

En revanche, le bevacizumab, inhibiteur du *Vascular Endothelial Growth Factor* (VEGF) indiqué en seconde ligne chez l'adulte, a été également évalué chez les enfants mais n'a pas démontré de bénéfice équivalent dans les gliomes infiltrants du tronc cérébral en rechute (Gururangan et al. 2010) (cf. **Tableau 2**). Son intérêt en combinaison avec l'irradiation comme traitement initial est en cours d'évaluation (*Molecularly Determined Treatment of Diffuse Intrinsic Pontine Gliomas*, NCT01182350).

5. Thérapies ciblées

Plus récemment, les thérapies moléculaires ciblées ont été introduites dans le traitement de ces tumeurs via des essais de phases précoces. En raison de la faible disponibilité de ces tissus, ces nouvelles approches thérapeutiques ont d'abord été influencées par les cibles définies dans les gliomes malins des adultes.

L'EGFR et le PDGFR dont l'activation liée à des amplifications et/ou à des mutations ont ainsi été des candidats privilégiés pour lesquels de nombreux inhibiteurs ont été développés. Ceux-ci regroupent des analogues de l'ATP se fixant sur les sites catalytiques tyrosine-kinase tels que l'erlotinib et le gefitinib (EGFR), l'imatinib (PDGFR), ainsi que des anticorps bloquants l'interaction du ligand avec son récepteur à l'image du nimotuzumab (EGFR). Certains inhibiteurs dits multi-ciblés ont la propriété d'inhiber simultanément l'activité tyrosine kinase de plusieurs récepteurs, et sont donc susceptibles d'agir sur plusieurs processus oncogéniques simultanés. C'est le cas de dasatinib (PDGFR, c-KIT, tyrosine-kinases de la famille Src) et de vandetanib (EGFR, VEGFR).

D'autres voies dérégulées dans les gliomes ont également leurs inhibiteurs. C'est le cas de la farnesyl-transférase, enzyme essentielle dans la transduction du signal de la voie RAS et qui contribuent au caractère radio-résistant des gliomes. Des altérations de la voie de signalisation PI3K/Akt/mTOR ont aussi été fréquemment observées justifiant leur intérêt de cible thérapeutique.

Malgré cette recherche intensive récemment menée sur la thérapie moléculaire ciblée, son efficacité reste faible (cf. **Tableau 2**).

Tableau 2 : Récapitulatifs des essais cliniques de thérapies ciblées dans les gliomes malins du tronc cérébral

Voie(s) ciblée(s)	Classe d'inhibiteur Molécule	Phase	n	Pronostics	Commentaires	Auteurs	Année
EGFR	**petites molécules:**						
	Gefitinib	II	43	Survie à 1 an : 56,4%	3 patients en maladie stable à plus de 36 mois du diagnostic	Pollack et al.	2011
	Erlotinib	I	21	Médiane de survie : 12 mois	Légère correlation entre le niveau d'expression d'EGFR et la PFS	Geoerger et al.	2011
EGFR/ VEGFR	Vandetanib	I	35	Survie à 1 an : 38%	2 survies à long-terme à 2 ans ; MTD : 145 mg/m2 ; Corrélation entre le niveau plasmatique de VEGF avant traitement et la PFS	Broniscer et al.	2010
	anticorps bloquant:						
EGFR	Nimotuzumab	II	47	Médiane de survie : 9,4 mois	Corrélation entre la réponse radiologique et la survie	Massimino et al.	2011
PDGFR	**petites molécules:**						
	Imatinib	I	35	Survie à 1 an : 46%	Risque cumulé d'hémorragie intra-tumorale, MTS : 265 mg/m2	Pollack et al.	2007
VEGFR	**anticorps bloquant:**						
	Bevacizumab	II	16 R	Pas d'amélioration	DIPG récidivants - Pas de réponse radiologique	Gururangan et al.	2010
mTOR	**petites molécules:**						
	Temsirolimus	II	11 R		45 % des DIPG ont présenté une stabilisation de la maladie	Geoerger et al.	2012
RAS	**petites molécules:**						
	Tipifarnib	II	40	Médiane de survie : 8,3 mois / Survie à 1 an : 34,3%		Haas-Kogan et al.	2011
EGFR/ PDGFR/ VEGFR	**petites molécules:**						
	Dasatinib + Vandetanib	I	25	Survie à 1 an : 52%±10%	MTS : 65 mg/m2 pour chaque molécule	Broniscer et al.	2013

MTS : Dose maximum tolérée ; n : nombre de patients ; PFS : Survie sans progression ; R : Récidivant. D'après (Kebudi et Cakir 2013)

6. Causes des échecs

Les causes de cet échec sont multiples. Parmi celles-ci, la biodisponibilité limitée de ces molécules au sein de la tumeur ainsi que l'hétérogénéité moléculaire et cellulaire dans ces tumeurs expliquent en partie l'échec de ces monothérapies ciblées. En réponse à ces problèmes, de nouveaux concepts thérapeutiques émergent, à l'image de la thérapie personnalisée. Dans celle-ci, le profil moléculaire tumoral du patient serait déterminé afin de proposer une thérapie adaptée aux caractéristiques moléculaires de la tumeur. L'émergence de ce concept offre des perspectives thérapeutiques à explorer mais nécessite pour cela une meilleure connaissance des processus qui régissent cette gliomagenèse très particulière.

Partie III: Biologie des gliomes infiltrants du tronc cérébral

Jusqu'à récemment, la connaissance sur la biologie de ces tumeurs était limitée en raison d'un manque d'accès au tissu tumoral. La mise en place de collectes d'échantillons tumoraux au diagnostic et à l'autopsie a permis d'avancer dans la compréhension de cette tumeur. Nous savons aujourd'hui que les DIPG sont des entités particulières non seulement biologiquement différentes des gliomes malins de l'adulte mais encore des autres gliomes de l'enfant.

1. Mise en évidence de sous ensembles anatomiques

1.1 Profils génomiques

Plusieurs analyses génomiques haute résolution sur puce à ADN révèlent que les gliomes malins pédiatriques partagent des caractéristiques moléculaires quelque soit leur localisation dont certaines varient en fréquence. Il n'est donc pas possible de distinguer clairement ces deux groupes sur la base des anomalies chromosomiques du nombre de copie (Paugh et al. 2011; Puget et al. 2012). Typiquement, le gain du chromosome 1q est plus fréquent dans les gliomes infiltrants du tronc cérébral que dans les glioblastomes adultes mais n'est pas significativement différent des supratentoriels pédiatriques.

En revanche, la comparaison de profils d'expression génique des gliomes malins infratentoriels avec les supratentoriels montrent clairement des différences. L'analyse en composante principale (PCA) a montré un regroupement des échantillons selon leur localisation et ainsi l'existence d'une signature transcriptomique (Paugh et al. 2011; Puget et al. 2012). Parmi les gènes les plus différentiellement exprimés entre les deux groupes, on retrouve de manière intéressante ceux impliqués dans le processus développemental de cette région du SNC, tels que les gènes de la famille HOX.

L'étude menée par notre groupe a également stratifié les tumeurs supratentorielles en distinguant les localisations hémisphérique, thalamique et celle de la ligne médiane. L'analyse transcriptomique montre une similitude transcriptomique entre les tumeurs du tronc et les échantillons issus de la région thalamique ou médiane et leur distinction de ceux issus des hémisphères (Puget et al. 2012). Ceci suggère l'existence probable d'un précurseur commun entre les tumeurs pontiques et thalamiques, raison pour laquelle cette ressemblance biologique devra être considérée par la suite dans la pratique clinique.

1.2 Répartition anatomique des mutations somatiques de l'histone H3

Nous savons désormais que les mutations de l'histone H3 sont spécifiques des gliomes malins pédiatriques (cf **Introduction Partie I,5**). Il a été de plus mis en évidence une répartition de chacune des ces mutations.

En effet, la mutation K27M survient surtout dans les tumeurs dites «de la ligne médiane » regroupant le pont et le thalamus chez le sujet jeune (âge médian : 11 ans) tandis que la mutation G34R/V a été retrouvée uniquement dans les tumeurs localisées dans les hémisphères cérébraux chez le sujet plus âgé (âge médian : 20 ans) (Sturm et al. 2012; Wu et al. 2012).

Ces observations soulignent d'importantes différences biologiques sous-jacentes de la gliomagenèse et corroborent l'existence de sous-ensembles anatomiques et à travers les âges indiquant l'existence probable d'une origine cellulaire différente à un instant critique du développement de ces structures cérébrales.

2. Cibles spécifiques dans les gliomes infiltrants du tronc cérébral

2.1 PDGFRα

PDGFRα reste encore la cible prédominante dans les gliomes infiltrant du tronc cérébral dont la signalisation aberrante a été rapportée dans de nombreuses études.

Ce récepteur transmembranaire appartient à la famille des récepteurs à activité tyrosine-kinase de classe III, qui comprend également PDGFRβ et KIT.

Suite à la liaison du ligand, la dimérisation du récepteur va se produire induisant une trans-phosphorylation du domaine intracellulaire et l'activation du récepteur. Une fois activés, les effecteurs vont être recrutés au niveau des résidus phosphorylés et induire l'activation des voies de signalisation en aval telles que celles des MAP-kinases (*mitogen-activated protein kinase*) et de PI3 kinase (*phosphatidylinositol-3 kinase*). Ces voies sont impliquées dans les phénomènes de prolifération, la différentiation et la migration cellulaire. Dans le SNC, la voie de signalisation du PDGF joue un rôle important dans le développement, en contrôlant la prolifération des cellules gliales, principalement celle des oligodendrocytes (Calver et al. 1998; Andrae, Gallini, et Betsholtz 2008).

Cette voie a souvent été mise en cause dans les gliomes malins où récepteurs du PDGF et ligands sont généralement co-exprimés, ce qui suggère une stimulation autocrine contribuant à la croissance tumorale. Dans différents modèles expérimentaux, il a été démontré que la surexpression du ligand conduisait à la formation de tumeurs de type glial (Uhrbom et al. 1998). A *contrario*, l'interruption de l'axe PDGF/PDGFR conduit à un ralentissement de la croissance tumorale dans ces modèles animaux (Uhrbom et al. 2000; Lokker et al. 2002).

Parmi les multiples causes conduisant à l'activation aberrante de cette voie, l'amplification de PDGFRA du gène a clairement été identifiée. Dans le cas des gliomes infiltrant du tronc cérébral, cette anomalie survient encore plus régulièrement que dans les autres tumeurs, avec une fréquence pouvant atteindre jusqu'à 36 % selon les études (Paugh et al. 2010; Zarghooni et al. 2010; Barrow et al. 2011; Puget et al. 2012; Paugh et al. 2013). L'amplification des gènes codant pour les ligands a également été rapportée (Zarghooni et al. 2010).

Enfin, l'activité oncogénique de PDGFRA peut être également liée à des mutations activatrices dites « gain-de-fonction ». Chez l'adulte, il a été observé que 40% des glioblastomes amplifiés PDGFRA présentaient une délétion des exons 8 et 9 ($PDGFRA^{\Delta 8,9}$) conduisant à la perte d'une portion dans le domaine extracellulaire et à l'activation constitutive du récepteur (Ozawa et al. 2010). Différentes délétions intragéniques surviennent également dans les gliomes de l'enfant, cependant la mutation $PDGFRA^{\Delta 8,9}$ n'a jamais été retrouvée. Le séquençage du gène comprenant 23 exons rapporte plusieurs mutations réparties dans différentes régions de la protéine sans définir de mutation dite « *hotspot* » à l'image de la D842V situé dans le domaine kinase et décrite dans les tumeurs gastro-intestinales. L'ensemble des mutations décrites est rapporté dans la **figure 9**. La fréquence totale de ces mutations a été définie à environ 10% (Puget et al. 2012; Schwartzentruber et al. 2012; Paugh et al. 2013). Récemment, Paugh et ses collaborateurs ont analysé des mutants pour les différents domaines fonctionnels de la protéine et ont démontré leur activation constitutive, leur pouvoir tumorigénique et leur sensibilité aux petites molécules inhibitrices. En pratique clinique, l'exploration d'inhibiteur de cette voie a déjà été menée en monothérapie (cf. **Tableau 2** plus haut) et ne rapporte pas d'efficacité probante avec l'imatinib à de rares exceptions près (I. F. Pollack et al. 2007; Geoerger et al. 2009).

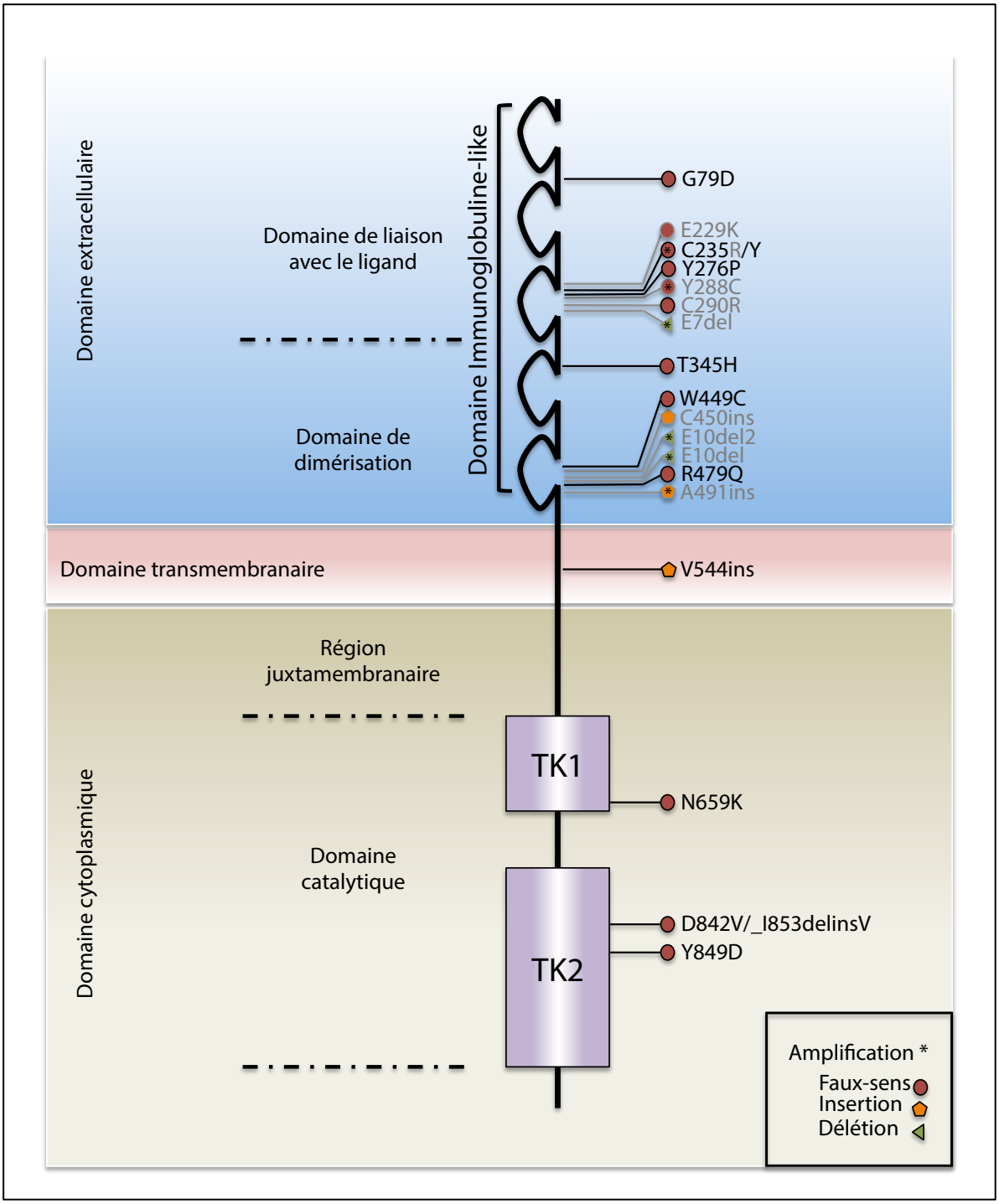

Figure 9 : Structure et mutations du PDGFRα décrites dans les gliomes malins pédiatriques. Ce récepteur est caractérisé par une structure moléculaire spécifique comprenant un domaine extracellulaire où se fixe le ligand, composé de cinq boucles immunoglobulin-like, un domaine cytoplasmique avec une région juxtamembranaire, un domaine tyrosine kinase (TK) divisé en deux partie : TK1, zone de fixation à l'adénosine triphosphate (ATP), et TK2, site actif de la phosphotransférase. Les mutations sont distribuées sur l'ensemble des domaines. En noir et en gris, les mutations décrites dans les gliomes infiltrants du tronc cérébral et celles dans les gliomes supratentoriels respectivement. L'étoile indique les mutations rapportées conjointement avec l'amplification du locus *PDGFRA*. D'après (Schwartzentruber et al. 2012; Puget et al. 2012; Paugh et al. 2013).

2.2 MET

Parmi les amplifications génomiques les plus fréquentes, le gène codant pour le récepteur MET apparaît également comme une cible privilégiée. Il est important de noter que certaines tumeurs présentent une amplification simultanée de plusieurs récepteurs à tyrosine-kinases et ce phénomène est particulièrement surreprésenté pour PDGFRA et MET dans les gliomes infiltrant du tronc cérébral (Paugh et al. 2011; Puget et al. 2012). De manière intéressante, la confirmation par FISH de ces évènements révèle une hétérogénéité intra-tumorale où coexistent des populations sous-clonales amplifiées pour l'un ou l'autre gène de manière indépendante ou bien encore des populations cellulaires co-amplifiées pour les deux gènes simultanément. Ces observations justifient l'utilisation d'inhibiteurs multi-ciblés ou bien de combinaisons d'inhibiteurs.

2.3 PI3KCA, 1er oncogène muté dans les gliomes infiltrants du tronc cérébral

Les PI3-Kinases sont une famille d'enzymes qui jouent un rôle important dans la transduction des signaux de croissance cellulaire en catalysant la phosphorylation du lipide membranaire PIP_2 en PIP_3. La PI3-Kinase est constituée d'une sous unité régulatrice (p85) et d'une sous-unité catalytique (p110α). Plusieurs études ont révélé l'existence de mutations « gain-de fonction » dans le gène PI3KCA qui code pour la sous-unité catalytique p110α dans différents cancers et notamment dans le glioblastome (Samuels et al. 2004).

Notre groupe a par ailleurs mené un criblage de 983 mutations dans 115 oncogènes et gènes suppresseurs de tumeur connus sur 20 biopsies de gliome infiltrant du tronc cérébral. Cette étude a révélé le gène PI3KCA 1er oncogène muté dans ces tumeurs avec un taux de 15% (Grill, Puget, Andreiuolo, Philippe, MacConaill, et al. 2012).

2.4 La mutation H3 K27M et dérégulation épigénétique

L'implication indirecte de modifications épigénétiques dans la genèse des cancers est de plus en plus reconnue. Cependant, les mutations de l'histone H3 nouvellement décrites dans ces gliomes pédiatriques constituent de manière inédite les premières anomalies affectant directement les histones.

La mutation H3K27M est donc retrouvée dans 80% des gliomes infiltrants du tronc cérébral et touche deux isoformes de l'histone H3 : H3.3 et sa forme canonique H3.1 codées par les gènes *H3F3A* et *HIST1H3B* respectivement. Comme la mutation G34R/V uniquement décrite dans les gliomes malins hémisphériques, la mutation faux-sens K27M concerne un résidu hautement conservé et est hétérozygote, ce qui suggère un gain de fonction de la protéine. Cette mutation affecte deux modifications post-traductionnelles : la méthylation (H3K27me2/3) et l'acétylation (H3K27ac). La première modification a pour conséquence la répression des gènes via l'intervention du complexe répresseur Polycomb 2 (PRC2) ; la seconde se produit au niveau des promoteurs de gène actifs. De manière étonnante, bien que la mutation soit hétérozygote, elle entraine une réduction globale de H3K27me2/3 mais pas de H3K27ac. Ce qui suggère que la mutation inhibe de manière dominante l'activité méthyltransférase de PRC2. En effet, les études biochimiques menées par Lewis ont démontré que le mutant H3K27M se liait au site catalytique de la sous-unité Ezh2 de PCR2 et en inhibait son activité enzymatique (Lewis et al. 2013) (cf. **Figure 10**). Cependant, ce phénomène n'est pas uniforme sur le génome. En effet, en comparant les données obtenues par la technique d'immunoprécipitation de la chromatine suivie de séquençage (ChIP-Seq) à partir d'une lignée cellulaire de DIPG mutée H3K27M et d'une lignée de cellules souches neurales (NSC), Chan et ses collaborateurs ont mis en évidence l'augmentation focalisée de la marque H3K27me2/3 sur certains *loci*, spécifiques au mutant. Par comparaison aux NSC, cette approche met en évidence 3 groupes de gènes dans la lignée mutée : ceux présentant une perte de H3K27me2/3 (groupe A), ceux dont la densité H3K27me2/3 n'est pas modifiée (groupe B) et ceux présentant un gain de H3K27me2/3. Pour savoir dans quelle mesure cette redistribution génomique des marques de méthylation affecte l'expression des gènes, les auteurs ensuite ont comparé le profil transcriptomique de 2 lignées mutées aux NSC par séquençage de l'ARN (RNA-Seq).

Cette analyse révèle une surexpression des gènes du groupe A et une sous expression des gènes du groupe C. Par la suite, l'analyse fonctionnelle de ces groupes montre que le groupe A est associé à des processus neurologiques variés tandis que le groupe C concernent des voies du cancer (Chan et al. 2013). De manière générale, cette observation fait apparaître un rôle fonctionnel de la mutation beaucoup plus complexe qu'attendu impliquant une redistribution spécifique des marques de méthylation.

L'effet de cette mutation a ensuite été exploré *in vivo* dans un modèle de gliome du tronc cérébral induit par PDGF. L'expression de H3K27M dans un contexte de suppresseur de tumeur p53 non fonctionnelle, n'est pas suffisante pour induire la formation d'une tumeur dans des progéniteurs neuronaux de souris néonatales, mais induit la prolifération ectopique de groupe de cellules dans 72% des cas (Lewis et al. 2013). Il n'est donc pas possible de répondre quant au rôle causal de cette mutation dans la progression tumorale. Cependant le fait que cette mutation soit retrouvée en combinaison avec des mutations de p53 et des protéines chaperonnes de l'histone H3, ATRX et DAXX (Schwartzentruber et al. 2012) suggère des interactions coopératives de ces mutations.

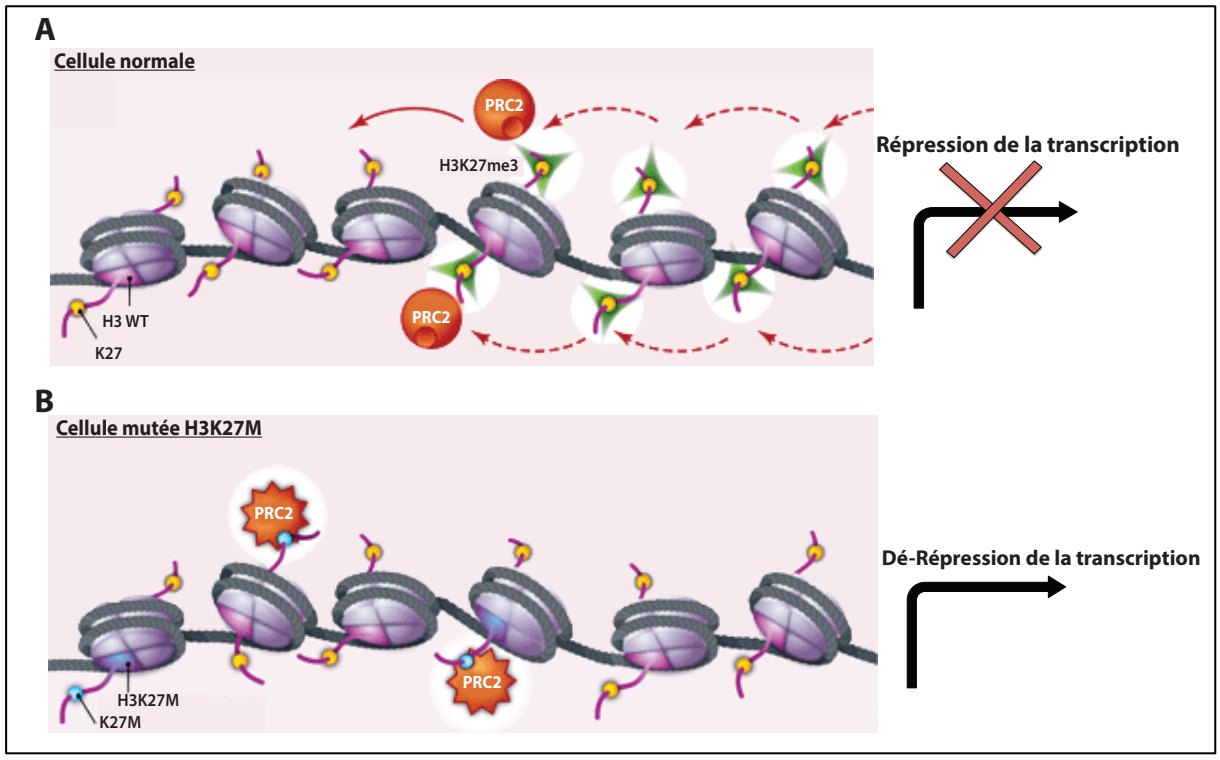

Figure 10 : Effet de la mutation d'histone H3K27M sur l'activité de PRC2. (**A**) Dans une cellule normale, PRC2 est recruté sur les gènes cibles pour effectuer la triméthylation (vert) de la lysine 27 (jaune) de l'histone H3 (H3K27me3) au niveau du gène réprimé. (**B**) Dans une cellule mutée H3K27M, PRC2 se lie plus fermement au peptide muté (bleu) induisant un défaut de triméthylation et une dé-répression des gènes cibles. D'après (Morgan et Shilatifard 2013).

3. Sous-groupes moléculaires de gliomes infiltrants du tronc cérébral

Alors même la biologie des gliomes infiltrants du tronc cérébral commence enfin à être décryptée au niveau génétique et épigénétique, deux études ont démontré l'existence de plusieurs sous-groupes décrits dans les gliomes malins de l'adulte, biologiquement et cliniquement différents. L'analyse non supervisée menée par notre groupe sur 23 biopsies de DIPG réalisées au diagnostic décrit 2 sous-groupes, chacun caractérisé par une signature transcriptomique spécifique impliquant des voies oncogéniques distinctes (Puget et al. 2012).

3.1 Sous-groupe 1 : Piloté par PDGFRA

Le premier sous-groupe montre un phénotype « proneural » (PN) associé à une différenciation oligodendrogliale et à des amplifications/mutations de *PDGFRA*. Le profil d'expression de ce sous-groupe présente un enrichissement des gènes constituant la signature des gliomes amplifiés *PDGFRA* décrite dans le TCGA (Verhaak et al. 2010). Ceci démontre le caractère robuste de cette signature liée à l'amplification quelque soit la localisation tumorale et l'âge du patient. Cette signature établie dans les gliomes de l'adulte est constituée de gènes impliqués dans la neurogenèse et dans le développement des oligodendrocytes, comme *PDGFRA* ou les facteurs de transcription *OLIG* et *SOX10*. D'autre part et à la différence des gliomes de l'adulte, ces tumeurs qui présentent un phénotype oligodendroglial et surexpriment Olig2 sont de plus mauvais pronostic que celles de l'autre sous-groupe. Ceci a été confirmé sur une série de 55 échantillons de DIPG en paraffine où la médiane de survie globale pour les patients présentant une tumeur du type oligodendroglial était de 7,8 mois contre 12,4 pour les autres. De plus, ces tumeurs ne présentent pas de mutation d'IDH1/2 contrairement au sous-groupe proneural des adultes.

3.2 Sous-groupe 2 : Mésenchymateux – Angiogénique – Cellules souches

Le second sous-type mis en évidence présente un phénotype « mésenchymateux » (MES) d'habitude rarement observé dans les gliomes malins pédiatriques supratentoriels. Par comparaison au premier groupe, celui-ci surexprime des facteurs de transcription ainsi que des marqueurs spécifiques de la transition épitélio-mésenchymateuse caractérisée dans le sous-groupe correspondant de glioblastomes de l'adulte (Carro et al. 2010). Ce phénotype mésenchymal est couplé au phénomène de « switch » angiogénique induit par l'hypoxie. L'activation de la voie HIF1A ainsi que l'expression de gènes pro-angiogéniques témoignent de ce phénomène. Enfin, ce profil mésenchymateux est également associé à la surexpression de nombreux marqueurs de cellules souches.

3.3 Sous-groupe « Prolifératif »

Par la même approche transcriptomique sur 27 DIPG issus majoritairement de cas autopsiques, Paugh et ses collaborateurs ont également mis en évidence l'existence des deux premiers sous-groupes mais constatent aussi celle d'un troisième : le sous-type « prolifératif » (Paugh et al. 2011). Il est possible que la présence de ce troisième sous-groupe uniquement dans la série autopsique soit liée à l'évolution des tumeurs après irradiation.

Partie IV : Modèles précliniques

Cette tumeur apparaît comme une entité à part présentant des caractéristiques spécifiques (tumeur infiltrante de très mauvais pronostic, localisée dans le pont au sein d'un organisme en croissance). De plus, les résultats apportés par les études récentes nous permettent désormais de lui considérer certaines particularités biologiques mais également une hétérogénéité inter-tumorale possiblement liée à la cellule d'origine. Ces données sont autant de paramètres à considérer pour les futures évaluations thérapeutiques.
A ce jour, aucun modèle expérimental mimant toutes les caractéristiques du gliome infiltrant du tronc cérébral n'est disponible. Cependant certaines équipes s'y sont essayées. Nous verrons ici quelques unes des stratégies proposées pour la mise en place de cette phase préclinique.

1. Modèles de greffes orthotopiques

Par manque de lignée cellulaire disponible, les premiers travaux visant à établir des modèles de gliome infiltrant du tronc cérébral ont fait appel à des lignées ou à des cultures primaires dérivées de gliomes adultes. Ces cellules primaires sont maintenues en culture sous forme de neurosphères ou entretenues sous forme de xénogreffes sous-cutanées (Siu et al. 2010). Certains proposent des modèles bioluminescents, permettant un suivi de la croissance tumorale et de la réponse à la thérapie (Hashizume et al. 2010; Aoki et al. 2012). D'autres ont mis en évidence une différence de comportement biologique de cellules de gliome C6 en greffant dans des cerveaux de rats juvéniles et adultes. En effet, les auteurs observent un mode de croissance et d'invasion différents selon l'âge de l'animal, et suggèrent le rôle du microenvironnement dans le développement de ces lésions (Q. Liu et al. 2008).

2. Modèles tumoraux inductibles

L'identification d'une sous-population de cellules de type précurseur neural située dans le quatrième ventricule et biologiquement proche des cellules souches issues de gliomes infiltrants du tronc cérébral a également permis d'induire par stimulation au PDGF via le système RCAS/tv-a des tumeurs de manière ciblée dans des cerveaux de souris néonatales (Becher et al. 2010). Masui et ses collaborateurs démontrent également la différence de mode de progression tumorale PDGF-induite selon la localisation et suggèrent l'importance de la composition du tissu en progéniteurs gliaux (Masui et al. 2010).

3. Modèles cellulaires

Au début de ce travail de thèse, seulement quelques études publiées rapportaient des travaux menés sur des cultures de cellules issues de gliome infiltrant de tronc cérébral recueillies au diagnostic (Thirant et al. 2011) ou à l'autopsie (Monje et al. 2011; Caretti et al. 2012). Celles-ci ont été développées en milieu cellule souche.

RESULTATS

CHAPITRE 1 :

CARACTERISATION DES GLIOMES INFILTRANTS DU TRONC CEREBRAL

Partie I : Recherche de nouvelles mutations dans les DIPG

Bien après un profilage moléculaire exhaustif des gliomes de l'adulte, les études dites « large-échelle » des gliomes pédiatriques ont enfin permis de les caractériser d'un point de vue génomique et épi-génomique. Même si ces résultats présentent clairement les gliomes infiltrants du tronc cérébral comme des entités moléculaires distinctes, ils n'avaient jusque là pas permis de mettre en évidence ni de mécanismes pathogéniques clés ni de marqueurs génétiques spécifiques de ces tumeurs. Mais ce retard est en passe d'être rattrapé avec la mise en place de collecte d'échantillons et l'évolution des techniques d'analyses.

En effet, grâce au développement des techniques de séquençage haut débit, deux équipes nord-américaines découvraient en 2012 les premières mutations somatiques d'histones jamais décrites dans aucun autre cancer (Schwartzentruber et al. 2012; Wu et al. 2012) (cf. **Introduction Partie I, 3**). Aujourd'hui, la fréquence de cette mutation est estimée à 80% dans les DIPG. Bien que cette découverte soit majeure pour la compréhension de la biologie de cette tumeur, son approche thérapeutique spécifique demeure encore pauvre, et elle ne peut décrire à elle seule la diversité de cette affection; ce qui justifie encore la recherche des nouvelles mutations.

Dans ce contexte, le séquençage « génome-entier » (WGS) a été réalisé sur un nombre plus important de biopsies (20) issues de gliomes infiltrants du tronc cérébral au diagnostic, ainsi que le séquençage « exome-entier » (WES) de six autres échantillons (dont 1 issu d'un cas au diagnostic et 5 issus de cas autopsiques). L'intérêt de cette approche faite dès le diagnostic est qu'elle permet une analyse des stades plus précoces de la maladie que les autopsies réalisées jusqu'ici outre-Atlantique. Ces dernières présentent des anomalies potentiellement induites par les traitements et notamment la radiothérapie. Par exemple, notre étude retrouvait deux sous-types de DIPG (Puget et al. 2012) quand celle du *St Jude Children's Hospital* en retrouvait 3 (Paugh et al. 2011); le troisième type présentait un profil de type prolifératif. De même, la fréquence d'amplification de PDGFRA semble nettement plus fréquente après irradiation qu'au diagnostic (Paugh et al. 2011).

Notre étude identifie de nouvelles mutations récurrentes dans le gène *ACVR1/ALK2* qui code pour le récepteur à l'activine de type I. De manière intéressante, ces mutations sont la cause d'une maladie congénitale rare invalidante appelée « Fibrodysplasie Ossifiante Progressive » (FOP) (Shore et al. 2006; Kaplan et al. 2009). Elles induisent l'activation constitutionnelle de la voie de signalisation des BMP (*Bone Morphogenic Proteins*) via la

phosphorylation des protéines SMAD1, SMAD5 et SMAD8. Une fois phosphorylés, ces facteurs de transcription vont être transloqués au noyau pour réguler l'expression de nombreux gènes cibles. Les BMP appartiennent à la super-famille du *Transforming Growth factor–beta (*TGF-β) et sont impliquées dans de nombreux processus de différentiation tissulaire.

Si ces mutations sont à l'origine de cette maladie congénitale, elles n'ont en revanche jamais été décrites dans aucun autre cancer et représentent une nouvelle cible thérapeutique dans les DIPG.

Excepté cette découverte importante, le séquençage révèle la présence d'autres altérations génétiques dans ces tumeurs. En effet, 38% (10/26) des échantillons présentent une mutation dans un des partenaires de la voie mTOR. Ceci suggère l'utilisation d'un inhibiteur spécifique. Il convient également de souligner la présence d'une nouvelle mutation récurrente (2/26 ; 8%) du récepteur à l'IGF-like de type 2 (IGF2R). Avec un cas amplifié pour le gène du récepteur MET, ceci porte à 46% (12/26) la fréquence des mutations de la voie RTK/PI3K/MAPK.

D'autre part, onze des 26 échantillons (46%) présentent des mutations de *TP53* comme nous l'avions démontré dans une étude précédente (Grill, Puget, Andreiuolo, Philippe, et MacConaill 2012). La perte de *TP53* observée dans 22% des cas lors d'une précédente étude constitue un autre type d'altération fréquente de ce suppresseur de tumeur qui a de plus, été associée à un mauvais pronostic (Puget et al. 2012). Plus largement, les mutations retrouvées dans les voies de réparation des dommages à l'ADN touchent 69% (18/26) des échantillons.

Notons que cette analyse n'a pas mis en évidence de translocation récurrente.

Enfin et comme attendu, les mutations de l'histone H3 touchent une large majorité des DIPG (H3.3 K27M : 15/26, 58% ; H3.1 K27M : 8/26, 31% ; H3 WT : 3/26, 11%). L'observation de ce « paysage » génomique laisse apparaître une ségrégation des mutations d'*ACVR1* avec d'autres anomalies. En effet, la mutation d'*ACVR1* co-ségrége avec la mutation de l'histone H3.1 et *TP53* non muté.

En outre, la découverte de ces mutations dans la FOP a déjà ouvert un champ d'investigation thérapeutique. Parmi les inhibiteurs ciblant ALK2, LDN-193189 a été testé sur un panel de cultures primaires de DIPG (et une issue d'un gliome malin pédiatrique issu de la région thalamique) présentant ou non une mutation d'*ACVR1.* Le traitement avec cet inhibiteur réduit la viabilité cellulaire de toutes ces cultures primaires (IC_{50}=0,86-2,1 µM) avec une meilleure sensibilité pour les lignées mutées. De plus, la transfection des cultures non mutées avec deux des mutations décrites met en évidence une augmentation de la phosphorylation des Smad 1/5/8. Enfin, la mutation de ce gène n'est que l'un des moyens par lequel cette voie est activée dans les DIPG puisque un niveau d'activation basale de cette voie est également observé en absence de mutation.

Enfin, cette analyse fait encore apparaître d'autres mutations récurrentes parmi nos échantillons: A2M (2/26), HERC2 (2/26), DYNC2H1 (2/26), CTBP2 (2/26), MUC17 (2/26), FAM185A (2/26), IGF2R (2/26), GNB2L1 (2/26), ASXL1 (3/26), FRG1 (3/26).

ARTICLE 1 :

Mutations activatrices récurrentes de *ACVR1/ALK2*
dans les gliomes infiltrant du tronc cérébral

Recurrent activating *ACVR1/ALK2* mutations in diffuse intrinsic pontine glioma

Kathryn R Taylor*, Alan Mackay*, Nathalène Truffaux, Yaron Butterfield, Olena Morozova, Cathy Philippe, David Castel, Catherine S Grasso, Maria Vinci, Diana Carvalho, Angel M Carcaboso, Carmen de Torres, Ofelia Cruz, Jaume Mora, Natacha Entz-Werle, Wendy J Ingram, Michelle Monje, Darren Hargrave, Alex N Bullock, Stéphanie Puget, Stephen Yip, Chris Jones[#], Jacques Grill[#]

* Contributed equally to the paper.

Nature Genetics in press

Recurrent activating *ACVR1* mutations in diffuse intrinsic pontine glioma

Kathryn R Taylor[1,13], Alan Mackay[1,13], Nathalène Truffaux[2], Yaron S Butterfield[3], Olena Morozova[4], Cathy Philippe[2], David Castel[2], Catherine S Grasso[5], Maria Vinci[1], Diana Carvalho[1], Angel M Carcaboso[6], Carmen de Torres[6], Ofelia Cruz[6], Jaume Mora[6], Natacha Entz-Werle[7], Wendy J Ingram[8], Michelle Monje[9], Darren Hargrave[10], Alex N Bullock[11], Stéphanie Puget[12], Stephen Yip[3], Chris Jones[1] & Jacques Grill[2]

Diffuse intrinsic pontine gliomas (DIPGs) are highly infiltrative malignant glial neoplasms of the ventral pons that, due to their location within the brain, are unsuitable for surgical resection and consequently have a universally dismal clinical outcome. The median survival time is 9–12 months, with neither chemotherapeutic nor targeted agents showing substantial survival benefit in clinical trials in children with these tumors[1]. We report the identification of recurrent activating mutations in the *ACVR1* gene, which encodes a type I activin receptor serine/threonine kinase, in 21% of DIPG samples. Strikingly, these somatic mutations (encoding p.Arg206His, p.Arg258Gly, p.Gly328Glu, p.Gly328Val, p.Gly328Trp and p.Gly356Asp substitutions) have not been reported previously in cancer but are identical to mutations found in the germ line of individuals with the congenital childhood developmental disorder fibrodysplasia ossificans progressiva (FOP)[2] and have been shown to constitutively activate the BMP–TGF-β signaling pathway. These mutations represent new targets for therapeutic intervention in this otherwise incurable disease.

Recent high-throughput sequencing approaches have found a striking prevalence of mutations in the genes for the histone variants H3.3 (*H3F3A*) or H3.1 (*HIST1H3B*) that encode p.Lys27Met substitutions in the childhood brain tumor DIPG[3]. This lysine-to-methionine substitution confers a *trans*-dominant ablation of global trimethylation at lysine 27 of histone H3 (H3K27me3), which likely profoundly alters gene expression through the derepression of Polycomb repressive complex 2 (PRC2) target genes[4]. Despite these advances in understanding of the distinct biology of these tumors[1], approaches for desperately needed specific therapeutic interventions are not clear, and little has been reported of the additional mutations accompanying these changes.

We carried out whole-genome sequencing on a unique series of 20 pretreatment biopsy samples of DIPG, for which the patients underwent a safe stereotactic procedure[5], and whole-exome sequencing on a further biopsy case as well as 5 samples obtained at autopsy (**Supplementary Table 1**). Histone H3 gene mutations encoding p.Lys27Met were observed in 23 of 26 cases (88%), comprising 15 (58%) *H3F3A* mutations and 8 (31%) *HIST1H3B* mutations (**Fig. 1a**). These were not found in concert with mutations in the chaperones *ATRX* or *DAXX* as has been described for supratentorial pediatric glioblastoma (pGBM)[6]. There was also an absence of other known glioma-related molecular abnormalities such as *IDH1*, *IDH2*, *BRAF* or *FGFR1* mutations and gene fusions. The mutational spectrum of the untreated biopsy cases was not significantly different from that of the autopsy cases ($P > 0.05$; **Fig. 1b**), although the treatment-naive samples had a low overall mutation rate, with a mean of 14.8 somatic single-nucleotide variants (SNVs) per sample (range of 0–25), that was significantly lower than observed in the radiation-treated autopsy cases (mean = 32.0, range = 14–50; $P = 0.004$, *t* test). Similarly, there was a significantly lower overall mutation rate in untreated samples taken at biopsy than in autopsy samples (mean of 0.76 versus 1.2 mutations per megabase; $P = 0.023$, *t* test).

Eleven of 26 DIPGs (42%) harbored somatic *TP53* mutations, with a further 6 cases (23%) shown to have SNVs in *PPM1D*, which encodes a regulator of p38 mitogen-activated protein kinase (p38-MAPK)-p53 signaling in response to cellular stress, and an additional case with a somatic *ATM* mutation (**Supplementary Fig. 1**), demonstrating non-overlapping targeting of a DNA damage response pathway in 18 of 26 DIPGs (69%) (**Supplementary Fig. 2**). We further identified non-overlapping recurrent alterations in the phosphoinositide 3-kinase (PI3K) pathway targeting *PIK3CA*, *PIK3R1* and *PTEN* through SNVs and microdeletion (**Supplementary Fig. 3**), in addition to amplification of *MET* (1/26; 4%) as previously described[7,8] and truncating

[1]Institute of Cancer Research, London, UK. [2]CNRS UMR 8203, Gustave Roussy, University Paris Sud, Villejuif, France. [3]BC Cancer Agency, Vancouver, British Columbia, Canada. [4]Biomolecular Engineering, University of California, Santa Cruz, Santa Cruz, California, USA. [5]Department of Molecular and Medical Genetics, Oregon Health and Science University, Portland, Oregon, USA. [6]Pediatric Hematology and Oncology, Hospital Sant Joan de Déu, Barcelona, Spain. [7]Centre Hospitalier Regional et Universitaire Hautepierre, Strasbourg, France. [8]Queensland Children's Tumour Bank, Queensland Children's Medical Research Institute, The University of Queensland, Brisbane, Queensland, Australia. [9]Stanford Institute for Stem Cell Biology and Regenerative Medicine, Stanford University School of Medicine, Stanford, California, USA. [10]Neuro-oncology and Experimental Therapeutics, Great Ormond Street Hospital, London, UK. [11]Structural Genomics Consortium, University of Oxford, Oxford, UK. [12]Pediatric Neurosurgery, Necker Sick Children's Hospital, Paris, France. [13]These authors contributed equally to this work. Correspondence should be addressed to C.J. (chris.jones@icr.ac.uk) or J.G. (grill@igr.fr).

Received 30 April 2013; accepted 21 February 2014; published online 6 April 2014; doi:10.1038/ng.2925

mutation of *NF1* (1/26; 4%) (**Fig. 1c**). We also identified new recurrent somatic mutations in *IGF2R* (2/26; 8%), although these mutations were concurrent with others in the pathway, such that their consequences are unknown. In total, 12 of 26 DIPG cases (46%) harbored some form of alteration predicted to activate the receptor tyrosine kinase (RTK)-PI3K-MAPK pathways (**Supplementary Fig. 4**).

Heterozygous somatic coding mutations in the *ACVR1* gene, which encodes the activin A type I receptor ALK2, were observed in 7 of 26 cases (27%) (**Fig. 1c**). These were restricted specifically to codons 328 (c.983G>T, p.Gly328Val, two cases; c.983G>A, p.Gly328Glu, two cases), 258 (c.772C>T, p.Arg258Gly, one case) and 356 (c.1067G>A, p.Gly356Asp, one case), all within the serine/threonine kinase domain, and 206 (c.617G>A, p.Arg206His, one case), within the glycine-serine-rich (GS) domain. Screening an extended series of 26 DIPG biopsy samples by Sanger sequencing identified further recurrences of these mutations and an additional variant at

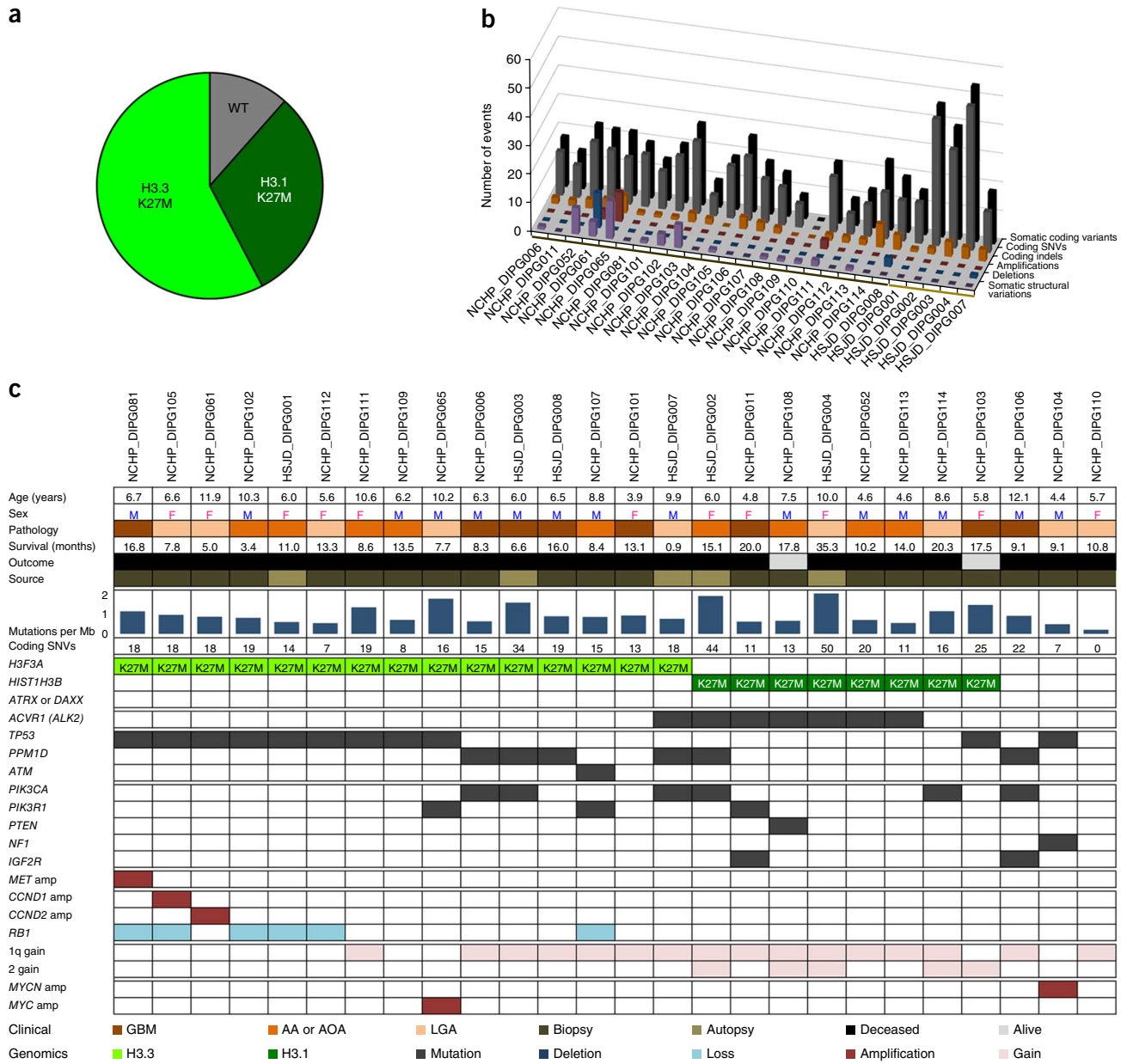

Figure 1 Genomic landscape of DIPG. (**a**) Pie chart showing the breakdown of histone H3 mutations in our series of 26 DIPG samples (*H3F3A* mutation encoding p.Lys27Met: 15/26, 58%; *HIST1H3B* mutation encoding p.Lys27Met: 8/26, 31%, wild-type histone H3: 3/26, 11%). (**b**) Mutational spectrum of DIPG. Bar chart showing the total number of somatic coding variants, coding SNVs, indels, amplifications, deletions and structural variations for each DIPG case. Biopsy cases are marked by the dark brown bar along the *x* axis, and autopsy cases are marked by the light brown bar. (**c**) Summary of major alterations found. Clinicopathological information for the 26 DIPG samples is provided along with the mutation rate and number of somatic coding SNVs. Mutations, amplifications and deletions are noted for the histone H3 genes and *ATRX* or *DAXX*, *ACVR1*, the *ATM-TP53-PPM1D* axis, members of the PI3K-MAPK signaling pathways, RTKs and members of the RB pathway as are chromosome 1q and 2 single-copy gains and amplification (amp) of *MYC* or *MYCN*. GBM, glioblastoma multiforme; AA, anaplastic astrocytoma; AOA, anaplastic oligoastrocytoma; LGA, low-grade astrocytoma; M, male; F, female.

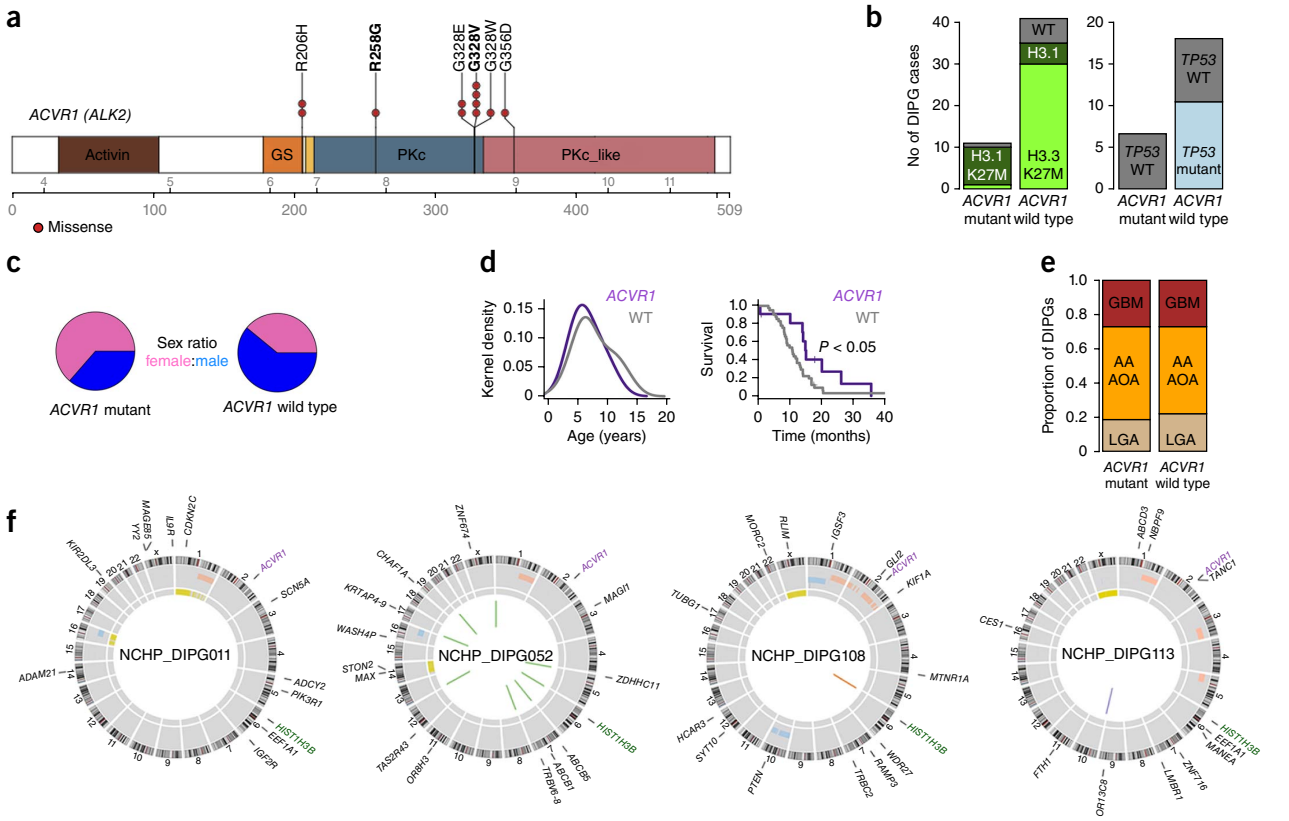

Figure 2 Recurrent *ACVR1* mutations in DIPG. (**a**) Schematic showing recurrent missense mutations in *ACVR1*, overlaid with functional protein domains and exon boundaries. In total, 11 of 52 DIPGs (21%) harbored somatic alterations at 4 residues, all of which have previously been described in the germ line of individuals with FOP. Specific base changes that may be unique to DIPG are highlighted in bold. Activin, activin type I and II receptor domain; GS, TGF-β glycine-serine-rich domain; PKc, protein kinase catalytic domain; PKc_like, protein kinase catalytic domain like. (**b**) Bar graphs showing segregation of activating mutations in *ACVR1* with *HIST1H3B* mutations encoding p.Lys27Met ($P < 0.0001$, Fisher's exact test) and with wild-type (WT) *TP53* ($P = 0.0103$, Fisher's exact test) in our extended series of 52 DIPG cases. (**c**) Sex distribution of cases with *ACVR1* mutations, showing a strong predominance of females in mutant samples. (**d**) Age distribution (left) and overall survival (right) of DIPG cases with *ACVR1* mutations compared to cases with wild-type *ACVR1*. (**e**) Bar plots representing the histological breakdown of samples with mutant and wild-type *ACVR1*. Brown, World Health Organization (WHO) grade 4; orange, WHO grade 3; tan, WHO grade 2. (**f**) Circos plots representing the whole-genome sequences of the four DIPG cases with concurrent *ACVR1* mutation, *HIST1H3B* mutation encoding p.Lys27Met and wild-type *TP53*. The outer ring contains chromosomal ideograms, annotated for somatic SNVs in coding genes. The middle ring plots copy number derived from coverage data: dark red, amplification; pink, gain; dark blue, deletion; light blue, loss. The inner ring represents loss of heterozygosity (LOH; yellow). Drawn inside the circle are structural variations: red, interchromosomal translocation; blue, intrachromosomal translocation; orange, deletion; purple, inversion.

position 328 (c.982G>T, p.Gly328Trp) (**Supplementary Fig. 5**). Overall, we identified 11 of 52 DIPG samples (21%) harboring mutation in *ACVR1* at 4 different codons (**Fig. 2a**). These mutations appear highly specific to DIPG. SNVs in the *ACVR1* coding region are present in the Catalogue of Somatic Mutations in Cancer (COSMIC) database[9] at an overall frequency of 20 in 5,965 (0.3%), with no individual tumor type harboring them with a frequency of greater than 2% and no mutations observed to affect any of the

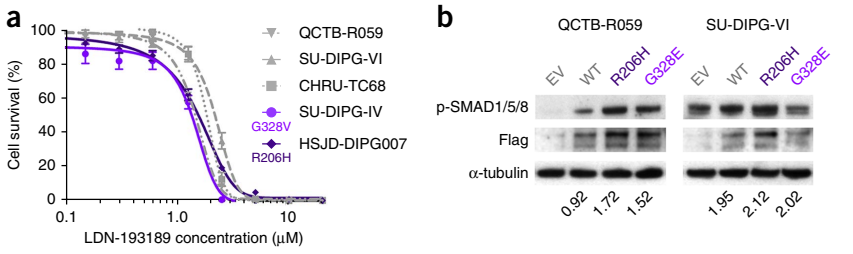

Figure 3 *ACVR1* mutations are weakly activating and responsive to targeted inhibition. (**a**) *In vitro* cytotoxicity of the ALK2 inhibitor LDN-193189. Primary cultures were treated with inhibitor for 72 h, and cell viability was measured by CellTiter-Glo in triplicate experiments. Error bars, s.d. The cells used were HSJD-DIPG007 (DIPG; *ACVR1* Arg206His, *H3F3A* Lys27Met), SU-DIPG-IV (DIPG; *ACVR1* Gly328Val, *HIST1H3B* Lys27Met), CHRU-TC68 (DIPG; *ACVR1* wild type, *H3F3A* Lys27Met), SU-DIPG-VI (DIPG; *ACVR1* wild type, *H3F3A* Lys27Met) and QCTB-R059 (thalamic pediatric GBM; *ACVR1* wild type, *H3F3A* Lys27Met). (**b**) *ACVR1* mutations confer increased signaling through phosphorylated SMAD1/5/8. QCTB-R059 and SU-DIPG-VI cells were transfected with construct encoding Flag-tagged Arg206His or Gly328Glu mutant ALK2 and assessed for phosphorylated SMAD1/5/8 (p-SMAD1/5/8) by protein blot. EV, empty vector; WT, wild-type ALK2. α-tubulin is included as a loading control. Numbers below each lane represent phosphorylated SMAD1/5/8 levels quantified relative to the levels of Flag expression.

residues described in the present study, suggestive of a 'passenger' effect in other cancers.

ACVR1 mutations were found to cosegregate with the less common *HIST1H3B* mutation encoding p.Lys27Met in the canonical histone H3.1 variant ($P < 0.0001$, Fisher's exact test) (**Fig. 2b**), as well as with wild-type *TP53* ($P = 0.0103$, Fisher's exact test). There was also an association between H3.1 alteration and chromosome 2 gain (on which *ACVR1* is found at 2q24.1; $P = 0.0009$, Fisher's exact test). *ACVR1* mutations seem to mark a distinct subset of DIPG cases (**Supplementary Table 2**). There was a marked predominance of females in the *ACVR1*-mutant tumor group compared to cases with wild-type *ACVR1* (1.75:1 versus 0.64:1 female to male ratios, respectively; $P = 0.05$, Fisher's exact test) (**Fig. 2c**), as well as a relatively restricted age of onset (**Fig. 2d**). Cases with tumors harboring *ACVR1* mutations also had longer overall survival times (median of 14.9 versus 10.9 months; $P = 0.05$, log-rank test) (**Fig. 2d**), although outcome remained very poor. There were no significant differences in histology between the groups (**Fig. 2e**). Whole-genome sequencing of biopsy samples exemplifying the genotype with concurrent *ACVR1* and *HIST1H3B* mutations harbored an additional 10–19 somatic SNVs and 0–9 structural variations (**Fig. 2f**).

Remarkably, these somatic mutations in *ACVR1* affected identical residues as the ones described in the germ line of individuals with the autosomal dominant congenital childhood developmental disorder FOP (MIM 135100)[2]. This debilitating disease is characterized by heterotopic ossification of soft connective tissue resulting in severe skeletal abnormalities[10]. Individuals with classical clinical features of FOP carry heterozygous mutations in *ACVR1* encoding p.Arg206His that affect the GS activation domain[11], whereas atypical cases with a less severe phenotype have been shown to harbor either mutations encoding p.Arg258Ser[12], p.Gly328Glu, p.Gly328Arg or p.Gly328Trp[13] or p.Gly356Asp[14] or other heterozygous mutations affecting the GS and kinase domains[2,15]. This latter series of alterations may be exposed to be present at the interface with the GS domain and may abrogate interactions with the negative regulator FKBP12 (refs. 12,13,15). These mutations have been shown to constitutively activate the bone morphogenetic protein (BMP)-dependent transforming growth factor (TGF)-β pathway in the absence of ligand binding, as evidenced by increased phosphorylation of SMAD1, SMAD5 and SMAD8 (SMAD1/5/8) *in vitro*[14,16].

To investigate the specific role of *ACVR1* mutations in the context of DIPG, we assembled a panel of four DIPG case-derived primary cultures (and one thalamic pediatric GBM (glioblastoma multiforme) culture harboring an *H3F3A* mutation encoding p.Lys27Met), representing two *ACVR1* mutations (encoding p.Arg206His and p.Gly328Val) and three wild-type lines (**Supplementary Table 3**). In these models, RNA sequencing (RNA-seq) data demonstrated that the mutant allele was expressed in approximately half of the reads, which was also evidenced by Sanger sequencing of cDNA from case sample NCHP_DIPG011 (**Supplementary Fig. 6**). Treatment with the selective ALK2 inhibitor LDN-193189 (ref. 17) resulted in marked inhibition of cell viability in all cells, with GI_{50} values (concentrations required to inhibit cell growth by 50%) ranging from 0.86–2.1 μM, approximately tenfold lower than with the less potent parent compound dorsomorphin, with a trend toward increased sensitivity in the mutant cultures ($P = 0.10$, F test) (**Fig. 3a**). Transfection of thalamic GBM and DIPG cells with wild-type *ACVR1* (both with *H3F3A* mutation encoding p.Lys27Met) with constructs encoding Flag-tagged mutants conferred increased signaling through phosphorylated SMAD1/5/8, particularly for the Arg206His mutant and, to a lesser extent, for the Gly328Glu mutant (**Fig. 3b**). *ACVR1* mutation may only be one mechanism by which this pathway is activated in DIPG, however, as high basal levels of phosphorylated SMAD1/5/8 were also observed for the cells with *H3F3A* mutation encoding p.Lys27Met and wild-type *ACVR1* that were used in this study (**Supplementary Fig. 7**). This finding may explain the lack of a more robust genotype-dependent response to the inhibitor and may also expand the population of patients who might benefit from targeting of the receptor.

There are no reports to our knowledge of coincident FOP and DIPG, although the clinical features of both typical and atypical cases of FOP can commonly include neurological symptoms and have been reported in children to include cerebellar and brain stem abnormalities[15,18], including demyelinated lesions in the pons, both in human cases and mouse models[19]. It will nonetheless be a challenge to identify the mechanism by which the temporal and spatial context of BMP–TGF-β pathway activation confers such differing clinical phenotypes. In experimental models of FOP, *ACVR1* mutations are associated with defects in stem cell maintenance, reprogramming and differentiation, offering links with cancer-related cellular processes. First-generation ALK2 inhibitors such as dorsomorphin[20] and LDN-193189 (ref. 17) have been shown to downregulate intracellular BMP–TGF-β signaling and to reduce heterotypic ossification, opening the tantalizing possibility of central nervous system (CNS)-penetrant compounds showing a similar potential in a childhood brain tumor otherwise devoid of efficacious treatment options.

URLs. Burrows-Wheeler Aligner (BWA), http://bio-bwa.sourceforge.net/; Picard, http://picard.sourceforge.net/; Genome Analysis Toolkit, http://www.broadinstitute.org/gatk/; SVDetect, http://svdetect.sourceforge.net/; Ensembl Variant Effect Predictor, http://www.ensembl.org/info/docs/variation/vep/; SIFT, http://sift.jcvi.org/; PolyPhen, http://genetics.bwh.harvard.edu/pph2; Catalogue of Somatic Mutations in Cancer (COSMIC) v64, http://www.sanger.ac.uk/genetics/CGP/cosmic/; dbSNP Build 137, http://www.ncbi.nlm.nih.gov/sites/SNP; circular binary segmentation, http://www.bioconductor.org/; APOLLOH, http://compbio.bccrc.ca/software/apolloh/; St. Jude Washington University Protein Paint tool, http://www.explorepcgp.org/; R3.0.1, http://www.r-project.org/.

METHODS

Methods and any associated references are available in the online version of the paper.

Accession codes. Raw data have been submitted to the European Genome-phenome Archive under accession EGAS00001000572.

Note: Any Supplementary Information and Source Data files are available in the online version of the paper.

ACKNOWLEDGMENTS

This study was funded by the Cancer Research UK Genomics Initiative (A14078) and makes use of data generated by the St. Jude Children's Research Hospital–Washington University Pediatric Cancer Genome Project. We are grateful to the DIPG Preclinical Consortium funded by The Cure Starts Now and the Lyla Nsouli Foundation for RNA-seq data. This work is supported by the Stavros Niarchos Foundation, Abbie's Army, the Lyla Nsouli Foundation, the Royal Marsden Hospital Children's Department Fund and Fondo Alicia Pueyo. M.M. gratefully acknowledges funding by the National Institutes of Neurological Disease and Stroke (NINDS; grant K08NS070926), Alex's Lemonade Stand Foundation, the McKenna Claire Foundation and the Dylan Jewett, Elizabeth Stein, Connor Johnson and Zoey Ganesh Memorial Funds. C.P. acknowledges funding from the Agence National de la Recherche. N.T., C.P. and J.G. acknowledge funding from the charity l'Etoile de Martin, and N.E.-W. acknowledges support from Enfants et Santé. A.M.C. acknowledges funding from the Fundación Científica de la Asociación Española Contra el Cáncer. W.J.I. acknowledges funding from the Children's Health Foundation Queensland and the Brainchild Foundation. The Structural Genomics Consortium is a registered charity (1097737) that receives funds from AbbVie, Boehringer Ingelheim, the Canada

Foundation for Innovation, the Canadian Institutes for Health Research, Genome Canada, GlaxoSmithKline, Janssen, Lilly Canada, the Novartis Research Foundation, the Ontario Ministry of Economic Development and Innovation, Pfizer, Takeda and the Wellcome Trust (092809/Z/10/Z). K.R.T., A.M., M.V., D. Carvalho, D.H. and C.J. acknowledge National Health Service (NHS) funding to the National Institute of Health Research Biomedical Research Centres.

AUTHOR CONTRIBUTIONS

C.J., J.G., D.H. and S.Y. designed the study. C.J. wrote the manuscript. K.R.T., A.M. and C.J. designed and reviewed experiments, and designed and reviewed statistical and bioinformatic analyses. K.R.T. performed experiments. A.M. performed bioinformatic analyses. N.T., D. Castel, M.V. and D. Carvalho performed sample preparation and experiments. Y.S.B., O.M., C.P., C.S.G. and S.Y. performed and reviewed bioinformatic analyses. A.M.C., C.d.T., O.C., J.M., N.E.-W., W.J.I., M.M., A.N.B., S.P. and J.G. provided and prepared samples and experimental materials. All authors reviewed the manuscript during its preparation.

COMPETING FINANCIAL INTERESTS

The authors declare no competing financial interests.

1. Jones, C., Perryman, L. & Hargrave, D. Paediatric and adult malignant glioma: close relatives or distant cousins? *Nat. Rev. Clin. Oncol.* **9**, 400–413 (2012).
2. Katagiri, T. Recent topics in fibrodysplasia ossificans progressiva. *J. Oral Biosciences* **54**, 119–123 (2012).
3. Wu, G. *et al.* Somatic histone H3 alterations in pediatric diffuse intrinsic pontine gliomas and non-brainstem glioblastomas. *Nat. Genet.* **44**, 251–253 (2012).
4. Lewis, P.W. *et al.* Inhibition of PRC2 activity by a gain-of-function H3 H3 mutation found in pediatric glioblastoma. *Science* **340**, 857–861 (2013).
5. Roujeau, T. *et al.* Stereotactic biopsy of diffuse pontine lesions in children. *J. Neurosurg.* **107**, 1–4 (2007).
6. Schwartzentruber, J. *et al.* Driver mutations in histone H3.3 and chromatin remodelling genes in paediatric glioblastoma. *Nature* **482**, 226–231 (2012).
7. Puget, S. *et al.* Mesenchymal transition and *PDGFRA* amplification/mutation are key distinct oncogenic events in pediatric diffuse intrinsic pontine gliomas. *PLoS ONE* **7**, e30313 (2012).
8. Paugh, B.S. *et al.* Genome-wide analyses identify recurrent amplifications of receptor tyrosine kinases and cell-cycle regulatory genes in diffuse intrinsic pontine glioma. *J. Clin. Oncol.* **29**, 3999–4006 (2011).
9. Forbes, S.A. *et al.* COSMIC: mining complete cancer genomes in the Catalogue of Somatic Mutations in Cancer. *Nucleic Acids Res.* **39**, D945–D950 (2011).
10. Shore, E.M. & Kaplan, F.S. Inherited human diseases of heterotopic bone formation. *Nat. Rev. Rheumatol.* **6**, 518–527 (2010).
11. Shore, E.M. *et al.* A recurrent mutation in the BMP type I receptor *ACVR1* causes inherited and sporadic fibrodysplasia ossificans progressiva. *Nat. Genet.* **38**, 525–527 (2006).
12. Bocciardi, R., Bordo, D., Di Duca, M., Di Rocco, M. & Ravazzolo, R. Mutational analysis of the *ACVR1* gene in Italian patients affected with fibrodysplasia ossificans progressiva: confirmations and advancements. *Eur. J. Hum. Genet.* **17**, 311–318 (2009).
13. Petrie, K.A. *et al.* Novel mutations in *ACVR1* result in atypical features in two fibrodysplasia ossificans progressiva patients. *PLoS ONE* **4**, e5005 (2009).
14. Fukuda, T. *et al.* A unique mutation of ALK2, G356D, found in a patient with fibrodysplasia ossificans progressiva is a moderately activated BMP type I receptor. *Biochem. Biophys. Res. Commun.* **377**, 905–909 (2008).
15. Kaplan, F.S. *et al.* Classic and atypical fibrodysplasia ossificans progressiva (FOP) phenotypes are caused by mutations in the bone morphogenetic protein (BMP) type I receptor ACVR1. *Hum. Mutat.* **30**, 379–390 (2009).
16. Chaikuad, A. *et al.* Structure of the bone morphogenetic protein receptor ALK2 and implications for fibrodysplasia ossificans progressiva. *J. Biol. Chem.* **287**, 36990–36998 (2012).
17. Yu, P.B. *et al.* BMP type I receptor inhibition reduces heterotopic ossification. *Nat. Med.* **14**, 1363–1369 (2008).
18. Tumolo, M., Moscatelli, A. & Silvestri, G. Anaesthetic management of a child with fibrodysplasia ossificans progressiva. *Br. J. Anaesth.* **97**, 701–703 (2006).
19. Kan, L. *et al.* CNS demyelination in fibrodysplasia ossificans progressiva. *J. Neurol.* **259**, 2644–2655 (2012).
20. Yu, P.B. *et al.* Dorsomorphin inhibits BMP signals required for embryogenesis and iron metabolism. *Nat. Chem. Biol.* **4**, 33–41 (2008).

ONLINE METHODS

Tumor cohort. DIPG samples and matched peripheral blood samples were available from 21 patients who underwent stereotactic biopsy at the Neurosurgery Department of Necker Sick Children's Hospital (Paris, France), 20 of which were subjected to whole-genome sequencing. All patients were clinically diagnosed as having DIPG on the basis of clinical presentation and radiography as part of a multidisciplinary assessment. These patients had diffuse intrinsic tumor centered in the pons and occupying at least 50% of the volume of this structure and had an associated short clinical history of less than 3 months. DNA from an additional 26 biopsy samples was available as a validation cohort. A further five DIPG cases with matched peripheral blood samples were obtained at autopsy at the Hospital Sant Joan de Déu (Barcelona, Spain) and were sequenced after exome capture using Agilent SureSelect technology. All patient material was collected after informed consent and was subject to local research ethics committee approval. Cases included 23 girls and 29 boys (1:1.26 ratio). The median age of the patients was 6.6 years, and the median overall survival time was 11.6 months. A summary of the tumor cohort and clinicopathological information are provided in **Supplementary Table 2**.

Whole-genome and whole-exome sequencing. Exome capture was carried out on the four autopsy cases using the 50Mb Agilent SureSelect platform (Agilent Technologies), and samples underwent paired-end sequencing on an Illumina HiSeq 2000 with a 100-bp read length. Library preparation for the biopsy samples was carried out by the Illumina FastTrack service, and entire genomes underwent paired-end sequencing on an Illumina HiSeq 2000. The median coverage for the tumor genomes was 37–67× (matched normal genomes, 34–41×). Reads were mapped to the hg19 build of the human genome using BWA (Burrows-Wheeler Aligner), and PCR duplicates were removed with PicardTools 1.5.

Genome analysis. Somatic SNVs were called using the Illumina Genome Network (IGN) Cancer Normal pipeline version 1.0.2 and the Genome Analysis Toolkit v2.4-9. Structural variations were called using IGN and SVDetect. Variants were annotated using the Ensembl Variant Effect Predictor v71 tool incorporating SIFT and PolyPhen predictions, COSMIC v64 and dbSNP Build 137 annotations. Copy number was obtained by calculating $\log_2$ ratios of tumor/normal coverage binned into exons of known genes, smoothed using circular binary segmentation and processed using in-house scripts. LOH was calculated using APOLLOH. Schematics showing the locations of recurrent mutations were produced by the St. Jude Washington University Protein Paint tool. Statistical analysis was carried out using R3.0.1. Continuous variables were analyzed using Student's *t* tests. Count data were compared using Fisher's exact test.

Cell culture and drug sensitivity. Primary cultures were derived from DIPG case samples taken at either biopsy or autopsy at multiple centers, representing both cases with mutant and wild-type *ACVR1* and with both *H3F3A* and *HIST1H3B* mutations encoding p.Lys27Met, in addition to cells from a pediatric glioblastoma specimen arising in the thalamus with an *H3F3A* mutation encoding p.Lys27Met. A summary of the cases from which these cells were derived is provided in **Supplementary Table 3**. Cells were grown under adherent stem cell conditions using flasks coated with laminin (Sigma) in neurobasal medium (Invitrogen) supplemented with B-27 (Invitrogen) and the growth factors epidermal growth factor (EGF), basal fibroblast growth factor (bFGF), platelet-derived growth factor (PDGF)-AA and PDGF-BB (all from Shenandoah Biotech). The ALK2 inhibitors LDN-193189 (Sigma) and dorsomorphin (Abcam) were tested for their effects on cell viability using a highly sensitive luminescent assay measuring cellular ATP levels (CellTiter-Glo, Promega). Drug was added in various concentrations, and cells were assayed in triplicate after 72 h. Statistical analysis was carried out using GraphPad Prism 6.0 (GraphPad Software).

Allelic expression of *ACVR1*. SU-DIPG-IV cells were subjected to full transcriptome sequencing as part of the DIPG Preclinical Consortium. Counts of reads aligned to the *ACVR1* coding region in NCBI_36 were analyzed for the ratio of mutant to wild-type sequence and visualized in Genome Browse (Golden Helix). RNA from the NCHP_DIPG011 primary tumor was reverse transcribed, PCR amplified and underwent Sanger sequencing to determine whether both mutant and wild-type alleles were expressed (**Supplementary Table 4**).

Overexpression of mutant ALK2. The *ACVR1* mutations encoding p.Arg206His and p.Gly328Glu were introduced into pcDNA3.1 by site-directed mutagenesis as previously described[16], and constructs were transfected into primary QCTB-R059 and SU-DIPG-VI cells using Lipofectamine (Invitrogen), with protein collected after 24 h using standard procedures. Protein blotting was carried out with horseradish peroxidase (HRP)-conjugated antibody to Flag (A8592, Sigma; 1:1,000 dilution) and antibody to phosphorylated SMAD1/5/8 (9511, Cell Signaling Technology; 1:1,000 dilution) under standard conditions. Relative levels of phosphorylated SMAD1/5/8 were measured with ImageJ software (National Institute of Mental Health).

Statistical analysis. Statistical analysis was carried out using GraphPad Prism 6.0 and R 3.0.1. Comparisons of the numbers of coding SNVs and the mutation rates in biopsy and autopsy cases were performed by *t* test. For analysis of categorical association between cases with *ACVR1* mutations and mutations in *HIST1H3B* or *TP53*, sex and histology, Fisher's exact test was used. Differences in survival were analyzed by the Kaplan-Meier method, and significance was determined by the log-rank test. All tests were two-sided, and a *P* value of less than 0.05 was considered significant. A sum-of-squares F test was used to assess differences in dose response curves for *ACVR1*-mutant versus wild-type cells.

doi:10.1038/ng.2925

Supplementary Information

Recurrent activating *ACVR1* mutations in diffuse intrinsic pontine glioma

Kathryn R Taylor[1]*, Alan Mackay[1]*, Nathalène Truffaux[2], Yaron Butterfield[3], Olena Morozova[4,5], Cathy Philippe[2], David Castel[2], Catherine S Grasso[6], Maria Vinci[1], Diana Carvalho[1], Angel M Carcaboso[7], Carmen de Torres[7] Ofelia Cruz[7], Jaume Mora[7], Natacha Entz-Werle[8], Wendy J Ingram[9], Michelle Monje[10], Darren Hargrave[11], Alex N Bullock[12], Stéphanie Puget[13], Stephen Yip[3], Chris Jones[1#], Jacques Grill[2#]

[1]Institute of Cancer Research, London, UK; [2]Institut Gustav Roussy, Villejuif, France; [3]BC Cancer Agency, Vancouver, Canada; [4]Howard Hughes Medical Institute, Los Angeles, CA, USA; [5]University of California, Los Angeles, CA, USA; [6]Oregon Health and Science University, Portland, OR, USA; [7]Hospital Sant Joan de Deu, Barcelona, Spain; [8]Centre Hospitalier Régional et Universitaire Hautepierre, Strasbourg, France; [9]Queensland Children's Tumour Bank, Queensland Children's Medical Research Institute, The University of Queensland, Brisbane, Queensland, Australia; [10]Stanford University School of Medicine, Stanford, CA, USA; [11]Great Ormond Street Hospital, London, UK; [12]Structural Genomics Consortium, University of Oxford, UK; [13]Necker Childrens Hospital, Paris, France

Supplementary Figures 1-7

Supplementary Tables 2-4

Nature Genetics: doi:10.1038/ng.2925

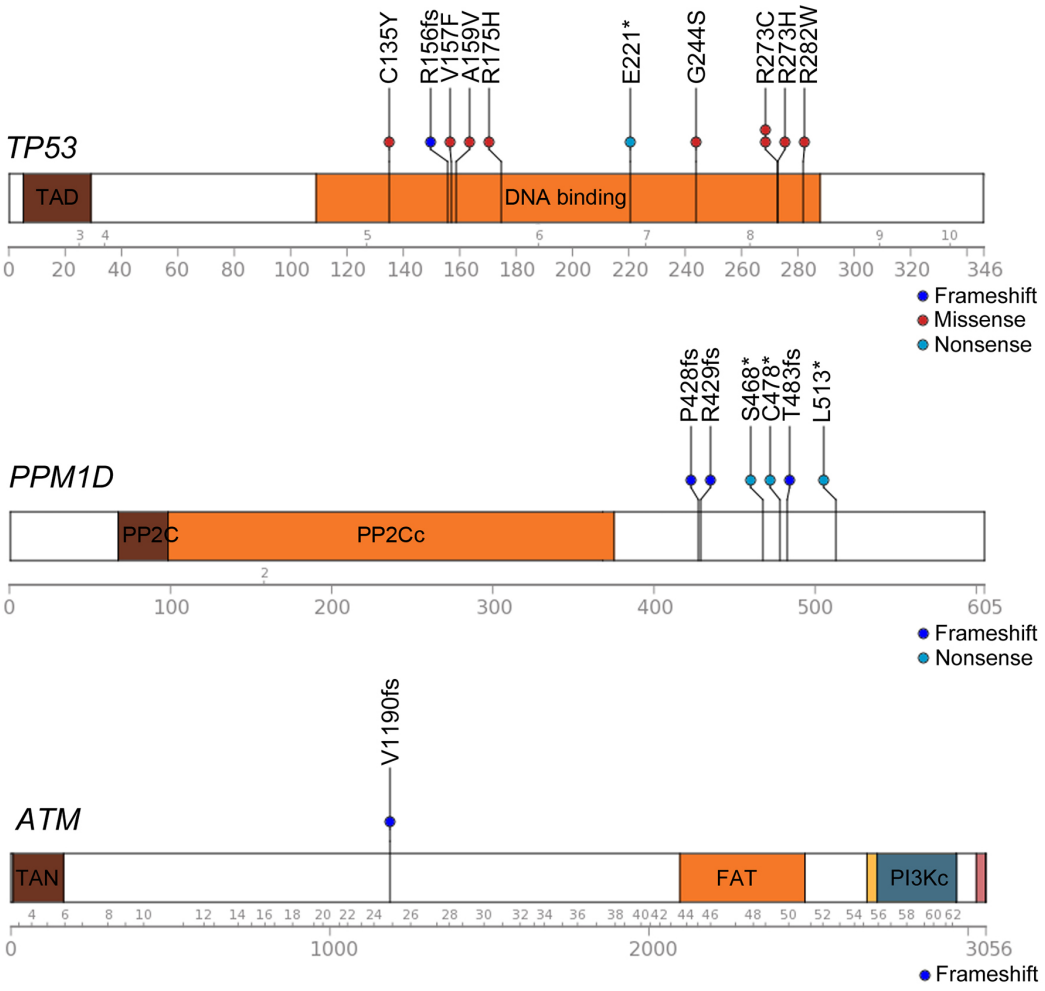

Supplementary Figure 1 – *Somatic mutations in TP53, PPM1D and ATM in DIPG.* Cartoon showing recurrent and non-overlapping missense and frameshift mutations in *TP53* (11/26, 42%), *PPM1D* (6/26, 23%) and *ATM* (1/26, 4%), overlaid with functional protein domains and exon boundaries. TAD: p53 transactivation motif; DNA binding: p53 DNA-binding domain; PP2C: protein phosphatase 2C domain; PP2Cc: Serine/threonine phosphatase, family 2C, catalytic domain. TAN: telomere length maintenance and DNA damage repair domain; FAT: FRAP, ATM and TRRAP associated domain; PI3Kc: phosphoinositide 3-kinase class I catalytic domain.

Nature Genetics: doi:10.1038/ng.2925

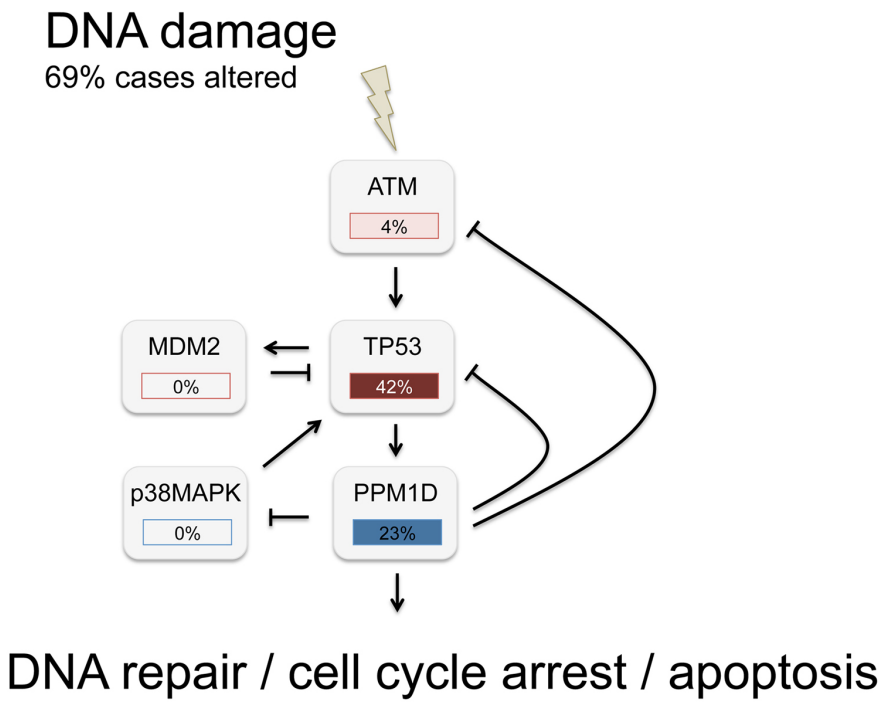

Supplementary Figure 2 – *Pathway-level recurrence of somatic alterations involved in DNA damage response.* Cartoon representing the frequency of distinct non-overlapping hits in intracellular components of ATM/p53-mediated DNA damage and stress response signalling. Bars are coloured according to frequency of alterations in the present cohort: red=gain of function, blue=loss of function. It total, 18/26 (69%) cases harboured alteration at some point in the pathway which would be predicted to be activating.

Nature Genetics: doi:10.1038/ng.2925

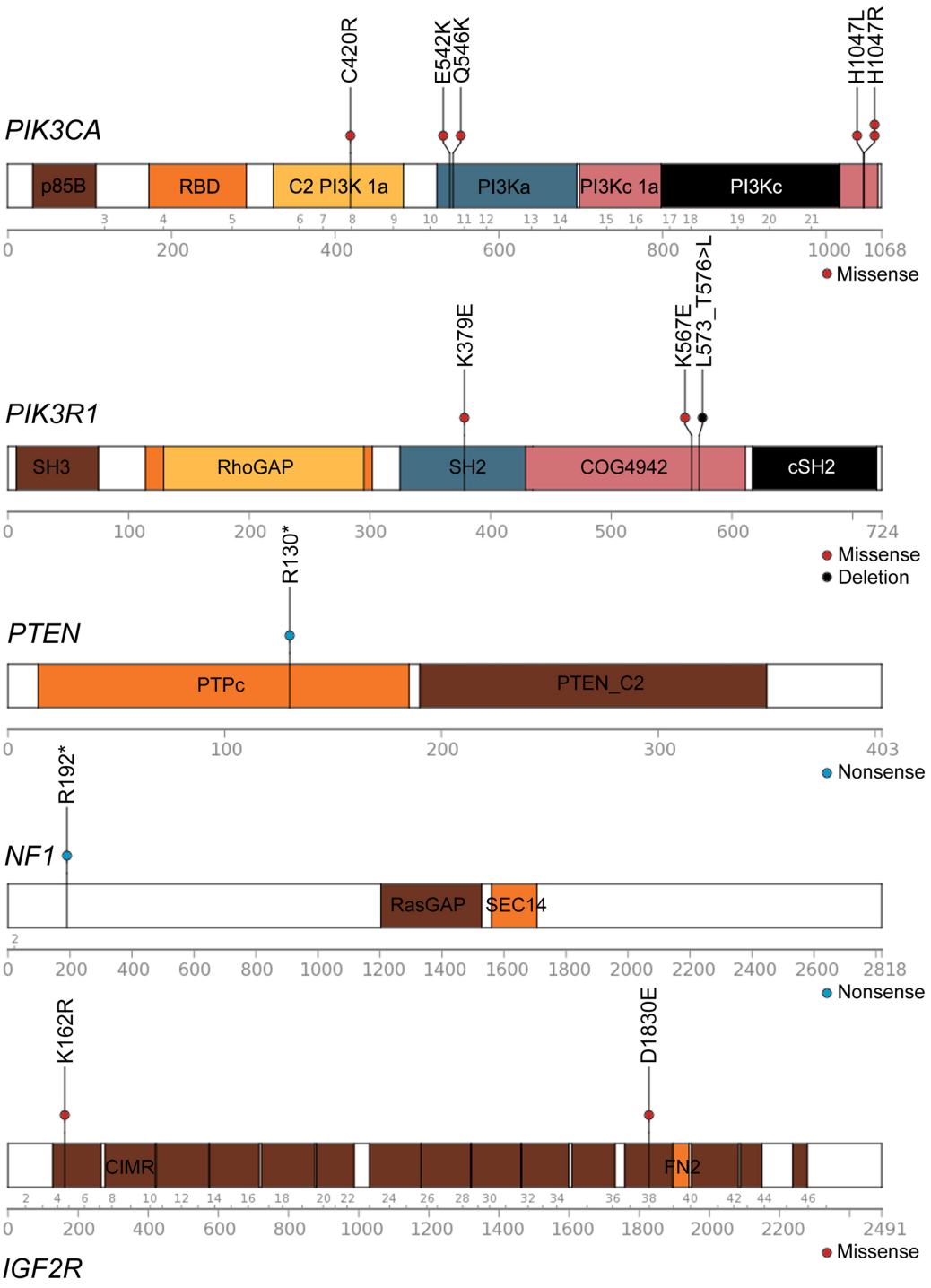

Supplementary Figure 3 – *Somatic mutations in genes involved in PI3K/MAPK signalling in DIPG*. Cartoon showing non-overlapping missense, nonsense truncating mutations, and deletions in *PIK3CA* (6/26,23%), PIK3R1 (3/26, 12%), PTEN (1/26, 4%) and *NF1* (1/26, 4%), overlaid with functional protein domains and exon boundaries. There were additional novel somatic mutations of unknown significance identified in *IGF2R*. Grey bars = deletions. p85B: p85 binding domain; RBD: Ras binding domain; C2 PI3K 1a: C2 domain present in class I alpha PI3 kinases; PI3Ka: PI3K class I accessory domain; PI3Kc: PI3K class I catalytic domain; SH: Src homology domain; RhoGAP: GTPase activator protein for Rho-like GTPases domain; COG4942: Membrane-bound metallopeptidase domain; PTPc: Protein tyrosine phosphatase, catalytic domain; PTEN_C2: PTEN C terminal 2 domain; RasGAP: Ras GTPase activating protein domain; SEC14: Sec14p-like lipid binding domain. CIMR: cation-independent mannose-6-phosphate receptor repeat; FN2: fibronectin type II domain.

Nature Genetics: doi:10.1038/ng.2925

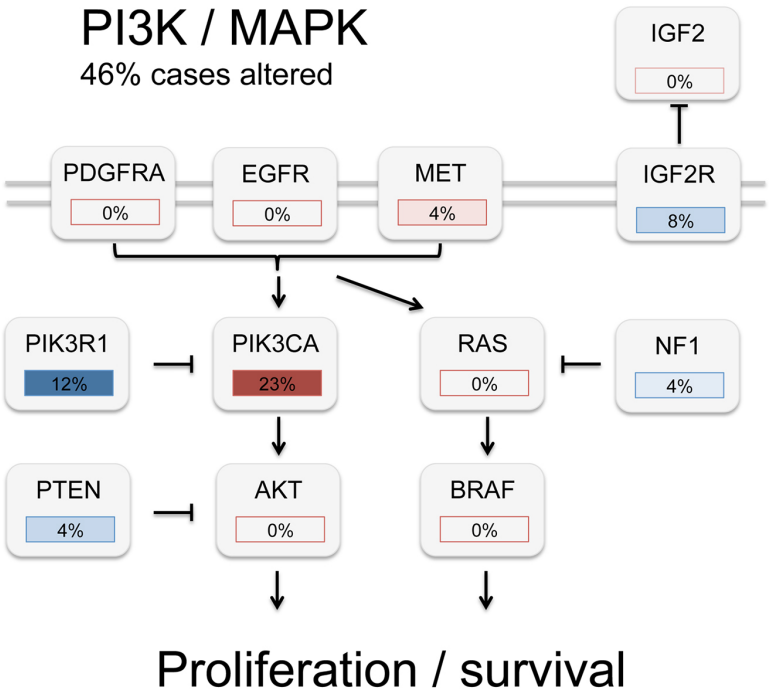

Supplementary Figure 4 – *Pathway-level recurrence of somatic alterations involved in RTK / PI3K / MAPK signalling.* Cartoon representing the frequency of distinct non-overlapping hits in intracellular components of PI3K/MAPK pathway signalling, as well as amplifications of receptor tyrosine kinases, in DIPG. Bars are coloured according to frequency of alterations in the present cohort: red=gain of function, blue=loss of function. IGF2R binds IGF2 ligand preventing signalling through IGF1R/PI3K, and is found to have a somatic missense K162R and D1830E mutations. It total, 12/26 (46%) cases harboured alteration at some point in the pathway which would be predicted to be activating.

Nature Genetics: doi:10.1038/ng.2925

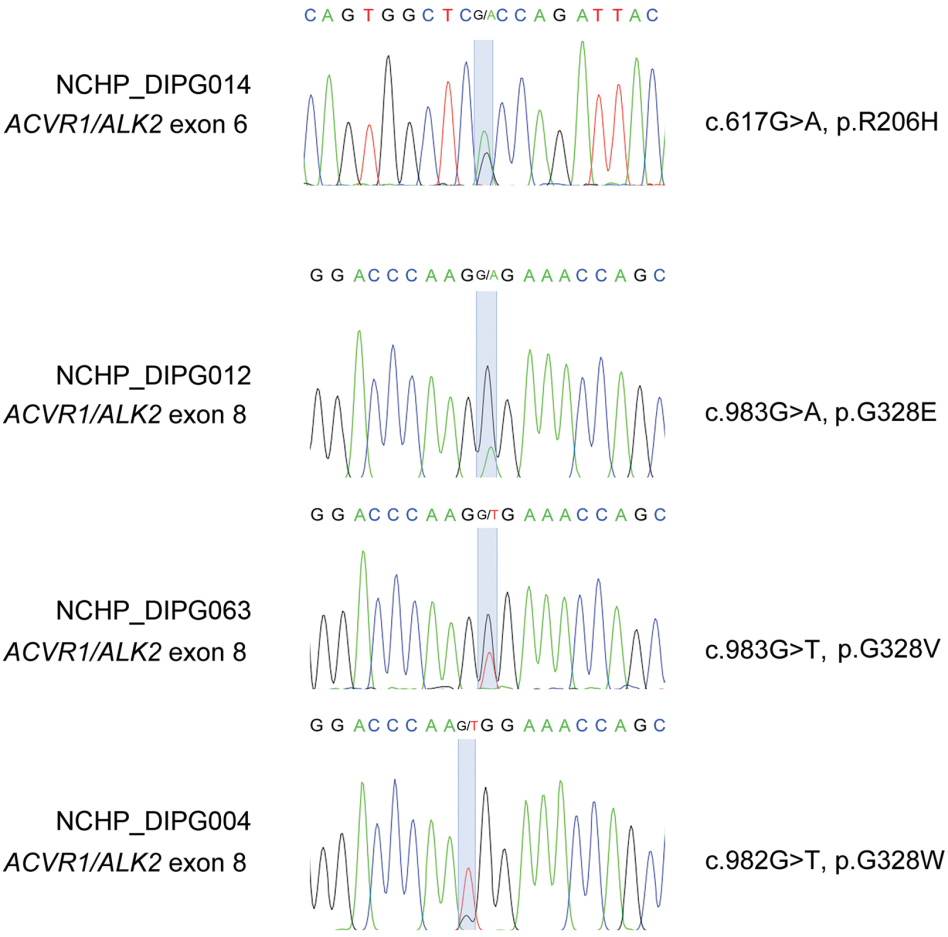

Supplementary Figure 5 – *Sanger sequencing validation of ACVR1/ALK2 mutations in an extended cohort of DIPG.* Sequence traces of heterozygous mutations in the activin A type I receptor (*ACVR1*/*ALK2*) observed in a series of 50 DIPG, including (a) c.617G>A, R206H; (b) c.983G>A, p.G328E; (c) c.983G>T, p.G328V; (d) c.982G>T, p.G328W. All are reported to be constitutively activating of the BMP/TGF-β signalling pathway in models of fibrodysplasia ossificans progressiva.

Nature Genetics: doi:10.1038/ng.2925

a

SU-DIPG-IV

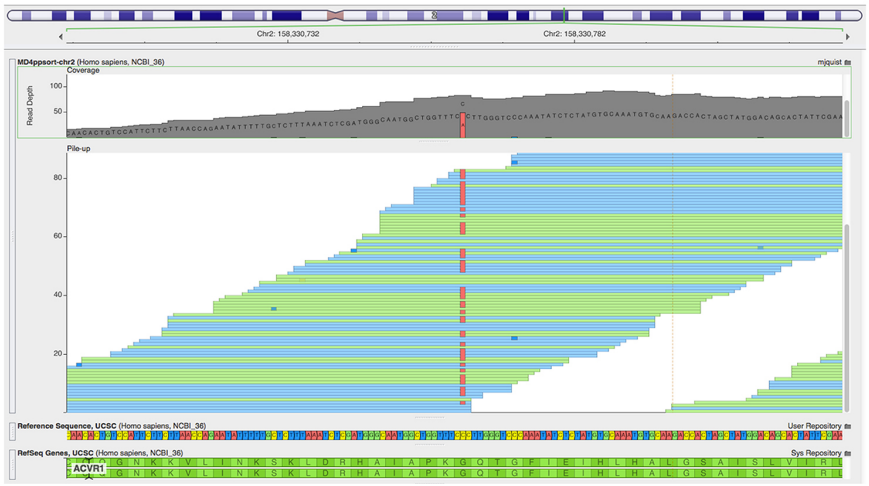

b

NCHP_DIPG011

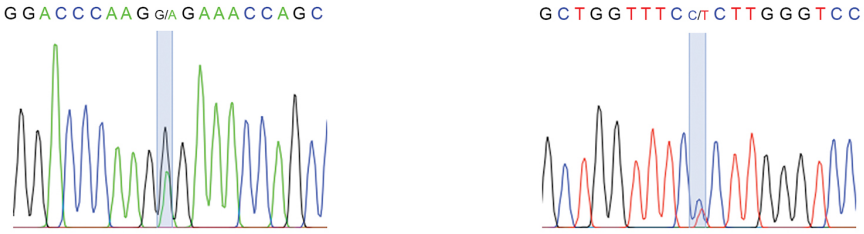

Forward cDNA sequence

Reverse cDNA sequence

Supplementary Figure 6 – *Allele-specific expression of ACVR1/ALK2 mutation*. (a) Pile-up of sequence reads from RNAseq data of SU-DIPG-IV cells, showing expression of both the wild-type and mutant alleles at position chr2:158330762, with 49/83 reads harbouring the C>A (c.983G>T) mutation (red) corresponding to ACVR1/ALK2 p.G328V. (b) Sanger sequencing of an *ACVR1/ALK2* exon 8 RT-PCR product from DIPG patient sample NCHP_DIPG011, showing heterozygous expression of the mutant p.G328E allele (c.983G>A), forward and reverse.

Nature Genetics: doi:10.1038/ng.2925

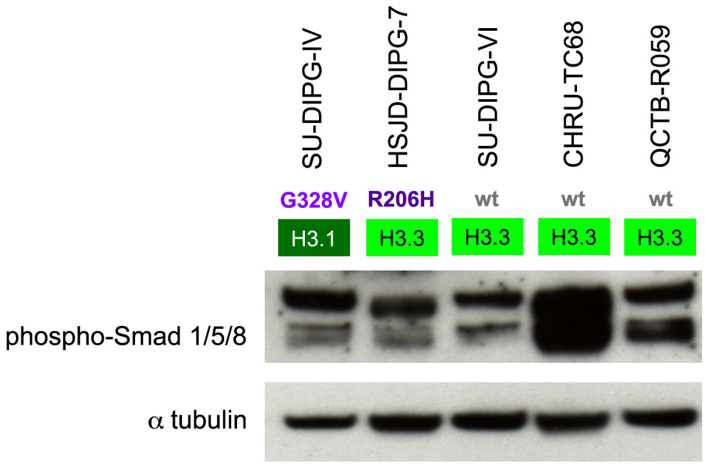

Supplementary Figure 7 – *Basal levels of phospo-Smad 1/5/8 in DIPG cells*. Western blot analysis of phospo-Smad 1/5/8 (lower band) in SU-DIPG-IV (DIPG, *ACVR1/ALK2* G328V, *HIST1H3B* K27M), HSJD-DIPG007 (DIPG, *ACVR1/ALK2* R206H, *H3F3A* K27M), SU-DIPG-VI (DIPG, *ACVR1/ALK2* wt, *H3F3A* K27M), CHRU-TC68 (DIPG, *ACVR1/ALK2* wt, *H3F3A* K27M) and QCTB-R059 (thalamic paediatric GBM, *ACVR1/ALK2* wt, *H3F3A* K27M). α-tubulin is included as a loading control.

Nature Genetics: doi:10.1038/ng.2925

Study ID	Local ID	Hospital	Clinical diagnosis	Location	Age (yrs)	Sex	Histology	WHO	Source	Survival (months)	Outcome	Seq	Histone H3	ACVR1
NCHP_DIPG006	BAUK	Necker Childrens Hospital, Paris	DIPG	Pons	6.3	Male	GBM	4	Biopsy	8.3	Died	WGS	*H3F3A*	wt
NCHP_DIPG011	BOUC	Necker Childrens Hospital, Paris	DIPG	Pons	4.8	Female	AA	3	Biopsy	20.0	Died	WGS	*HIST1H3B*	G328E
NCHP_DIPG052	INAR	Necker Childrens Hospital, Paris	DIPG	Pons	4.6	Male	AA	3	Biopsy	10.2	Died	WGS	*HIST1H3B*	G328V
NCHP_DIPG061	MAHJ	Necker Childrens Hospital, Paris	DIPG	Pons	11.9	Female	LGA	2	Biopsy	5.0	Died	WGS	*H3F3A*	wt
NCHP_DIPG065	MJAY	Necker Childrens Hospital, Paris	DIPG	Pons	10.2	Male	GBM	4	Biopsy	16.8	Died	WGS	*H3F3A*	wt
NCHP_DIPG081	RUSL	Necker Childrens Hospital, Paris	DIPG	Pons	6.7	Male	GBM	4	Biopsy	16.8	Died	WGS	*H3F3A*	wt
NCHP_DIPG101	BAMN	Necker Childrens Hospital, Paris	DIPG	Pons	3.9	Female	GBM	4	Biopsy	13.1	Died	WGS	*H3F3A*	wt
NCHP_DIPG102	BENM	Necker Childrens Hospital, Paris	DIPG	Pons	10.3	Male	AOA	3	Biopsy	3.4	Died	WGS	*H3F3A*	wt
NCHP_DIPG103	DANA	Necker Childrens Hospital, Paris	DIPG	Pons	5.8	Female	GBM	4	Biopsy	17.5	Alive	WGS	*HIST1H3B*	wt
NCHP_DIPG104	DUJJ	Necker Childrens Hospital, Paris	DIPG	Pons	4.4	Male	LGA	2	Biopsy	9.1	Died	WGS	wt	wt
NCHP_DIPG105	GIBG	Necker Childrens Hospital, Paris	DIPG	Pons	6.6	Female	LGA	2	Biopsy	7.8	Died	WGS	*H3F3A*	wt
NCHP_DIPG106	HENJ	Necker Childrens Hospital, Paris	DIPG	Pons	12.1	Male	GBM	4	Biopsy	9.1	Died	WGS	wt	wt
NCHP_DIPG107	LACL	Necker Childrens Hospital, Paris	DIPG	Pons	8.8	Male	AA	3	Biopsy	8.4	Died	WGS	*H3F3A*	wt
NCHP_DIPG108	LEMN	Necker Childrens Hospital, Paris	DIPG	Pons	7.5	Male	AA	3	Biopsy	17.8	Alive	WGS	*HIST1H3B*	G328V
NCHP_DIPG109	MUCM	Necker Childrens Hospital, Paris	DIPG	Pons	6.2	Male	AOA	3	Biopsy	13.5	Died	WGS	*H3F3A*	wt
NCHP_DIPG110	PHIA	Necker Childrens Hospital, Paris	DIPG	Pons	5.7	Male	LGA	2	Biopsy	10.8	Died	WGS	wt	wt
NCHP_DIPG111	SCHL	Necker Childrens Hospital, Paris	DIPG	Pons	10.6	Female	AOA	3	Biopsy	8.6	Died	WGS	*H3F3A*	wt
NCHP_DIPG112	ZERR	Necker Childrens Hospital, Paris	DIPG	Pons	5.6	Female	LGA	2	Biopsy	13.3	Died	WGS	*H3F3A*	wt
NCHP_DIPG113	BLAG	Necker Childrens Hospital, Paris	DIPG	Pons	4.6	Male	AA	3	Biopsy	14.0	Died	WGS	*HIST1H3B*	G356D
NCHP_DIPG114	GONJ	Necker Childrens Hospital, Paris	DIPG	Pons	8.6	Male	LGA	2	Biopsy	20.3	Died	WGS	*HIST1H3B*	wt

HSJD_DIPG001	N06.48	Hospital Sant Joan de Déu, Barcelona	DIPG	Pons	6.0	Female	AA	3	Autopsy	11.0	Died	WES	*H3F3A*	wt
HSJD_DIPG002	N07.92	Hospital Sant Joan de Déu, Barcelona	DIPG	Pons	6.0	Female	AA	3	Autopsy	15.1	Died	WES	*HIST1H3B*	R258G
HSJD_DIPG003	N08.55	Hospital Sant Joan de Déu, Barcelona	DIPG	Pons	6.0	Male	GBM	4	Autopsy	6.6	Died	WES	*H3F3A*	wt
HSJD_DIPG004	N11.49	Hospital Sant Joan de Déu, Barcelona	DIPG	Pons	10.0	Female	LGA	2	Autopsy	35.3	Died	WES	*HIST1H3B*	G328E
HSJD_DIPG007	N12.32	Hospital Sant Joan de Déu, Barcelona	DIPG	Pons	9.9	Male	GBM	4	Biopsy	0.9	Died	WES	*H3F3A*	R206H
HSJD_DIPG008	HSJD-DIPG-8	Hospital Sant Joan de Déu, Barcelona	DIPG	Pons	6.5	Male	LGA	2	Autopsy	16.0	Died	WES	*H3F3A*	wt
NCHP_DIPG004	ADOM	Necker Childrens Hospital, Paris	DIPG	Pons	8.0	Female	LGA	3	Biopsy	26.0	Died	VAL	*HIST1H3B*	G328W
NCHP_DIPG008	BERG	Necker Childrens Hospital, Paris	DIPG	Pons	4.7	Male	AA	3	Biopsy	8.9	Died	VAL	*H3F3A*	wt
NCHP_DIPG012	BOUL	Necker Childrens Hospital, Paris	DIPG	Pons	4.5	Female	GBM	4	Biopsy	14.2	Died	VAL	*HIST1H3B*	G328V
NCHP_DIPG013	BOUM	Necker Childrens Hospital, Paris	DIPG	Pons	7.3	Female	AA	3	Biopsy	5.7	Died	VAL	*H3F3A*	wt
NCHP_DIPG014	BOUS	Necker Childrens Hospital, Paris	DIPG	Pons	6.2	Female	AA	3	Biopsy	1.2	Alive	VAL	wt	R206H
NCHP_DIPG025	CORC	Necker Childrens Hospital, Paris	DIPG	Pons	4.6	Male	AA	3	Biopsy	11.3	Died	VAL	*H3F3A*	wt
NCHP_DIPG026	CREA	Necker Childrens Hospital, Paris	DIPG	Pons	7.1	Male	LGA	2	Biopsy	12.3	Died	VAL	*H3F3A*	wt
NCHP_DIPG029	DECC	Necker Childrens Hospital, Paris	DIPG	Pons	3.4	Female	AA	3	Biopsy	14.1	Died	VAL	*H3F3A*	wt
NCHP_DIPG030	DECS	Necker Childrens Hospital, Paris	DIPG	Pons	13.6	Male	AA	3	Biopsy	9.3	Died	VAL	wt	wt
NCHP_DIPG032	DELT	Necker Childrens Hospital, Paris	DIPG	Pons	12.1	Male	AA	3	Biopsy	16.8	Died	VAL	*H3F3A*	wt
NCHP_DIPG043	GALC	Necker Childrens Hospital, Paris	DIPG	Pons	9.2	Male	AA	3	Biopsy	3.8	Died	VAL	wt	wt
NCHP_DIPG044	GALF	Necker Childrens Hospital, Paris	DIPG	Pons	9.4	Female	AA	3	Biopsy	8.3	Died	VAL	*H3F3A*	wt
NCHP_DIPG048	GVEE	Necker Childrens Hospital, Paris	DIPG	Pons	6.4	Female	AA	3	Biopsy	7.3	Died	VAL	*HIST1H3B*	wt
NCHP_DIPG050	HADZ	Necker Childrens Hospital, Paris	DIPG	Pons	6.5	Male	AA	3	Biopsy	7.2	Died	VAL	*H3F3A*	wt
NCHP_DIPG056	LEFL	Necker Childrens Hospital, Paris	DIPG	Pons	11.0	Male	AA	3	Biopsy	17.7	Died	VAL	*H3F3A*	wt

Nature Genetics: doi:10.1038/ng.2925

NCHP_DIPG062	MAKM	Necker Childrens Hospital, Paris	DIPG	Pons	10.8	Male	AA	3	Biopsy	12.3	Died	VAL	*H3F3A*	wt
NCHP_DIPG063	MAUM	Necker Childrens Hospital, Paris	DIPG	Pons	5.3	Female	GBM	4	Biopsy	14.9	Died	VAL	*HIST1H3B*	G328E
NCHP_DIPG069	NALF	Necker Childrens Hospital, Paris	DIPG	Pons	6.8	Female	GBM	4	Biopsy	6.0	Died	VAL	*H3F3A*	wt
NCHP_DIPG072	PAIC	Necker Childrens Hospital, Paris	DIPG	Pons	13.5	Female	GBM	4	Biopsy	10.9	Died	VAL	*H3F3A*	wt
NCHP_DIPG075	POIJ	Necker Childrens Hospital, Paris	DIPG	Pons	4.5	Female	GBM	4	Biopsy	20.4	Died	VAL	*HIST1H3B*	wt
NCHP_DIPG077	RAHR	Necker Childrens Hospital, Paris	DIPG	Pons	7.4	Female	AA	3	Biopsy	4.9	Died	VAL	*H3F3A*	wt
NCHP_DIPG079	RIER	Necker Childrens Hospital, Paris	DIPG	Pons	7.6	Male	GBM	4	Biopsy	14.1	Died	VAL	*H3F3A*	wt
NCHP_DIPG083	SANC	Necker Childrens Hospital, Paris	DIPG	Pons	11.3	Female	AA	3	Biopsy	14.2	Died	VAL	*H3F3A*	wt
NCHP_DIPG115	GREL	Necker Childrens Hospital, Paris	DIPG	Pons	1.7	Male	LGA	2	Biopsy	58.0	Died	VAL	*H3F3A*	wt
NCHP_DIPG116	HUPN	Necker Childrens Hospital, Paris	DIPG	Pons	4.4	Male	AOA	3	Biopsy	10.0	Died	VAL	wt	wt
NCHP_DIPG117	OWGC	Necker Childrens Hospital, Paris	DIPG	Pons	5.0	Male	AA	3	Biopsy	11.9	Died	VAL	*HIST1H3B*	wt

Supplementary Table 2 – *Description of samples used in this study.* Clinicopathological annotation of the 26 DIPG cases profiled by whole genome or exome sequencing in this study, as well as those used in the validation cohort. DIPG: diffuse intrinsic pontine glioma; GBM: glioblastoma multiforme; AA: anaplastic astrocytoma; AOA: anaplastic oligoastrocytoma; LGA: low grade astrocytoma. WGS: whole genome sequencing; WES: whole exome sequencing; VAL: validation.

Cell line ID	Originator	Clinical diagnosis	Location	Age (yrs)	Sex	Histology	WHO	Source	Survival (months)	Outcome	Histone H3	ACVR1
CHRU-TC68	Centre Hospitalier Régional Universitaire, Strasbourg	DIPG	Pons	9.8	Female	AA	3	Biopsy	7.0	Alive	*H3F3A*	wt
HSJD-DIPG007	Hospital Sant Joan de Déu, Barcelona	DIPG	Pons	9.9	Male	GBM	4	Biopsy	0.9	Died	*H3F3A*	R206H
QCTB-R059	Queensland Children's Medical Research Institute, Brisbane	GBM	Thalamus	10.4	Female	GBM	4	Surgery	0.9	Died	*H3F3A*	wt
SU-DIPG-IV	Stanford University, California	DIPG	Pons	3.0	Female	GBM	4	Autopsy	8.0	Died	*HIST1H3B*	G328V
SU-DIPG-VI	Stanford University, California	DIPG	Pons	7.0	Female	GBM	4	Autopsy	6.0	Died	*H3F3A*	wt

Supplementary Table 3 – *Details of primary cell cultures used.* Clinical and molecular data relating to the four DIPG and one H3F3A K27M mutant thalamic paediatric GBM cell cultures used for preclinical and mechanistic studies. DIPG: diffuse intrinsic pontine glioma; GBM: glioblastoma multiforme; AA: anaplastic astrocytoma.

Nature Genetics: doi:10.1038/ng.2925

Name	Forward	Reverse
H3F3A	GATTTTGGGTAGACGTAATCTTCA	TTTCCTGTTATCCATCTTTTTGTT
HIST1H3B	GGGCAGGAGCCTCTCTTAAT	ACCAAGTAGGCCTCACAAGC
ACVR1 exon 6	GATTGCTGCCCTTCATGTG	AAAAGCAGATTTTCCAAGTTCC
ACVR1 exon 7	TAATGATGGGCTGGCTGC	AAAACGGAGAGAGCAAAGGC
ACVR1 exon 8	GATGACATTTACTGTGTAGGTCGC	GATGCAACTCACCTAACCATTG
ACVR1 exon 9	TGGTTTAAAATCCTTCAGCAGC	TTTTAAAGGTAGCTGGATCAAGAG
ACVR1 exon 8 mRNA	TCAGGAAGTGGCTCTGGTCT	CAAGTCCAAAGGCCCAAATA

Supplementary Table 4 – *PCR primers used*. Sequences are given for PCR amplification of H3F3A, HIST1H3B and ACVR1 from genomic DNA for mutation detection, and ACVR1 from mRNA to determine allele-specific expression of the mutant.

Partie II : Dérégulation du code des histones dans les DIPG

La forte prévalence des mutations de l'histone H3 dans les gliomes malins pédiatriques témoigne de leur rôle fondamental dans la genèse de ces tumeurs.
Dans la suite de cette partie, nous considérons uniquement l'effet de la substitution K27M puisque celle-ci concerne particulièrement les tumeurs du tronc cérébral ou plus largement celles de la ligne médiane, à la différence de la substitution G34R/V uniquement retrouvée dans les tumeurs des hémisphères cérébraux.

En résumé, les travaux de Chan et Lewis ont montré que les tumeurs mutées H3K27M présentaient un niveau réduit des marques de méthylation H3K27me3 en raison de l'effet dominant négatif du mutant K27M quelle que soit l'histone H3 mutée (H3.1 ou H3.3). Ce phénomène se traduite par une dé-répression de l'expression génique, cependant celui-ci n'est pas uniforme à travers le génome, comme en témoigne la présence de marques H3K27me3 persistantes sur certains *loci* spécifiques (cf. **INTRODUCTION Partie III 2.4**).

1. Dérégulation épigénétique : Perte de triméthylation de H3K27 et hypométhylation de l'ADN

Les régulations épigénétiques recouvrent 2 grands types de modifications : au niveau du code des histones d'une part, mais également au niveau de l'ADN par méthylation des cytosines des ilots CpG. En effet, la méthylation des ilots CpG des régions promotrices est également associée à l'extinction génique et elle participe au recrutement d'une machinerie de répression transcriptionnelle au niveau de la chromatine. Cette machinerie regroupe de nombreuses protéines telles que les ADN-méthyltransférases (DNMT), les histones méthyltransférases, les histones désacétylases (HDAC). Ces deux phénomènes peuvent s'opérer de concert ou de façons indépendantes pour moduler l'expression des gènes. Dans le cas de la méthylation de la lysine 27 de l'histone H3, il a été démontré que ces deux phénomènes étaient indépendants (Kondo et al. 2008). Cependant, ceci semble être remis en question par les effets observés dans le cas de cette mutation d'histone.

C'est précisément sur ces deux mécanismes et en relation avec la mutation H3K27M dans les DIPG que Bender et ses collaborateurs se sont penchés.

A la différence des travaux précédents menés *in vitro*, les auteurs ont analysé l'effet de cette mutation sur des tumeurs primaires. Par intégration de données de ChIP-Seq et de transcriptome et en accord avec les résultats précédents, ils mettent en évidence que la réduction de l'expression de H3K27me3 induite par la mutation est associée à une

surexpression globale et à une dé-répression transcriptionnelle spécifique de certains gènes cibles connus de PCR2.

D'autre part, les auteurs se sont intéressés à la méthylation de l'ADN par technique de séquençage du génome entier après traitement au bisulfite de sodium. Précédemment, une autre étude menée par le même groupe mettait en évidence que le type de mutation de l'histone H3 définissait un sous-groupe épigénétique présentant un profil de méthylation distinct et une signature transcriptomique spécifique (Sturm et al. 2012). En accord avec ces résultats, les auteurs montrent que l'activation transcriptionnelle des gènes différentiellement exprimés est accompagnée par une perte de méthylation au niveau des promoteurs de ces gènes. Les auteurs ont ensuite cherché à savoir s'il existait une relation entre ces régions hypométhylées, cette répartition hétérogène des marques H3K27me3 et la régulation de l'expression de ces gènes. Alors que la majorité des gènes sous-exprimés dans les mutants H3K27M n'est liée à aucun de ces deux mécanismes en particulier, l'augmentation de l'expression de 74% des gènes surexprimés est liée à au moins un des deux mécanismes. Néanmoins, l'observation des *loci* spécifiques présentant un gain de la marque H3K27me3 dans un contexte de réduction globale des marques épigénétiques dans ces tumeurs mutées H3K27M n'a pas été expliquée et suggèrent l'établissement d'une relation particulière entre ces 2 mécanismes dans ce contexte.

De manière générale, les auteurs concluent que la réduction de H3K27me3 et l'hypométhylation de l'ADN sont des mécanismes majeures conduisant à l'activation d'un programme d'expression génique spécifique dans les gliomes malins pédiatriques (Bender et al. 2013) (cf. **ANNEXE**).

Les lignées tumorales, dont celles dérivées dans notre laboratoire à partir des tumeurs primitives des patients, ont permis de confirmer la baisse considérable de la marque de triméthylation des histones H3 sur la Lysine 27. Cette perte de triméthylation est détectable en immunohistochimie et pourrait devenir un test diagnostique.

2. Comparaison H3.1 *versus* H3.3

De manière intéressante, cette mutation « gain-de-fonction » retrouvée spécifiquement dans les gliomes malins de la ligne médiane (incluant le tronc cérébral) touche deux fois plus souvent le variant d'histone H3.3 (*H3F3A*) que le variant canonique H3.1 (*HIST1H3B*) (Wu et al. 2012). Ces deux histones structurellement très proches ne diffèrent que par 5 acides aminés et présentent des propriétés distinctes dans l'organisation de la chromatine. Les différences entre ces deux variants sont exposées dans la **figure 11**. Cette observation permet d'émettre l'hypothèse selon laquelle la mutation K27M de chacun de ces variants d'histone impacterait de manière spécifique sur le comportement de la tumeur. Nous avons donc choisi de décrire précisément les différences cliniques et biologiques associées à chacune de ces mutations. Les résultats préliminaires non publiés seront abordés dans la suite de cette partie.

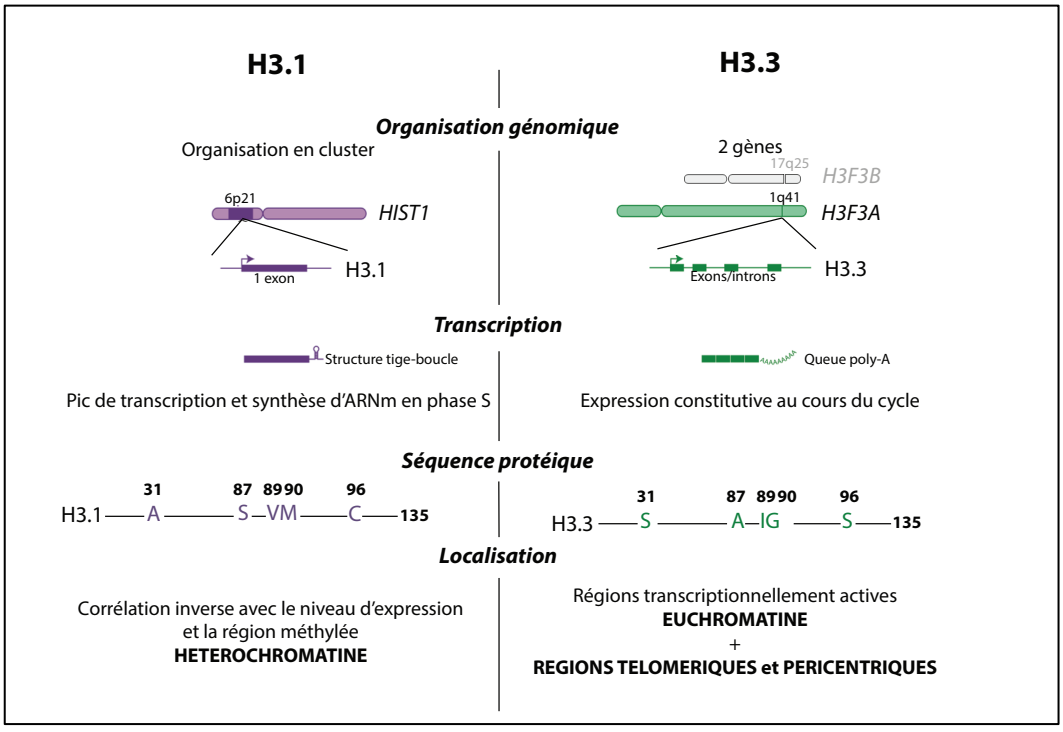

Figure 11 : Comparaison des variants de l'histone H3, H3.1 et H3.3.

Les gènes de l'histone canonique H3.1 sont organisés au sein d'un cluster (*HIST1*) sur le chromosome 6p21 à la différence du variant H3.3 codé par 2 gènes (*H3F3A* et *H3F3B*) sur les chromosomes 17q25 et 1q41. A la différence de variant H3.3, l'histone canonique H3.1 présente un seul exon et pas de queue poly-adénylée. Les acides aminés divergeant sont illustrés. Alors que le H3.1 est retrouvé dans des régions hétérochromatiniennes, le H3.3 se situe dans des régions transcriptionnellement actives mais également télomériques et péricentriques. D'après (Szenker 2012).

ARTICLE 2 :

Le type de variant d'histone H3 portant la mutation K27M est un marqueur pronostique associé à deux phénotypes différents de gliomes infiltrants du tronc cérébral

The type of histone H3 variant with Lys27Met (K27M) change is a prognostic marker associated with two different phenotypes of diffuse intrinsic pontine gliomas (DIPG)

David Castel[1] *, Marie-Anne Debily[1,2] *, Cathy Philippe[1] *, Nathalène Truffaux[1], Kathy Taylor[3], Raphaël Calmon[4], Nathalie Boddaert[4], Ludivine Le Dret[1], Patrick Saulnier[5], Ludovic Lacroix[5], Alan McKay,[3] Chris Jones[3], Stéphanie Puget[6], Christian Sainte-Rose[6], Thomas Blauwblomme[6], Pascale Varlet[7] #, Jacques Grill[1,8] #.

* all three co-authors contributed equally to the work.
# co-senior authors

En préparation

MATERIEL ET METHODES

Cinquante-et-un patients atteints de DIPG ont été caractérisés cliniquement, radiologiquement et biologiquement (mutations, analyse transcriptomique et analyse CGHarray) ainsi que 90 gliomes malins pédiatriques non-DIPG. Le matériel tumoral a été obtenu à partir de biopsies réalisées au diagnostic.

RESULTATS

La plupart des DIPG présentent une mutation du variant H3 K27M ou une perte de la triméthylation

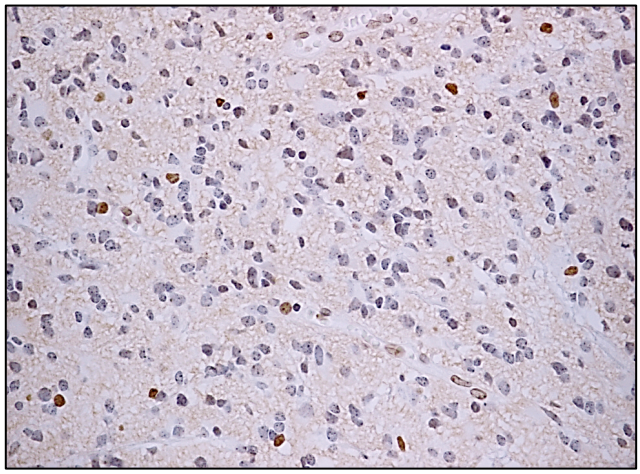

Figure 12 : Immunohistochimie de la marque H3K27me3 dans un DIPG

Les cellules tumorales ont perdu la marque de triméthylation alors que les cellules résidentes (en brun) l'ont conservée. 69/74 gliomes infiltrants du tronc cérébral analysés par immunohistochimie par le Dr Varlet à Sainte-Anne ont une perte d'expression de la marque de triméthylation des histones en K27. Parmi les cinq tumeurs pour lesquelles aucune mutation en K27M n'a été retrouvée, toutes avaient une perte de la marque de triméthylation dans la tumeur.

Répartition anatomique des mutations de l'histone H3

Comme attendu, l'analyse des mutations fait apparaître une répartition spécifique à chacune d'entre-elles (cf. **Figure 13**). En effet, la mutation H3.3 G34V/R se retrouve spécifiquement dans les tumeurs des hémisphères cérébraux. En revanche, la mutation H3.3 K27M touche les tumeurs de la ligne médiane (thalamus, tronc cérébral et moelle épinière) et la mutation H3.1 K27M touche exclusivement les DIPG.

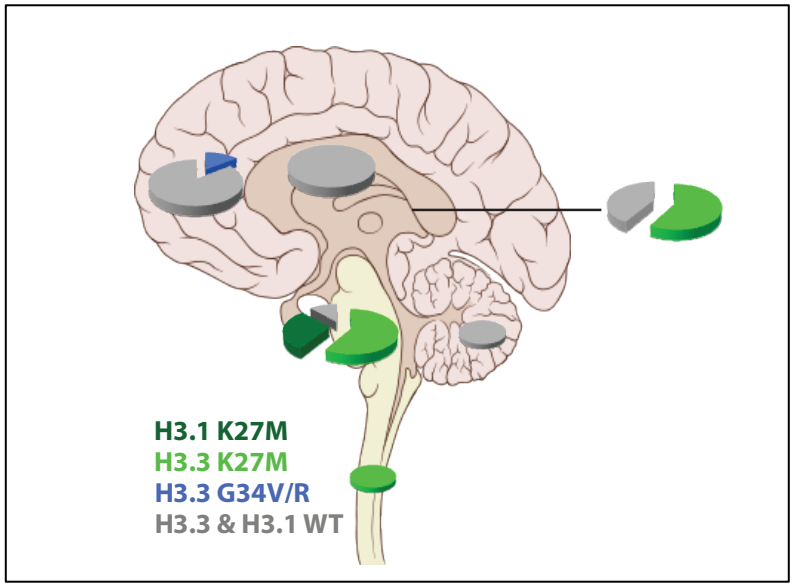

Figure 13 : Répartition anatomique des mutations de l'histone H3 parmi les gliomes malins pédiatriques. Etablie sur une cohorte de 140 gliomes malins pédiatriques opérés ou biopsiés au sein du service de Neurochirurgie de l'Hôpital Necker-Enfants Malades (Paris), séquencés par technique Sanger.

Impact pronostique des mutations K27M de l'histone H3

L'analyse des données de survie fait apparaître l'influence probable du variant d'histone muté sur la biologie de la tumeur. En effet, la durée de survie globale du groupe muté H3.3 K27M est significativement plus courte que le groupe H3.1 K27M (**Figure 14**).

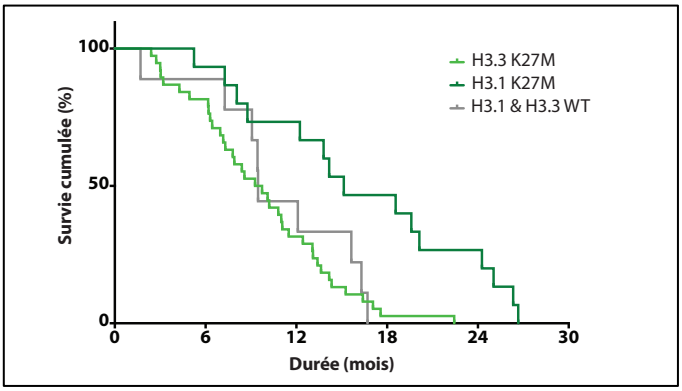

Figure 14 : Courbe de survie globale des 63 patients atteints d'un DIPG selon le statut de l'histone H3. La médiane de survie du groupe H3.3 K27M (vert clair) est 9,5 mois *versus* 15,1 mois pour le groupe H3.1 K27M (vert foncé) (p=0,0005, log rank test).

Les altérations génomiques associées aux mutations des histones

De manière intéressante, l'analyse de ségrégation de chacune de deux mutations H3 K27M avec les autres mutations décrites dans les DIPG met en évidence une répartition particulière de celles-ci. En effet, la mutation H3.3 K27M est associée à l'amplification du gène *PDGFRA* alors que la mutation H3.1 K27M est associée aux mutations du gène *ACVR1* (**Figure 15**).

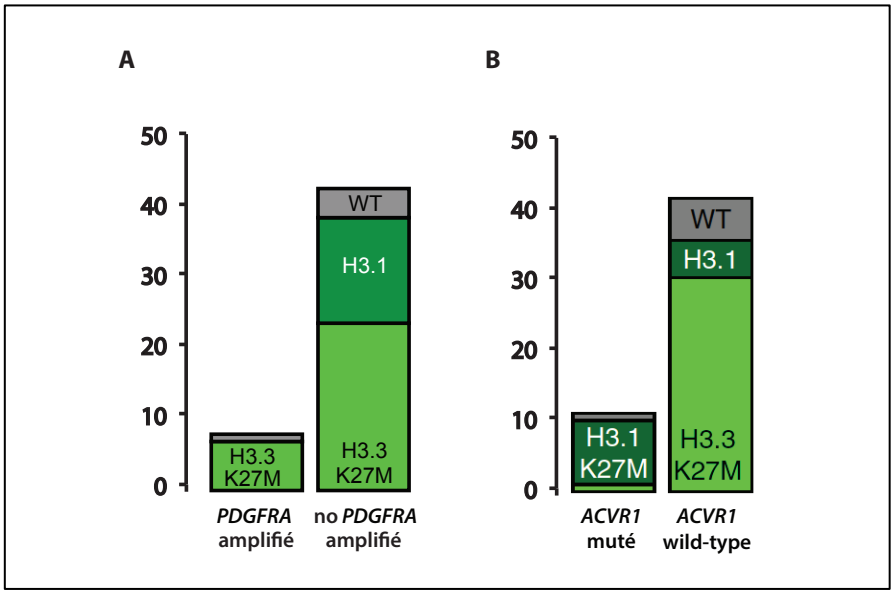

Figure 15 : Ségrégation des mutations d'histone H3 avec les autres anomalies génétiques décrites dans les DIPG. La mutation de l'histone H3.3 K27M ségrége avec l'amplification de *PDGFRA* (**(A) ;** p=0,005, Fisher test) tandis que la mutation H3.1 K27M ségrége avec *ACVR1* muté H3.1 K27M (**(B) ;** p<0,001, Fisher test).

COMMENTAIRES

En dépit des conséquences similaires sur le complexe PRC2, les mutations de *H3F3A* et *HIST1H3B* sont associées à deux phénotypes biologiques différents. En plus de leur impact pronostique, ces données suggèrent la possibilité d'une approche thérapeutique distincte.

Enfin l'existence de ces deux phénotypes biologiques différents définis par l'histone muté n'est pas sans rappeler celle des deux sous-groupes biologiques établis par analyse transcriptomique (cf. **INTRODUCTION Partie III 3.1 & 3.2**).

Nous avons tenté de mettre en perspectives ces observations à partir des données disponibles sur nos échantillons (cf. **Figure 16**).

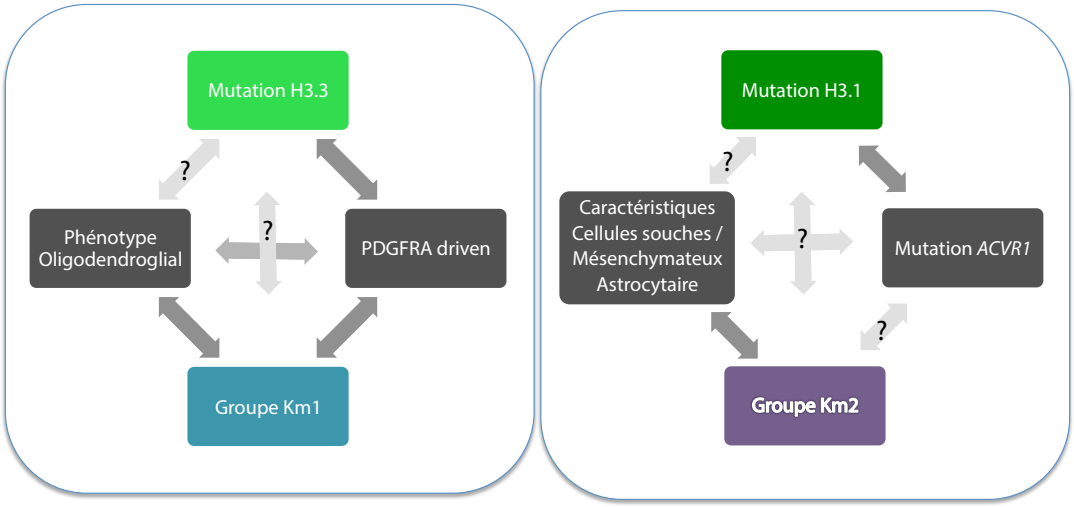

Figure 16 : Comparaison des 2 sous-groupes de DIPG

Le sous-groupe Km1 se rapproche en effet du groupe portant la mutation H3.3 K27M de part son profil d'expression génique enrichi en gènes de la signature *PDGFRA* (*PDGFRA* driven). D'autre part, le phénotype oligodendroglial associé au Km1 devra être vérifié dans DIPG H3.3 mutés.

En revanche la correspondance entre le sous-groupe Km2 et les DIPG mutés H3.1 semble moins évidente pour le moment. Il s'agira de savoir si les tumeurs mutées H3.1, à l'image des tumeurs du groupe Km2, expriment des marqueurs de type «Cellules souches / Mésenchymateux » et présentent un phénotype astrocytaire. D'autre part, on peut se demander si l'on retrouve spécifiquement des mutations d'ACVR1 dans le sous-groupe Km2.

Egalement, la différence de pronostic associé à chacun de ces sous-groupes appuit cette comparaison.

CHAPITRE 2 :
EVALUATION PRECLINIQUE

Partie I :

ARTICLE 3 :

Evaluation préclinique de dasatinib seul ou en combinaison avec cabozantinib pour le traitement du gliome infiltrant du tronc cérébral

Preclinical evaluation of dasatinib alone and in combination with cabozantinib for the treatment of Diffuse Intrinsic Pontine Glioma

Nathalène Truffaux[1], Cathy Philippe[1], Janna Paulsson[2], Felipe Andreiuolo[1], Léa Guerrini-Rousseau[1], Gaétan Cornilleau[1], Ludivine Le Dret[1], Catherine Richon[3], Ludovic Lacroix[4], Stéphanie Puget[6], Birgit Geoerger[1,7], Gilles Vassal[1], Arne Ostman[2], Jacques Grill[1,7].

Soumis à Clinical Cancer Research

Les analyses moléculaires d'échantillons tumoraux issus de patients atteints de DIPG ont démontré que l'oncogène le plus fréquemment amplifié était le *PDGFRA* (cf. **INTRODUCTION Partie III 2.1)**. De même, un des deux sous-groupes identifiés par l'analyse non supervisée montre un profil enrichi pour la signature d'expression génique décrite dans les gliomes malins de type adulte avec une amplification de *PDGFRA*; toutes les tumeurs avec une amplification de *PDGFRA* sauf une font partie de ce sous-groupe (Puget et al. 2012). Parmi les inhibiteurs en développement pouvant cibler cette voie, se trouve le dasatinib (cf. **Tableau 3**). Il s'agit d'un inhibiteur oral qui cible plusieurs tyrosine kinases, notamment bcr-abl, les membres de la famille src, PDGFRα/β et EPHA2-5 (cf. **Tableau 4**). Il est désormais indiqué dans certaines leucémies et est encore en développement dans d'autres types de cancers solides. Ainsi, plusieurs études se sont aussi intéressées à cet inhibiteur dans le cadre de thérapies anti-gliome à la fois en préclinique et dans des essais cliniques précoces (Du et al. 2009; K. V. Lu et al. 2009; Milano et al. 2009; Ahluwalia et al. 2010; I. Pollack et al. 2010; Agarwal et al. 2012; Benezra et al. 2012; Broniscer et al. 2013; Huveldt et al. 2013). A notre tour, nous avons voulu explorer son efficacité dans le traitement des DIPG.

De la même manière, le second oncogène fréquemment amplifié concerne le récepteur MET (Taylor et al. 2014) et l'amplification concomitante de *PDGFRA* et *MET* a été constatée plusieurs fois (Paugh et al. 2011; Puget et al. 2012). Compte tenu de l'activation probable de plusieurs récepteurs à tyrosine-kinase, nous pensons que l'anticipation des phénomènes de résistance passe par l'utilisation combinée d'inhibiteurs de ces voies. En effet, plusieurs exemples de ce type ont déjà été décrits dans la littérature (Little et al. 2012).

Cette étude rapporte donc l'évaluation préclinique du dasatinib seul et en combinaison avec un inhibiteur de MET, le cabozantinib.

Dans un premier temps, par analyse en immunohistochimie d'un échantillon représentatif de 11 DIPG au diagnostic présentant ou non des anomalies génomiques (amplification ou mutation) du *PDGFRA*, nous mettons en évidence une surexpression et une suractivation fréquente de PDGFRα même en l'absence d'anomalie génétique détectée. Ceci est compatible avec l'existence d'une surexpression du *PDGFRA* dans les DIPG en général comme nous l'avons montré dans l'analyse du transcriptome de ces tumeurs (Puget et al, 2012). Parallèlement, l'analyse du profil d'expression génique (GE) d'une nouvelle cohorte 41 échantillons tumoraux prélevés au diagnostic montre un enrichissement des gènes appartenant à la signature de sensibilité de cet inhibiteur décrite par Huang et al. pour les carcinomes mammaires et pulmonaires (Huang et al. 2007).

Dans un deuxième temps, ce travail rapporte l'établissement et la caractérisation (par CGH array, et GE) d'un panel de 4 lignées cellulaires nouvellement développées à partir de biopsies réalisées au diagnostic. De la même manière, l'analyse GE met en évidence l'expression de la signature prédictive de réponse au dasatinib dans ces lignées cellulaires.

Nous avons donc évalué l'efficacité de cet inhibiteur *in vitro* sur ces modèles. Dasatinib réduit la prolifération (IC_{50}=10-100 nM) et l'invasion cellulaire (réduction : 30-60%) à 100nM sur l'ensemble de ces lignées et induit l'apoptose dans 1 des 4 lignées testées. Par analyse en western blot, l'effet de cet inhibiteur s'accompagne d'une réduction significative de la phosphorylation d'Akt et d'une réduction partielle d'activation de la voie des MAPK.
D'autre part, ACVR1 dont les mutations activatrices nouvellement décrites dans les DIPG sont responsables de l'activation constitutionnelle de la voie des BMP-TGFβ, est une cible secondaire du dasatinib. Nos lignées présentent également une activation basale de cette voie en absence de mutation. Nous observons une diminution significative de l'activation de cette voie de signalisation avec des doses plus élevées de dasatinib qui pourrait participer à l'effet de ce médicament en préclinique.

En revanche, l'analyse du profil d'activation d'un large panel de récepteurs à activité tyrosine kinase (RTK) montrent une coactivation d'autres récepteurs notamment celle du récepteur MET. Compte tenu de l'amplification récurrente de ce gène, nous avons donc testé la combinaison de dasatinib avec le cabozantinib. Nos résultats montrent un effet synergique de ces 2 inhibiteurs sur la prolifération cellulaire dans 3 des 4 lignées, et un effet au moins additif dans la 4ème.
De surcroit, la voie HGF/MET étant incriminée dans le phénomène d'invasion cellulaire, nous avons testé cette combinaison sur la lignée la plus invasive et la moins sensible au dasatinib. Cette combinaison améliore nettement l'effet anti-invasif constaté avec l'inhibiteur seul (réduction de 70% à 0,1 µM dasatinib + 0,1 µM cabozantinib).

En conclusion, ces résultats montrent les effets synergiques antiprolifératif et anti-invasif en réponse au traitement combiné de dasatinib avec un inhibiteur de MET. Ceci supporte la poursuite de cette stratégie vers l'application clinique dans le traitement des DIPG. En effet, les capacités d'invasion sont une cause très plausible de l'échec de nos thérapeutiques jusqu'ici.

Tableau 3 : Liste (non exhaustive) des inhibiteurs d'activité kinase en développement et leur constante d'inhibition (Kd) pour PDGFRA. D'après (Davis et al. 2011)

Composé	*Kd (nM)*
AZD-2171	0,41
Dasatinib	0,47
Ki-20227	0,49
AG-013736	0,51
Sunitinib	0,79
SU-14813	1,10
MLN-518	2,40
ABT-869	4,20
EXEL-2880/GSK-1363089	4,50
Pazopanib	4,90
PD-173955	5,60
AMG-706	10
Staurosporine	10
AC220	11
BMS-540215	11
BIBF-1120	16
AB-1010	25
AST-487	27
JNJ-28312141	27
Imatinib	31
AZD-1152HQPA	38
CHIR-258/TKI-258	54
R406	60
Sorafenib	62
PTK-787	96
KW-2449	130
Nilotinib	180
PLX-4720	190
PP-242	220
Vandetanib	230
CEP-701	350
PKC-412	380
TAE-684	840
CHIR-265/RAF-265	1100
BIRB-796	1200
VX-680/MK-0457	1600
Erlotinib	1800
PHA-665752	2000
TG-101348	2700
SKI-606	5100
CI-1033	5200
Flavopiridol	5900
VX-745	8800

Tableau 4 : Liste (non exhaustive) de kinases et leur constante d'inhibition (Kd) par dasatinib. D'après (Davis et al. 2011)

Cible	Kd (nM)
EPHA3	0,09
ABL2	0,17
LCK	0,20
BLK	0,21
EPHA5	0,24
EPHA8	0,24
YES1	0,30
EPHB4	0,34
EPHB2	0,39
EPHB1	0,45
PDGFRA	0,47
FGR	0,50
ABL1	0,53
LYN	0,57
CSF1R	0,58
KIT	0,62
PDGFRB	0,63
DDR1	0,69
FYN	0,79
EPHA2	0,85
CSK	1,00
EPHA4	1,20
BMX	1,40
BTK	1,40
TXK	2,10
GAK	2,60
DDR2	3,20
EPHA1	4,10
TNK2	5,60
SRC	6,40
EPHB3	6,90
PTK6	7,80
TNNI3K	11,00
TEC	13,00
MAPK14	27,00
RIPK2	31,00
TESK1	33,00
MAP4K5	45,00
ERBB4	55,00
LIMK2	86,00
EGFR	120,00
ACVR2A	210,00
STK36	210,00
NLK	260,00
MAP3K4	310,00
ACVR1B	330,00
MYT1	410,00
BRAF	500,00
ACVR2B	570,00
LIMK1	570,00
RAF1	570,00
ACVR1	620,00
SLK	720,00
RET	730,00
MAP4K1	980,00
MAP2K1	1000,00
ERBB2	1400,00
MAP2K2	1400,00
SYK	2900,00
MAP4K4	3100,00

Preclinical evaluation of dasatinib alone and in combination with cabozantinib for the treatment of Diffuse Intrinsic Pontine Glioma

Nathalène Truffaux[1], Cathy Philippe [1], Janna Paulsson [2], Felipe Andreiuolo [1], Léa Guerrini-Rousseau [1], Gaétan Cornilleau [1], Ludivine Le Dret [1], Catherine Richon [3], Ludovic Lacroix [4], Stéphanie Puget [5], Birgit Geoerger [1,6], Gilles Vassal [1], Arne Ostman [2], Jacques Grill [1,6].

[1] CNRS UMR 8203 « Vectorology and Anticancer Therapeutics », Gustave Roussy Cancer Institute, Paris XI University, Villejuif, France.

[2] Department of Oncology and Pathology, Karolinska Institutet, Stockholm, Sweden

[3] Functional Genomics Unit, Gustave Roussy Cancer Institute, Paris XI University, Villejuif, France.

[4] Gustave Roussy, Translational Research Laboratory and Biobank, Villejuif F-94805, France; Gustave Roussy, Inserm U981, Villejuif F-94805, France; Gustave Roussy, Department of Medical Biology and Pathology, Villejuif F-94805, France.

[5] Department of Neurosurgery, Necker-Sick Children Hospital, Université Paris Descartes, Paris 75015, France.

[6] Department of Paediatric and Adolescent Oncology, Gustave Roussy Cancer Institute, Paris XI University, Villejuif, France.

Running title: Dasatinib alone and in combination for DIPG treatment

Keywords: Brainstem, preclinical model, PDGFRA, Src, ACVR1

Financial Support:

Bristol-Myers Squibb for drug supply and grant support (JG), Etoile de Martin (NT), Foundation TIGRE (JG and GC) and Le Défi de Fortunée (JG).

Corresponding author:

Jacques GRILL, MD-PhD

CNRS UMR 8203 « Vectorology and Anticancer Therapeutics » and Department of Paediatric and Adolescent Oncology, Gustave Roussy Cancer Institute, Paris XI University, 114 rue Edouard Vaillant, 94805 Villejuif, France.

TEL: +33 142 11 62 09

FAX: +33 1 42 11 52 75

Email: grill@igr.fr

Conflict of interest: BMS partially funded this study and also provided one of the study drugs.

Word count: 4878

Total number of figures: 7

Total number of tables: 4

Abstract

The platelet-derived growth factor receptor A (*PDGFRA*) is altered by amplification and/or mutation in DIPG. We explored *in vitro* the efficacy of dasatinib, a multi-tyrosine kinase inhibitor targeting this receptor, on new DIPG models.

Gene expression (GE) profiles were obtained from 41 DIPG biopsied at diagnosis and compared with the signature associated with sensitivity/resistance to dasatinib. A panel of 12 new DIPG cell lines were established from biopsy at diagnosis, serially passaged and characterized by GE analyses. Effects of dasatinib (1nM to 10μM) on proliferation, invasion and cytotoxicity were determined on 4 of these cell lines using live-cell imaging and flow cytometry assays. Downstream signaling and receptor tyrosine-kinases (RTK) were assessed by Western blot and phospho-RTK array. Combination with cabozantinib (inhibitor of MET and other RTKs) was studied on cellular growth and invasion analyzed by the Chou-Talalay method.

DIPG primary tumors and cell lines exhibited the signature of dasatinib sensitivity. Dasatinib reduced proliferation (IC50=10-100nM), and invasion (30-60% reduction) at 100nM in 4/4 cultures and induced apoptosis in 1 out 4 DIPG cell lines. Activity of downstream effectors of dasatinib targets including *ACVR1* was strongly reduced. Multiple RTKs were activated simultaneously in DIPG cell lines, including MET, suggesting benefit of combination treatment. Since *MET* is amplified in DIPG, we tested combinations of dasatinib with cabozantinib. Synergistic effects on proliferation and migration/invasion were observed in all cell lines.

Dasatinib exhibits anti-tumor effects *in vitro* that could be increased by the combination with another RTK inhibitor targeting MET.

INTRODUCTION

DIPG is one of the most frequent malignant brain tumors in children. Its prognosis is dismal with almost all patients dying before the second year after diagnosis (1). Due to its infiltrative nature, surgery cannot be performed without severe functional damages. Radiotherapy is the only effective treatment, albeit only transiently while the addition of chemotherapy did not increase survival significantly (2).

Diagnosis is usually made by radiology without biopsy collection. Lack of tumor tissue has limited our knowledge about the biology of this tumor. However, autopsy programs and systematic diagnostic biopsies performed by some groups allowed the conduct of specific high-throughput genomic studies (3).

The most striking features of these neoplasms are first their ability to grow fast thanks to the overexpression of various growth factors (4) and second their propensity to infiltrate the brain tissue (2) ; symptoms are often only present a few weeks before diagnosis, while this interval is usually over three months for the other brain tumors, and during the course of the disease, the tumor tend to spread extensively in the cerebellum and the deep gray nuclei.

PDGFRA signaling plays key role in paediatric gliomagenesis (5) and represents one of the few drugable target in DIPG so far. PDGFRA is the most commonly amplified receptor tyrosine kinase gene in DIPG (6–10) and activating mutations occur in 10% of DIPG (9–11). Previous study by gene expression analysis revealed the existence of a subgroup of DIPG characterized by the gene expression signature related to *PDGFRA* amplification not necessarily associated to the gene amplification or mutation (9). In DIPG, the second most frequently amplified/mutated gene is *MET* (4,9,12). These alterations in one of the major pathway of invasion are in accordance with the highly infiltrative nature of this tumor.

We established new adherent DIPG cell lines from stereotactic biopsies performed at diagnosis to explore agents currently in development for their potential role in the treatment of DIPG. Dasatinib is an oral inhibitor of multiple targets, including PDGFRA and B, c-Kit, and Src (13). Cabozantinib is a potent, ATP-competitive inhibitor of MET, VEGFR2

and RET (14). Each one is approved for other malignancies and is currently tested individually in clinical trials in adults with glioblastoma.

We show here *in vitro* on newly developed DIPG models the efficacy on cell growth and invasion of dasatinib alone and its synergistic effect in combination with cabozantinib.

MATERIALS AND METHODS

Immunohistochemistry (IHC)

Samples were stained in the Ventana autostainer (Roche) using the Omnimap kit and anti-rabbit secondary antibody (Roche). For antigen retrieval high pH buffer was used (T6455, Sigma Aldrich). The primary antibody for PDGFRα (#5241, Cell signaling technology) was used at a 1:125 dilution in antibody diluent from Ventana. Samples were then dehydrated in ethanol (70%, 95%, 99%) and xylene and mounted using PERTEX (00871, Histolab).

Proximity ligation assay (PLA)

Sections were deparaffinized, rehydrated and antigen retrieval was performed in a pressure cooker (5 min at 110°C, Decloaker chamber, Biocare Medical) using Diva decloaker as antigen retrieval (DV2004MX, Biocare Medical) followed by washes in Hot Rinse (HTR1001M, Biocare Medical). After wash in TBS-Tween 20 (0.05%) staining was continued according to manufacturers instructions (Sigma Aldrich) with the exception for blocking solution were 20% goat serum in TBS-Tween 20 (0.05%) was used instead. Primary antibodies: anti-PDGFRα at a 1:100 dilution (#3164, Cell signaling technology) and anti-phospho-tyrosine at a 1:2000 dilution (#9411, Cell signaling technology) in 20% goat serum in TBS-Tween 20 (0.05%). All washes were done in TBS-Tween 20 (0.05%). Staining was performed using PLA probes donkey anti-mouse minus (DUO92004, Sigma Aldrich) and donkey anti-rabbit plus (DUO92002, Sigma Aldrich) and brightfield detection kit (DUO92012, Sigma Aldrich). Samples were then mounted using PERTEX (Histolab).

Tumor and acid nucleic extraction

Tumor samples and clinical information were collected with written informed consent of the parents/guardians before inclusion into protocols approved by the Internal Review

Board of the Necker-Enfants Malades Hospital in Paris and the Gustave Roussy Cancer Institute in Villejuif. Only patient with classical diagnostic features of DIPG were included: 1) short clinical history of less than three months, 2) infiltrating neoplasm centered on the pons and involving at least 50% of the anatomical structure, 3) histology excluding a pilocytic astrocytoma or ganglioglioma. Tumor biopsies were snap frozen in liquid nitrogen in the operating room to ensure preservation of high quality RNA until extraction performed using DNA/RNA Mini Kit (Qiagen).

Gene Expression Analyses

RNA microarray hybridization was carried out by the Functional Genomics Platform of the Integrated Research Cancer Institute in Villejuif using the Agilent SurePrint G3 Hmn GE 8*60K Whole Human Gene Expression microarray, respectively (http://www.agilent.com). *The microarray data related to this paper are MIAME compliant and the raw data will be submitted to the Array Express data repository at the European Bioinformatics Institute (http://www.ebi.ac.uk/arrayexpress/) upon publication.*

Bioinformatics analysis

Raw gene expression data using normal brainstem as reference (BSR) were transferred into R software for statistical analysis. GSEA analysis (15) was performed with the pre-ranked tool on gene list ranked by increasing FDR adjusted p-values, for each contrast of interest, with default parameter values. A nominal False Discovery Rate (FDR) of <0.25 was considered statistically significant for GSEA. We ran GSEA analysis with t-test option as metric parameter.

Establishment of DIPG cell lines and cell culture

Tumor pieces were collected into DMEM (Dulbecco's Modified Eagles Medium, PAA Laboratories GmbH, Pasching, Austria). Biopsies were cut into 1 mm^3 pieces and placed into either DMEM for immediate processing or into freezing medium (90% serum, 10% DMSO) prior to being progressively cooled to –80°C. Cell dissociation was performed mechanically by passage through increasingly finer needles (19G to 26G). Single cells were seeded in AmnioMAX™ C-100 complete medium (Gibco, Invitrogen, Paisley, UK) and

maintained at 37°C in a 5% CO_2 humidified atmosphere. The cells were further cultured until appearance of adherent cells and colony formation and then weekly passaged.
Adult glioblastoma cell line T98G was obtained from American Type Culture Collection (ATCC) and paediatric cell line SF188 was kindly provided by Dr Chris Jones (The Institute of Cancer Research, Sutton, UK). Both were maintained as monolayers in DMEM-GlutaMAX™+10% FCS in 5% CO_2.

Drugs

Dasatinib (Sprycel, BMS-354825) and cabozantinib (Cometriq, XL184) were provided by Bristol-Myers Squibb (New York, NY) and Exelixis (San Francisco, CA) respectively and were prepared as a 20 mmol/L stock solution in DMSO.

Growth inhibition

Cells (2,000-3,000 cells/well) were plated in a 96-well plate. After 24 hours, the cells were subsequently exposed to dasatinib at various concentrations for 72 hours. Growth curves were constructed by imaging plates using the Incucyte system (Essen Instruments, Ann Arbor, MI), where the growth curves were built from confluence measurements acquired during automated kinetic imaging. IC_{50} concentrations were determined using sigmoidal dose-response (variable slope) statistics and normalized in GraphPad Prism (LaJolla, CA).
For the assessment of combination effects, cells were treated with increasing concentrations of drugs either alone or concurrently at their equipotent molar ratio and combination indices calculated by Chou&Talalay methods (16) and CalcuSyn software (Biosoft, Cambridge, Great Britain).

Cytotoxicity

Cells were plated in triplicate in 96-well plate to achieve optimal confluence of 25-30% before treatment. Cells were then treated with 100 nmol/l dasatinib or vehicle (DMSO) diluted with complete medium containing Yoyo-1 (Life Technologies) at final concentration of 0.1 μM. Images automatically were collected by the IncuCyte system every 2-3 hours in both contrast phase and fluorescence. Quantitative measurement of nuclear staining was determined by object counting with image analysis IncuCyte Zoom software.

Apoptosis assay

Subconfluent cells were treated with 50 and 100 nmol/L dasatinib for 72 hours. Cells were then harvested and stained with Annexin V and propidium iodide according to the protocol indicated by the Annexin V-FITC Apoptosis Detection Kit from Calbiochem and analyzed on Accuri C6 flow cytometer and software (BD Bioscience).

Invasion / Migration assays

Cells were grown to confluence on 96-well Essen Bioscience ImageLoke plate previously coated with BD Matrigel. Using an IncuCyte wound maker, scratch wounds were made simultaneously in all culture wells. Cells growing as monolayer were washed with PBS, cells were overlaid with BD Matrigel; subsequently complete medium containing 100 nmol/L of dasatinib or DMSO alone was added. Wound images were automatically acquired and analyzed by integrated metric calculated through confluence algorithm. Migration protocol included same procedure without coating and overlay with BD Matrigel.

Western Blot

After washing in cold PBS, cells were treated with the indicated dose of dasatinib or vehicle (DMSO) and harvested in TNEN (Tris NaCl EDTA NP40) containing 250 mM NaCl, 50 mM Tris-HCl pH 7.5, 5mM EDTA (pH 8.0), 0.1% NP-40, anti-protease (Complete mini, Roche Diagnostics, Meylan, France), anti-phosphastases NaF and $NaVO_4$ at 1/200 (Sigma Aldrich, Saint Quentin Fallavier, France). Lysates were spun in a centrifuge at 14,000 rpm for 5 minutes and the supernatant was collected. Protein extracts were resolved on 4%-15% SDS-PAGE gels and transferred to nitrocellulose membrane (Trans-Blot Turbo system, Bio-Rad), following the manufacturer instructions. Membranes were incubated at 4°C overnight with the following antibodies: p-PDGFRα, PDGFRα, p-Src family kinase, Src, p-MEK, MEK, p-Erk, Erk, p-Smad1/5/8 and actin (Cell Signaling) diluted (1:1000) in 5% bovine serum albumin in 20 mmol/L Tris, pH 7.4, 138 mmol/L NaCl, 0.1% Tween (TBST). Blots were incubated with secondary goat anti-rabbit horseradish peroxidase–conjugated antibodies and enhanced by chemiluminescence reagent. The signals were captured and analyzed using a ChemiDoc™ MP Imaging System (Bio-Rad, Richmont, CA).

Phospho-RTK array

A human phospho-RTK array (R&D Systems, Minneapolis, MN) was used to detect simultaneously the phosphorylation status of RTKs (n=49) in DIPG cells. Membranes were incubated with whole-cell lysates (1 mg) overnight according to the manufacturer's protocol. After washing, the membranes were incubated with a phosphotyrosine antibody conjugated to horseradish peroxidase to allow the detection of captured RTKs that are phosphorylated.

RESULTS

PDGFRα is activated in DIPG tumor samples independently from genomic alterations

PDGFRα expression and phosphorylation status were analyzed for tumors formalin-fixed paraffin-embedded tissues from 13 DIPG patients at diagnosis (Table S1). Most of these samples showed a strong expression of the PDGFRα with associated phosphorylation. Although activation, expression and gene copy number of PDGFRA may be related in some cases (Fig. 1 A, upper-left image), there was no significant correlation because some samples harbored overexpression/phosphorylation without amplification and/or mutation (Fig. 1 A, upper-right image).

***In silico* prediction of sensitivity to dasatinib in DIPG patients**

Using Gene Set Enrichment Analysis (GSEA), the expression profiles of 41 DIPG samples compared to normal brainstem samples were compared with the gene expression signature associated with sensitivity or resistance to dasatinib (17). This signature of sensitivity to dasatinib, determined in breast cancer cell lines and validated in lung cancer cell lines, was significantly enriched in the gene expression profile of DIPG (enrichment score = 0.4995; nominal p= 0.0; FDR q=0.0) (Fig 1 B, upper left panel). Conversely the gene signature related to resistance to dasatinib was significantly downregulated in these samples (enrichment score = -0.32; nominal p= 0.04574; FDR q= 0.0492) (Fig 1 B, upper right panel). Because dasatinib is a broad-spectrum inhibitor, we looked the expression of its target genes (Table S2). We found an enrichment of the gene sets of the major targets (IC_{50} <100 nM) or all known targets of dasatinib (n=64) and also for the Src Pathway described by De Groot (18).

Isolation and establishment of DIPG cell lines

Over a period of 10 months, twelve patients underwent stereotactic biopsies, leading to recovery of 4 to 8 tumor samples in the Neurosurgery Department of Necker-Enfants Malades Hospital in Paris. Only patients at diagnosis without prior radiotherapy or chemotherapy were selected. In most instances, one biopsy was transferred immediately to the laboratory to establish cell cultures, one or two biopsies were used for histological diagnosis and immunohistochemistry and the remaining biopsies were snap-frozen. Dissociation of the tumor infiltrating the surrounding brain tissue did not allow assessing cell viability but we observed the emergence of growing cells systematically. We did not notice any correlation between the period of culture implementation and the delay for appearance of growing cells. All of these cultures were weekly passaged and maintained during thirteen weeks at least.

We performed CGH analysis in 9 DIPG tumors from which the panel of DIPG cultures were established and in these cultures per se at early passage (passage 2-8). While we observed the recurrent gain of chromosome 1q (6/9), no tumor exhibited *PDGFRA* amplification. Broadly, DIPG culture showed a flattening of the copy number profile compared to the primary tumors. However the presence of the H3K27M mutation in 9 of the 12 DIPG cultures demonstrates reasonable similarity of these cell lines with the corresponding primary tumors. Among the 12 cultures, four gave rise to cell lines that could be passaged without undergoing senescence. Interestingly, NEM157 and NEM168 have disruptive TP53 mutations. Clinical data and biological characteristics relating to these four DIPG cell lines are summarized in Table 1. Both PDGFR alpha and Src were expressed and activated at different level depending on the DIPG cell line (Fig. 4A). GSEA further demonstrated an enrichment of dasatinib sensitivity signature (enrichment score = 0; nominal p=0.0; FDR q=0.0, Fig. S1).

Dasatinib inhibits cell growth at submicromolar concentration

IC_{50} were calculated after treatment in complete medium for 72 hours. MTS assay which measures cell viability was simultaneously performed at this end-point and we observed a good correlation of both methods (Fig. S2). All of the DIPG cells lines tested showed clear sensitivity to dasatinib, with lower IC_{50} value than the well-described dasatinib sensitive

adult glioma cell line T98G and paediatric supratentorial glioma cell line SF188. Representative data of the ranking of sensitivity are shown in Fig. 2B.

Effect of dasatinib on cell death

Cytotoxicity assay showed massive cytotoxicity in NEM168 treated cells whereas its effect was less pronounced in the other DIPG cell lines (data not shown).

We next assessed whether dasatinib induced apoptosis. DIPG and T98G cell lines were treated with 50 or 100 nM dasatinib in complete medium for 72 hours. Cells were stained with both Annexin V-FITC and propidium iodide and analyzed by flow cytometry. Induction of apoptosis was calculated as fold change of Annexin V positive cells compared to the control (Fig. 2D). We observed a significant induction of apoptosis in NEM168 and as expected in the well-described sensitive T98G cell line. By contrast, no apoptosis was found in the other DIPG lines

Dasatinib decreases migration and invasion of DIPG cells

Relative Wound Density (RWD) was calculated after 12 hours to study migration and invasion regardless of proliferation by relying on the measurement of the spatial cell density in the wound area relative to spatial cell density outside of the wound area at every time point with self-normalization by the initial wound density. Results are shown in Fig. 3A. All untreated cell lines migrated and invaded in this assay with similar rate with complete wound closure in 24 to 36 hours. Cell migration and invasion were significantly inhibited by dasatinib at 12h.

Effects of dasatinib treatment on targets and downstream signaling

In response to dasatinib treatment for 1 hour in 4 DIPG cell lines, PDGFRα and Src activities were significantly downregulated for all DIPG cell lines as shown on Western blot analyses (Fig. 4B). We found a significant inhibition of AKT (50-60% reduction) in NEM157, NEM163 and NEM168 but this effect was lower in NEM165 (20% reduction). However, dasatinib induced partial inhibition of MEK/ERK pathway (10-30% reduction).

ACVR1 is a known secondary target of dasatinib and recently unveiled as being mutated in DIPG (12). ACVR1 is responsible of the activation of the bone morphogenic protein (BMP)-dependent transforming growth factor (TGF)-β pathway by increased phosphorylation of

Smad1/5/8. In our cell lines, ACVR1 was not mutated but overexpressed compared to normal brainstem (Log2 ratios between 2.14 and 2.71). We showed here a significant inhibition of phospho-Smad1/5/8 could be obtained at high doses of dasatinib (1 and 10 μM) (Fig.4C).

Multiple receptor tyrosine kinases are concomitantly activated in DIPG cell lines

To define other coactivated RTK in these DIPG cell lines, we used an antibody array that allows simultaneous assessment of phosphorylation status of 49 RTKs (Fig.4D). Profiling of the phosphorylation status of 49 RTKs showed prominent coactivation of multiple phosphorylated RTKs, including targets of dasatinib: PDGFRα/β (4/4) and Ephrin receptors (EphA2, EphB2 and EphB3) (4/4), as well as other RTKs that could potentially be responsible of escape mechanisms. The other recurrent coactivated RTKs not targeted by dasatinib were: EGFR (4/4), MET(4/4), Insulin Receptor(4/4), and AXL(4/4), IGF1R(3/4) RYK(3/4), ALK(2/4) and FGFR(1/4). These results indicate that various RTKs are activated in the DIPG cell lines and contribute to maintain the activation of several downstream signaling pathways. This suggests that targeting multiple tyrosine kinases might be effective in DIPG cells.

Anti-proliferative of dasatinib is synergized by cabozantinib *in vitro*

MET amplification or mutation was been found in 5-10% of DIPG primary tumors and this genomic aberration is frequently found concomitantly with the PDGFRA amplification (4,9) (Taylor Nat Genet in press). Transcriptomic data exhibited an overexpression of HGF and MET compared with brain stem reference in the 41 DIPGs (see Suppl_Fig5A) and also in these four DIPG cell lines, suggesting autocrine activation of the MET pathway as also suggested by the phospho-RTK array (Fig. 4D).

According to these genomic data, the MET phosphorylation and evidence that HGF contributes to resistance to RTK inhibitors (19), we analyzed the MET pathway as a therapeutic target alone, or in combination with dasatinib. Treatment of the cells with the MET inhibitor cabozantinib as a single agent did not show strong effects, with IC_{50} values higher than micromolar concentration (data not shown).

We then tested the combination of both dasatinib and cabozantinib to assess synergy on cell growth *in vitro*. At IC_{50} of dasatinib and submicromolar dose of cabozantinib (0.75μM)

the combination showed synergistic effect on the cell proliferation of 3 of the 4 DIPG cell lines including NEM157 (CI=0.53), NEM163 (CI=0.28) and NEM165 (CI=0.45) while it was additive for NEM168 (CI=0.81) (Fig. 5A).

Dasatinib combined with cabozantinib inhibits cell invasion

Given the importance of MET pathway in the invasive phenotype of glioma cells (20,21), we studied the effect of cabozantinib on invasion assay. We chose the least dasatinib sensitive cell line NEM 157, which is also the most invasive cell line. We found an anti-invasive effect of cabozantinib alone at submicromolar concentration (Fig.5B). Combination of both targeted inhibitors showed enhanced activity compared to each agent alone and abrogated invasion (Fig. 5B,C and suppl. Movie1).

DISCUSSION

We have shown by PLA that DIPG samples exhibit frequent PDGFRA activation irrespective of its genomic status. These observations are consistent with the PDGFRA signature found in DIPG without PDGFRA amplification. We have previously shown that the gene expression signature associated with PDGRA amplification is observed in a large subset of DIPG with worse survival including tumors without PDGFRA amplification (9). Accordingly, the broad activation of PDGFRA in DIPG would expand the usefulness to target this receptor in patients. Dasatinib appeared to be the most suitable inhibitor since it has a better activity *in vitro* than imatinib, which by the way had only limited activity in DIPG patients (22,23). Elsewhere, gene expression profiling performed in 41 DIPG samples could predict dasatinib sensitivity (Fig. 1B) and this signature was also expressed in these DIPG cell lines (see Suppl_Fig1). Dasatinib showed *in vitro* efficacy on this unique DIPG cell panel with anti-proliferative effect for all, anti-invasive for most of the cells and cytotoxic effect for some. The doses tested here were achievable clinically given the Cmax reached in serum and measured in cerebrospinal fluid (24) but higher doses may prove to be useful when delivered directly to the tumor by alternative drug delivery strategies such as convection enhanced delivery (CED), co-administration of an inhibitor of P-gp (25) or nanoformulations for increased delivery in the brain (26). Dasatinib has been tested in

patients together with vandetanib in a recently published phase I trial for DIPG (24); the maximal tolerated dose of dasatinib in combination with vandetanib could not be escalated to the levels achievable when given in monotherapy but the authors concluded that dasatinib was an interesting agent to develop further which is now supported with our preclinical data.

Given that DIPG show activation of multiple RTKs, inhibiting concomitantly these other pathway by using other small inhibitor molecule is worth to be investigated. Moreover, multiple co-amplification may be a relatively common phenomenon in high-grade glioma (27) and in this respect, DIPG tumors show simultaneous amplification of *PDGFRA* and *MET* (4,9)

Our interest then focused on MET pathway, which we think is a relevant target in DIPG due to its activation in our cell lines shown by RTK arrays and by western blot and due to its known role in the invasive phenotype in glioma (20). We explored here the effect of cabozantinib, which is a tyrosine kinase inhibitor of MET, RET and VEGFR2. Navis *et al*. have showed its anti-tumoral activity in an invasive glioma model, where the phenotype was driven by MET (28). Clinical activity of this compound has been reported in phase II trial for recurrent glioblastoma (29). Among the DIPG cell lines of the present study, none exhibited either a mutation or an amplification of *MET*. However, we observed synergistic anti-proliferative effect for 3 of the four and additive activity for the fourth. The benefit of MET inhibition was particularly strong in DIPG cell lines less sensitive to dasatinib.

These results should be reproduced *in vivo* when orthotopic models become available Engineered mouse PDGF-induced model is available (30) to date but do not recapitulate the patient tumors especially with respect to multi-RTK activation and therefore will not be the most relevant model to test combinations. Xenograft models that mimic more closely DIPG are still needed.

The synergy of dasatinib and cabozantinib suggests combination trials in patients. This has been attempted with dasatinib and vandetanib, which is EGFR and VEGFR inhibitor (24). An important future task will be to define markers to identify the patients most suitable for combination treatment or dasatinib single treatment. The fact that aberrant PDGFRα pathway is not necessarily linked to amplification and/or mutation raises the question of the best test method to detect the involvement of this receptor in DIPG. Proximity ligation assay might be the suitable solution to explore this pathway activation.

However, it should also be considered that part of the efficacy may come through the inhibition of other targets such as the non-receptor membrane-associated Src tyrosine kinase (31–33) or ACVR1 that can be activated in these tumors as shown here. ACVR1 is responsible of the activation of the bone morphogenic protein (BMP)-dependent transforming growth factor (TGF)-β pathway by increased phosphorylation of Smad1/5/8. We show here that we obtain.

In summary, these results demonstrate synergistic anti-proliferative and anti-invasive effects of dasatinib with an MET inhibitor in DIPG cell line models in vitro, which warrant further translational efforts.

Acknowledgments:

The authors would like to thank the sponsors of the study: the associations "L'Etoile de Martin" and "Le Défi de Fortunée" and the Foundation TIGRE.

The authors thank to Tumor Bank of Necker Hospital

Grant Support: Etoile de Martin (NT), Foundation TIGRE (JG and GC) and Le Défi de Fortunée (JG).

REFERENCES

1. Hargrave D, Bartels U, Bouffet E. Diffuse brainstem glioma in children: critical review of clinical trials. Lancet Oncol. 2006;7:241–8.
2. Warren KE. Diffuse intrinsic pontine glioma: poised for progress. Front Oncol [Internet]. 2012 [cited 2013 Mar 10];2. Available from: http://www.ncbi.nlm.nih.gov/pmc/articles/PMC3531714/
3. Sturm D, Bender S, Jones DTW, Lichter P, Grill J, Becher O, et al. Paediatric and adult glioblastoma: multiform (epi)genomic culprits emerge. Nat Rev Cancer. 2014;14:92–107.
4. Paugh BS, Broniscer A, Qu C, Miller CP, Zhang J, Tatevossian RG, et al. Genome-Wide Analyses Identify Recurrent Amplifications of Receptor Tyrosine Kinases and Cell-Cycle Regulatory Genes in Diffuse Intrinsic Pontine Glioma. J Clin Oncol. 2011;29:3999–4006.
5. MacDonald TJ. Pediatric Glioma: Role of Platelet Derived Growth Factor Receptor. Pediatr Cancer. 2012;2: Teratoid/Rhabdoid, Brain Tumors, and Glioma:259–67.
6. Barrow J, Adamowicz-Brice M, Cartmill M, MacArthur D, Lowe J, Robson K, et al. Homozygous loss of ADAM3A revealed by genome-wide analysis of pediatric high-grade glioma and diffuse intrinsic pontine gliomas. Neuro-Oncol. 2011;13:212–22.
7. Zarghooni M, Bartels U, Lee E, Buczkowicz P, Morrison A, Huang A, et al. Whole-genome profiling of pediatric diffuse intrinsic pontine gliomas highlights platelet-derived growth factor receptor alpha and poly (ADP-ribose) polymerase as potential therapeutic targets. J Clin Oncol Off J Am Soc Clin Oncol. 2010;28:1337–44.
8. Paugh BS, Qu C, Jones C, Liu Z, Adamowicz-Brice M, Zhang J, et al. Integrated molecular genetic profiling of pediatric high-grade gliomas reveals key differences with the adult disease. J Clin Oncol Off J Am Soc Clin Oncol. 2010;28:3061–8.
9. Puget S, Philippe C, Bax DA, Job B, Varlet P, Junier M-P, et al. Mesenchymal Transition and PDGFRA Amplification/Mutation Are Key Distinct Oncogenic Events in Pediatric Diffuse Intrinsic Pontine Gliomas. PLoS ONE [Internet]. 2012 [cited 2013 Feb 20];7. Available from: http://www.ncbi.nlm.nih.gov/pmc/articles/PMC3289615/
10. Paugh BS, Zhu X, Qu C, Endersby R, Diaz AK, Zhang J, et al. Novel Oncogenic PDGFRA Mutations in Pediatric High-Grade Gliomas. Cancer Res. 2013;canres.1491.2013.
11. Schwartzentruber J, Korshunov A, Liu X-Y, Jones DTW, Pfaff E, Jacob K, et al. Driver mutations in histone H3.3 and chromatin remodelling genes in paediatric glioblastoma. Nature. 2012;482:226–31.

12. Taylor KR, Mackay A, Truffaux N, Butterfield YS, Morozova O, Philippe C, et al. Recurrent activating ACVR1 mutations in diffuse intrinsic pontine glioma. Nat Genet. 2014;
13. Karaman MW, Herrgard S, Treiber DK, Gallant P, Atteridge CE, Campbell BT, et al. A quantitative analysis of kinase inhibitor selectivity. Nat Biotechnol. 2008;26:127–32.
14. Yakes FM, Chen J, Tan J, Yamaguchi K, Shi Y, Yu P, et al. Cabozantinib (XL184), a Novel MET and VEGFR2 Inhibitor, Simultaneously Suppresses Metastasis, Angiogenesis, and Tumor Growth. Mol Cancer Ther. 2011;10:2298–308.
15. Subramanian A, Tamayo P, Mootha VK, Mukherjee S, Ebert BL, Gillette MA, et al. Gene set enrichment analysis: A knowledge-based approach for interpreting genome-wide expression profiles. Proc Natl Acad Sci U S A. 2005;102:15545–50.
16. Chou TC, Talaly P. A simple generalized equation for the analysis of multiple inhibitions of Michaelis-Menten kinetic systems. J Biol Chem. 1977;252:6438–42.
17. Huang F, Reeves K, Han X, Fairchild C, Platero S, Wong TW, et al. Identification of candidate molecular markers predicting sensitivity in solid tumors to dasatinib: rationale for patient selection. Cancer Res. 2007;67:2226–38.
18. Ahluwalia MS, Groot J de, Liu W (Michael), Gladson CL. Targeting SRC in glioblastoma tumors and brain metastases: Rationale and preclinical studies. Cancer Lett. 2010;298:139–49.
19. Wilson TR, Fridlyand J, Yan Y, Penuel E, Burton L, Chan E, et al. Widespread potential for growth-factor-driven resistance to anticancer kinase inhibitors. Nature. 2012;487:505–9.
20. Kong D-S, Song S-Y, Kim D-H, Joo KM, Yoo J-S, Koh JS, et al. Prognostic significance of c-Met expression in glioblastomas. Cancer. 2009;115:140–8.
21. Abounader R, Laterra J. Scatter factor/hepatocyte growth factor in brain tumor growth and angiogenesis. Neuro-Oncol. 2005;7:436–51.
22. Pollack IF, Jakacki RI, Blaney SM, Hancock ML, Kieran MW, Phillips P, et al. Phase I trial of imatinib in children with newly diagnosed brainstem and recurrent malignant gliomas: A Pediatric Brain Tumor Consortium report. Neuro-Oncol. 2007;9:145–60.
23. Geoerger B, Morland B, Ndiaye A, Doz F, Kalifa G, Geoffray A, et al. Target-driven exploratory study of imatinib mesylate in children with solid malignancies by the Innovative Therapies for Children with Cancer (ITCC) European Consortium. Eur J Cancer Oxf Engl 1990. 2009;45:2342–51.
24. Broniscer A, Baker SD, Wetmore C, Panandiker ASP, Huang J, Davidoff AM, et al. Phase I Trial, Pharmacokinetics, and Pharmacodynamics of Vandetanib and Dasatinib in Children with Newly Diagnosed Diffuse Intrinsic Pontine Glioma. Clin Cancer Res. 2013;19:3050–8.
25. Lagas JS, van Waterschoot RAB, van Tilburg VACJ, Hillebrand MJ, Lankheet N, Rosing H, et al. Brain accumulation of dasatinib is restricted by P-glycoprotein (ABCB1) and breast cancer resistance protein (ABCG2) and can be enhanced by elacridar treatment. Clin Cancer Res Off J Am Assoc Cancer Res. 2009;15:2344–51.
26. Benezra M, Hambardzumyan D, Penate-Medina O, Veach DR, Pillarsetty N, Smith-Jones P, et al. Fluorine-labeled Dasatinib Nanoformulations as Targeted Molecular Imaging Probes in a PDGFB-driven Murine Glioblastoma Model. Neoplasia N Y N. 2012;14:1132.
27. Little SE, Popov S, Jury A, Bax DA, Doey L, Al-Sarraj S, et al. Receptor tyrosine kinase genes amplified in glioblastoma exhibit a mutual exclusivity in variable proportions reflective of individual tumor heterogeneity. Cancer Res. 2012;72:1614–20.
28. Navis AC, Bourgonje A, Wesseling P, Wright A, Hendriks W, Verrijp K, et al. Effects of Dual Targeting of Tumor Cells and Stroma in Human Glioblastoma Xenografts with a Tyrosine Kinase Inhibitor against c-MET and VEGFR2. PLoS ONE [Internet]. 2013 [cited 2013

Mar 19];8. Available from: http://www.ncbi.nlm.nih.gov/pmc/articles/PMC3587584/
29. Wen PY, Macdonald DR, Reardon DA, Cloughesy TF, Sorensen AG, Galanis E, et al. Updated response assessment criteria for high-grade gliomas: response assessment in neuro-oncology working group. J Clin Oncol Off J Am Soc Clin Oncol. 2010;28:1963–72.
30. Becher OJ, Hambardzumyan D, Walker TR, Helmy K, Nazarian J, Albrecht S, et al. Preclinical Evaluation of Radiation and Perifosine in a Genetically and Histologically Accurate Model of Brainstem Glioma. Cancer Res. 2010;70:2548–57.
31. Groot J, Milano V. Improving the prognosis for patients with glioblastoma: the rationale for targeting Src. J Neurooncol. 2009;95:151–63.
32. Du J, Bernasconi P, Clauser KR, Mani DR, Finn SP, Beroukhim R, et al. Bead-based profiling of tyrosine kinase phosphorylation identifies SRC as a potential target for glioblastoma therapy. Nat Biotechnol. 2009;27:77–83.
33. Sikkema AH, Diks SH, Dunnen WFA den, Elst A ter, Scherpen FJG, Hoving EW, et al. Kinome Profiling in Pediatric Brain Tumors as a New Approach for Target Discovery. Cancer Res. 2009;69:5987–95.
34. Davis MI, Hunt JP, Herrgard S, Ciceri P, Wodicka LM, Pallares G, et al. Comprehensive analysis of kinase inhibitor selectivity. Nat Biotechnol. 2011;29:1046–51.

Figures:

A

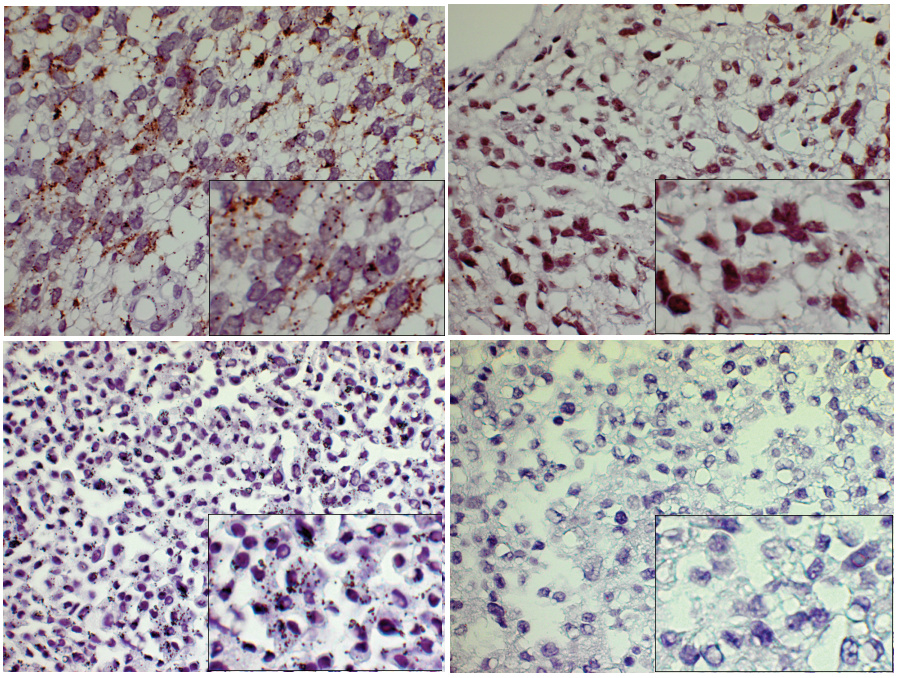

B

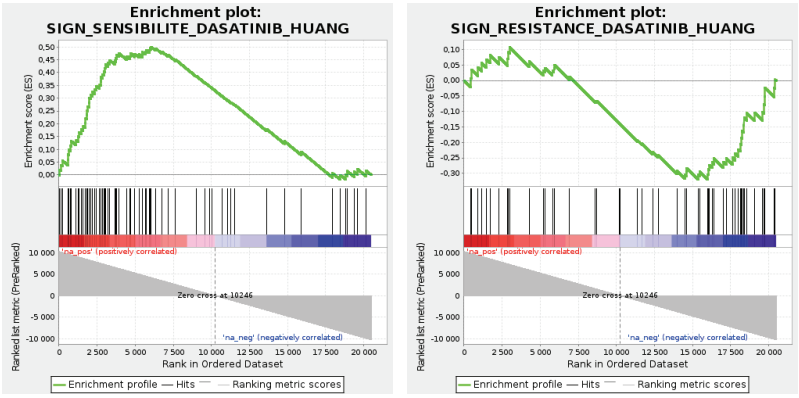

Gene Set	Size	Enrichment Score	p-value	FDR
Signature of sensitivity to dasatinib (Huang 2007)	71	0.4995	0.0	0.0
Major Targets of dasatinib	39	0.4815	0.0021	0.0006
PDGF pathway BIOCARTA	12	0.5346	0.0402	0.0227
Src pathway De Groot	7	0.6726	0.0262	0.0294
Signature of resistance to dasatinib (Huang 2007)	54	-0.3205	0.0457	0.0492
All dasatinib targets	19	0.3327	0.2353	0.2389

Fig. 1. Frequent activation of PDGFRα and *in silico* prediction of sensitivity to dasatinib in DIPG patients. A, Phospho-PDGFRα proximity ligation assay. Upper panels represent tumors from DIPG patients (n°4 and n°11, described in the supplemental Table 1). Lower panels represent positive and negative controls. Positive immunochemical staining appears as cytoplasmic brown dots. **B,** Gene set enrichment analysis (GSEA) plot comparing DIPG GE profile to the signature described for sensitivity and resistance to dasatinib (upper panels) and summary of other significant gene sets (FDR ≤ 0.25) related to dasatinib targets (lower panel).

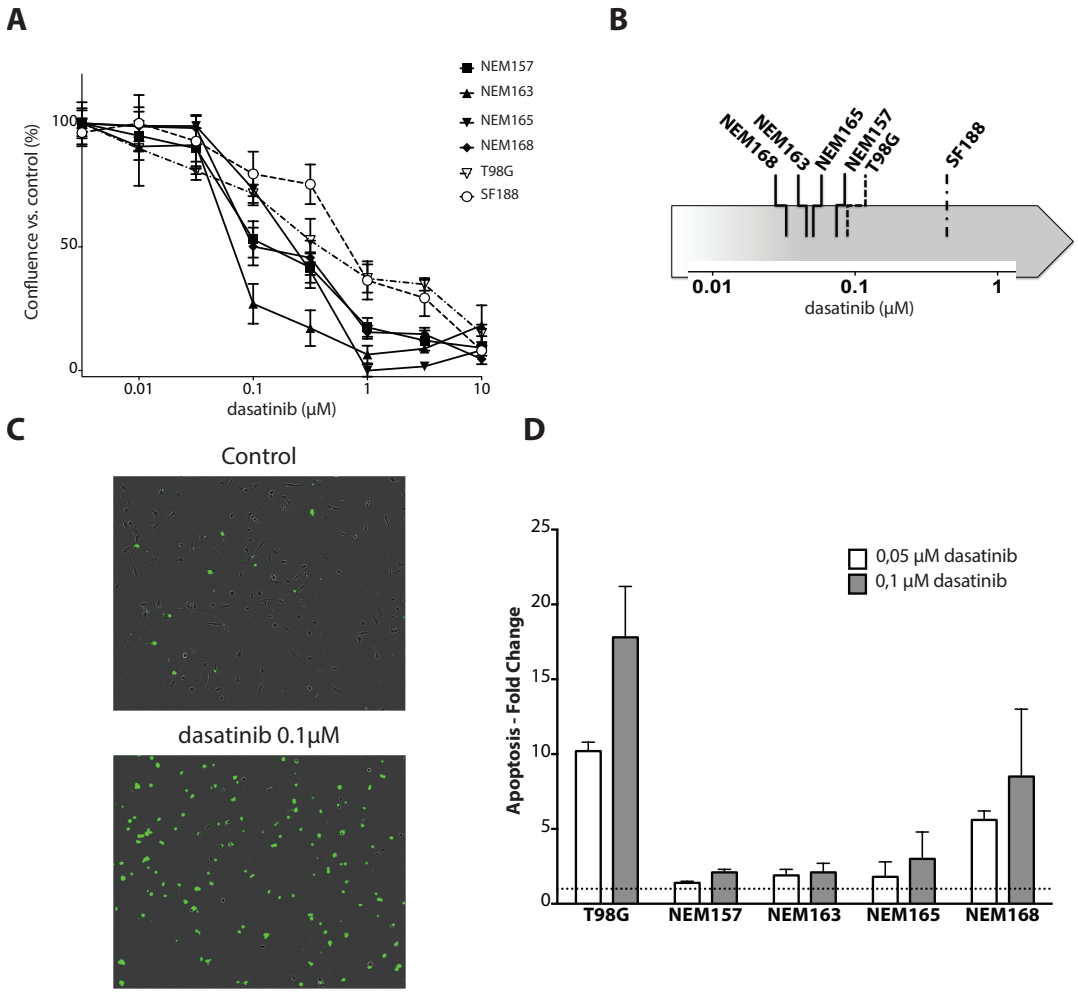

Fig. 2. Effect of dasatinib on DIPG cell line *in vitro*. A, DIPG cell lines (NEM), T98G and SF188 were treated with the indicated doses of dasatinib or vehicle for 3 days and growth was measured using the confluence algorithm. Results are the mean percent inhibition compared with control cells ± SEM of 3 experiments carried out in triplicate. **B,** Representative classification of dasatinib sensitivity by IC50 determination for each cell line. **C,** Contrast phase fluorescent images of NEM168 12 hours post-treatment. Nuclear staining indicates loss of membrane integrity. **D,** cells were plated in complete medium with or without the indicated dose of dasatinib or vehicle for 72 hours, stained with Annexin V and propidium iodide, and analyzed by flow cytometer, as described in Materials and Methods. Apoptosis detected in the control cells was set to 1 and is represented by the dashed line. Results are the mean ± SD of duplicate representative of 3 experiments carried out.

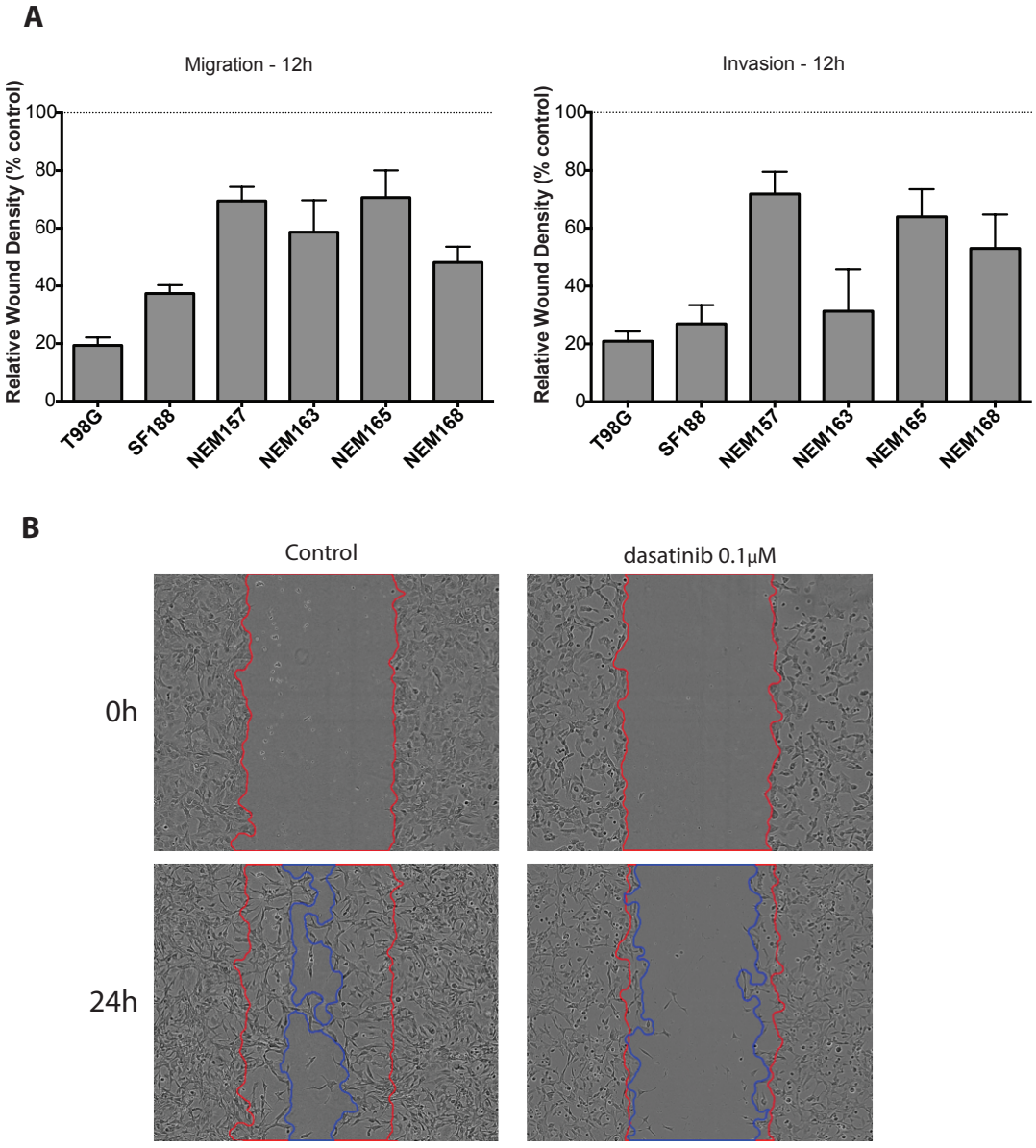

Fig. 3. Effect of dasatinib on cell migration and cell invasion. Cells were seeded in 96 well plated and incubated until subconfluent. A wound was scratched across each well (Wound Maker, Essen BioScience) and BD Matrigel™ is then added (or not for migration assay) and treatment. Wound closure was automatically imaged each 6 hours and calculated as a percentage of wound confluence that the cell gained. **A,** Quantitative wound-repair analysis at 12 hours after dasatinib treatment (0,1µM) for migration and invasion assay respectively. **B,** Contrast-phase images of NEM168 invasion at 24h. Red and blue lines correspond to the frontline of the scratch wound at 0h and 24h respectively.

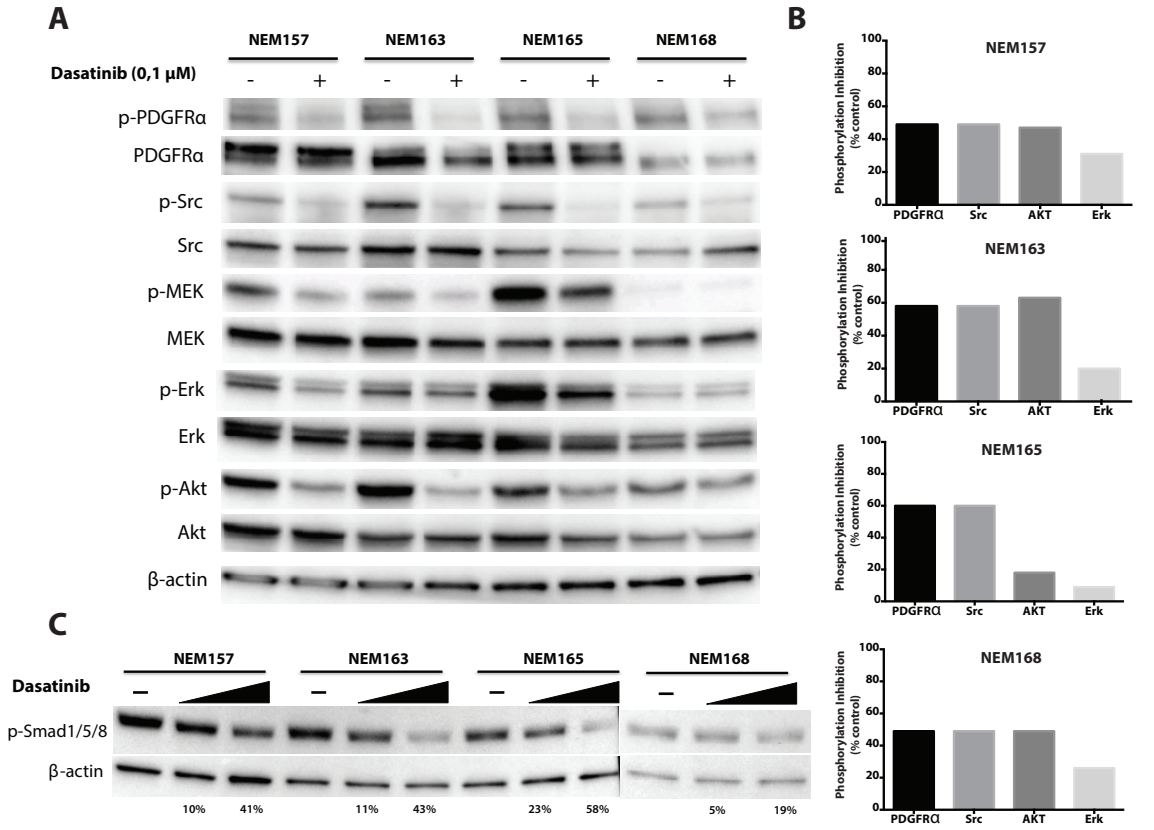

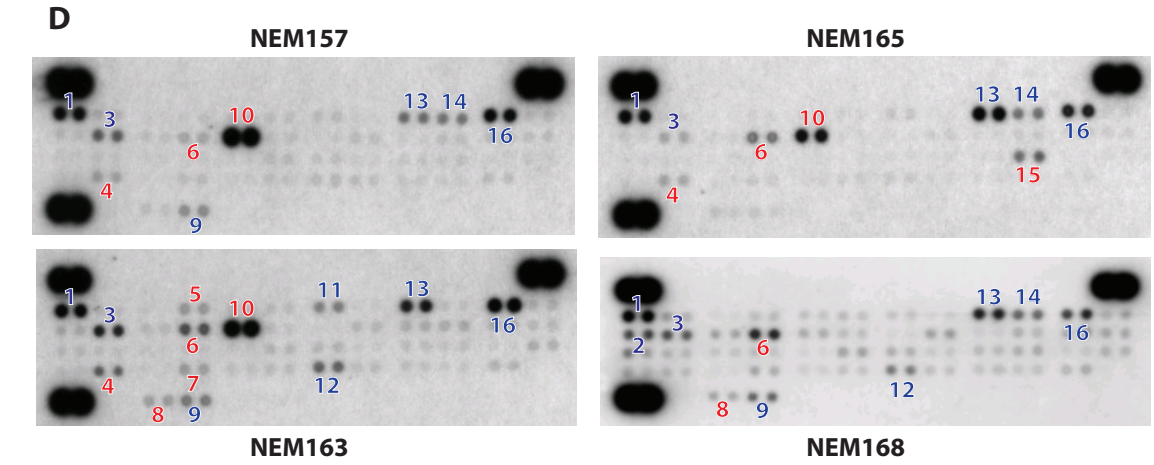

1.P-EGFR 2.P-Mer 3.P-MET 4.P-EphA7 5.P-ErbB4
6.P-PDGFRα 7.P- EphB2 8.P- EphB3 9.P-RYK
10.P-PDGFRβ 11.P-FGFR3 12.P-ALK 13.P-InsulinR
14.P-IGF1R 15.P-EphA2 16.P-Axl

Fig. 4. Targets, downstream of dasatinib and potential escape mechanisms. A, Effect of dasatinib on target activation and downstream signaling was assessed by Western Blot. Cells were treated with the indicated doses of dasatinib or vehicle for 1 hour, in complete medium. Cells were lysed in TNEN buffer and equal protein (30 µg) was analyzed by Western blotting on 4%-15% SDS-PAGE gels with the indicated antibodies. **B,** Inhibition phosphorylation induced by dasatinib was calculated by densitometric analysis for each DIPG cell line. **C,** Effect of dasatinib (1 and 10 µM) on Smad1/5/8 signaling. **D,** Multiple RTKs were activated simultaneously in glioma cell lines. Whole-cell extracts (WCEs) from the DIPG cell lines were incubated on RTK antibody arrays, and phosphorylation status was determined by subsequent incubation with anti-phosphotyrosine horse-radish peroxidase. Each RTK is spotted in duplicate: The pairs of dots in each corner are positive controls. Each pair of positive RTK dots is denoted by a numeral, with the identity of the corresponding RTKs listed below the arrays. In red and blue for dasatinib target or not respectively.

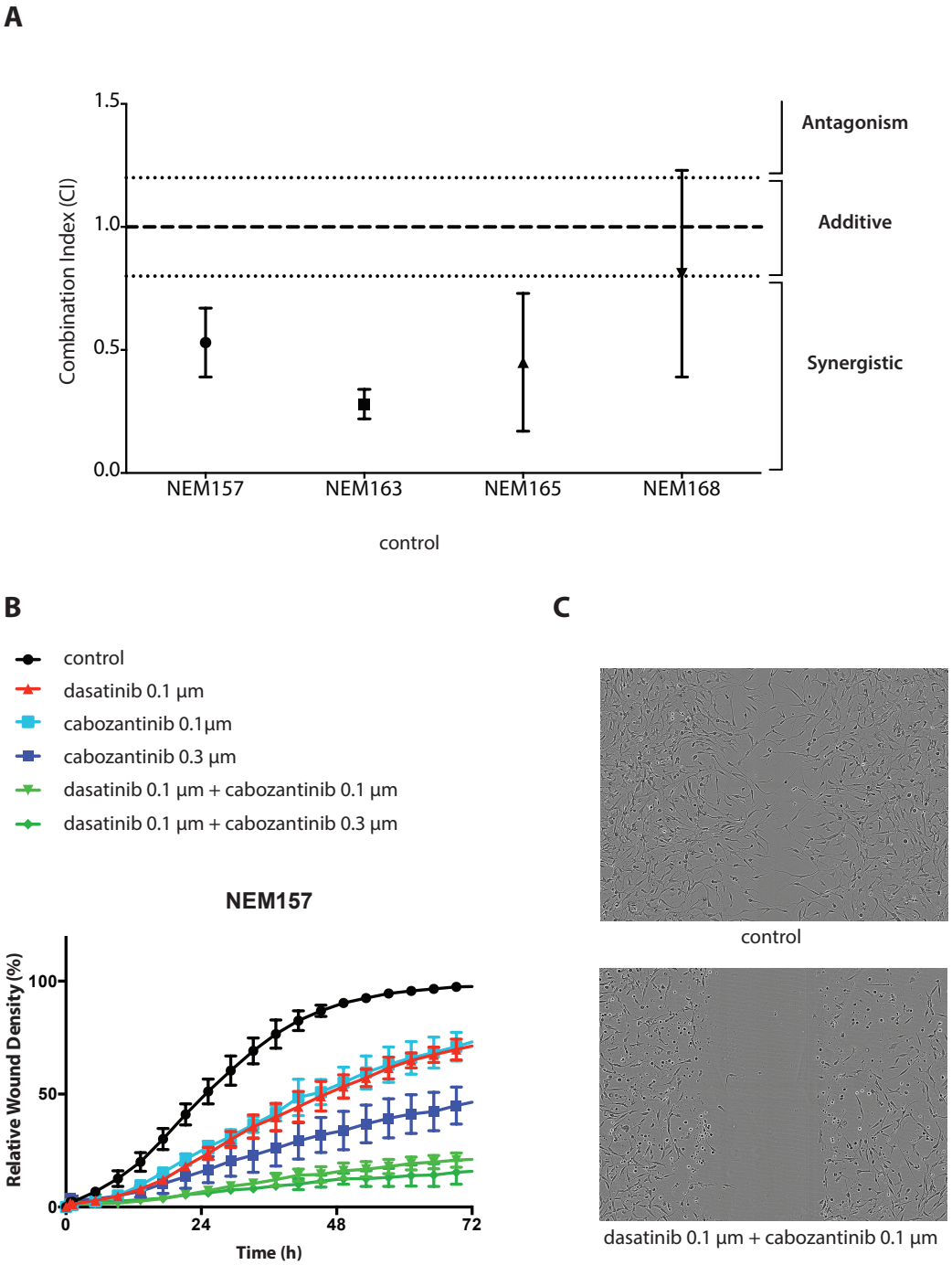

Fig. 5. Synergistic effect of dasatinib and cabozantinib combination *in vitro*.
A, Synergistic effect of dasatinib and MET inhibitor (cabozantinib) on cell growth *in* vitro at median effect of dasatinib. Cells were treated with increasing concentrations of drugs either alone or concurrently at their equipotent molar ratio and combination indices (CI) calculated by the method of Chou&Talalay (CI calculates synergism <0.8; additivity between >0.8 and <1.2; antagonism >1.2. All values are given as mean± standard deviation of at least three independent experiments. **B,** Time-course of relative wound density of the high invasive NEM157 cell line. **C,** Contrast-phase images of NEM157 invasion at 24h in control and combined condition (upper and lower panel respectively).

Table 1: Clinical and experimental characteristics of DIPG cell lines.

		NEM157	NEM163	NEM165	NEM168
Clinical characterics	**Age at Diagnosis (years)**	5,7	5,7	3,3	10,6
	Sex	F	M	M	F
	Histological diagnosis	Oligoastrocytoma	Oligoastrocytoma	Oligoastrocytoma	Astrocytoma
	Grade	II	II	III	III
	Time to progression (months)	10,3	8,5	16,9	7,0
	Survival (months)	12,9	10,6	23,9	8,4
***In vitro* characteristics**	**Doubling time**	30 hrs	36 hrs	32 hrs	34 hrs
	PDGFR alpha activation	+	++	++	+++
	Src activation	+	++	++	+
	Histone Mutation	K27M H3F3A	K27M H3F3A	K27M H3F3A	K27M H3F3A
	P53 status	Δ337-340 R273C	WT	WT	Δ156

Supplementary materials:

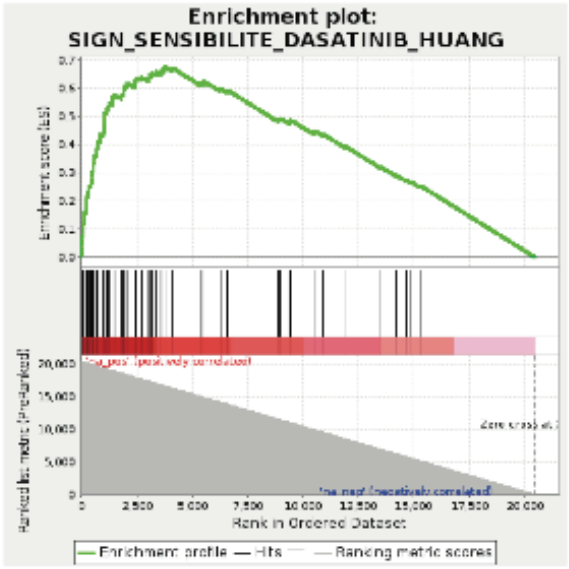

Figure S1: Gene expression of DIPG cell panel predicts dasatinib sensitivity. GSEA plot comparing GE profile of the four DIPG cell lines to the signature described for sensitivity to dasatinib (16).

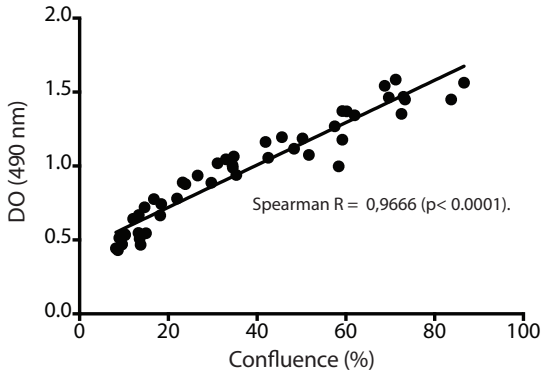

Figure S2: Correlation between cell confluence measured by IncuCyte and MTS assay. The individual images are processed by an imbedded contrast-based confluence algorithm which computes monolayer confluence for each image at 72 hours. Concomitantly metabolic activity is assessed by MTS assay which is an other method to evaluate cell proliferation. Spearman correlation test confirms the good relationship between these two parameters.

Table S1: PDGFRA characterization of 13 DIPG patients: genomic status, expression and activation. PDGFRA staining was evaluated by scoring the percentage of stained cells [0 (absent), 1 (<10%), 2 (10–50%) and 3 (51–100%)] and staining intensity [0 (absent), 1 (weak), 2 (distinct) and 3 (strong)].

DIPG Patient No	Sex	Age (years)	Histology (Grade)	PDGFRA Genomic Status	PDGFRα (IHC)	pPDGFRα (PLA)
1	M	7,4	Astrocytoma (IV)	no	0	0
2	M	5,7	Astrocytoma (III)	no	2+	1+
3	M	5,9	Astrocytoma (II)	no	2+	0 or 1+
4	F	7,6	Astrocytoma (IV)	Amplified Mutated	3+	3+
5	F	7,1	Astrocytoma (IV)	Gained	3+	2 or 3+
6	M	6,6	Astrocytoma (IV)	Gained	3+	1+
7	M	9,5	Oligo-astrocytoma (III)	Gained	part 2+ most -	0 or 1+
8	F	3,9	Astrocytoma (IV)	no	3+	2+
9	M	7,5	Astrocytoma (III)	Gained	1-2+	1+
10	F	4,9	Astrocytoma (IV)	Amplified	1-2+ v+	few 1+
11	F	5,1	Astrocytoma (IV)	no	3+	1 or 2+
12	F	11,7	Oligo-astrocytoma (III)	Gained	3+	1+
13	M	14,4	Astrocytoma (II)	Amplified Mutated	0	1+

Table S2: Gene set list for GSEA.

SRC_PATHWAY_deGROOT	SIGN_RESISTANCE_DASATINIB_HUANG	SIGN_SENSIBILITE_DASATINIB_HUANG	ALL_DASATINIB_TARGETS_TRUFFAUX	MAJOR_DASATINIB_TARGETS_TRUFFAUX
SRC	CDC42SE1	ANTXR2	ABL1	ABL1
YES1	TRPS1	TFPI	ABL2	ABL2
BLK	ISOC1	RAI14	ACVR1	EPHA3
FYN	CLN3	SAMD9L	ACVR2A	LCK
LYN	ASCL2	EXT1	ACVR2B	BLK
LCK	IRX5	MAML2	ARG1	EPHA5
HCK	CREB3L4	GNG12	ARG2	EPHA8
FGR	CBX5	MSN	BLK	YES1
	EMP2	CDC42EP3	BMX	EPHB4
	SCARB1	IFI16	BRAF	EPHB2
	PDCD4	MYO10	CSK	EPHB1
	CA12	AGPS	DDR1	PDGFRA
	IGFBP2	ELK3	DDR2	FGR
	YME1L1	TGFBR2	EGFR	LYN
	UBL3	EGFR	EPHA3	CSF1R
	CRNKL1	FSTL1	EPHA4	KIT
	SLC25A15	PSMB8	EPHA5	PDGFRB
	TOB1	EPHB2	EPHA8	DDR1
	VPS37C	F2RL1	EPHB1	FYN
	ABHD11	PDGFC	EPHB2	EPHA2
	ABCG1	LEPREL1	EPHB6	CSK
	RHOB	ZNF559	ERBB2	EPHA4
	KIAA1324	TNFRSF21	ERBB4	BMX
	MYEF2	CAV2	PTK2	BTK
	SLC35A1	ST5	FGR	TXK
	PREX1	LYN	FRK	GAK
	CYB561	BTN3A2	FYN	DDR2
	ABCA3	FXYD5	GAK	EPHA1
	EPB41L5	IFIT3	GCK	TNK2
	SBK1	UBE2E3	ILK	SRC
	GREB1	COTL1	KIT	EPHB3
	CHPT1	JAG1	LCK	PTK6
	SPIN1	PLAU	LIMK1	TNNI3K
	STARD10	PSMB9	LIMK2	TEC
	TFF1	NNMT	LYN	MAPK14
	SLC16A6	TGFBI	MAP3K1	RIPK2
	PRLR	AKR1C3	MAP3K2	TESK1
	ICA1	RIPK4	MAP3K3	MAP4K5
	PLEKHH1	PCDH7	MAP3K4	ERBB4
	MAPT	ANXA1	MAP4K1	LIMK2
	EPS15L1	PGM1	MAP4K5	
	EIF4E3	CAV1	MAPK11	

	SLC38A1	SNAI2	MYT1	
	GPD1L	OSMR	NLK	
	ACSL3	RAC2	PDGFRA	
	SLC1A2	KCTD12	PDGFRB	
	DEGS2	DPYD	PTK6	
	PLCB4	ITGA5	SIK3	
	CALM1	GBP3	RAF1	
	CLDN3	ZYX	RET	
	CHRM1	SH3KBP1	RIPK1	
	TPD52	DCBLD2	RIPK2	
	JPH1	COL5A1	RIPK3	
	ARX	CALD1	RIPK4	
	TBC1D30	EPHA2	SLK	
	METTL9	PARVA	SRC	
	TRIM13	CAST	STK36	
	DMC1	INPP1	SYK	
	LUC7L3	F3	TAOK3	
	PLCH1	PTRF	TEC	
	SORBS2	UPP1	TESK2	
	C6orf108	DUSP10	TNNI3K	
	C14orf93	IL15RA	TXK	
	MEGF9	MET	TYK2	
	LASS6	POPDC3	YES1	
	CCDC58	ELL2		
	WBSCR20B	LAMB3		
	BBIP1	PRNP		
		LARP6		
		SOCS5		
		ARHGAP29		
		MAP7D1		
		LAYN		
		LIMA1		
		NDC80		
		REXO2		
		CCDC50		
		AKAP2		
		PPP1R18		
		BTN3A3		
		BTN3A2		

Table S3: Determination of combination index at equipotent molar ratio for dosing rang of dasatinib of 0.25-4IC$_{50}$. CI calculates synergism <0.8; additivity between >0.8 and <1.2; antagonism >1.2. All values are given as mean± standard deviation of at least three independent experiments.

Cell line	0.25*IC50 + 0.188µM	0.5*IC50 + 0.375 µM	IC50 + 0.75 µM	2*IC50 + 1.5 µM	4*IC50 + 3 µM
NEM-157	0,55±0,55	0,45±0,05	0,53±0,14	0,65±0,37	1,06±0,64
NEM-163	0,47±0,47	0,19±0,01	0,28±0,06	0,37±0,02	0,55±0,11
NEM-165	0,31±0,16	0,31±0,06	0,45±0,28	0,54±0,33	0,56±0,21
NEM-168	0,72±0,43	0,6±0,04	0,81±0,42	0,61±0,24	0,72±0,09

Supplemental movie 1

Partie II :

ARTICLE 4 :

Cibles thérapeutiques fonctionnellement définies dans les gliomes infiltrants du tronc cérébral

Functionally-defined Therapeutic Targets in Diffuse Intrinsic Pontine Glioma

A Report of the Children's Oncology Group DIPG Preclinical Consortium

Catherine S. Grasso*†1, Nathalene Truffaux†2, Noah Berlow3††, Lining Liu4††, Marie-Anne Debily2,5, Michael J. Quist1, Lara E. Davis6, Elaine Huang6, Pamelyn J Woo4, Yujie Tang4, Anitha Ponnuswami4, Spenser Chen4, Yulun Huang7, Marianne Hütt-Cabezas8, Katherine E. Warren9, Ludivine Le Dret2, Paul S. Meltzer9, Hua Mao7, Martha Quezado9, Dannis G. van Vuurden10, Jinu Abraham6, Maryam Fouladi11, Matthew N. Svalina6, Nicholas Wang1, Cynthia Hawkins12, Eric Raabe8, Esther Hulleman10, Xiao-Nan Li7, Charles Keller*6, Paul T. Spellman1, Ranadip Pal*4, Jacques Grill*2,13, Michelle Monje*4

† contributed equally
†† contributed equally
* co-senior authors

La recherche dans les DIPG a longtemps été limitée par un manque de ressource biologique et de modèle expérimental. Jusqu'à présent, la plupart des essais cliniques ont donc été conduits en l'absence de donnée préclinique rationnelle supportant une efficacité probable des médicaments testés dans les DIPG. Ces dernières années, l'effort mené par de nombreux centres à travers le monde pour recueillir des échantillons tumoraux a permis les découvertes génomiques majeures nécessaires à la compréhension biologique de ces tumeurs et à l'approche thérapeutique ciblée. Depuis, ces centres ont également développé des modèles d'études sur lesquels certaines pistes thérapeutiques ont déjà été explorées (Monje et al. 2011; Mueller et al. 2014). Compte-tenu de la rareté de ces modèles et pour mutualiser les efforts, une approche préclinique en collaboration et globalisée a été mise en place.

En 2011, le *DIPG Preclinical Consortium* réunissait la plupart des équipes concernées autour du projet intitulé « *Rapid Preclinical Development of a Targeted Therapy Combination for DIPG »* (soutenu par le Children Oncology Group et plusieurs associations philanthropiques nord-américaines) avec pour objectif de proposer un médicament candidat ou une combinaison thérapeutique prometteuse en essai de phase précoce dans un délai rapide (18-24 mois).

Pour cela, plusieurs types d'analyse ont été réalisés parallèlement sur des échantillons de tumeurs primaires de DIPG (17) ainsi que sur un panel de lignées cellulaires de DIPG (14) apparentées aux tumeurs d'origine ou non.

Dans un premier temps, afin de déterminer le profil de sensibilité de ces lignées à une liste d'inhibiteurs, un criblage de 84 médicaments a été réalisé. Ces évaluations effectuées en monothérapie mettent en évidence un effet antiprolifératif pour un nombre limité de composés. Parmi les composés actifs, seuls ont été retenus (« Hits ») ceux pour lesquels la concentration inhibant 50% de la prolifération cellulaire (IC_{50}) était inférieure à la concentration maximale mesurée dans le sérum (C_{max}), pour 3 ou plus des 14 lignées testées.

D'autre part, des analyses moléculaires ont été réalisées sur ces tumeurs primaires ainsi que sur le panel de lignées.

Par séquençage du transcriptome (RNA-Seq) des tumeurs primaires de DIPG, nous avons d'abord voulu interpréter les résultats du criblage médicamenteux dans un contexte moléculaire de DIPG. De manière supervisée, les gènes associés aux cibles des inhibiteurs testés ainsi que d'autres gènes de la littérature ayant un rôle dans les DIPG ont été sélectionnés. Parmi ceux-ci, ont été retenus ceux étant différentiellement exprimés dans les tumeurs par rapport au cerveau normal et correspondant à des cibles des « hits » établis lors

du criblage. Cette sélection a mis en évidence la surexpression des gènes du cycle cellulaire tels que *CDK2, 3 et 4* ciblés par des inhibiteurs spécifiques. D'autre part, plusieurs oncogènes dont *MYC* apparaissent surexprimés dans ces échantillons.
De manière intéressante, l'analyse fonctionnelle de type GO (*Gene Ontology*) de cet ensemble de gènes fait apparaître que le processus le plus différentiellement exprimé par rapport au cerveau normal concerne la catégorie « Modifications d'histone et de la chromatine ». Enfin, en analyse GSEA, le profil d'expression de ces tumeurs montre un enrichissement en gènes des signatures mésenchymateuse, astrocytaire et cellules-souches embryonnaires.

Parmi les différentes classes de nos « hits », celle des modificateurs épigénétiques de type inhibiteurs d'HDAC (HDACi) semble particulièrement efficace. Pour comprendre les modifications d'expression génique à l'origine de l'efficacité constatée, nous avons donc étudié l'effet du panobinostat *in vitro* sur l'expression génique de lignées cellulaires de DIPG par RNA-Seq. Le traitement par le panobinostat induit non seulement une normalisation des signatures d'expression génique observées dans les tumeurs primaires (sous-expression des gènes de la signature mésenchymateuse, réversion de la signature astrocytaire vers une signature oligodendrogliale, sous-expression de la signature de type « cellule-souche embryonnaire »), mais encore il induit une surexpression de certains gènes suppresseurs de tumeurs (tels que *TP53*, p21 et *EphB6*) et la sous-expression d'oncogènes (dont *MYC, cyclin D2, BIRC5* et *FOXM1*).

Le ciblage de plusieurs *HDAC* via l'utilisation du panobinostat a été testé *in* vivo par infusion convective dans un modèle de xénogreffe de DIPG. Les résultats montrent un retard de croissance tumorale significatif sous traitement.

La suite de cette étude concerne l'apport des données de génomiques dans la prédiction de sensibilité aux médicaments. A partir d'une méthode de modélisation prédictive de la sensibilité à des inhibiteurs ciblés, appelée méthode TIM (*Target Inhibition Map*), nous avons voulu connaître la valeur prédictive des anomalies génétiques à cibler. La méthode de prédiction TIM consiste à intégrer des données d'affinité de liaison « inhibiteur-cible » à des résultats de criblage médicamenteux afin d'identifier les cibles spécifiques à inhiber, en série ou en parallèle en fonction des réseaux de protéines identifiés dans les bases de données KEGG (Berlow et al. 2013; Tang et al. 2013). A cela est ajoutée dans ce travail, une information supplémentaire de valeur d'expression du gène de la cible prise (ici en comparant l'expression du gène dans les tumeurs et dans le tissu cérébral normal). Cette analyse révèle que les données d'expression permettent une meilleure prédiction de la

sensibilité d'une lignée à un inhibiteur donné par rapport à l'information liée à la drogue uniquement ou à l'addition d'une information sur le séquençage des tumeurs.

Cette méthode peut aussi définir grâce à l'intégration des réseaux protéiques, les cibles qu'il faut atteindre simultanément. Nous avons par exemple identifié pour une lignée donnée NEM157 que la combinaison entre un HDACi et un inhibiteur de Src devrait être efficace. Les études de combinaisons réalisées ont confirmé la synergie entre ces deux drogues.

Des expériences de validation sont planifiées pour valider cette approche en i) testant la valeur prédictive de la TIM globale sur de nouvelles lignées, ii) en testant de nouvelles drogues inhibant les cibles définies par la TIM, comme un autre inhibiteur du protéasome par exemple, iii) en testant des combinaisons de drogues identifiées par la TIM (soit globale, soit propre à chacune des lignées). On pourra alors tester *in vitro* les meilleures combinaisons.

Enfin, la recherche d'anomalies génétiques dans les 17 tumeurs primaires par séquençage d'exome révèle globalement un faible taux de mutations (17,2 mutations / tumeurs) et un profil génomique « plat ». Parmi les anomalies les plus souvent rencontrées, aucune corrélation avérée avec une sensibilité pharmacologique n'est à retenir.
Outre la présence d'anomalies génétiques connues dans les DIPG (perte/mutations de *TP53* (9/17 ; 53%), mutations *H3K27M* (13/17 ; 78%) et mutations d'ACVR1 (4/17 ; 23%)), cette analyse dévoile de nouvelles anomalies récurrentes notamment dans *NTRK1* (7/17, 41%) et une mutation du gène suppresseur de tumeur *EphB6*.

L'approche innovante décrite ici montre sa capacité à découvrir des drogues efficaces dans les DIPG même en l'absence de connaissance *a priori* sur la biologie de la maladie. Sa capacité à intégrer de la connaissance biologique *a priori* (pathway KEGG) et expérimentale (crible de drogues ayant des cibles connues) la rend très versatile pour de futurs développements de nouveaux traitements dans les DIPG.

Michelle Monje, Departments of Neurology, Neurosurgery and Pediatrics, Stanford University, Lucile Packard Children's Hospital at Stanford, 265 Campus Drive G3065, Stanford CA 94305, Tel (650) 721-5750, Fax (650) 724-3748, email mmonje@stanford.edu

Jacques Grill, Departement de Cancerologie de l'Enfant et de l'Adolescent, Unite Mixte de Recherche du Centre National de la Recherche Scientifique 8203, Institut Gustave-Roussy et Universite Paris-Sud, 114 rue Edouard Vaillant, 94805 Villejuif, France, Tel +3314216209, Fax +33142115275, email jacques.grill@gustaveroussy.fr

Ranadip Pal, Electrical and Computer Engineering, Texas Tech University, Lubbock, TX, 79409 USA, Tel (806) 742-2533 ext 240, Fax (860)742-1245, email ranadip.pal@ttu.edu
Charles Keller, Pediatric Cancer Biology Program, Department of Pediatrics, Oregon Health & Science University, Portland OR USA, Tel (503) 494-1210, Fax (503) 418-5044, email keller@ohsu.edu

Catherine Grasso, Department of Molecular and Medical Genetics, Pediatric Cancer Center, Biology Program, Papé Family Pediatric Research Institute, Dept. of Pediatrics, Oregon Health & Science University, Portland, OR 97239, USA, grasso@OHSU.edu

Science Translational Medicine
AAAS

Title: **Functionally-defined Therapeutic Targets in Diffuse Intrinsic Pontine Glioma**
A Report of the Children's Oncology Group DIPG Preclinical Consortium

Authors: Catherine S. Grasso*†[1], Nathalene Truffaux†[2], Noah Berlow[3††], Lining Liu[4††], Marie-Anne Debily[2,5], Michael J. Quist[1], Lara E. Davis[6], Elaine Huang[6], Pamelyn J Woo[4], Yujie Tang[4], Anitha Ponnuswami[4], Spenser Chen[4], Yulun Huang[7], Marianne Hütt-Cabezas[8], Katherine E. Warren[9], Ludivine Le Dret[2], Paul S. Meltzer[9], Hua Mao[7], Martha Quezado[9], Dannis G. van Vuurden[10], Jinu Abraham[6], Maryam Fouladi[11], Matthew N. Svalina[6], Nicholas Wang[1], Cynthia Hawkins[12], Eric Raabe[8], Esther Hulleman[10], Xiao-Nan Li[7], Charles Keller*[6], Paul T. Spellman[1], Ranadip Pal*[4], Jacques Grill*[2,13], Michelle Monje*[4]

Affiliations:
(1) Center for Spatial Systems Biomedicine Department of Molecular and Medical Genetics, Oregon Health & Science University, Portland, OR, USA
(2) Unité Mixte de Recherche du Centre National de la Recherche Scientifique 8203, Institut Gustave Roussy et Université Paris-Sud, Villejuif, France.
(3) Electrical and Computer Engineering, Texas Tech University, Lubbock, TX, USA
(4) Depts. of Neurology, Neurosurgery and Pediatrics, Stanford University, Stanford, CA, USA
(5) Université d'Evry-Val d'Essone, 91037, Evry, France.
(6) Pediatric Biology Program, Papé Family Pediatric Research Institute, Dept. of Pediatrics, Oregon Health & Science University
(7) Laboratory of Molecular Neurooncology, Texas Children's Cancer Center, Baylor College of Medicine, Houston, TX, USA
(8) Departments of Oncology and Pathology, Johns Hopkins University, Baltimore, MD, USA
(9) National Cancer Institute, Bethesda, MD, USA
(10) Department of Pediatric Oncology, Hematology and Neuro-Oncology Research Group Cancer Center Amsterdam, VU University Medical Center, Amsterdam, The Netherlands
(11) Cancer and Blood Diseases Institute, Cincinnati Children's Hospital Medical Center, Cincinnati, OH, USA
(12) Dept. of Paediatric Laboratory Medicine, University of Toronto; Scientist, Labatt Brain Tumour Research Centre, Hospital for Sick Children, University of Toronto, Toronto, ON, Canada
(13) Departement de Cancerologie de l'Enfant et de l'Adolescent, Institut Gustave Roussy, Université Paris-Sud, Villejuif, France

† contributed equally
†† contributed equally
* Co-corresponding authors:

One Sentence Summary: Genomic, transcriptomic, chemical screening and computational data converge to define a promising therapeutic strategy for Diffuse Intrinsic Pontine Glioma (DIPG), the leading cause of brain tumor death in children.

Abstract: Diffuse Intrinsic Pontine Glioma (DIPG) is a universally fatal cancer with only a 9-month median survival. The present study represents an international, multi-institutional collaboration to pool DIPG tissue resources and evaluate comprehensive molecular and functional targets of DIPG therapy. We performed whole exome sequencing of 17 DIPG tumors, RNAseq expression analysis and a chemical screen against 14 DIPG cell lines along with integrated computational analysis to identify potentially effective therapeutic strategies. Whole exome sequencing underscores the relatively quiet mutational landscape of this pediatric malignancy, with demonstration of known genomic aberrations such as *histone H3* K27M mutations and *TP53* loss/mutations, as well as discovery of previously unrecognized recurrent aberrations in *ACVR1*, *NTRK1* and *EphB6*. The chemical screen identified consensus sensitivity to two classes of agents, histone deacetylase inhibitors and CDK inhibitors, with additional agents demonstrating efficacy for subsets of DIPG cell lines. Integrative computational analysis of drug screen data and paired RNAseq expression data additionally identified multiple candidate genes that have the potential to yield an effective treatment, if targeted in combination. Among these, combinatorial targeting of HDAC 1, together with HDAC 2 or 4 is predicted to be an effective strategy. Panobinostat, among the more promising agents identified by the chemical screen, inhibits these three HDACs. Accordingly, *in vivo* testing of panobinostat demonstrated efficacy in a pontine orthotopic xenograft model of DIPG. RNAseq expression analysis before and after exposure to panobinostat highlighted normalization of gene expression patterns, including up-regulation of tumor suppressor gene levels (e.g. *EphB6*) and down-regulation of oncogenes (e.g. *MYC*). Taken together, these data suggest the potential utility of specific drug combinations and provides evidence of *in vivo* treatment efficacy of the multi-HDAC inhibitor panobinostat.

Introduction

Diffuse Intrinsic Pontine Glioma (DIPG) is a devastating childhood cancer with a dismal prognosis. According to Central Brain Tumor Registry of the United States (CBTRUS),

DIPG affects approximately 400 children each year in the United States (*1*); it is the second most common malignant brain tumor of childhood and the leading cause of pediatric brain tumor death. Median survival is only 9 months, and 5 year survival is less than 1% (*2*).

Standard therapy consists of conventional local field radiotherapy to a dose of 54-60 Gy for 6 weeks. Without radiotherapy, median survival is approximately 20 weeks (*3, 4*). Radiotherapy leads to improved neurological function for a few months and improves overall survival by approximately 3 months on average. No advances in DIPG therapy have been made since the introduction of radiotherapy over three decades ago. Multiple studies using a variety of conventional, high-dose and targeted chemotherapies have failed to demonstrate a survival advantage in patients with DIPG (*5-12*). The majority of clinical trials of drug therapies to date, however, have been conducted in the absence of preclinical data to support efficacy in DIPG. Because of the diffusely infiltrative growth pattern of the tumor and the highly eloquent nature of the pons, surgical resection plays no role in therapy of DIPG. Biopsy is usually not performed in standard cases, as diagnosis can typically be made based on imaging appearance alone (*2*, *13*). Thus, DIPG research has been limited historically by a dearth of tumor tissue available for study and lack of experimental model systems.

In recent years, however, this has begun to change. Employing early post-mortem tissue harvest (*14-16*) and performing biopsy for the purpose of research (*17*), scientists have now described genomic alterations (*18, 19*), transcriptomic changes in DIPG (*19, 20*), and established DIPG cell lines and orthotopic xenograft model systems (*15*). An important insight that has resulted from these new tissue resources is that point mutations in histone H3 genes *H3F3A* or *HIST1H3B* affecting Lysine 27 in the N terminal tail are found in the majority of DIPG cases and disrupt global epigenetic regulation in these tumors (*21-24*). Now armed with the tools to design clinical trials based on preclinical data, an international, multi-institutional collaboration has formed to pool DIPG tissue resources and evaluate comprehensive molecular and functional targets for DIPG therapy. Our DIPG preclinical consortium has screened potential single agent therapies in the breadth of DIPG cell line models available at the initiation of the study. The present manuscript describes the collective results of chemical screening, RNA sequencing, DIPG whole exome sequencing and integrated computational analyses to identify potentially effective therapeutic strategies.

Results

Chemical screen

A total of 14 human DIPG cell lines representing the diversity of preclinical *in vitro* models derived from patient material were utilized in the drug screen. Seven cell lines were established from tumor biopsies performed at diagnosis and grown as monolayers, five from autopsy tissue and grown as neurospheres and two lines were established from serially xenografted DIPG tumor derived from autopsy tissue. Of these DIPG cell lines, four cell lines were tested against version 1 of the drug screen; 10 cell lines were tested against version 2 of the drug screen and three cell lines were tested against both. The main endpoint was 72-hour cell viability assessed with the MTS assay, and confirmed using continuous cell imaging (Supplementary Fig. 1). The responses of the DIPG cell lines to the agents screened within a range of doses from 0.001 μM to 10 or 100 μM are summarized in Fig 1. Consistent with the known chemotherapy insensitivity of the tumor clinically, cell lines exhibited notable chemoresistance, with most drugs demonstrating efficacy in only a minority of the cell lines tested. The majority of DIPG cell lines showed decreased growth as measured by the cell viability MTS assay to only a limited number of drugs. The sensitivity profiles of the drugs did not cluster with the type of cell line (Fig. 1 and Table S1). To be conservative, those drugs with IC_{50} values less than the published human peak serum concentration (C_{max}) were considered "hits"; drugs that are "hits" in three or more cell lines are shown in Fig. 1B. The chemical screens revealed recurrent sensitivity to the HDAC inhibitors vorinostat (4/14 cell lines) and panobinostat (9/14), CDK inhibitors SNS-032 (13/14), dinaciclib (10/10) and alvocidib (10/10), proteasome inhibitor carfilzomib (5/14), tyrosine kinase inhibitor dasatinib (6/14), Aurora Kinase inhibitor alisertib (7/14), IGF1R inhibitor BMS754807 (3/14), PI3K/mTOR inhibitor BEZ235 (6/10), HSP90 inhibitor AUY922 (9/10), SYK inhibitor fostamatinib (4/10), MDM2 inhibitor nutlin-3 (6/10), and microtubule dynamic inhibitor eribulin (3/9) (Fig. 1). Some drugs were only effective in unique cell lines such as enzastaurin in VU-DIPG-B or AZD8931 in JHH-DIPG1 (Fig. 1A). Notable "misses" that highlight the relative resistance of this tumor to traditional chemotherapies include temozolomide, carboplatin and vincristine (Fig. 1A). Other notable "misses" include targeted agents erlotinib, sunitinib and imatinib (Fig. 1A and Fig. S2). Other agents showed modest efficacy, such as

crizotinib, cediranib and entinostat (Fig 1A), but not at concentrations achievable in serum with published systemic dosing regimens. These agents may prove to be useful when delivered directly to the tumor by alternative drug delivery strategies such as convection enhanced delivery (CED). The drugs Picropodophyllin (PPP), BIX 01294 and chromeceptin had three or more IC_{50}s in range, but a clinical C_{max} is not available for these agents. The penetration of these agents through the blood-brain barrier (Table S2) of the pons in particular is not known and may vary from penetration in other regions of the central nervous system.

The demonstrated sensitivity to CDK inhibitors and HDAC inhibitors is common to multiple tumor types. To assess the relative specificity of the findings, we assessed the sensitivity of an *H3F3A* wild type pediatric cortical glioblastoma neurosphere line (SU-pcGBM-2; obtained from a 15 year old male at the time of initial surgery) to a CDK inhibitor (alvocidib) and an HDAC inhibitor (panobinostat) in comparison to two DIPG neurosphere lines bearing a mutation in *H3F3A* (SU-DIPG VI) or *HIST1H3B* (SU-DIPG IV) re-tested in the same experiment. Alvocidib (flavopiridol) affected the pediatric GBM line similarly to the two DIPG cell lines, but panobinostat was more efficacious in both DIPG lines compared to the pediatric GBM line (Fig. S3).

Gene Expression

To examine the molecular context of the functional drug screening results, RNA sequencing was performed to analyze mRNA expression in primary DIPG tumors in comparison to normal brain tissue from the same patients (Fig. 2). We focused on those genes (429) that are associated with the targets of the drugs tested or are reported in the literature as having a potential role in DIPG. We found up-regulated expression ($P < 0.01$) of several genes targeted by the top drug screen hits. Specifically, we found up-regulated expression of *CDK 2*, *3* and *4*, targeted by SNS-032, dinaciclib and alvocidib, and *PSMB8*, targeted by carfilzomib (Fig. 2A). In addition to those genes directly targeted by "drug hits" from the chemical screen (Table S3), we also noted up-regulation of several oncogenes

such as *MYC*, *CLK2*, *AKT2*, *WEE1*, *EPHB3*, *NRAS, STK10* and *PLK1* (Fig. 2A). In comparison to normal pediatric brain tissue, the most important Gene Ontology (GO) category differentially expressed was the "chromatin and histone modification" category. Furthermore, an overexpression of the mesenchymal, astrocytic and embryonic stem cell signatures was observed (Fig. S4).

Changes in gene expression following histone deacetylase inhibition

The finding that two top hits from the drug screen were epigenetic modifying HDAC inhibitors was intriguing, since the majority of DIPG tumors harbor K27M mutations in either of the histone 3 genes *HIST1H3B* or *H3F3A*. Despite recent insights that H3K27M mutation results in broad changes in the epigenetic landscape (*23, 24*), it remains unclear how H3K27M mutations drive DIPG. We thus sought to investigate more deeply the mechanism by which HDAC inhibition is efficacious in these tumors. We performed RNAseq analysis on two DIPG neurosphere cell lines before and after exposure to panobinostat (1 μM for 48 hours; Fig. 2B) in order to explore mechanisms of HDAC inhibitor efficacy and to gain insight into the gene expression changes that may highlight targets for a promising drug combination. Following panobinostat treatment, we observed sweeping changes in gene expression as would be expected from modulation of the epigenetic landscape. Broadly, we observed changes in expression pattern representing a normalization of gene expression observed in DIPG primary tumor samples compared to normal brain tissue, as described above. Gene Set Enrichment Analysis (GSEA) revealed down-regulation of the mesenchymal gene expression signature (*25*), a phenotypic switch with a loss of astroglial markers and an increase of oligodendroglial markers (*26*) and a down-regulation of the embryonic stem cell signatures in these panobinostat-treated DIPG cells (Fig. S4) (*27, 28*). Furthermore, panobinostat induced a global increase in histone gene expression (Fig. 2B), indicating an unexpected mechanism by which it may remodel the epigenome of DIPG. We found a decrease in gene expression of *MYC* (Fig. S4) and alterations in cyclin and cyclin dependent kinase-related genes, with a decrease in expression of *Cyclin D2* and an increase in cyclin-dependent kinase inhibitor 1A (P21). We also noted up-regulation of *VGF*, a growth factor regulated by TrkA signaling, and, in one of two cell lines, *DHRS2*, a negative modulator of MDM2 that thus results in improved P53 function. *TP53* levels themselves go up following panobinostat exposure (Supplementary data file 1). *FOXM1,*

which acts as an oncogene in multiple cancer types through its role as a transcriptional activator of proliferation that is up-regulated in DIPG tumors relative to normal brain and *BIRC5*, an inhibitor of apoptosis that is up-reguated in DIPG tumors relative to normal brain, are both strongly downregulated by panobinostat (Figure S4). *EphB6*, a tumor suppressor whose expression is decreased in DIPG tumors relative to normal brain, is increased by panobinostat (Fig S4). Taken together, these data indicated that HDAC inhibition with panobinostat results in broad changes in gene expression and possibly epigenetic remodeling through the increased expression of histones. It also suggests that the beneficial effects of panobinostat may be mediated in part by down-regulation of oncogenes (such as *MYC*, cyclin D2, *BIRC5 and FOXM1)* and augmentation of tumor suppressors (such as P53, p21 and EphB6). An exciting aspect of panobinostat's effect on the DIPG transcriptome is the ability to increase and decrease the expression of genes that cannot currently be directly targeted: increasing the expression of a tumor suppressor, like *TP53* and *EPHB6*, or decreasing the expression of oncogenes, like *MYC* and *FOXM1*. Together, these findings all point to putative reasons for the efficacy of this drug or class of drugs.

Identification of effective combination targets for DIPG

The TIM (Target Inhibitor Map) method is a predictive modeling approach to tumor drug sensitivity prediction based on inference of Boolean Relationships (*29, 30*). Our approach considers that the underlying mechanism for sensitivity to targeted drugs consists of a combination of series (inhibiting any one target in the series will block tumor proliferation and thus this behavior is similar to Boolean 'OR' logic) and parallel (all the parallel targets need to be inhibited to block tumor proliferation and thus this behavior is similar to Boolean 'AND' logic) targets being inhibited. The seven blocks shown in Figure 3 represent the seven most relevant blocks derived from the drug screen analysis with RNAseq data integration. The analysis was performed on the complete drug screen dataset consisting of 5 tumor samples with RNAseq data, and 9 cell line samples without RNAseq data. Of this set, 2 samples (SU-DIPG IV, SU-DIPG VI) had matched normal RNAseq data. The mean expression values of the entire set of normal RNAseq data was used as a surrogate matched normal for remaining unmatched samples. Two of the cell line samples (NEM157 and NEM175) were tested using multiple drug screens, which resulted in a total of 16 sets of functional data.

Based on the TIM analysis, HDAC1 along with HDAC2 or HDAC4 appear to be effective treatment targets for many of the DIPG samples. HDAC1 appears as an important target due to the high efficacy of drugs panobinostat, trichostatin A and vorinostat with HDAC1 as a common target with low EC_{50}. The possible importance of HDAC4 is hypothesized based on the fact that the observed IC_{50} for a number of cell cultures for panobinostat is closer to the EC_{50} of HDAC4 for panobinostat. In Figure 3, CDK2 (often a high importance target in kinase inhibitor drug screens) is paired as an effective treatment with GSK3B or two other cyclin-dependent kinases CDK3 and CDK9. The combinations of CDK inhibitors appear in three targeted therapeutics, BMS-387032, flavopiridol, and dinaciclib that were more often effective than therapeutics in which CDK2 appears individually. Similarly, drugs where mTOR and PIK3CA both appear separately are less effective than when they appear together (*e.g.* sirolimus as an mTOR inhibitor was ineffective, while BEZ-235 was a more effective dual mTOR and PI3KCA inhibitor). However, this combination has a lower score due to BEZ-235 demonstrating sensitivity in a smaller set of samples.

PDGFRB is identified as important in combination with other targets of interest, namely CLK2, FGFR2, EPHA5 and ULK1 (part of the mTOR and PI3K pathway). These combinations were identified in part due to the success of dasatinib on several samples. However, these targets were ineffective on their own, as evidenced by the lack of sensitivity to imatinib and barasertib, as well as other compounds. It should be noted that EPHA5 may be one of multiple EPH-family kinases of interest. The proteasome inhibitor carfilzomib identifies PSMB5 and PSMB8 as a viable combination of targets. PSMB5 is not selected as a single point of failure due to the response of carfilzomib occurring after the dissociation constant threshold for PSMB5. The frequent efficacy of AUY922 identifies HSP90 and HSPB as a target combination of interest. Finally, NTRK1 appears as a potential combination of interest with several targets. We focus on potential synergy with GSK3B, CLK2 and most notably HDAC1 and HDAC2. The predicted sensitivity is overall lower for these combinations, primarily due to lesser sensitivity to NTRK1 inhibition *in vitro*, but may still be of interest as a potential combination therapy.

It is important to note that these seven blocks are a small set of representatives for possible DIPG treatments; the analysis performed identified several other possible combinations based on drug screen performance. Table S5 (TIM Prediction

Performance) contains the correlation coefficients and mean absolute errors for the TIM analysis using 10 fold cross validation. The detailed possible combinations with corresponding scores are included in supplementary Table S6 (TIM top performing blocks). Individual cell line TIM circuits are included as a supplemental data file, and serve as predictors of response for each tumor. For example, targeting Src together with HDAC1 is predicted to be efficacious for DIPG cell line NEM 157, and drugs that hit these targets, dasatinib and vorinostat, proves to be synergistic in vitro for this cell line (Fig. Sx).

Figure 4 shows a connectivity mapping for the 32 targets inferred from the TIM analysis. For generating the network connectivity, we utilized STRING (http://string-db.org/) and considered only the protein interactions that were derived from experimental data. We added two additional proteins, TP53 and UBC, which acted as possible bridges between the different targets and sub-networks elucidated from the TIM analysis. Figure 6 shows that the targets are highly connected based on previously published protein interaction experiments. To show that the TIM-informed interaction network is significant, we compared interactions observed in the TIM-informed network against randomly generated networks of equivalent size from the set of drug protein targets. The TIM informed network had 67 observed interactions at String DB confidence > 0.4. In comparison, 20 randomly generated networks of 34 genes from the 404 drug protein targets along with UBC and TP53 had mean number of interactions (μ) of 23.1 and standard deviation (σ) of 4.63. Thus, the number of interactions observed in the TIM-informed network are more than $\mu + 9\ \sigma$ of same size networks randomly generated from the drug targets.

Furthermore, GO enrichment on the targets shows that large subsets of the targets selected by TIM analysis belongs to few specific biological processes (details included in Table S7, S8 (TIM targets in Biological Pathways).

A parallel ensemble analysis was performed to evaluate the predictive power of functional and genetic characterizations. The results indicate that sensitivity was best predicted by drug target profiles integrated with RNAseq data as compared to individual RNAseq or mutation data or integration of drug profile and mutation data. Furthermore, the ensemble analysis also confirmed that PSMB, HDAC and CDK gene families play important roles in the tumor proliferation map for DIPG. The details of this analysis is included in supplementary methods and table S4.

In vivo validation of therapeutic efficacy with the HDAC inhibitor panobinostat

Given that TIM analysis predicts targeting HDAC1, and HDAC 2 or 4 as a particularly promising combination strategy, we chose the multi-HDAC inhibitor panobinostat to test *in vivo*. Because drug delivery to the pons is a particular challenge and data regarding the pontine penetration of panobinostat is unavailable, we sought to demonstrate efficacy of panobinostat using convection enhanced delivery (CED) to directly infuse panobinostat into the pons in a pontine orthotopic xenograft model of DIPG. SU-DIPG VI cells expressing green fluorescent protein (GFP) and firefly luciferase were stereotactically injected in the fourth ventricle and dorsal pons at postnatal day 2 (P2) and allowed to engraft for two months. Panobinostat (5 μl of 2 μM solution, infused at a rate of 0.4 μl/min over a period of 12.5 minutes) or vehicle-only control was administered into the pons following stereotactic placement of a 31 G Hamilton needle threaded through a 27 G needle to create the convection effect (Fig. 5A). This method results in delivery of the infusate throughout the brainstem, as illustrated by CED delivery of blue dye (Fig. 5B). Mice tolerated the procedure well, with no apparent behavior changes following panobinostat CED. *In vivo* bioluminescent imaging was performed immediately prior to and 7 days after panobinostat (or vehicle control) administration in order to measure tumor growth by quantitative assessment of photon emission (Fig. 5C). We found a marked effect of panobinostat on the rate of tumor xenograft growth. In vehicle-treated control mice, the rate of xenograft growth was approximately 6.5 fold greater than that in mice treated with a single dose of panobinostat by CED (Fig. 5D).

Whole exome sequencing to identify drug targets in DIPG patients

Another way to identify therapeutic targets in DIPG is to consider the genomics data with a goal of identifying driving aberrations that are likely to respond to a targeted drug therapy. To explore whether there are actionable genomic aberrations in DIPG we performed Whole Exome Sequencing (WES) on 17 primary tumors with a duplicate sample for one case. WES can be used to identify nonsynonymous point mutations and indels, as well as copy number alterations with potential use as therapeutic targets.

The rate of somatic point mutations among the DIPG tumor samples was compared with other childhood brain cancers and with a few common adult cancers. The mean somatic mutation count of DIPG patients, which averaged 17.2 per sample (Fig. S6), was lower than adult tumors . However, this was slightly higher than the mutation rates for other childhood neural cancers. Medulloblastoma was reported to have on average 8.3 somatic mutations (*31*) and neuroblastoma was reported to have an average of 13 somatic mutations per sample (*32*). If the two hyper-mutated samples in this series, OHSU-DIPG#2 with 47 mutations, Li-C7 with 31 mutations, are removed from consideration, this mutation rate drops to 13.3, bringing it in line with the similar childhood brain cancers (Fig. S6). The low mutational burden may be explained by the high incidence rate of H3K27M mutations in DIPG, which may drive cancer through epigenetic remodeling. Regardless, the low mutational burden makes it less likely that many treatment opportunities will be defined by point mutations and indels.

Using the WES data, we also considered the copy number alterations to identify recurrent focal gains that could act as a potential drug target. Figure 6A shows the sum log copy number data for the matched and unmatched DIPG samples, while Figure S6, shows the log copy number ratios for all of the samples. All of the samples except two, JHH-DIPG1 and VU-DIPG.A, which we excluded from the sum log copy number figure, were very quiet with respect to copy number alterations in general (Fig. S7). JHH-DIPG1 is an interesting case, because it is highly rearranged (Fig. S7) with a single high-level aberration including *MYC*, which may have resulted from the extensive treatment this patient underwent (Table S1 and Fig. S7A), suggesting that treatment may drive the acquisition of CNAs in DIPG. One sample, SU-DIPG-IX, exhibited multiple focal high-level gains containing oncogenes, including *AKT3, MYCN*, *KRAS,* and *PIK3C2G*, indicating that there may be DIPG cases that are driven by genomic aberrations rather than epigenetics that can be treated using therapies targeting specific genes (Figure S6B). In the rest of the DIPG samples, we didn't find any recurrent or high-level focal gains; instead the genome aberrations that were the most recurrent were gains of 1q and of chromosome 2, which is gained in 6 tumors and contains *MYCN, ACVR1* and *ALK*, and loss of chromosome 14, chromosome 16, which peaks at *CDH1* and *CDH11*, two cadherins that suppress the EMT transition, and chromosome 17, which peaks in the region containing *TP53* (Fig. 6). Figure 6 shows the chromosome 1q single copy gain that is present in six DIPG tumor samples: SK-DIPG-27, SU-DIPG-II, SU-DIPG-IV (and

derived cell line), Li-A1, Li-C7, and Li-F15. This region contains single copy gains of *H3F3A* (no gains were observed for *HIST1H3B*), suggesting additional evidence for this gene driving cancer. In addition, this region contains multiple drug targets, including but not limited to *ABL2, CLK2*, *NTRK1*, *PIK3C2B, PARP1, AKT3*, *CDK18.* Since this is a low copy number gain of a large region it is unclear whether drug targeting this region has the potential to affect tumor progression. With that said, multiple top hit drugs did target genes in this region, suggesting that genes in this gain may be important drivers to consider when selecting therapies.

Next, we looked at the most highly mutated genes considering both point mutations and copy number alterations (Fig. 7) from a drug target perspective. Consistent with the reported literature, we found disruptive *TP53* mutations in 53% (9/17) of tumor cases. Gains of *MDM4*, which negatively regulates *P53*, is a drug target for SJ-172550. *MDM4* is on the chromosome 1q amplification and is amplified in 7/17 samples; a total of 76% (13/17) tumors harbored a mutation of *P53*, amplification of *MDM4* or both. Disappointingly, the drug SJ-172550 was not a hit in a single sample, indicating that *MDM4* may not be an effective target on its own, despite being elevated in so many samples.

In this series, we did not observe the same frequency (30% in other case series) of recurrent tyrosine receptor kinase amplifications reported in other DIPG cohorts (*18, 19*). We did have one sample (1/17 cases) with a low-level *PDGFRA* amplification and two samples with *PDGFRA* outlier mRNA expression, present in both SU-DIPG-IV and SU-DIPG-VI in both the tumors and the matched cell lines; neither of these samples responded to drugs targeting *PDGFRA*. While two samples had *MET* amplifications, one of which was focal, and SU-DIPG-I had outlier mRNA expression, neither of these samples were tested in the drug screen, making it difficult to assess how effective targeting *MET* would be for DIPG. With that said, no *MET* inhibitors nor specific *PDGFRA* inhibitors were a top hit in the drug screen.

The recently discovered histone mutation, H3.3 or H3.1 K27M, occurring in 78% of DIPG patients (*21*), reprograms the epigenetic landscape and gene expression in ways that may drive tumorigenesis (*24, 33*). Accordingly, we found the presence of histone H3.1 or H3.3 K27M mutations in 76% of cases in this series. *H3F3A* gene mutations were found in 52% (9/17); *HIST1H3B* in 24% (4/17). *HIST1H3B* was not amplified in a single sample, had expression levels barely detectable in all samples (RPKM max was

0.62 in SU-DIPG-VIII), and did not exhibit differential expression. On the other hand, *H3F3A* is on the chromosome 1q gain that is present in six samples (see Figure 6A), half of which have the *H3F3A* point mutation as well. One sample, Li-F15 had the *H3F3A* amplification without the K27M mutation in either H3.1 or H3.3. In addition, *H3F3A* was overexpressed in tumors relative to normals (P-value of 0.003), regardless of whether the mutations or amplifications were present. While in two of the samples with amplifications, SU-DIPG-II and SU-DIPG-IV, *H3F3A* was over-expressed, we also observed a sample, SU-DIPG-1, that exhibits *H3F3A* over-expression despite having no amplification and without the presence of the H3K27M mutation. Cases with over-expression alone may add to the number of cases driven by histone 3 aberrations. Together these data indicate multiple mechanisms for dysregulation of *H3F3A* and suggest a larger role for this gene in DIPG etiology and potentially more treatment opportunities.

In 41% (7/17) of tumor cases, we found gains of neurotrophic tyrosine kinase receptor type 1 (*NTRK1*), also known as TrkA (Figure 7). Whether TrkA signaling represents a novel target remains an open question, but it should be noted that SU-DIPG-IV, the only tumor in the series exhibiting the *NTRK1* amplification that also had a correlate cell line, did respond to BMS-074807, the drug in the screen that targets NTRK1 (Fig. 1A and Table S3).

In one case (1/17) we observed an indel mutation in *EphB6* (Fig. 7A), a kinase-deficient Ephrin receptor whose loss has been linked to tumor cell invasiveness (*34*). The expression of *EphB6* was decreased in comparison to normal brain tissue in all cases examined by RNAseq (Fig. 2A and Fig. S4) consistent with its role as a tumor suppressor in other cancer types (*34*). Taken together, these observations along with the observation that *EphB6* expression can be restored in two DIPG cell lines in response to panobinostat treatment indicate that *EphB6* may be playing the role of a tumor suppressor in DIPG. While *EphB6* may not be a direct target, it is suggestive of novel treatment strategies related to ephrin regulation.

Consistent with recent reports of whole genome sequencing (WGS) (Taylor et al, *in press*), DNA exome sequencing of this DIPG case series revealed recurrent mutations in four tumors in *ACVR1,* involved in TGFβ and BMP signaling, at residue 328, in the serine/threonine kinase domain (Figs. 6A, 7A, 8). Two different amino acid changes were found at this position - G328V in tumor SU-DIPG-IV (and matched cell line) and G328E in

tumors OHSU-DIPG#1, Li-F15 (and matched xenografts Li-F17 and Li-F18) and Li-A1 (and matched xenograft Li-A2), suggesting a possible role in oncogenesis. Different amino acid changes at the same residue typically indicate a role in oncogenesis. Figure 6A shows the single copy gain of chromosome 2, which contains *ACVR1,* that occurs in OHSU-DIPG#1, Li-A1, Li-F15, SU-DIPG-VIII, SU-DIPG-IX. This list includes all of the tumor samples that contain the G328E mutation, OHSU-DIPG#1, Li-A1 and Li-F15, but not SU-DIPG-IV, which contains the G328V mutation (Fig. 8A). This high-level of co-occurrence of the point mutation and the copy number gain of *ACVR1*, suggests that this gene may be driving amplification of chromosome 2 in these samples. RNAseq analysis also showed that *ACVR1* is over-expressed in tumors relative to normal brain with a P-value of 7.71E-06. These data show that SU-DIPG-VIII and SU-DIPG-IX, both of which are amplified and do not have the *ACVR1* point mutation, are over-expressed relative to normal brain. Interestingly, two samples that did not exhibit somatic point mutations at this position or copy number gains, SU-DIPG-1 and VU-DIPG.A, exhibit high outlier mRNA expression in DIPG tumors relative to normal brain (Fig 8C). Together these data suggest that there may be multiple mechanisms to dysregulate *ACVR1* and indicate that this gene may be disrupted in 47% (8 of 17) of DIPG tumors in ways that may be targetable.

Since the top hits from the drug screen were therapies targeting particular genes, we next explored the question of whether effective drugs were associated with genomic alterations in targeted genes in the 17 sequenced tumors. Overall, the observed drug sensitivities do not correlate well with the genomic aberrations found by WES (Fig 6-7). For CDK inhibitors, effective in 13/14 cell lines, we found mutations in *CDK3* in 5.8% (1/17), and amplifications of *CDK1* (1/17), *CDK2* (1/17), *CDK4* (2/17), *CDK6* (2/17), *CDK7* (0/17), *CDK9* (1/17), *CDK11a* (3/17), *CDK11b* (2/17), *CDK14* (1/17), *CDK17* (1/17), and *CDK18* (6/17) (Fig. 7). For HDAC inhibitors effective in the majority of DIPG cell lines, but whose mechanism may not be expected to depend upon alterations in HDAC genes per se, we found genomic aberrations in *HDAC1* in 0% (0/17), *HDAC2* in 5.8% (1/17; loss), *HDAC4* in 11.8% (2/17; amplification), and *HDAC5* in 11.8% (2/17; one amplification and one loss) (Fig. 7). Alisertib is an Aurora Kinase A inhibitor effective in 7/14 cell lines, but Aurora Kinase A or B genes were only amplified in 5.8% (1/17) of the sequenced samples, and Aurora Kinase B was lost in 3/17 tumors (Fig. 7). *IGF1R*, which is targeted by BMS754807, a drug screen hit in 3/14 cell lines, was not mutated or amplified in any of the 17 samples (Fig. 7). Taken

together, the relative paucity of focal mutations lends more evidence for an epigenetic basis to this disease.

Discussion

The present study represents a unique multi-institutional, international collaborative effort to identify functionally relevant targets and develop an effective DIPG treatment strategy. Integration of genomic data and chemical screening data converge to identify HDAC inhibitors (panobinostat and vorinostat) and CDK inhibitors (alvocidib and dinaciclib) as the most promising targets. Matching the RNAseq data and the drug screen results, we were able to identify with TIM analysis the points of survival failure in the DIPG cell lines. These data are generated to define which targets best explain the drug sensitivity in the cells provided these targets are expressed. The identification of such points of failure in these DIPG cell lines is one prerequisite to select the most relevant combinations of targets to hit with specific agents. These results confirm that CDKs and histone deacetylases would be the most promising targets. The Ensemble prediction analysis showed that drug target profiles and drug target profiles integrated with gene expression data are better predictors of drug sensitivity as compared to drug target profiles integrated with mutation data or individual gene expression and mutation data. Thus, we considered TIM analysis based on combination of drug target profiles and gene expression information. These lines of evidence and predictive modeling converged to highlight panobinostat, a multi-HDAC inhibitor, as a particularly promising therapeutic agent. Indeed, *in vivo* testing of panobinostat administered in a DIPG orthotopic xenograft model by convection enhanced delivery (CED) demonstrated therapeutic efficacy and elucidates one strategy for immediate translation of the findings.

Whole exome sequencing of 17 DIPG tumors identified expected genomic aberrations such as the *H3F3A* mutation (*21, 22*) and *TP53* mutation. Overall, the mutational landscape was relatively quiet. The significance of the recurrent gain of chromosome 1q, as reported here and previously (*18, 19*) remains to be determined. Other investigators have associated recurrent gains of 1q with higher proliferative activity and poor prognosis in pediatric glioma (*35*). We report recurrent mutations in *ACVR1*, a TGFβ superfamily receptor involved in BMP signaling (Taylor et al, *in press*), as well as an instance of focal amplification of this gene and two cases of strongly up-regulated gene expression without underlying genomic aberration. Taken together, the

data suggest that ACVR1 signaling is dysregulated in a larger group of DIPG cases than those harboring the mutation and may represent an important therapeutic target.

We also discovered a previously un-described recurrent amplification in the neurotrophin receptor *NTRK1* (also known as TrkA, which binds nerve growth factor and (to a lesser extent) neurotrophin 3 and signals to the MAPK pathway). *NTRK1* thus emerged as an intriguing potential target. Activation of TrkA classically results in neuronal differentiation and survival. Dysregulation of TrkA signaling is implicated in other cancers of childhood, such as neuroblastoma (*36, 37*). Intriguingly, HDAC inhibition with panobinostat results in strongly increased expression of VGF, which is up-regulated by TrkA signaling. The functional role of TrkA signaling and *NTRK1* amplification in DIPG pathobiology remains an open question to be further explored.

Key caveats should be kept in mind. The drug screen used focused on agents presently in clinical trials in children to facilitate rapid translation of the findings. It is not, however, an exhaustive list of agents, and future screening efforts may elucidate additional useful drugs. The series of tumors from which the panel of DIPG cultures were established do not exhibit amplification of *PDGFRA* or *MET*, and so do not represent the fraction of DIPG tumors that do express these genomic aberrations (*18, 19*). However, the high percentage of H3K27M mutant cell lines shows that our models preserve reasonable fidelity to the scope of primary tumors. Neurosphere cultures enrich for the self-renewing, tumor-initiating cellular subpopulation. By contrast, DIPG is quite heterogeneous (*19*), with multiple subpopulations of cells that may need to be accounted for in designing a therapeutic strategy. The neurosphere culture system is serum-free, and so does not account for the degree to which a given drug may be protein-bound *in vivo*. However, this study also included cell lines grown as a monolayer in the presence of serum; since they were derived from biopsies performed at diagnosis they may reflect earlier stages of the disease than the cell lines derived from autopsies but also may be more heterogeneous in terms of cell content. Consensus sensitivity of drugs in both culture systems adds to the robustness of the results. Finally, *in vitro* systems do not model the cellular complexity of the tumor's microenvironment in the pons and so does not screen for drugs that target key microenvironmental interactions.

The next steps in translating these findings in the clinic will depend critically on the degree to which the most promising agents can reach the pons when delivered

systemically. Drug delivery is a major challenge in the treatment of DIPG. While the chemical screen data are presented in terms of clinically achievable serum concentrations, the concentration of drug that penetrates the blood-brain barrier of the pons is likely to be considerably less, even if radiotherapy enhances drug delivery to the brain tumor by disrupting the blood-brain-barrier itself (reviewed in van Vulpen *et al* (*38*)). Direct measurement of the amount of drug that penetrates the pons in experimental models is needed before use in a clinical trial of systemic drug delivery. Alternative strategies for drug delivery, such as direct intratumoral infusion by convection enhanced delivery (CED) (*39*) or blood brain barrier disruption strategies (*e.g.*, with inhibitors of efflux pumps such as elacridar (*40*)) may need to be part of a clinically efficacious treatment strategy. Indeed, a clinical trial designed to demonstrate feasibility of CED for use in DIPG is presently completing (clinical trials.gov ID NCT01502917) to address this very problem. The present study highlights agents that may be useful to administer using this neurosurgical technique, and demonstrates *in vivo* efficacy of panobinostat delivered by CED.

In conclusion, the data presented here support the concept that DIPG is a disease likely resulting from a broadly-reprogrammed epigenetic landscape. Targeting the dysfunctional epigenetic landscape of DIPG in combination with other agents will be essential. The integrated chemical and genomic data presented here facilitates the next steps towards development of an effective treatment combination for this devastating disease.

Materials and Methods

Chemical screens

A panel of 60-drugs (Supplementary Table 1) was developed for screening drug sensitivity of DIPG cells; the majority of these compounds are in clinical trials currently. Each compound was plated in four concentrations (10 μM, 1 μM, 100 nM, 10 nM) in triplicate in 384-well format. Early passage cells cultured from autopsy or biopsy tissue were plated at a density of [2,500] cells per well and incubated at 37C with humidified 5% CO_2 for three days. Cell viability was determined by the CellTiterGlo luminescent assay (cat #G7572, Promega, WI) per manufacturer's instructions and measured with the IVIS Lumina II imaging system. IC_{50} values were determined by a nonlinear best-fit method.

Drug efficacy in 9 cell lines were also screened simultaneously with the INCUCYTE™ Kinetic Imaging System (Essen Bioscience, Ann Arbor, MI). Briefly, it is an automated microscope system for kinetic, real time live content imaging inside the incubator. Confluence readouts algorithms are used to monitor growth and cell death continuously on the pictures taken at regular intervals (*e.g.* every 4 hours over a 72h period).

DIPG orthotopic xenograft and *in vivo* testing of panobinostat by CED

DIPG pontine xenografts were generated as previously described (*15*). Briefly, a single cell suspension was made of SU-DIPG VI neurospheres and 100,000 cells (50, 000 cells/ul, 2 μl) were stereotactically injected into the fourth ventricle/pons of NOD-SCID-IL2 gamma chain-deficient cold-anesthetized postnatal day 2 mouse pups by stereotactic injection through a 31 gauge burr hole (stereotactic coordinates: 3 mm posterior to lambda suture and 3 mm deep.)

CED was performed two months post-xenograft using a 31 G Hamilton with a 27 G needle threaded on the outside in isofluorane-anesthetized animals (*41*). (The inside needle is 1 mm longer than the outside needle in order to create the convection effects.) Infusion was performed using a digital pump set at a rate of 0.4 μl/min. Five μl of 2 μM panobinostat was delivered over a period of 12.5 min. Stereotactic coordinates (from surface of brain) used were from lambda AP -0.8mm, lateral 1 mm and 5 mm deep. Controls received vehicle (DMSO diluted in 5% dextrose). All animal procedures were performed with institutional approval and adhered to the NIH guide for the care and use of laboratory animals. *In vivo* bioluminescent imaging was performed prior to CED of panobinostat or vehicle, and again 7 days later, using an IVIS imaging system (Xenogen) under isofluorane anesthesia.

TIM predictive algorithm to identify drug combination for therapeutic intervention

The TIM analysis was based on the approach in (*30*). Further details on the TIM and ensemble analysis are included in the supplementary methods section.

References and Notes:

References

1. C. C. B. T. R. o. t. U. States), CBTRUS Statistical Report: Primary Brain and Central Nervous System Tumors Diagnosed in the United States in 2004 - 2006. . (2010).
2. S. S. Donaldson, F. Laningham, P. G. Fisher, Advances toward an understanding of brainstem gliomas. *J Clin Oncol* **24**, 1266 (Mar 10, 2006).
3. I. A. Langmoen, T. Lundar, I. Storm-Mathisen, S. O. Lie, K. H. Hovind, Management of pediatric pontine gliomas. *Childs Nerv Syst* **7**, 13 (Feb, 1991).
4. R. J. Packer *et al.*, Hyperfractionated radiotherapy for children with brainstem gliomas: a pilot study using 7,200 cGy. *Ann Neurol* **27**, 167 (Feb, 1990).
5. D. Hargrave, U. Bartels, E. Bouffet, Diffuse brainstem glioma in children: critical review of clinical trials. *Lancet Oncol* **7**, 241 (Mar, 2006).
6. M. H. Jansen, D. G. van Vuurden, W. P. Vandertop, G. J. Kaspers, Diffuse intrinsic pontine gliomas: a systematic update on clinical trials and biology. *Cancer treatment reviews* **38**, 27 (Feb, 2012).
7. M. T. Jennings *et al.*, Preradiation chemotherapy in primary high-risk brainstem tumors: phase II study CCG-9941 of the Children's Cancer Group. *J Clin Oncol* **20**, 3431 (Aug 15, 2002).
8. J. L. Finlay *et al.*, High-dose multi-agent chemotherapy followed by bone marrow 'rescue' for malignant astrocytomas of childhood and adolescence. *J Neurooncol* **9**, 239 (Dec, 1990).
9. E. Bouffet *et al.*, Radiotherapy followed by high dose busulfan and thiotepa: a prospective assessment of high dose chemotherapy in children with diffuse pontine gliomas. *Cancer* **88**, 685 (Feb 1, 2000).
10. I. J. Dunkel, B. O'Malley, J. L. Finlay, Is there a role for high-dose chemotherapy with stem cell rescue for brain stem tumors of childhood? *Pediatr Neurosurg* **24**, 263 (1996).
11. K. J. Cohen *et al.*, Temozolomide in the treatment of children with newly diagnosed diffuse intrinsic pontine gliomas: a report from the Children's Oncology Group. *Neuro Oncol* **13**, 410 (Apr, 2011).
12. R. Jalali *et al.*, Prospective evaluation of radiotherapy with concurrent and adjuvant temozolomide in children with newly diagnosed diffuse intrinsic pontine glioma. *Int J Radiat Oncol Biol Phys* **77**, 113 (May 1, 2010).
13. P. G. Fisher *et al.*, A clinicopathologic reappraisal of brain stem tumor classification. Identification of pilocystic astrocytoma and fibrillary astrocytoma as distinct entities. *Cancer* **89**, 1569 (Oct 1, 2000).
14. A. Broniscer *et al.*, Prospective collection of tissue samples at autopsy in children with diffuse intrinsic pontine glioma. *Cancer* **116**, 4632 (Oct 1, 2010).
15. M. Monje *et al.*, Hedgehog-responsive candidate cell of origin for diffuse intrinsic pontine glioma. *Proc Natl Acad Sci U S A* **108**, 4453 (Mar 15, 2011).
16. V. Caretti *et al.*, Implementation of a multi-institutional diffuse intrinsic pontine glioma autopsy protocol and characterization of a primary cell culture. *Neuropathology and applied neurobiology* **39**, 426 (Jun, 2013).
17. J. Grill *et al.*, Critical oncogenic mutations in newly diagnosed pediatric diffuse intrinsic pontine glioma. *Pediatr Blood Cancer* **58**, 489 (Apr, 2012).

18. M. Zarghooni *et al.*, Whole-genome profiling of pediatric diffuse intrinsic pontine gliomas highlights platelet-derived growth factor receptor alpha and poly (ADP-ribose) polymerase as potential therapeutic targets. *J Clin Oncol* **28**, 1337 (Mar 10, 2010).
19. B. S. Paugh *et al.*, Genome-wide analyses identify recurrent amplifications of receptor tyrosine kinases and cell-cycle regulatory genes in diffuse intrinsic pontine glioma. *J Clin Oncol* **29**, 3999 (Oct 20, 2011).
20. S. Puget *et al.*, Mesenchymal transition and PDGFRA amplification/mutation are key distinct oncogenic events in pediatric diffuse intrinsic pontine gliomas. *PLoS One* **7**, e30313 (2012).
21. G. Wu *et al.*, Somatic histone H3 alterations in pediatric diffuse intrinsic pontine gliomas and non-brainstem glioblastomas. *Nat Genet* **44**, 251 (Mar, 2012).
22. D. A. Khuong-Quang *et al.*, K27M mutation in histone H3.3 defines clinically and biologically distinct subgroups of pediatric diffuse intrinsic pontine gliomas. *Acta Neuropathol* **124**, 439 (Sep, 2012).
23. P. W. Lewis *et al.*, Inhibition of PRC2 activity by a gain-of-function H3 mutation found in pediatric glioblastoma. *Science* **340**, 857 (May 17, 2013).
24. S. Bender *et al.*, Reduced H3K27me3 and DNA Hypomethylation Are Major Drivers of Gene Expression in K27M Mutant Pediatric High-Grade Gliomas. *Cancer Cell* **24**, 660 (Nov 11, 2013).
25. M. S. Carro *et al.*, The transcriptional network for mesenchymal transformation of brain tumours. *Nature* **463**, 318 (Jan 21, 2010).
26. J. D. Cahoy *et al.*, A transcriptome database for astrocytes, neurons, and oligodendrocytes: a new resource for understanding brain development and function. *J Neurosci* **28**, 264 (Jan 2, 2008).
27. D. J. Wong *et al.*, Module map of stem cell genes guides creation of epithelial cancer stem cells. *Cell Stem Cell* **2**, 333 (Apr 10, 2008).
28. B. Bhattacharya *et al.*, Gene expression in human embryonic stem cell lines: unique molecular signature. *Blood* **103**, 2956 (Apr 15, 2004).
29. R. Pal, N. Berlow, A kinase inhibition map approach for tumor sensitivity prediction and combination therapy design for targeted drugs. *Pacific Symposium on Biocomputing. Pacific Symposium on Biocomputing*, 351 (2012).
30. N. Berlow *et al.*, A new approach for prediction of tumor sensitivity to targeted drugs based on functional data. *BMC bioinformatics* **14**, 239 (2013).
31. D. W. Parsons *et al.*, The genetic landscape of the childhood cancer medulloblastoma. *Science* **331**, 435 (Jan 28, 2011).
32. M. Sausen *et al.*, Integrated genomic analyses identify ARID1A and ARID1B alterations in the childhood cancer neuroblastoma. *Nat Genet* **45**, 12 (Jan, 2013).
33. K. M. Chan *et al.*, The histone H3.3K27M mutation in pediatric glioma reprograms H3K27 methylation and gene expression. *Genes Dev* **27**, 985 (May 1, 2013).
34. B. P. Fox, R. P. Kandpal, EphB6 receptor significantly alters invasiveness and other phenotypic characteristics of human breast carcinoma cells. *Oncogene* **28**, 1706 (Apr 9, 2009).
35. T. Miwa *et al.*, Single-copy gain of chromosome 1q is a negative prognostic marker in pediatric nonependymal, nonpilocytic gliomas. *Neurosurgery* **68**, 206 (Jan, 2011).
36. L. Harel *et al.*, CCM2 mediates death signaling by the TrkA receptor tyrosine kinase. *Neuron* **63**, 585 (Sep 10, 2009).

37. J. E. Light *et al.*, Clinical significance of NTRK family gene expression in neuroblastomas. *Pediatr Blood Cancer* **59**, 226 (Aug, 2012).
38. M. van Vulpen, H. B. Kal, M. J. Taphoorn, S. Y. El-Sharouni, Changes in blood-brain barrier permeability induced by radiotherapy: implications for timing of chemotherapy? (Review). *Oncology reports* **9**, 683 (Jul-Aug, 2002).
39. R. C. Anderson *et al.*, Convection-enhanced delivery of topotecan into diffuse intrinsic brainstem tumors in children. *Journal of neurosurgery. Pediatrics* **11**, 289 (Mar, 2013).
40. J. S. Lagas *et al.*, Brain accumulation of dasatinib is restricted by P-glycoprotein (ABCB1) and breast cancer resistance protein (ABCG2) and can be enhanced by elacridar treatment. *Clin Cancer Res* **15**, 2344 (Apr 1, 2009).
41. V. Caretti, VU University Medical Center (2012).
42. C. S. Grasso *et al.*, The mutational landscape of lethal castration-resistant prostate cancer. *Nature* **487**, 239 (Jul 12, 2012).
43. B. Langmead, C. Trapnell, M. Pop, S. L. Salzberg, Ultrafast and memory-efficient alignment of short DNA sequences to the human genome. *Genome biology* **10**, R25 (2009).
44. S. B. Ng *et al.*, Targeted capture and massively parallel sequencing of 12 human exomes. *Nature* **461**, 272 (Sep 10, 2009).
45. R. J. Lonigro *et al.*, Detection of somatic copy number alterations in cancer using targeted exome capture sequencing. *Neoplasia* **13**, 1019 (Nov, 2011).
46. A. Mortazavi, B. A. Williams, K. McCue, L. Schaeffer, B. Wold, Mapping and quantifying mammalian transcriptomes by RNA-Seq. *Nature methods* **5**, 621 (Jul, 2008).
47. L. Breiman, Random forests. *Machine Learning* **45**, 5 (2001).
48. Q. a. P. Wan, R, An ensemble based top performing approach for NCI-DREAM drug sensitivity prediction challenge. *PLOS ONE*, (in press).
49. I. F. Martins, A. L. Teixeira, L. Pinheiro, A. O. Falcao, A Bayesian approach to in silico blood-brain barrier penetration modeling. *Journal of chemical information and modeling* **52**, 1686 (Jun 25, 2012).

Acknowledgments: We thank the many patients and families who selflessly contributed to this study through tissue donations from surgery or autopsy and Amar Gajjar, for his guidance and vision throughout this study. We also thank Darren Hargrave, James Olsen and Sarah Leary for selection of V.2 chemical screen agents. We are grateful for the critical questions and comments by Simone Nsouli. We also acknowledge important comments by other DIPG Preclinical Consortium member Oren Becher.

Funding: Supported by the Children's Oncology Group (COG) CNS Committee, The DIPG Collaborative (The Cure Starts Now Foundation, Reflections of Grace Foundation, Smiles for Sophie Foundation, Cancer-Free Kids Foundation, Carly's Crusade Foundation, Jeffrey Thomas Hayden Foundation, Soar with Grace Foundation), Accelerate Brain Cancer Cures Foundation (ABC^2), The Lyla Nsouli Foundation, CureSearch for Childhood Cancer, The Team Julian Foundation and the COG Chair's Grant (5UOCA098543). Additional funding support was provided by K08NS070926 (to MM), Alex's Lemonade

Stand Foundation (to MM), McKenna Claire Foundation (to MM), Connor Johnson Memorial Fund (to MM), Dylan Jewett Memorial Fund (to MM), Dylan Frick Memorial Fund (to MM), Abigail Jensen Memorial Fund (to MM), Zoey Ganesh Memorial Fund (to MM), Wayland Villars Memorial Fund (to MM), Virginia & D.K. Ludwig Fund for Cancer Research (to MM), Etoile de Martin (to JG and NT), Foundation TIGRE and Le Defi de Fortunee (to JG), Scott Carter Foundation (to NB), Semmy Foundation (to DVV, EH), Department of Defense (to XL).

Author contributions:
Participated in the design and/or interpretation of the reported experiments or results.
CK, MM, MF, AG, CG, KEW, DVV, RP, CG
Participated in the acquisition and/or analysis of data. JA, EH, LL, YT, AP, SC, PJW, MHC, LD, LLD, NT, MM, KEW, RP, NEB, DVV, LED, JA, CK, CG, MQ, MAD.
Participated in drafting and/or revising the manuscript. MM, CG, CK, JG, MAD, LL, RP, NEB
Was primarily responsible for a particular, specialized role in the research, e.g. statistical
analysis, crystallography, preparation of cell lines; please briefly state which.
Extracted and purified RNA from the normal brain and tumor samples (JA, YT)
Computational analysis (RP, NEB)
Developed and generated chemical screening plates (EH)
Provided administrative, technical or supervisory support.

Competing interests: The Authors have no competing interests to report.

Data and materials availability:

All cells lines described here can be obtained through an MTA with the institution at which it was created (Stanford University, Johns Hopkins University, Oregon Health & Science University, Institut Gustave Russay, VU Medical Center or Texas Children's Cancer Center).

All sequence data will be made available through dbGAP.

Figures:

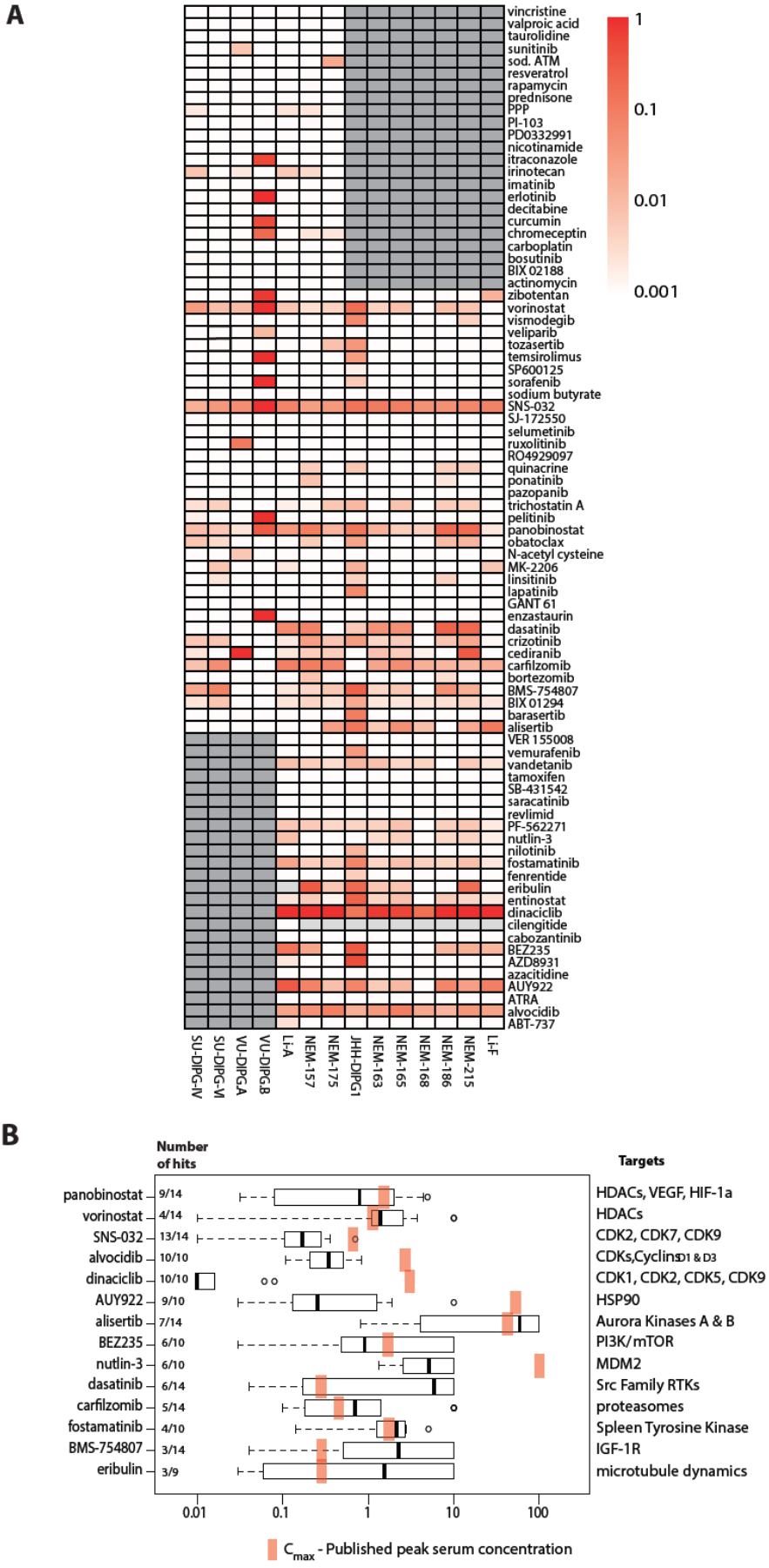
A
vincristine
valproic acid
taurolidine
sunitinib
sod. ATM
resveratrol
rapamycin
prednisone
PPP
PI-103
PD0332991
nicotinamide
itraconazole
irinotecan
imatinib
erlotinib
decitabine
curcumin
chromeceptin
carboplatin
bosutinib
BIX 02188
actinomycin
zibotentan
vorinostat
vismodegib
veliparib
tozasertib
temsirolimus
SP600125
sorafenib
sodium butyrate
SNS-032
SJ-172550
selumetinib
ruxolitinib
RO4929097
quinacrine
ponatinib
pazopanib
trichostatin A
pelitinib
panobinostat
obatoclax
N-acetyl cysteine
MK-2206
linsitinib
lapatinib
GANT 61
enzastaurin
dasatinib
crizotinib
cediranib
carfilzomib
bortezomib
BMS-754807
BIX 01294
barasertib
alisertib
VER 155008
vemurafenib
vandetanib
tamoxifen
SB-431542
saracatinib
revlimid
PF-562271
nutlin-3
nilotinib
fostamatinib
fenrentide
eribulin
entinostat
dinaciclib
cilengitide
cabozantinib
BEZ235
AZD8931
azacitidine
AUY922
ATRA
alvocidib
ABT-737
1
0.1
0.01
0.001
SU-DIPG-IV
SU-DIPG-M
VU-DIPG-A
VU-DIPG-B
Li-A
NEM-157
NEM-175
JHH-DIPG1
NEM-163
NEM-165
NEM-168
NEM-186
NEM-215
Li-F
B
Number of hits
Targets
panobinostat 9/14
vorinostat 4/14
SNS-032 13/14
alvocidib 10/10
dinaciclib 10/10
AUY922 9/10
alisertib 7/14
BEZ235 6/10
nutlin-3 6/10
dasatinib 6/14
carfilzomib 5/14
fostamatinib 4/10
BMS-754807 3/14
eribulin 3/9
HDACs, VEGF, HIF-1a
HDACs
CDK2, CDK7, CDK9
CDKs,CyclinsD1 & D3
CDK1, CDK2, CDK5, CDK9
HSP90
Aurora Kinases A & B
PI3K/mTOR
MDM2
Src Family RTKs
proteasomes
Spleen Tyrosine Kinase
IGF-1R
microtubule dynamics
0.01
0.1
1
10
100
Cmax - Published peak serum concentration

Figure 1. Chemical Screen A) Chemical screen of 14 DIPG cell cultures. Heatmap demonstrating DIPG cell line sensitivity to each of the 83 agents tested. The values shown are the absolute IC_{50} divided by the maximum dose. All drugs had a maximum dose of 10 μM except for vismodegib, sodium butyrate, pazopanib, alisertib, and vemurafenib, which had a maximum dose of 100 μM. Values are shown as gradations of red to white, with red representing submicromolar IC_{50} values, white indicating IC_{50} greater than the maximum dose for that drug (i.e. 10 μM or 100 μM), and pink showing the range in between. Grey boxes indicate those drugs not included in the screen for that cell line. Drug names are listed on the vertical axis, patient IDs listed on the horizontal axis. Recurrent "hits" are visualized as a row of red or pink and include CDK inhibitors such as SNS-032, dinaciclib and alvocidib and HDAC inhibitors such as panobinostat and vorinostat
B) Chemical screen 'hits' within the context of clinically-achievable serum drug levels. Box and whisker plot demonstrating the average absolute IC_{50} values ("box") +/- 1.5 standard deviation ("whiskers") for each of the top "hits", listed on the vertical axis, with concentration in μM on the horizontal axis. C_{max} (the peak serum concentration reported in the literature) for each drug is represented as a red bar. The number of cell lines responding to each agent (out of the number of cells lines tested for that agent) at an IC_{50} value less than that drug's C_{max} is indicated to the left of the plot. For example, if 9 of 14 cell lines responded to panobinostat with an $IC_{50} < C_{max,}$ that is indicated as 9/14. Only those drugs that were "hits" in three or more cell lines are shown.

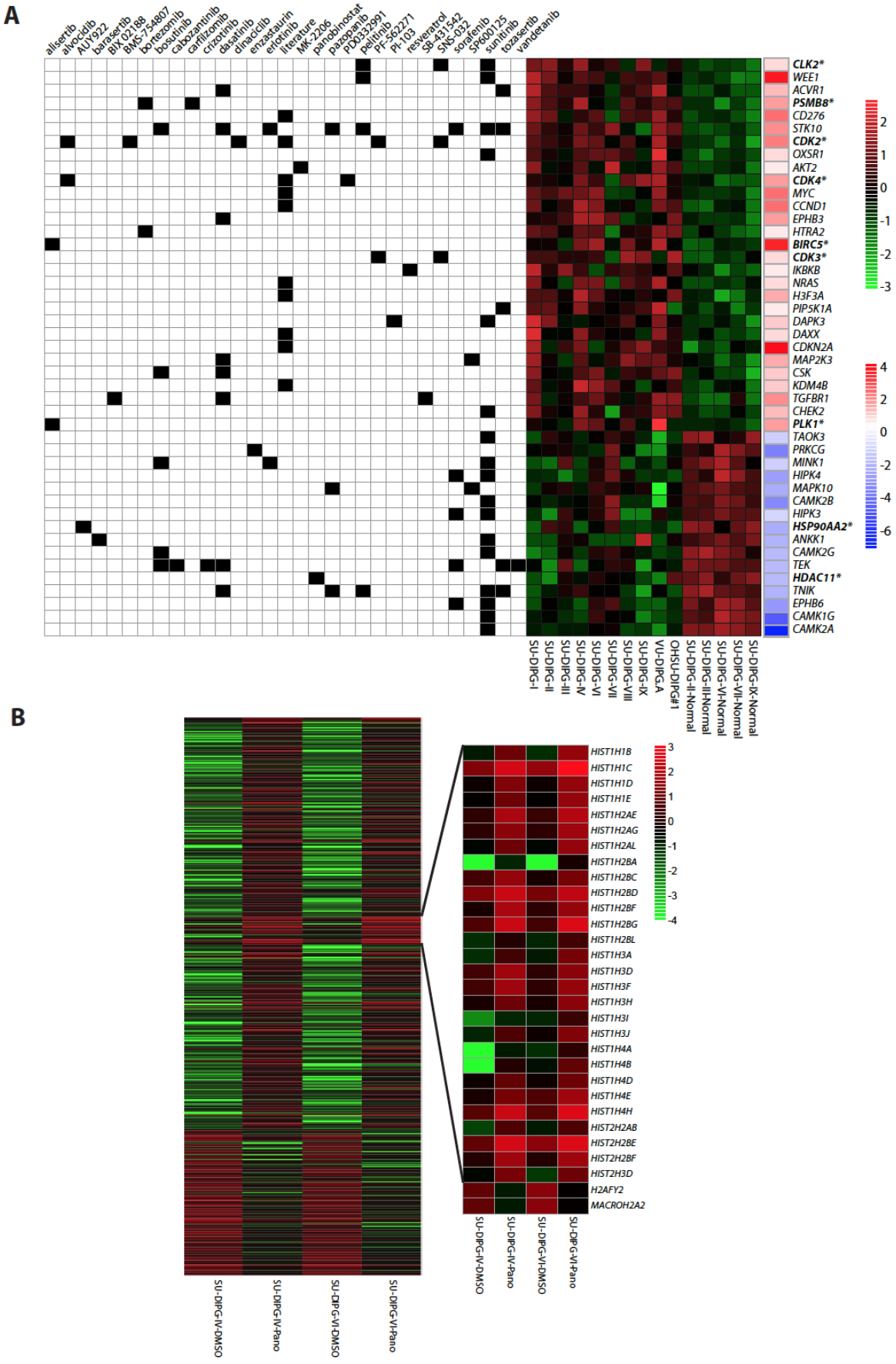
A
alisertib
alvocidib
AUY922
barasertib
BIX-02188
BMS-754807
bortezomib
bosutinib
cabozantinib
canfilzomib
crizotinib
dasatinib
dinaciclib
enzastaurin
erlotinib
literature
MK-2206
panobinostat
pazopanib
PD0332991
pelitinib
PF-562271
Ph-103
resveratrol
SB-431542
SNS-032
sorafenib
SP600125
sunitinib
tozasertib
vandetanib
CLK2*
WEE1
ACVR1
PSMB8*
CD276
STK10
CDK2*
OXSR1
AKT2
CDK4*
MYC
CCND1
EPHB3
HTRA2
BIRC5*
CDK3*
IKBKB
NRAS
H3F3A
PIP5K1A
DAPK3
DAXX
CDKN2A
MAP2K3
CSK
KDM4B
TGFBR1
CHEK2
PLK1*
TAOK3
PRKCG
MINK1
HIPK4
MAPK10
CAMK2B
HIPK3
HSP90AA2*
ANKK1
CAMK2G
TEK
HDAC11*
TNIK
EPHB6
CAMK1G
CAMK2A
SU-DIPG-I
SU-DIPG-II
SU-DIPG-III
SU-DIPG-IV
SU-DIPG-VI
SU-DIPG-VII
SU-DIPG-VIII
SU-DIPG-IX
VU-DIPG.A
OHSU-DIPG#1
SU-DIPG-II-Normal
SU-DIPG-VI-Normal
SU-DIPG-VII-Normal
SU-DIPG-IX-Normal
2
1
0
-1
-2
-3
4
2
0
-2
-4
-6
B
HIST1H1B
HIST1H1C
HIST1H1D
HIST1H1E
HIST1H2AE
HIST1H2AG
HIST1H2AL
HIST1H2BA
HIST1H2BC
HIST1H2BD
HIST1H2BF
HIST1H2BG
HIST1H2BL
HIST1H3A
HIST1H3D
HIST1H3F
HIST1H3H
HIST1H3I
HIST1H3J
HIST1H4A
HIST1H4B
HIST1H4D
HIST1H4E
HIST1H4H
HIST2H2AB
HIST2H2BE
HIST2H2BF
HIST2H3D
H2AFY2
MACROH2A2
3
2
1
0
-1
-2
-3
-4
SU-DIPG-IV-DMSO
SU-DIPG-IV-Pano
SU-DIPG-VI-DMSO
SU-DIPG-VI-Pano
SU-DIPG-IV-DMSO
SU-DIPG-IV-Pano
SU-DIPG-VI-DMSO
SU-DIPG-VI-Pano

Figure 2. Gene Expression biomarker results in the context of the chemical screen. A) Heatmap of gene expression data illustrating those genes with statistically significant differential expression in primary tumor samples compared to normal brain tissue. Gene names are on the vertical axis and tumor sample names are on the horizontal axis. Differentially regulated genes that are targets of the top drug "hits" are listed. B) Heatmap of DIPG cell lines derived from SU-DIPG-IV and SU-DIPG-VI before and after treatment with panobinostat (1 μM for 48 hours). Genes with greater than 10-fold change in both cell lines are shown with histone genes shown in a separate heatmap.

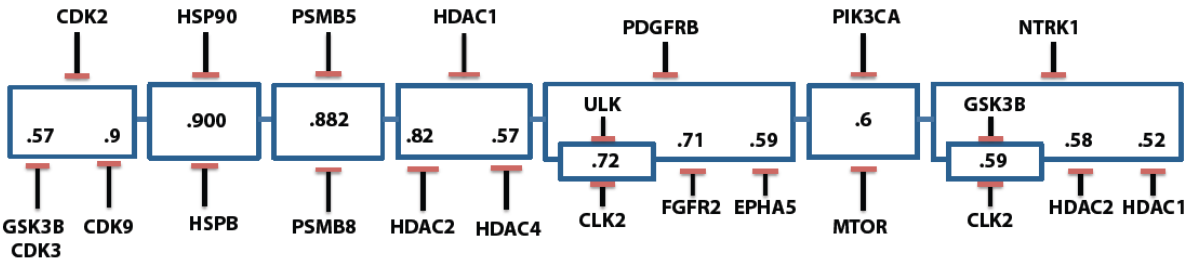

Figure 3. Target Inhibitor Map circuit for the overall set of DIPG tumor sample drug responses. The circuit was derived from the complete set of 13 DIPG RNAseq-matched drug screen responses, and is a model for a general DIPG sample. Here, each block represents potential effective target inhibition combinations, *e.g.* inhibiting both CDK2 and GSK3B would result in an effective treatment, or inhibiting HDAC1 and HDAC4 would be an effective treatment. Shown here are the seven most relevant blocks. The scores under each block represent the predicted efficacy of the block in terms of the expected sensitivity following inhibition of the block targets.

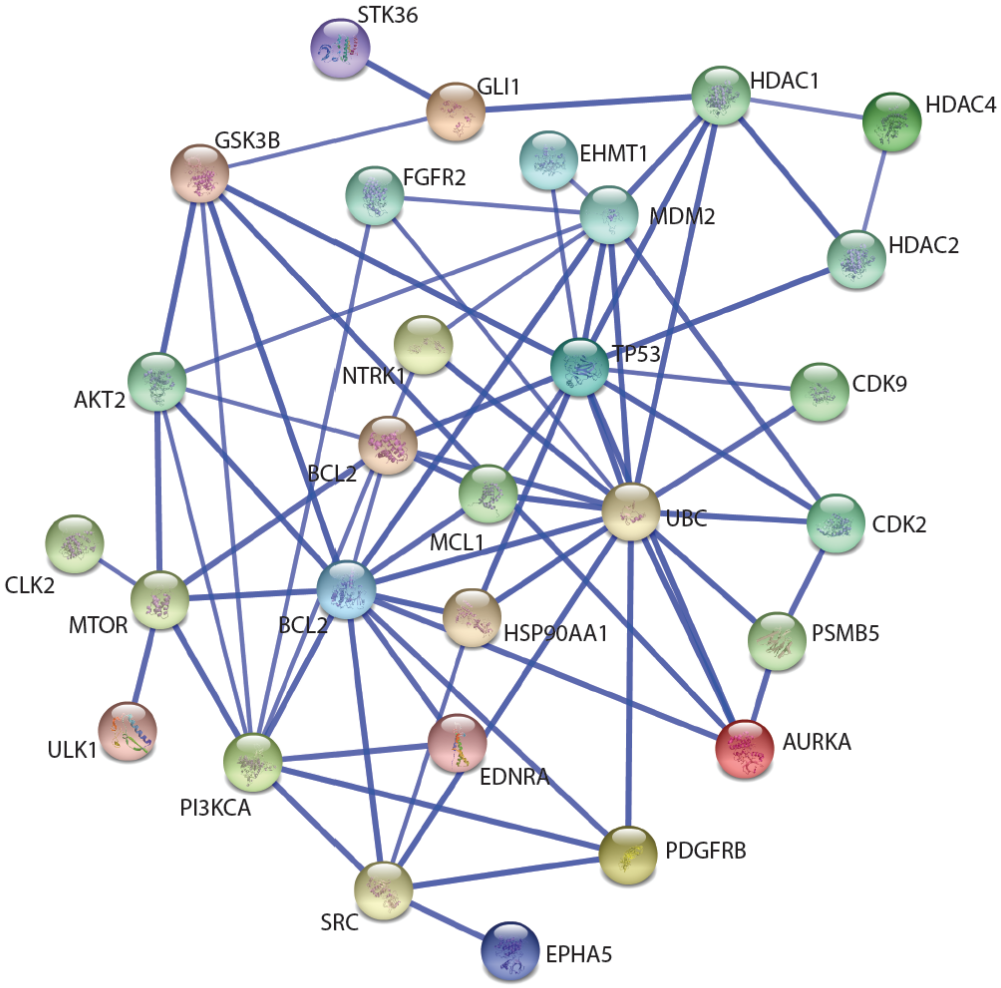

Figure 4. Protein-protein interaction map for the targets inferred from the TIM analysis generated using STRING database considering only the protein interactions derived from experimental data. The strength of the edges is determined by the confidence in the edge. The targets are connected to each other except a small number of targets without reported experimentally observed interactions (PSMB8, CMA1, ULK1, CLK3 and HSBAP1). The network is focused around TP53, which is highly mutated in many cancers, and has members of the mTOR, Cell Cycle and HDAC pathways. Additionally the Hedgehog pathway is present, consistent with prior research in DIPG. The network is highly enriched based on genomic background per String-DB enrichment analysis (67 interactions observed vs. 14.2 expected interactions).

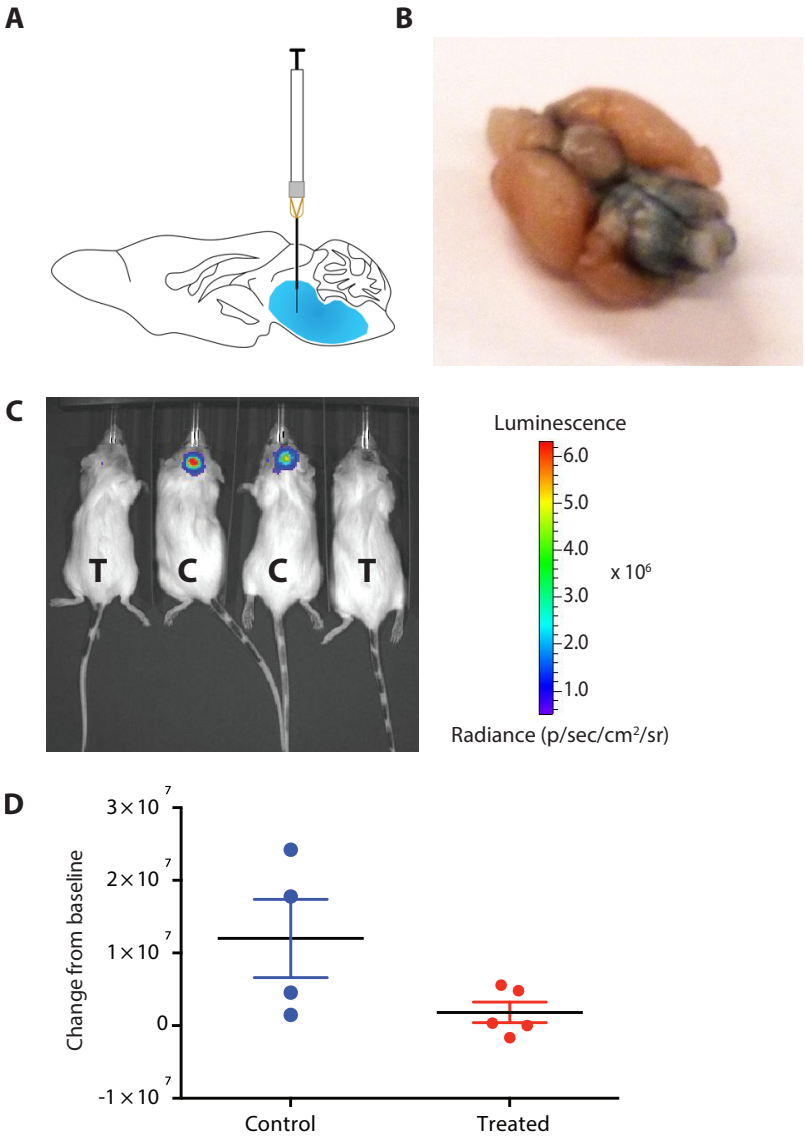

Figure 5. Convection enhanced delivery of panobinostat inhibits tumor growth in a DIPG orthotopic xenograft

A) Schematic illustrating convection enhanced delivery strategy to infuse drug into brainstem. Blue illustrates approximate distribution of the infused solution.

B) Distribution of infusate illustrated by delivering blue dye to the brainstem by CED. Ventral side of a mouse brain is shown immediately following CED delivery of Comassie Blue dye.

C) *in vivo* bioluminescent imaging of DIPG xenografts 7 days following CED delivery of panobinostat (T = treated with panobinostat; 5 µl of 2 µM panobinostat infused over 12.5 min on Day 0) or vehicle control (C = control). The heat map superimposed over the mouse head represents the degree of photon emission by DIPG cells expressing firefly luciferase.

D) *in vivo* DIPG xenograft tumor growth as measured by change in bioluminescent photon emission over the seven days following CED delivery of panobinostat (Panobinostat group, red squares) or vehicle control (Control group, blue circles). Data points represent the difference in maximum photon flux between Day 0 and Day 7 for each mouse; each data point represents one mouse. *N*= 4 control, 5 treatment mice. Error bars, s.e.m. $P < 0.05$ (Student's t test

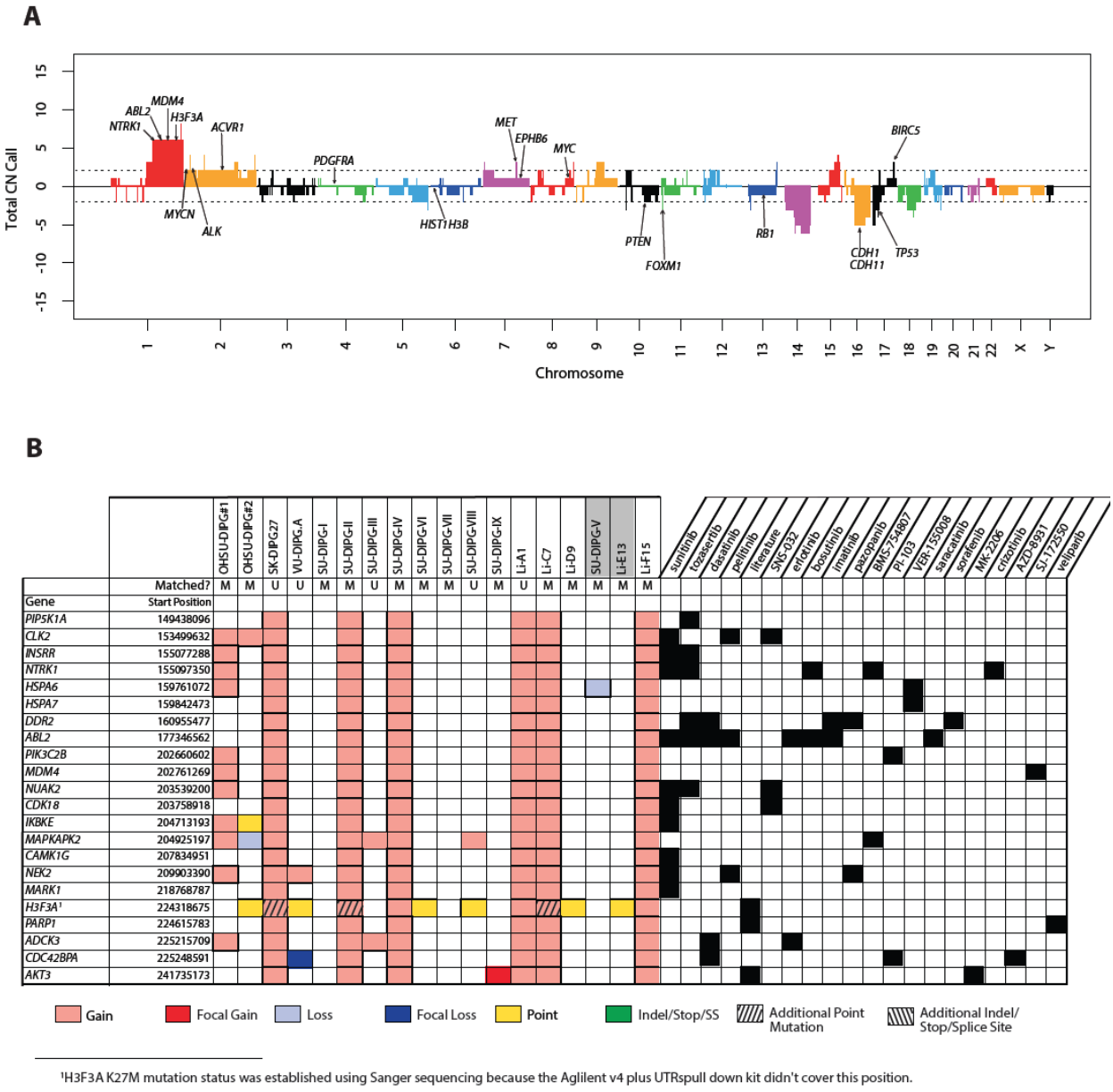

¹H3F3A K27M mutation status was established using Sanger sequencing because the Aglilent v4 plus UTRspull down kit didn't cover this position.

Figure 6. Genome wide copy number analysis to identify recurrent abberrations containing drug targets. Exomes of 17 DIPG primary tumors were sequenced to identify somatic mutations and copy number alterations. A) Genome wide copy number analysis of each sample was performed. For all genes, the sum of all somatic copy number (+/-1 for genes gained or lost by 30% and +/-2 for genes gained or lost by 60%) across all samples is shown. B) Heatmap of high-level copy number alterations and non-synonymous mutations, along with drug targeting genes. The genes have been restricted to the ones located on the highly recurrent 1q gain region that are targets of drugs tried in the drug screen.

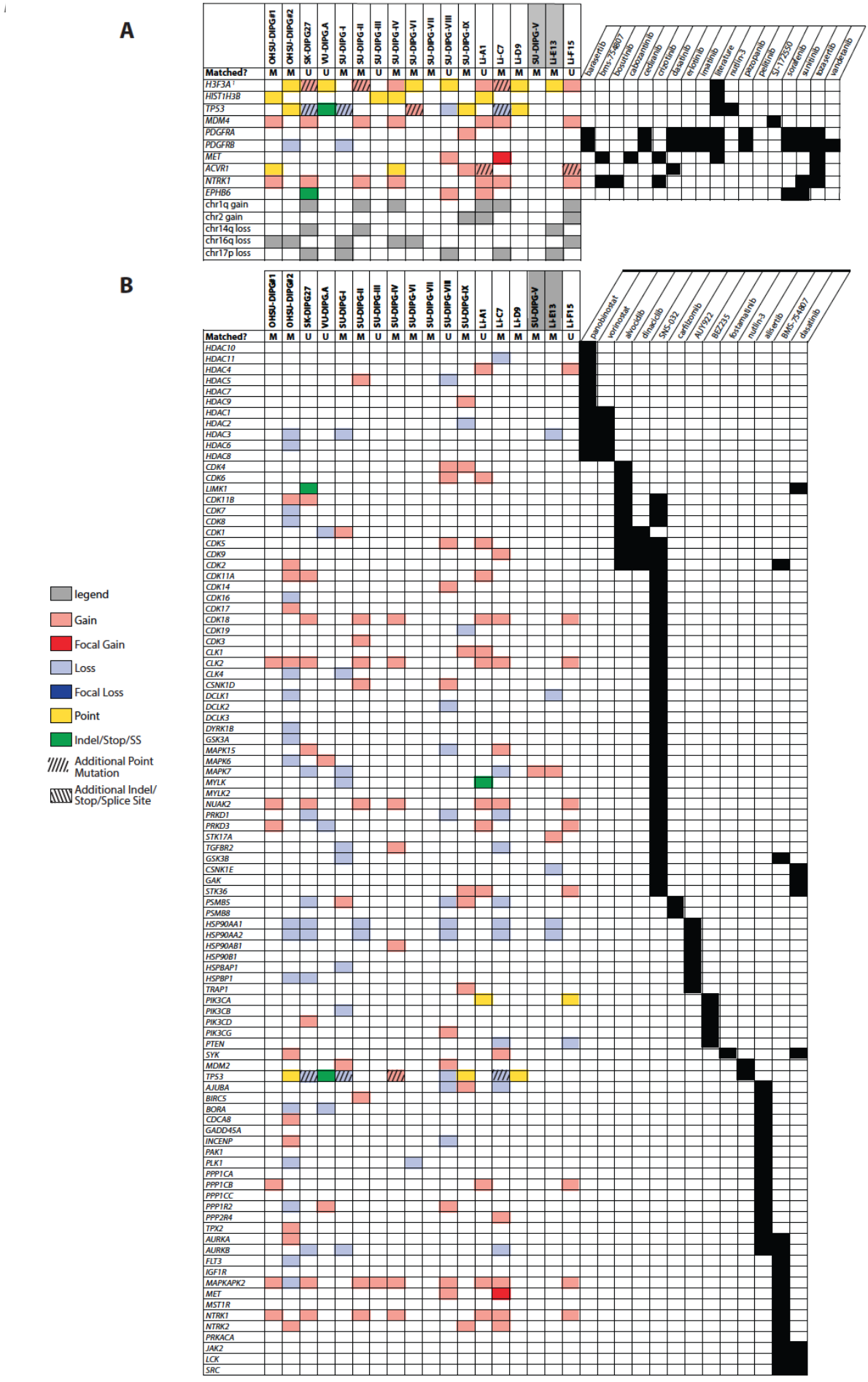
A
OHSU-DIPG#1
OHSU-DIPG#2
SK-DIPG27
VU-DIPG.A
SU-DIPG-I
SU-DIPG-II
SU-DIPG-III
SU-DIPG-IV
SU-DIPG-VI
SU-DIPG-VII
SU-DIPG-VIII
SU-DIPG-IX
Li-A1
Li-C7
Li-D9
SU-DIPG-V
Li-E13
Li-F15
Matched?
M M U U M M U M M M U M U M M M M U
H3F3A
HIST1H3B
TP53
MDM4
PDGFRA
PDGFRB
MET
ACVR1
NTRK1
EPHB6
chr1q gain
chr2 gain
chr14q loss
chr16q loss
chr17p loss
tarasertib
bms-754807
bosutinib
calyculin-a
cediranib
crizotinib
dasatinib
erlotinib
imatinib
lifirafenib
nutlin-3
panobinostat
pelitinib
sj-172550
sorafenib
sunitinib
vorinostat
vandetanib
B
OHSU-DIPG#1
OHSU-DIPG#2
SK-DIPG27
VU-DIPG.A
SU-DIPG-I
SU-DIPG-II
SU-DIPG-III
SU-DIPG-IV
SU-DIPG-VI
SU-DIPG-VII
SU-DIPG-VIII
SU-DIPG-IX
Li-A1
Li-C7
Li-D9
SU-DIPG-V
Li-E13
Li-F15
Matched?
M M U U M M U M M M U M U M M M M U
HDAC10
HDAC11
HDAC4
HDAC5
HDAC7
HDAC9
HDAC1
HDAC2
HDAC3
HDAC6
HDAC8
CDK4
CDK6
LIMK1
CDK11B
CDK7
CDK8
CDK1
CDK5
CDK9
CDK2
CDK11A
CDK14
CDK16
CDK17
CDK18
CDK19
CDK3
CLK1
CLK2
CLK4
CSNK1D
DCLK1
DCLK2
DCLK3
DYRK1B
GSK3A
MAPK1S
MAPK6
MAPK7
MYLK
MYLK2
NUAK2
PRKD1
PRKD3
STK17A
TGFBR2
GSK3B
CSNK1E
GAK
STK36
PSMB5
PSMB8
HSP90AA1
HSP90AA2
HSP90AB1
HSP90B1
HSPBAP1
HSPBP1
TRAP1
PIK3CA
PIK3CB
PIK3CD
PIK3CG
PTEN
SYK
MDM2
TP53
AJUBA
BIRC5
BORA
CDCA8
GADD45A
INCENP
PAK1
PLK1
PPP1CA
PPP1CB
PPP1CC
PPP1R2
PPP2R4
TPX2
AURKA
AURKB
FLT3
IGF1R
MAPKAPK2
MET
MST1R
NTRK1
NTRK2
PRKACA
JAK2
LCK
SRC
panobinostat
vorinostat
alvocidib
dinaciclib
SNS-032
carfilzomib
AUY922
BEZ235
fostamatinib
nutlin-3
alk-in1b
BMS-754807
desatinib
legend
Gain
Focal Gain
Loss
Focal Loss
Point
Indel/Stop/SS
Additional Point Mutation
Additional Indel/ Stop/Splice Site

Figure 7. Integrated mutational landscape of DIPG drug target genes Exomes of 17 DIPG primary tumors were sequenced to identify somatic mutations and copy number alterations. Heatmaps of high-level copy number alterations and non-synonymous mutations in mutations targeted by drugs tried in the drug screen, along with the drugs targeting the genes. In A), the mutation landscape has been restricted to highly-recurrent aberrations, while in B), the mutation landscape has been restricted to genes targeted by top hits from the drug screen.

A

SAMPLE	LOC	PROTEIN	VARIANT/TOTAL TUMOR	VARIANT/TOTAL NORMAL
OHSU-DIPG#1	chr2:158330762C>T	p.G328E	20/25	1/38
LiF15	chr2:158330762C>T	p.G328E	33/53	Unmatched
LiF17-xeno	chr2:158330762C>T	p.G328E	12/19	Unmatched
LiF18-xeno	chr2:158330762C>T	p.G328E	7/15	Unmatched
LiA1	chr2:158330762C>T	p.G328E	28/50	Unmatched
LiA2	chr2:158330762C>T	p.G328E	16/37	Unmatched
SU-DIPG-IV	chr2:158330762C>A	p.G328V	15/38	0/18
4"	chr2:158330762C>A	p.G328V	25/54	0/18

Rows with the same grayscale are derived from the same parental tumor.

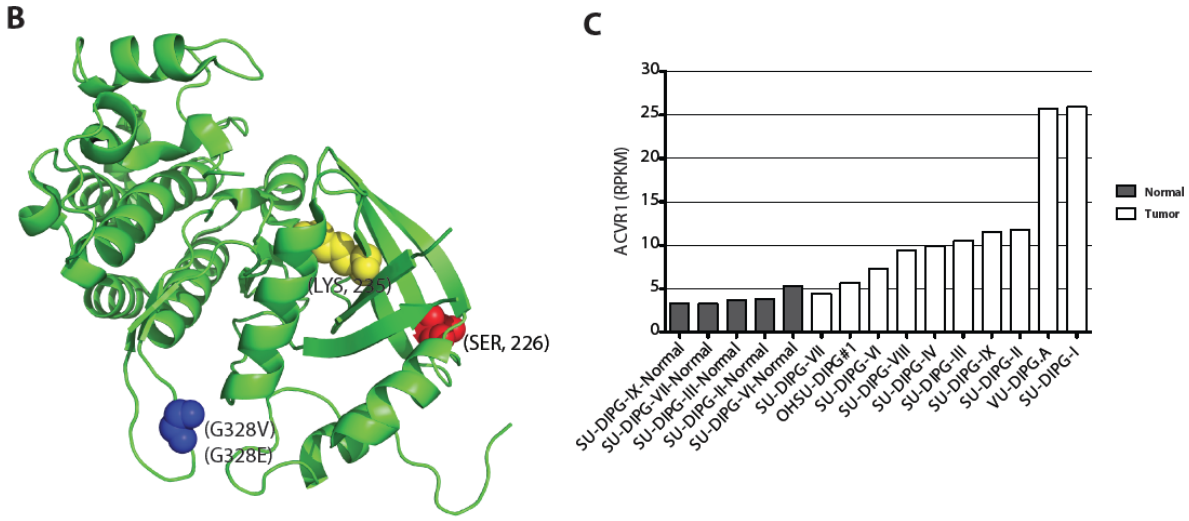

Figure 8. Integrated exome and transcriptome sequencing reveals recurrent dysregulation of ACVR1 A) Exomes of 17 DIPG primary tumors and 3 cell lines and 3 xenografts were sequenced to identify somatic mutations resulting in four recurrent ACVR1 mutations at G328, further confirmed by their presence in related samples. B) Residue 328 which that is mutated recurrently from G to V and G to E is shown in blue in the three dimensional ribbon structure of the serine/threonine kinase domain of ACVR1, in which the ATP binding residue is shown in yellow, the site of phosphorylation is shown in red. C) The gene expression in RPKM of ACVR1 is shown as a bar plot where white represents tumor tissue and grey represents normal tissue.

Supplementary Materials

Supplementary Data Set 1: RNA sequence data

Supplementary Materials:

Supplementary Methods
DNA and RNA sequencing:

Generation of exome-capture libraries

Exome libraries of matched pairs of tumor / normal genomic DNAs were generated using the Agilent SureSelect XT kit and Agilent Automation Systems NGS system per manufacturer's instructions. 1 ug of each genomic DNA was sheared using a Covaris E220 to a peak target size of 150 bp. Fragmented DNA was concentrated using AMPureXP beads (Beckman Coulter), and DNA ends were repaired using T4 DNA polymerase, Klenow polymerase, and T4 polynucleotide kinase. 3' A-tailing with exo-minus Klenow polymerase was followed by ligation of Agilent paired-end oligo adapters to the genomic DNA fragment. Ligated DNA was PCR amplified for 8 cycles and purified using AMPure XP beads and quantitated using the Quant-It BR kit (Invitrogen). 500 ng of sample libraries were hybridized to the Agilent biotinylated SureSelect v4 Exome + UTR Capture Library at 65°C for 72 hr following the manuufacturer's protocol. The targeted exon fragments were captured on Dynabeads MyOne Strepavidin T1 (Invitrogen), washed, eluted, and enriched by amplification with Agilent post-capture primer and an indexed reverse primer for multiplexing 12 additional cycles. After purification of the PCR products with AMPure XP beads, the quality and quantity of the resulting exome libraries were analyzed using an Agilent Bioanalyzer High Sensitivity chip.

Somatic point mutation identification by exome capture sequencing

The methodology described below is a minor modification of the approach described in (*42*). All captured DNA libraries were sequenced with the Illumina HiSeq in paired end mode, yielding 80 base pairs from the final library fragments. The reads that passed the chastity filter of Illumina BaseCall software were used for subsequent analysis. Matepairs were pooled and mapped as single reads to the reference human genome (NCBI build 36.1, hg18), excluding unordered sequence and alternate haplotypes, using Bowtie (*43*) keeping unique best hits, and allowing up to two mismatched bases per read. Likely PCR duplicates, defined as reads with equal match intervals on the reference genome, were removed; and individual basecalls with Phred quality less than Q20 were excluded. A mismatched base (SNV) was identified as a variant when 1) it

had at least six reads of support, 2) it constituted at least 10% of the coverage at that position, 3) it was observed on both strands, and 4) it fell within 50 bases of a region targeted for capture.

In matched samples (samples with matched normals), a variant was called somatic if 4) there was 8x coverage in the matched normal, 5) it did not occur in the matched normal sample in more than two reads and 2% of the coverage (or 4% of the coverage if the tumor variant fraction was at least 20%), and 6) if it had any support in the matched normal, it was not present in either dbSNP (v137) or the Exome Sequencing Project dataset (ESP6500).

In unmatched samples, a variant was called probable somatic if it affected the same codon as either a somatic point mutation observed in the matched samples or a somatic mutation from COSMIC (v66).

Finally, all somatic/probable somatic variants were screened against the full set of benign samples. Variants were removed from further consideration if they appeared in any benign sample with at least 3 reads and 10% of the coverage.

Identification of coding indels in exome capture data

The methodology for identifying indels in exome capture data was adapted from (*44*) with minor modifications. Reads for which Bowtie was unsuccessful in identifying an ungapped alignment were converted to fasta format and mapped to the target regions, padded by 200 bases on either side, with cross_match (v0.990329, http://www.phrap.org), using parameters –gap_ext -1 –bandwidth 10 –minmatch 20 –maxmatch 24. Output options were –tags –discrep_lists –alignments. Alignments with an indel were then filtered for those that: 1) had a score at least 40 more than the next best alignment, 2) mapped at least 75 bases of the read, and 3) had two or fewer substitutions in addition to the indel. Reads from filtered alignments that mapped to the negative strand were then reverse-complemented and, together with the rest of the filtered reads, remapped with cross-match using the same parameters (to reduce ambiguity in called indel positions due to different read orientations). After the second mapping, alignments were re-filtered using criteria 1-3. Reads that had redundant start sites were removed as likely PCR duplicates, after which the number of reads mapping to either the reference or the non-reference allele was counted for each. An indel was

identified as a variant when 1) it had at least six reads of support, 2) it constituted at least 10% of the coverage at that position, 3) it was observed on both strands, and 4) it fell within 50 bases of a region targeted for capture. Indels were reported with respect to genomic coordinates. For insertions, the position reported is the last base before the insertion. For deletions, the position reported is the first deleted base.

In matched samples, an indel was called somatic if 4) there was 8x coverage in the matched normal, 5) if it had any support in the matched normal, it was not present in either dbSNP (v137) or the Exome Sequencing Project dataset (ESP6500). In both matched and unmatched samples, all remaining indels were screened against the full set of benign samples. Variants were removed from further consideration if they appeared in any benign sample with at least 3 reads.

Annotation

We annotated the resulting somatic mutations using CCDS transcripts wherever possible. If no CCDS transcript was available, we use the coding regions of RefSeq transcripts. HUGO gene names were used.

Exome copy number analysis

Copy number aberrations were quantified and reported for each gene as the segmented normalized log2-transformed exon coverage ratios between each tumor sample and its matched normal as described in (*45*). For unmatched samples, we used the average coverage derived from the full set of benign samples as a "normal pool;" for chromosomes X and Y only, we formed separate normal pools from the XX and XY benign samples. We identified segments as focal if they contained ten or fewer CCDS gene annotations. To identify a gene as gained or lost we first considered the segmented data, requiring a copy number gain or loss of 30% (ratio >= 1.3 or <= 0.7) to call the gene as gained or lost. In addition, we considered the distribution of copy number estimates for each gene's individual exons. If the mean exonic copy number showed a gain or loss of at least 30% and deviated from the null hypothesis by at least 2.5 standard deviations, we called the gene as gained or lost.

For the total copy-number call over all tumor tissue samples (Figure 6), we counted each gain or loss of at least 60% as +/-2 on its respective segment, and each gain or loss of 30-60% as +/-1, and summed these contributions across all tumor tissue samples. In order to omit germline CNVs from the total, we looked at segmented exon

coverage ratios between the individual normal samples and the normal pool. Any segment that was gained or lost by 30% in at least two normal samples was flagged as a probable CNV, and was not included in the total copy-number sum

Generation of RNAseq libraries

RNAseq libraries for transcriptome analysis were prepared using the TruSeq RNA Sample Preparation Kit (Illumina) and Agilent Automation NGS system per manufacturers' instructions. Sample prep began with 1 µg of total RNA from each sample. Poly-A RNA was purified from the sample with oligo dT magnetic beads, and the poly(A) RNA was fragmented with divalent cations. Fragmented poly-A RNA was converted into cDNA through reverse transcription and were repaired using T4 DNA polymerase, Klenow polymerase, and T4 polynucleotide kinase. 3' A-tailing with exo-minus Klenow polymerase was followed by ligation of Illumina paired-end oligo adapters to the cDNA fragment. Ligated DNA was PCR amplified for 15 cycles and purified using AMPure XP beads. After purification of the PCR products with AMPure XP beads, the quality and quantity of the resulting transcriptome libraries were analyzed using an Agilent Bioanalyzer High Sensitivity chip.

Gene expression RNAseq outlier analysis

All transcriptome libraries were sequenced with the Illumina HiSeq in paired end mode. The reads that passed the chastity filter of Illumina BaseCall software were used for subsequent analysis. We trimmed all reads to 85-mers and aligned them to the reference human genome (NCBI build 36.1, hg18), plus a splice junction set including 84 bases on either side of the 2008 Illumina splice junction set, using Bowtie (*43*) in single read mode keeping unique best hits and allowing up to two mismatched bases. Mate pairs from paired end runs were pooled and treated as single reads.

Next, all of the exons for a single gene were concatenated to form a single "transcript" for that gene. Reads that mapped to the exons in the gene, as well as reads that mapped to the splice junctions, were remapped to the "transcript". We then walked the transcript and summed the coverage at each position, then divided the result by the transcript length times the number of reads in the sample, and then multiplied the result by one million. This method is a modified version of the one described in (*46*).

RNAseq of panobinostat-treated cultures

RNAseq was performed as above in SU-DIPG-IV and SU-DIPG-VI cell lines following exposure to 1 µM panobinostat (Selleck Chemicals) for 48 hours. Cells were then lysed and RNA extracted in TRIzol solution.

Post-panobinostat RNAseq data analysis: There was a good concordance for the ratio of panobinostat-treated to vehicle-treated cell gene expression and the distribution of RPKM values were similar in both cell lines and with the two conditions. In general, the variability in terms of ratio was low, usually below 1. We removed from the analyses genes with less than 100 reads in all the samples. We selected the 559 genes with a fold change superior to 10 and concordant in the two cell lines; 412 were up-regulated and 147 were down-regulated (Fig. 2 and Fig. S4). We then performed a Gene Ontology (GO) analysis on this list of genes (p-value<0.01 with a FDR correction <0.01):

Primary cell culture establishment & propagation

Stanford Cell Lines and primary tumor cell culture. Tumor tissue was harvested under sterile conditions in the autopsy suite, collected in serum-free DMEM/12 (Cellgro) and transported on ice to the laboratory. The tissue was then minced with a sterile No.10 scalpel and washed twice in HEPES-HBSS (HeHBSS) to remove debris. Minced tissue was then added to dissociation buffer (HeHBSS) with DNaseI (250U/ml) and collagenase type IV (1mg/ml). Minimal mechanical force was utilized and the cells were allowed to dissociate at 37C on a Nutator. The cells were then sequentially strained through a 100, 70 and 40 µM cell strainer and centrifuged and processed through a sucrose gradient. Dissociated cells were treated with ACK/RBC lysis buffer (0.15M NH_4Cl, 1.0mM $KHCO_3$ and 0.1mM Na_2-EDTA) and plated at subclonal density of 100 cells/ml, for neurosphere formation in Tumor Stem Media (TSM) consisting of Neurobasal(-A) (Invitrogen, Carlsbad, CA), B27(-A) (Invitrogen, Carlsbad, CA), human-bFGF (20ng/ml) (Shenandoah Biotech, Warwick, PA), human-EGF (20ng/ml) (Shenandoah, Biotech, Warwick, PA), human PDGF-AB (20ng/ml) (Shenandoah, Biotech, Warwick, PA) and heparin (10ng/ml). Cells were subsequently cultured as tumor neurospheres and passaged every one to two weeks.

Gustave Roussy Cell Lines and primary cell cultures. Tumor pieces were collected into DMEM (Dulbecco's Modified Eagles Medium, PAA Laboratories GmbH, Pasching, Austria). Biopsies were cut into 1 mm^3 pieces and placed into either DMEM for immediate processing or into freezing medium (90% serum, 10% DMSO) prior to being progressively cooled to −80°C. Cell dissociation was performed mechanically by passage through increasingly finer needles (19G to 26G). Single cells were seeded in

AmnioMAX™ C-100 complete medium containing gentamycine, L-glutamine and FBS (Gibco, Invitrogen, Paisley, UK) and maintained at 37°C in a 5% CO_2 humidified atmosphere. The cells were further cultured until appearance of adherent cells and colony formation and then weekly passaged.

Predictive analysis to identify relevant targets for therapeutic intervention

In this section, we discuss two separate analyses: (a) We evaluated the power of mutational and RNA expression characterizations in combination with drug profile information to predict drug sensitivities. We utilized an ensemble of regression trees as the predictive model [46,47] and our results indicate that drug target profile information or drug target profiles integrated with RNA expressions are the best predictors of drug sensitivity. (b) We integrated drug response and profile information with RNAseq data to identify relevant functional targets of DIPG. We utilized the Target Inhibition Map approach [29, 30] to generate multivariate blocks of targets whose joint inhibition is predicted to increase the sensitivity.

Data Pre-processing and Notations:

For this analysis, we considered a total of 6 samples that had both drug sensitivity and RNA expression data. A subset consisting of 8 cell lines was tested on Drug Screen 1(SU-DIPG-I, SU-DIPG-II, SU-DIPG-IV, SU-DIPG-VI, VU-DIPG.A, NEM-145, NEM157) and another subset of 7 cell lines was tested on Drug Screen 2 (NEM-163, NEM-165,NEM-168, NEM-175, JHH-DIPG1, NEM-157, NEM-215) with 2 cell lines tested on both screens. Of these, SU-DIPG-I, SU-DIPG-II, SU-DIPG-IV, SU-DIPG-VI, VU-DIPG.A, and JHH-DIPG1 have matched RNAseq data and genome sequence data and is used in the Ensemble analysis.

To identify the mechanistic targets through which drugs derive their sensitivity, prior information on the kinase targets of the compounds are utilized. The Drug target inhibition information is contained in a matrix Δ which quantifies the ability of a drug to inhibit its kinase targets. Each row vector is relatively sparse, as most drugs inhibit a select few primary targets and a small set of secondary, but often relevant, side targets. Each entry of Δ is a real number between 0 and 1 denoting the inhibition of the kinase target. An entry of Δ is close to 1 when a small concentration of a drug can phosphorylate 50% of the kinase target. The matrix Δ is generated based on published

drug target Kd's or EC50's from http://pubchem.ncbi.nlm.nih.gov/ and related publications. We used a hill curve interpolation with hill coefficient of 1 and drug concentration of 10,000nM to convert the EC50's to normalized inhibitions between 0 and 1. For each drug tested over a cell line, the functional response is measured as cell viability, the percentage of living cancerous cells following 72 hour application of a drug. The cell kill for each drug, considered as the percentage of cancerous cells killed following 72 hour application of the drug, is simply (1 - cell viability). The cell kill values are tested with 3 replicates in 4 concentrations. The cell kill values are converted to IC50's via hill curve interpolation. The IC50 values are then converted to sensitivities between 0 and 1 using a hill curve with hill coefficient of 1 and drug concentration of 10,000nM. A NaN or NA IC50 is converted to sensitivity 0. This set of sensitivities is a matrix denoted by Σ. Note that we have a matrix Σ of size 60x8 for drug screen 1 and a matrix Σ of size 60x7 for drug screen 2.

To incorporate the mutation characterization, we consider the set of kinase targets present in the drug screen (denoted by Θ_1) and created a binary matrix M_0 which denotes whether each of the drug target is mutated or not for each cell line. Considering the common 404 targets of the two drug screens, the size of M_0 is 15x404 where 15 denotes the cell lines (two rows are repeated as there are unique 13 cell lines).

To incorporate RNA expression data generated from the RNAseq experiments, we consider the set of kinase targets present in the drug screen (denoted Θ_1) and the targets with quantified expression present in the RNAseq data (denoted Θ_2). The set of targets for which we have usable information is then $\Theta_1 \cap \Theta_2$, the intersection of the two target sets. The remaining targets in Θ_1 are targets for which we do not have any RNA expression information and thus we are only able to gain information on these kinase targets from the drug screen data. Let the RNA expression be given by matrix G_0. In this analysis, the set $\Theta_1 \cap \Theta_2$ has 403 targets and thus the size of G_0 is 15 x 403. The RNA expression matrix is converted to a normalized matrix G by dividing the RNA expression of each gene by the mean expression of the matched normal samples or mean expression values. Thus a value $\gg 1$ in G denotes that the gene is highly expressed for that sample compared to normal matched samples or the expression mean.

Ensemble prediction

As mentioned earlier, our objective is to evaluate the capability of different genetic and functional characterizations for predicting drug sensitivity. We considered the following five characterizations:

(**C1**) Mutation information on the drug targets (M_0)

(**C2**) RNA expression for the genes common with the drug targets and normalized by the mean expression of the matched normal samples (G)

(**C3**) Drug Target Profiles (Δ)

(**C4**) Drug Target Profiles Integrated with Mutation Information ($\Delta \odot M_0$) where $\odot$ denotes element wise product.

(**C5**) Drug Target Profiles Integrated with gene expression $(1 - \Delta) \odot G$. Note that each entry of $(1 - \Delta) \odot G$ estimates the gene expression following the application of the drug. For instance, if normalized gene expression G(1, 50) is 2.5 and Δ(5, 50) = 0.4, then G(1, 50) *(1- Δ(5,50)) = 1.5 which denotes that gene 50 expression for sample 1 has been 40% reduced by application of drug 5. Note that when we apply this approach to estimate the gene expression after application of the drugs, the genes that are not directly inhibited by a drug but maybe downstream to targets that are inhibited will show up as highly expressed. This can possibly be addressed if we have prior knowledge on the pathways or gene expression is measured after application of the drug. For the current analysis, we didn't consider any prior knowledge or gene expression measurements following drug application and thus non-target gene expressions are not altered.

The above characterizations are converted to an input feature matrix X of size 900x404 for **C1, C3, C4** and 900x403 for **C2, C5**. The 900 denotes the characterization for each cell line (15) and each drug (60), thus 15x60=900. Note that for **C1** and **C2**, a row of M_0 or G is repeated 60 times as mutation or RNA expression is not dependent on the drug used. For **C3**, a row of Δ is repeated 15 times as drug target profile is independent of the cell line.

Corresponding to the matrix X, there is a sensitivity matrix Y of size 900x1 formed from Σ based on the sensitivity for each cell line and each drug.

We next apply an *ensemble* approach (*47*) for prediction of Y based on X for the five different characterizations. Ensemble approaches such as random forests are known to provide high accuracies in multiple prediction scenarios (*48*). For designing the ensemble of regression trees, we utilized the Matlab *fitensemble* function. We created an ensemble of 500 regression trees using Bagging (Bootstrap aggregating). The prediction performance is shown in table S4 (Ensemble Prediction Performance). We have reported the correlation coefficients between the predicted and experimental sensitivities using 10 fold cross validation approach. The table also shows the mean absolute error in prediction for the five different predictions. The top 40 predictors along with their weights are also included in table S4 (Ensemble Prediction Performance). The results indicate that mutation information or RNA seq information on the 403 drug targets alone is not highly predictive of drug sensitivity (10-fold CV correlation coefficients of 0.1536 and 0.3392 respectively). When mutation information is combined with drug target information, the predictive capability is still limited producing a 10-fold CV correlation coefficient of 0.2418. The drug target information alone can produce higher accuracy sensitivity predictions with 10-fold CV correlation coefficient of 0.5325. The combination of drug target information with RNA sequence information seems to further increase the precision by providing a 10-fold CV correlation coefficient of 0.6299.

TIM predictive algorithm to identify multivariate target combinations for therapeutic intervention

In this section, we utilize the Target Inhibition Map approach for target selection and sensitivity prediction. We next provide a brief outline of the approach (for details, please refer to [30]).

There are two primary steps in the TIM method: step one is selection of the optimal drug targets based on functional data generated from drug screens. This is the model generation step in the TIM algorithm. The model generation is approached from a Boolean logic perspective, where we aim to generate logical relationships between targets that identify the mechanisms by which tumors persist. Due to the Boolean nature of the approach, the matrix Δ generated for this analysis consists of 0's or 1's. The drug inhibition profiles (in the form of target EC50's) are used to generate the

binarized inhibition vectors based on the drug's IC50 value. The binarized vectors are generated based on the following equation

$a\log(IC_{50}) \leq \log(EC_{50}) \leq b\log(IC_{50}), 0 \leq a \ll b$ This binarization approach uses the functional drug sensitivity data to generate vectors of relevant drug targets. We assume that any target sufficiently beyond the IC50 point is unlikely to have been the cause of the drug response, and thus we assume that we cannot gain information from it.

To generate drug sensitivity values from the IC_{50} response data, we use the following equation: $y_i = \frac{\log(MaxDose_i) - \log(IC_{50}i)}{\log(MaxDose_i)}$ where $IC_{50}i$ is the IC_{50} of drug i, $MaxDose_i$ is the maximum tested dosage of drug i, and y_i is the resulting sensitivity value of drug i.

To incorporate RNAseq data into the TIM analysis, we eliminate unlikely kinase targets from consideration based on G, the matrix of normalized RNA expressions over the set $\Theta_1 \cap \Theta_2$. A kinase target is kept in the dataset for consideration if G(i,j) > ρ, a threshold for minimum relative expression. Note that we are considering expressed targets only as the effect of a molecularly-targeted drug is to inhibit the target when it is expressed and thus, non-expressed drug targets will have limited effect on predicting the drug response. For the purpose of this project, the RNA expressions constraint was G(i,j) > ρ = 1 meaning the RNA expression of the cancerous line must be at least that of the matched normal expression. As G does not provide information about the remaining targets in $\Theta_1 - \Theta_2$, they are not eliminated from consideration as they could potentially be driver mechanisms for the tumor. We performed the primary analysis on the 16 sets of joint RNAseq-matched drug screen data and cell line drug screen data.

Subset-Superset Biological Constraint

We utilize the following biological constraints to identify consistent and inconsistent sets of protein targets [3].

For any drug d_1 and any kinase target set S_T,

Constraint1: If $\Delta(d_1, S_T) \preccurlyeq \Delta(d_2, S_T)$, then $\Sigma(i, d_1) \leq \Sigma(i, d_2)$ (more inhibition of oncogenes should improve sensitivity)

Constraint2: If $\Delta(d_1, S_T) \succcurlyeq \Delta(d_2, S_T)$, then $\Sigma(i, d_1) \geq \Sigma(i, d_2)$ (less inhibition of oncogenes will reduce sensitivity)

Here, the $\preccurlyeq, \succcurlyeq$ operators signify component-wise inequality in all components.

The vectors and associated sensitivity values from matrix Σ are used to select the optimal targets for the TIM model. The optimal targets are selected by solving the following optimization problem that incorporates the inter-bin error (the error associated with multiple drugs having the same inhibition profile but differences in their sensitivity values) and the inconsistency error (the error associated with drug A being less effective than drug B but the targets of drug B are a subset of the drug A's targets). In this context, a bin is any subset of a set of kinase targets selected to build the model. The equation for inter-bin error is given by $\sum_{bins}\sum_{j\in bin}\left|P(s_j|T) - Y(s_j|T)\right|$, where $P(\bullet)$ is expected sensitivity of s_j under target set T, and $Y(\bullet)$ is the experimental sensitivity of s_j under target set T. The inter-bin error amounts to ensuring that kinase inhibitors with similar inhibition profiles with respect to the model have similar experimental sensitivities, indicating the likely mechanisms have been identified. The inconsistency error incorporates the subset-superset biological constraint introduced previously and is given by the following equation: $\sum_{drugs}\sum_{bins}\chi(bin, drug)\left|P(s_j|T) - Y(s_j|T)\right|$, where $P(\bullet)$ and $Y(\bullet)$ are as above and $\chi(\bullet)$ is an indicator function which is 1 when the subset-superset constraint is violated. The total optimization problem we wish to solve then is $\sum_{bins}\sum_{j\in bin}\left|P(s_j|T) - Y(s_j|T)\right| + \sum_{drugs}\sum_{bins}\chi(bin, drug)\left|P(s_j|T) - Y(s_j|T)\right|$. We find the minimum solution to the optimization problem using a suboptimal search algorithm known as Sequential Floating Forward Search (SFFS). The TIM framework requires that the subset-superset biological constraints are satisfied during model generation. This allows for identification of unique target combinations that may not be identified as relevant through a standard linear modeling approach.

Step two in TIM analysis is sensitivity prediction based on selected targets from step one. This step is used to generate the TIM circuit, which provides a visual representation of effective treatments inferred from the functional data. To generate the target blocks, viable target combinations are explored systematically in a breadth-first search style approach. Here, desired sensitivity levels for each level of inhibition (in terms of targets inhibited) is specified by the user; based on this specification, combinations of targets that satisfy the desired sensitivity levels are selected and no further supersets of the combination are considered. The inferential steps are based on bounding the expected sensitivity by the closest subset of the target combination and

the closest superset of the target combination. The equation for inferred sensitivity for a target set $\{t_1,t_2,\ldots t_n\}$ is given by $y(\{t_1, t_2, \ldots, t_n\}) = y_l + (y_u - y_l)\left(\frac{\sum_{i=1}^{n} \alpha(t_i)}{\sum_{i=1}^{h} \alpha(t_i)}\right)^{\beta}$, where y_l is the maximum sensitivity of the subsets of $\{t_1,t_2,\ldots t_n\}$, y_u is the minimum sensitivity of the supersets of $\{t_1,t_2,\ldots t_n\}$, $\alpha(\bullet)$ is weight for a kinase target, and β determines the order of the curve fit for $y(\{t_1, t_2, \ldots, t_n\})$. For this analysis, $\alpha(\bullet) = 1$ for all targets meaning all targets have equal weight and $\beta = 1$ which provides a linear fit. The sum in the denominator is the sum of weights between the subset generating y_l and the superset generating y_u. In this way, the predicted sensitivity lies between y_l and y_u depending on the distance of $\{t_1, t_2, \ldots, t_n\}$ to the subset and superset. Based on the number of additional targets needed to move from the subset to the desired target combination, the sensitivity of the drug combination is inferred. In the event, the predicted sensitivity $y(\{t_1, t_2, \ldots, t_n\})$ is sufficient to satisfy the sensitivity level defined by the user, the target combination is designated a valid block combination, and the supersets are no longer considered.

To provide quantification for the predictive power of the TIM approach, 10-fold cross validation mean absolute errors (MAE) and correlation coefficients between experimental and predictive sensitivities were calculated. The first test used only the functional data generated from the Drug Screens for prediction. For this analysis the 10-fold CV error was 0.101 and a correlation coefficient of 0.848. The second test incorporated the RNA expression data to eliminate potential false positive before model development. Here the 10-fold CV error was 0.111 and correlation coefficient of 0.773. The prediction performance along with the targets selected by TIM analysis is included in table S5 (TIM Prediction Performance). The top performing blocks based on TIM analysis is included in table S6 (TIM Top performing blocks).

We have also created the individual TIM circuits for each tumor culture or cell line which are included on the supplementary folder Individual TIM Circuits. The suffix raw denotes that only drug target profiles and drug screen responses were used to generate the proliferation circuit whereas the suffix RNA denotes that RNA expression data was integrated to eliminate potential false positive before model development.

TIM and Ensemble Approach Target Comparison

The comparison of the top predictors generated by the TIM and Ensemble (**C3** and **C5**) approaches shows that most of the targets are common to both approaches. Both approaches select multiple members from the following gene families CDKs, PSMB, HDAC and EHMT.

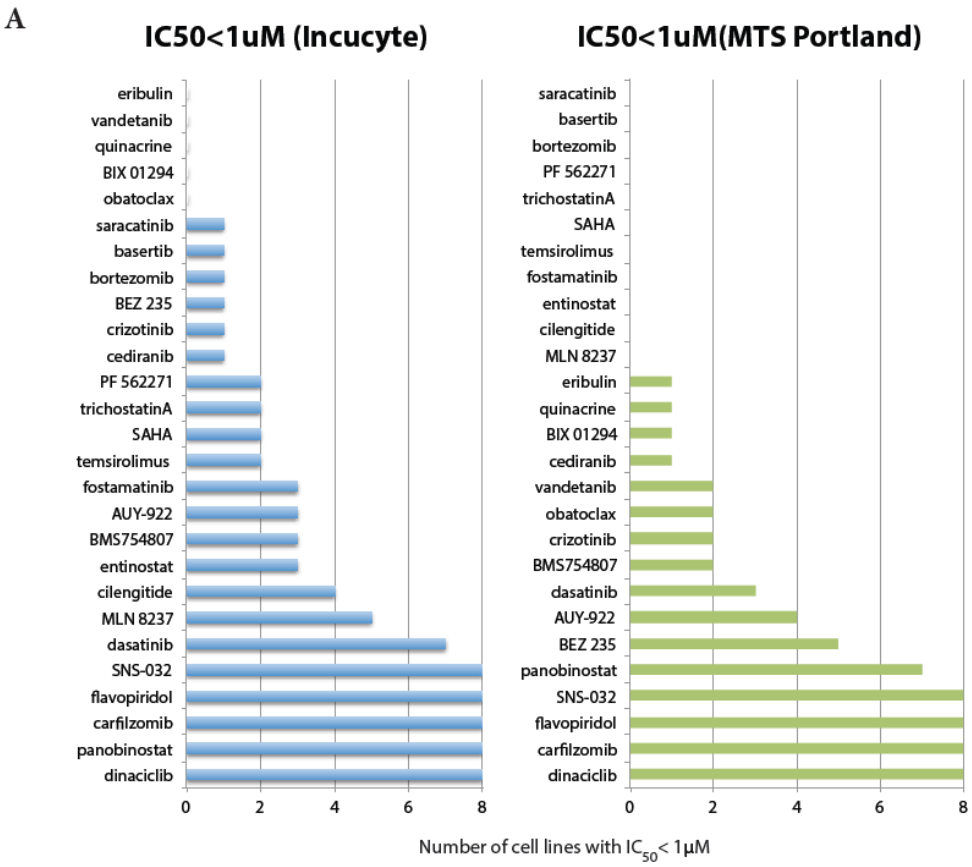
A
IC50<1uM (Incucyte)
IC50<1uM(MTS Portland)
eribulin
vandetanib
quinacrine
BIX 01294
obatoclax
saracatinib
basertib
bortezomib
BEZ 235
crizotinib
cediranib
PF 562271
trichostatinA
SAHA
temsirolimus
fostamatinib
AUY-922
BMS754807
entinostat
cilengitide
MLN 8237
dasatinib
SNS-032
flavopiridol
carfilzomib
panobinostat
dinaciclib
0
2
4
6
8
Number of cell lines with IC50< 1µM

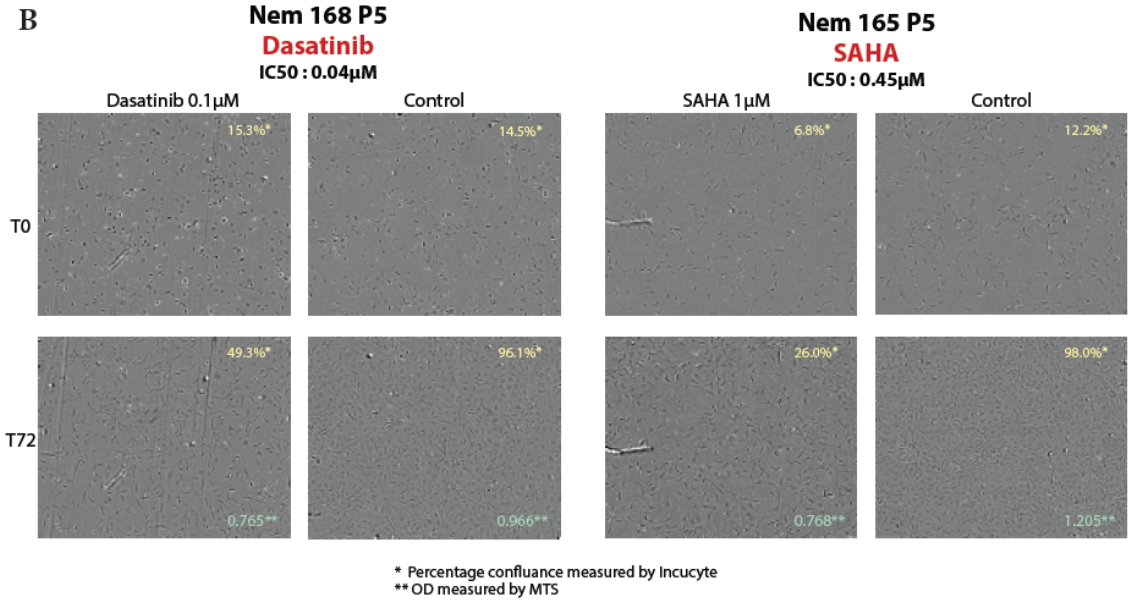
B
Nem 168 P5
Dasatinib
IC50 : 0.04µM
Dasatinib 0.1µM
Control
Nem 165 P5
SAHA
IC50 : 0.45µM
SAHA 1µM
Control
T0
T72
15.3%*
14.5%*
6.8%*
12.2%*
49.3%*
96.1%*
26.0%*
98.0%*
0.765**
0.966**
0.768**
1.205**
* Percentage confluance measured by Incucyte
** OD measured by MTS

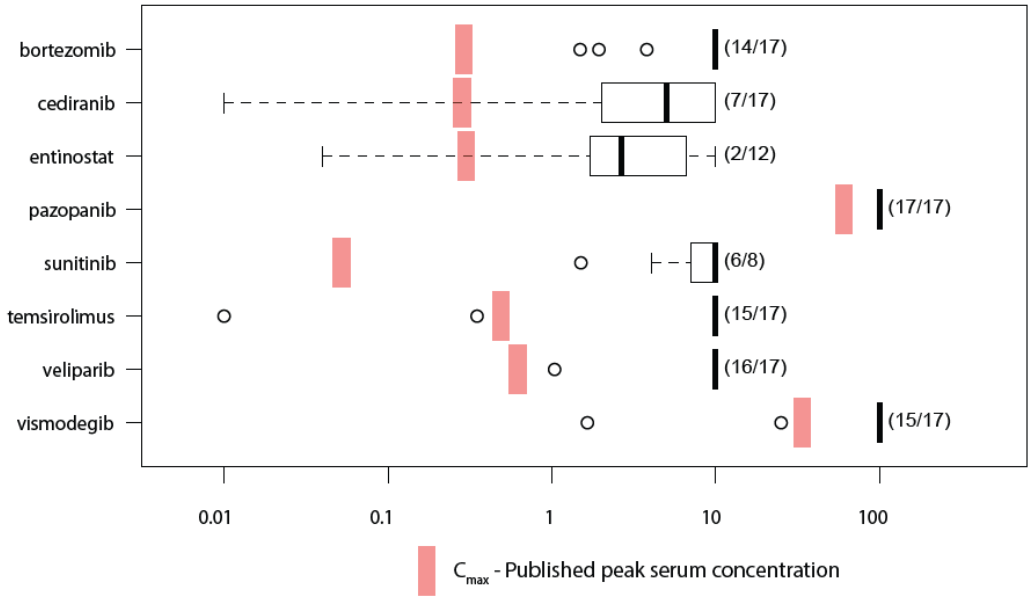

Figure S2. Chemical screen 'non-hits' within the context of clinically-achievable serum drug levels. Box and whisker plot demonstrating the average absolute IC_{50} values ("box") +/- 1.5 standard deviation ("whiskers") for each of the top "hits", listed on the vertical axis, with concentration in μM on the horizontal axis. C_{max} (the peak serum concentration reported in the literature) for each drug is represented as a red bar. The number of cultures that were insensitive, where insensitive is defined as having an IC_{50} higher than the maximum dose tried.

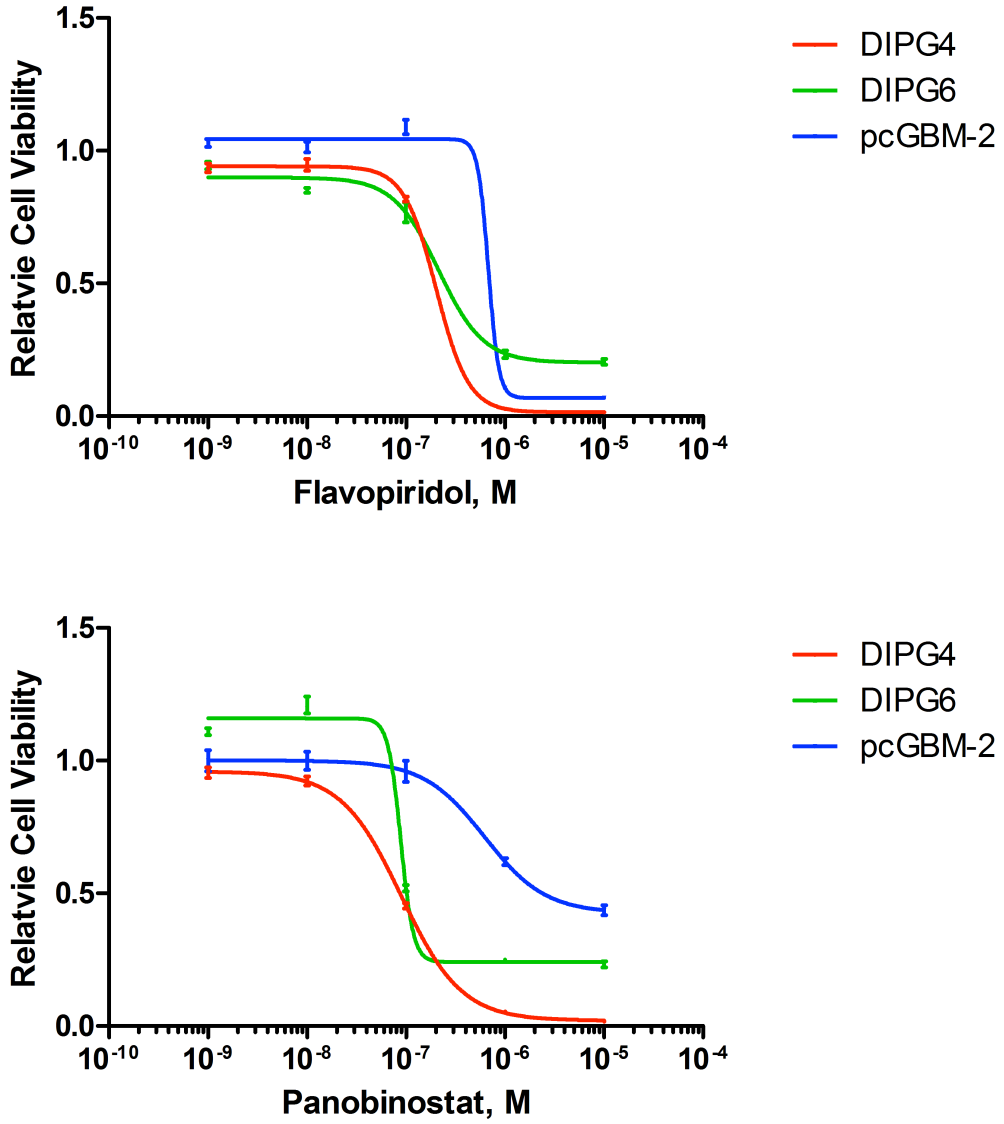

Figure S3 Comparison of relative sensitivity of DIPG and pediatric cortical GBM DIPG cell lines SU-DIPG IV (red), SU-DIPG VI (green) and a pediatric cortical glioblastoma cell line (SU-pcGBM-2; blue)) were exposed at various concentrations of CDK inhibitor flavopiridol (alvocidib; upper graph) or Panobinostat (lower graph) and evaluated three days later using the Cell Titer Glo viability assay. All three lines exhibited a similar response to flavopiridol (IC50 = 0.24 μM, 0.45 μM and 0.39 μM for SU-DIPG-IV, SU-DIPG-VI and SU-pcGBM2, respectively). In contrast, the DIPG cell lines were more sensitive with a lower IC_{50} in comparison to the pediatric cortical GBM in response to panobinostat (IC50 = 0. 09μM, 0.10 μM and 7.96 μM for SU-DIPG-IV, SU-DIPG-VI and SU-pcGBM2, respectively). Error bars, s.e.m,

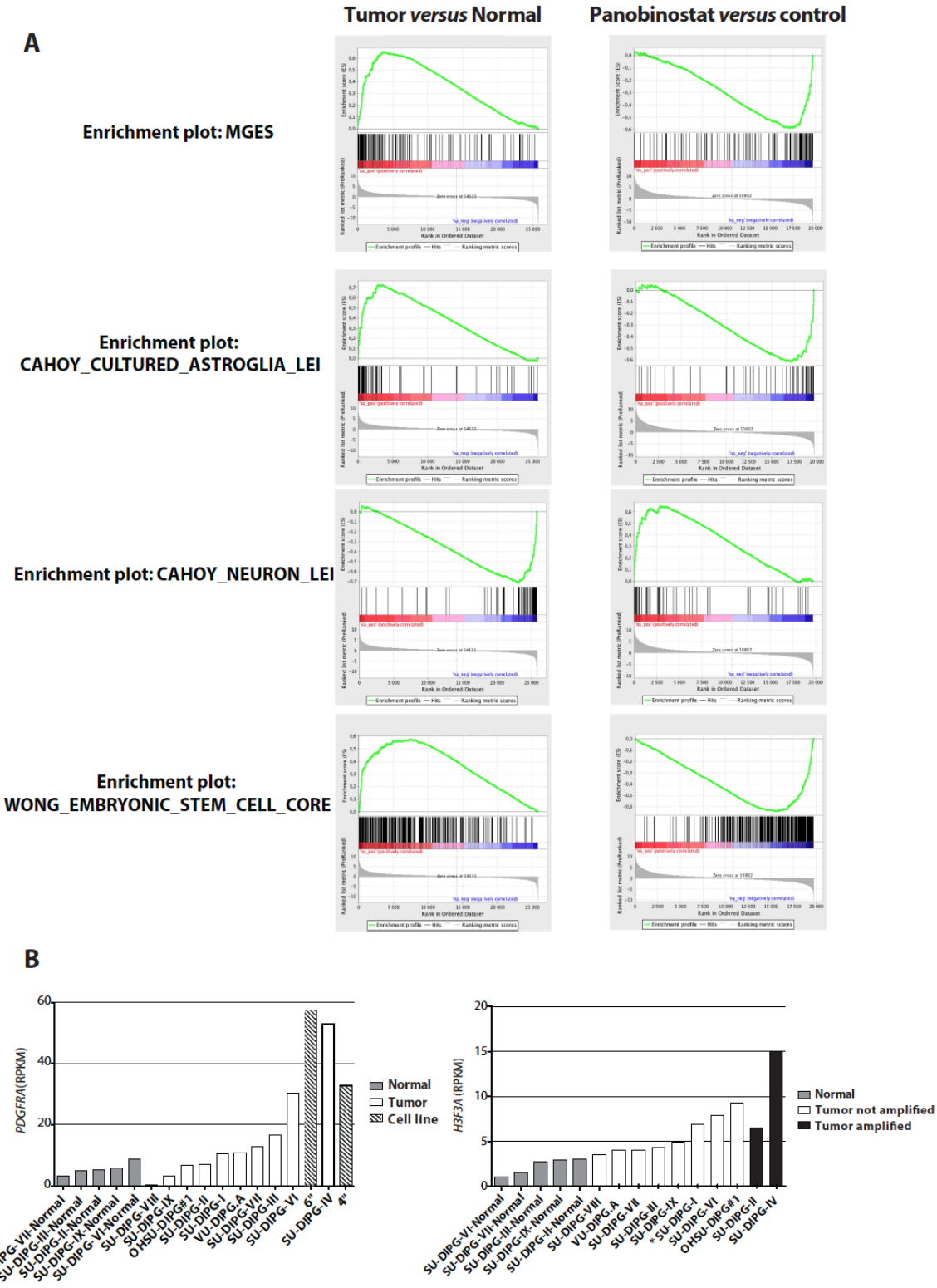
A
Tumor versus Normal
Panobinostat versus control
Enrichment plot: MGES
Enrichment plot: CAHOY_CULTURED_ASTROGLIA_LEI
Enrichment plot: CAHOY_NEURON_LEI
Enrichment plot: WONG_EMBRYONIC_STEM_CELL_CORE
B
PDGFRA (RPKM)
Normal
Tumor
Cell line
SU-DIPG-VII-Normal
SU-DIPG-III-Normal
SU-DIPG-II-Normal
SU-DIPG-IX-Normal
SU-DIPG-VI-Normal
SU-DIPG-VIII
OHSU-DIPG-IX
SU-DIPG#1
SU-DIPG-II
SU-DIPG-I
VU-DIPG.A
SU-DIPG-VII
SU-DIPG-III
SU-DIPG-VI
6*
SU-DIPG-IV
4*
H3F3A (RPKM)
Normal
Tumor not amplified
Tumor amplified
SU-DIPG-VI-Normal
SU-DIPG-VII-Normal
SU-DIPG-III-Normal
SU-DIPG-IX-Normal
SU-DIPG-II-Normal
SU-DIPG-VIII
VU-DIPG.A
SU-DIPG-VII
SU-DIPG-III
SU-DIPG-IX
* SU-DIPG-I
SU-DIPG-VI
OHSU-DIPG#1
SU-DIPG-II
SU-DIPG-IV

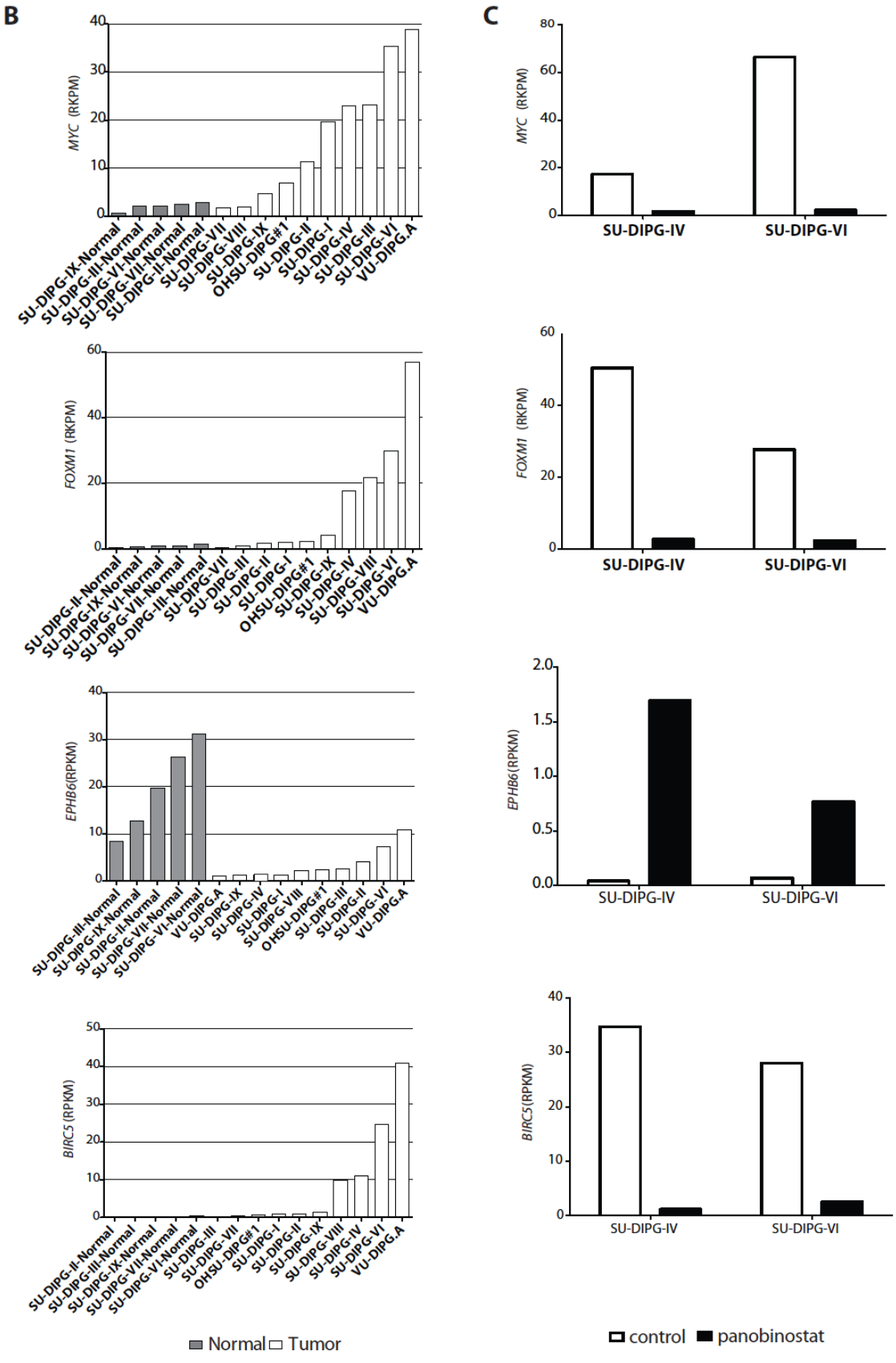
B
C
MYC (RKPM)
FOXM1 (RKPM)
EPHB6(RPKM)
BIRC5 (RPKM)
SU-DIPG-IX-Normal
SU-DIPG-III-Normal
SU-DIPG-VI-Normal
SU-DIPG-VII-Normal
SU-DIPG-II-Normal
SU-DIPG-VII
SU-DIPG-VIII
SU-DIPG-IX
OHSU-DIPG#1
SU-DIPG-II
SU-DIPG-I
SU-DIPG-IV
SU-DIPG-III
SU-DIPG-VI
VU-DIPG.A
SU-DIPG-IV
SU-DIPG-VI
Normal
Tumor
control
panobinostat

Figure. S4 DIPG gene expression A) GSEA of differentially expressed genes identified by RNAseq in primary tumors vs normal samples show that up-regulated genes in tumor samples are enriched in mesenchymal, astrocytic and embryonic stem cell signatures (left panels, (*25-28*) and down-regulated genes in neuronal markers. Conversly, genes induced by panobinostat treatment are enriched in neuronal signature but depleted in the gene sets enriched in primary tumors (right panels). The color bar depicts the gene list ranked by fold-change, and vertical black lines indicate the position of each gene of the gene set analyzed. Red and blue are indicative of significantly up-regulated and down-regulated genes, respectively, in panobinostat treated vs untreated cell line or in primary tumors vs normal sample comparisons.
B) Gene expression level in RPKM of *PDGFRA* and *H3F3A* in normal cortex (grey), DIPG tumors with or without amplification (black and white bars respectively) and DIPG cell lines (hatched bars respectively).
C) Gene expression level of *MYC*, *FOXM1*, *EPHB6* and *BIRC5* in DIPG tumors (white) and normal brain samples (grey) are represented in RPKM (Left panel). Effect of panobinostat treatment (1 µM for 48 hours) on expression level of these genes in SU-DIPG-IV cell line is shown (Right panel).

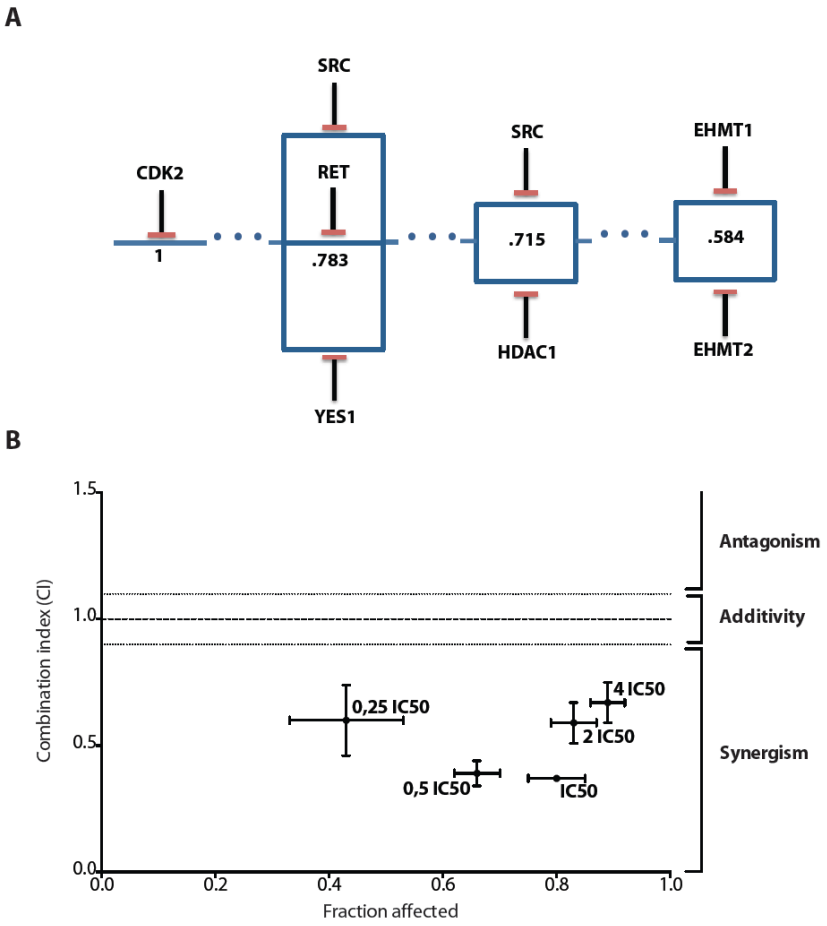

Figure S5 Combination testing of dasatinib and vorinostat

A) Individual Target Inhibition Map circuit generated for NEM157 cell line derived from RNAseq-matched drug screen responses.

B) Synergistic effect of Src inhibitor (dasatinib) and HDAC1 inhibitor (vorinostat) on NEM157 cell growth *in vitro*. Cells were treated with increasing concentrations of drugs either alone or concurrently at their equipotent molar ratio and combination indices calculated by the method of Chou&Talalay. Each combination dose is represented by fraction affected corresponding to the percentage of cell growth inhibition and the combination indice calculated. CI calculates synergism <0.8; additivity between >0.8 and <1.2; antagonism >1.2. All values are given as mean± standard deviation of at least three independent experiments.

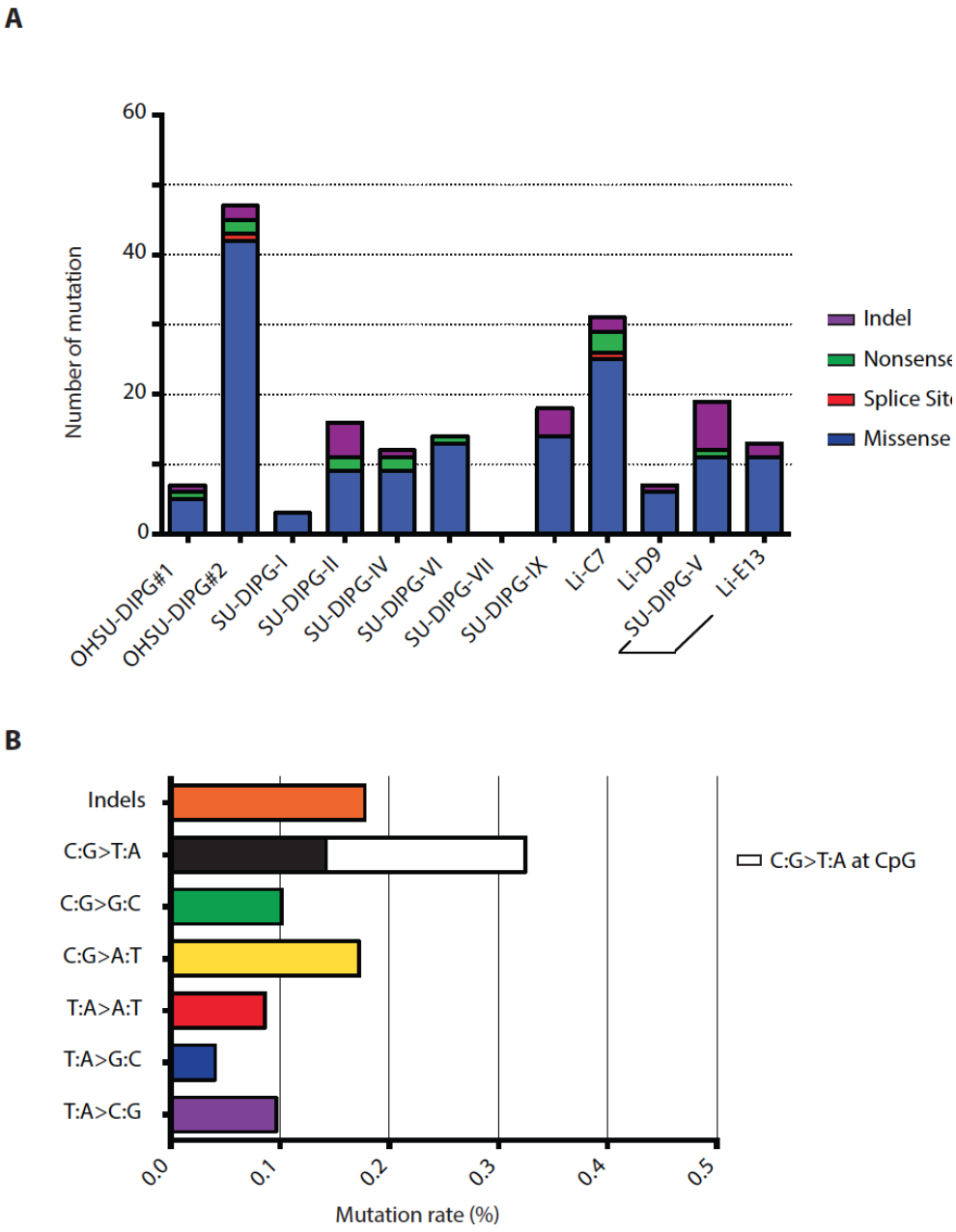

Figure S6. Mutational burden and spectrum of DIPG. The exomes of 12 DIPG tumors were sequenced for the determination of somatic mutations and copy number alterations. A) The mutation burden of DIPG is show for the 12 exomes sequencing. The number of nonsynonymous mutations, including missense (blue), nonsense (green), splice site mutations (red) and indels (purple) for each sample are shown. B) The mutation spectrum of DIPG shown as the percentage of coding somatic mutations for each of the six classes of base substitutions and indels is show for the 12 DIPG tumors.

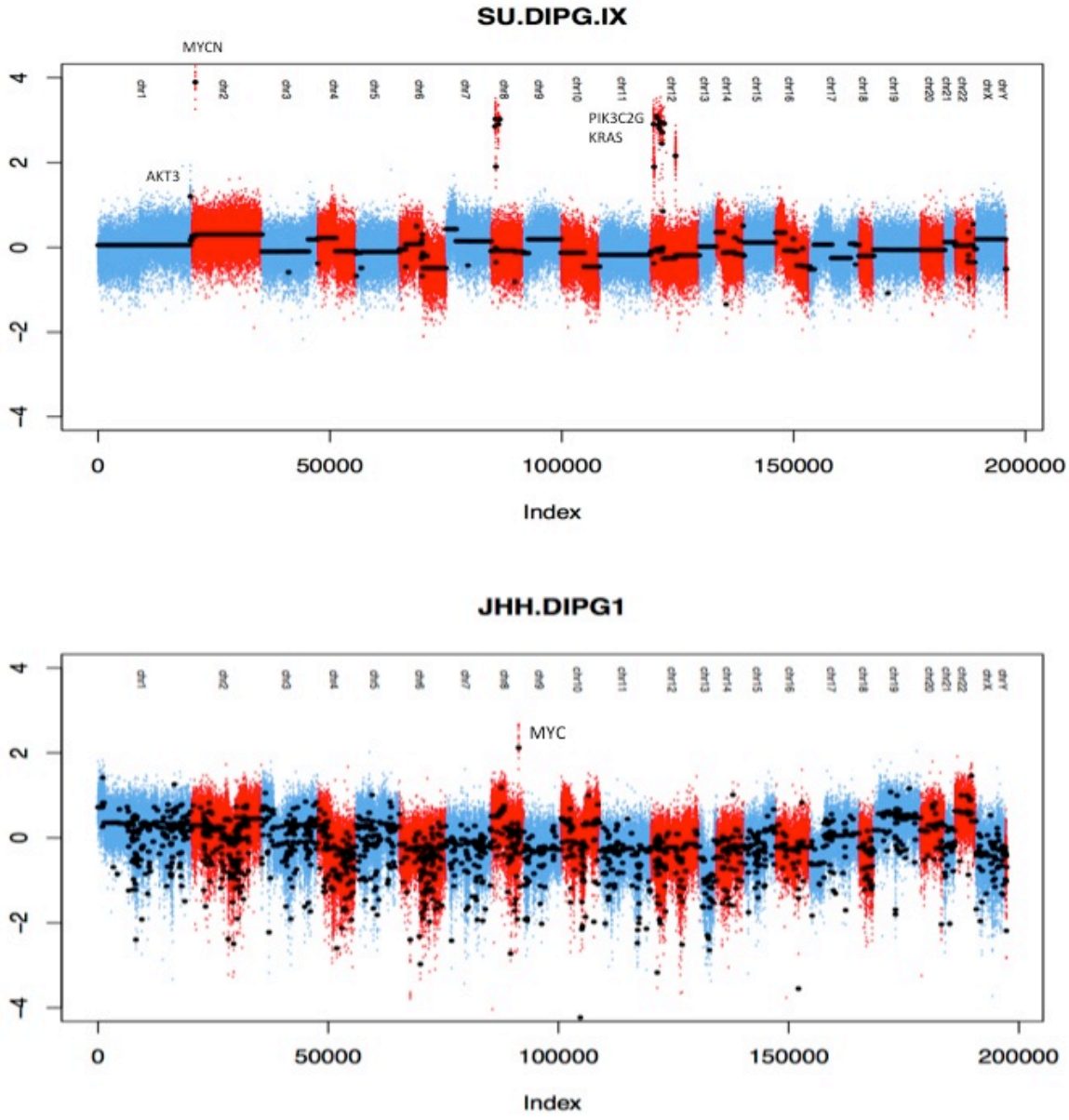

Figure S7 Amplifications of known cancer drivers in samples that do not exhibit typical patterns of copy number alterations. Genome wide copy number plots by exome sequencing for two atypical samples JHH-DIPG1 and SU-DIPG-IX. For each sample, the Log2 copy number ratio between the tumor and its matched normal are shown is plotted for each exon. Each chromosome is colored in alternating red and blue.

Table S1 Clinical characteristics of subjects and their DIPG tumors included in the study. The anonymous identifying code ("patient ID"), age at diagnosis, histological diagnosis and grade of the DIPG tumor and treatment the patient received is indicated. In all cases other than the NEM lines, the tissue sample was obtained after treatment; for NEM samples, tissue was obtained prior to treatment.

Clinical characteristics

Patient ID	Age (Diag)	Histology	Grade	Treatment
SU-DIPG-I	5	glioma	III-IV	XRT (3 days only)
SU-DIPG-II	7	glioblastoma	IV	XRT + temozolomide
SU-DIPG-III	12	diffuse astrocytoma	II	XRT + trisenox
SU-DIPG-IV	2	glioblastoma	IV	XRT + cetuximab/irinotecan
SU-DIPG-V	12	glioblastoma	IV	XRT, temodar
SU-DIPG-VI	7	glioblastoma	IV	XRT + vorinostat
SU-DIPG-VII	8	glioblastoma	IV	XRT (2 days only)
SU-DIPG-VIII	9	anaplastic astrocytoma	III	XRT then XRT + antineoplaston
SU-DIPG-IX	13	high grade glioma	sample too small to judge	XRT
SK-DIPG27	6	glioblastoma	IV	XRT+ bevacizumab, Temozolamide
VU-DIPG.A	3	diffuse astrocytoma	II	multiagent chemotherapy
VU-DIPG.B	4	anaplastic astrocytoma	III	XRT
Li-A	5	Glioblastoma	IV	XRT
Li-C	13.5	glioblastoma	IV	XRT + renatecan
Li-D	12	high grade glioma	III	XRT + valproic acid, avastin
Li-E	12	glioblastoma	III	(same patient as SU-DIPG-V)
Li-F	8.5	glioblastom	IV	XRT-TMZ, Avastin
OHSU-DIPG#1	4	glioblastoma	IV	none (radon mine)
OHSU-DIPG#2	19	glioblastoma	IV	unknown
JHH-DIPG1	6	glioblastoma	IV	XRT + TMZ/CPT11/bevacizumab
NEM-157	5	oligo-astrocytoma	II	XRT + erlotinib
NEM-163	5	diffuse astrocytoma	II	XRT + erlotinib
NEM-165	3	oligo-astrocytoma	III	XRT + erlotinib
NEM-168	9	diffuse astrocytoma	III	chemotherapy then RT + erlotinib
NEM-175	9	dffuse astrocytoma	II	XRT + erlotinib
NEM-186	3	glioblastoma	IV	XRT (40 Gy hypofractionated)
NEM-198	7	oligodendroglioma	III	chemotherapy then RT + erlotinib
NEM-215	6	oligo-astrocytoma	II	XRT + erlotinib then sirolimus
NEM-226	5	oligo-astrocytoma	III	XRT + cilengitide then sirolimus/CPT11

Table S2 *In silico* prediction of Blood-Brain-Barrier (BBB) Penetration. Potential crossing of the BBB was predicted by a computational approach based on Bayesian statistics, using the B3PPP prediction model (http://b3pp.lasige.di.fc.ul.pt/)(*49*).

Predicted blood brain barrier penetration			
Drug Name	**Prediction**	**Drug Name**	**Prediction**
alisertib	Penetration	OSI-906	No penetration
alvocidib	No penetration	panobinostat	Penetration
AUY922	No penetration	pazopanib	No penetration
AZD-8931	No penetration	pelitinib	Penetration
barasertib	No penetration	PF-04554878	-
BEZ 235	No penetration	ponatinib	-
BIX 01294	>600kD	quinacrine	Penetration
BMS 754807	Penetration	ranimustine	No penetration
bortezomib	No penetration	RO4929097	Penetration
cabozantinib	No penetration	RO5045337	-
carfilzomib	>600kD	ruxolitinib	-
cediranib	Penetration	saracatinib	Penetration
cilengitide	No penetration	SB-431542	Penetration
crizotinib	Penetration	selumetinib	No penetration
dasatinib	Penetration	SJ-172550	No penetration
decitabine	No penetration	SNS-032	Penetration
dinaciclib	Penetration	sodium butyrate	No penetration
entinostat	No penetration	sorafenib	Penetration
enzastaurin	Penetration	SP600125	No penetration
erlotinib	No penetration	tamoxifen	No penetration
estramustine	-	tauromustine	No penetration
etoposide	No penetration	temozolomide	Penetration
fenretinide	No penetration	temsirolimus	>600kD
fostamatinib	Penetration	teniposide	>600kD
GANT61	Penetration	tipifarnib	No penetration
gefitinib	No penetration	tozasertib	Penetration
imatinib	Penetration	tretinoin	Penetration
lapatinib	No penetration	trichostatin	Penetration
lenalidomide	Penetration	vandetanib	Penetration
liposomal daunorubicin	-	veliparib	Penetration
methotrexate	No penetration	vemurafenib	No penetration
mitoxantrone	No penetration	VER-155008	No penetration
MK-2206	No penetration	vismodegib	Penetration
N-acetyl cysteine	No penetration	vorinostat	No penetration
nilotinib	Penetration	zibotentan	No penetration
obatoclax	Penetration		

Table S3 Genes targets affected by drugs in the chemical screen.

Primary targets of compounds			
ABT-737	BCL2,BCLXL	Nutlin-3	MDM2,TP53
Actinomycin		Obatoclax	BCL2,BCL2L10
Alisertib	AURKA,AURKB	Panobinostat	HDAC1,HDAC10,HDAC11,HDAC2,HDAC3,HDAC4,HDAC5,HDAC6,HDAC7,HDAC8,HDAC9
Alvocidib	CDC2L1,CDK1,CDK2,CDK4,CDK5,CDK6,CDK7,CDK8,CDK9,LIMK1	Pazopanib	PDGFRB,KIT,PDGFRA,CSF1R,FLT1,KDR,FLT4,DDR1,STK10,DDR2
ATRA		PD0332991	CDK4,CDK6
AUY922	HSP90,HSPA,HSPB	Pelitinib	EGFR,GAK,MAP4K5,ERBB4,JAK3,DMPK,BLK,LCK,CSNK1E,MAP4K3
Azacytadine		PF-562271	PTK2,PTK2B,CDK2,CDK3,CDK1,CDK7,FLT3,GSK3A,CDK5,GSK3B
AZD-8931	CDC42BPA,EGFR,ERBB2	PI-103	CDC42BPA,DAPK1,DAPK3,MYLK,PIK3C2B,PIK3CA,PIK3CB,PIK3CD,PIK3CG
Barasertib	AURKC,AURKB,FLT3,KIT,PDGFRA,PDGFRB,RET,FLT1,MAP4K5,TIE1	Ponatinib	FGFR1,FGFR2,FGFR3,FGFR4
BEZ235	AXL,KDR,KIT,MET,MST1R,MTOR,PIK3CA,PIK3CB,PIK3CD,PIK3CG,RET	PPP	
BIX01294	EHMT1,EHMT2	Prednisone	
BIX02188	MAP2K5,MAPK7,TGFBR1	Quinacrine	
BMS-754807	IGF1R,NTRK2,MET,NTRK1,AURKA,AURKB,MST1R,FLT3,JAK2,GSK3B	Rapamycin	MTOR
Bortezomib	CMA1,CTSA,CTSG,HTRA2,PSMB8	Resveratrol	IKBKB
Bosutinib	MAP4K5,YES1,ABL1,ABL2,SRC,FGR,LCK,FYN,FRK,BTK	Revlimid	
Cabozantinib	FLT3	RO4929097	NOTCH1,PSENEN
Carboplatin		Ruxolitinib	JAK1,JAK2,JAK3,TYK2
Carfilzomib	PSMB5,PSMB8	Saracatinib	ABL1,ABL2,BLK,EGFR,EPHA2,FGR,FYN,KIT,LCK,LYN,PTK2,SRC,YES1
Cediranib	KDR,KIT,FLT4,FLT1,PDGFRB,FGFR1,FGFR2,FGFR3,PDGFRA,CSF1R	SB-431542	ALK4,ALK5
Chromeceptin		Selumetinib	MAP2K1,MAP2K2,MAPK1,MAPK3
Cilengitide	alphavbeta3,alphavbeta5,alphavbeta6	SJ-172550	MDM4
Crizotinib	ALK,AXL,MET,MST1R,NTRK1,NTRK2,TEK	SNS-032	CDK9,PCTK1,PCTK2,GSK3A,GSK3B,CDK2,PCTK3,CDC2L2,CDK3,CDK7
Curcumin	GST	Sodium Aurothiomalate	PTPRC
Dasatinib	EPHA3,ABL2,FYN,PTK2,BLK,EPHA8,TXK,WEE2,FRK,EPHB4	Sodium Butyrate	
Dinaciclib	CDK1,CDK2,CDK5,CDK9	Sorafenib	DDR1,HIPK4,ZAK,DDR2,BRAF,CSF1R,FLT1,FLT3,KIT,TIE1
Entinostat	HDAC1,HDAC3	SP600125	AKT1,MAP2K3,MAP2K4,MAP2K6,MAPK10,MAPK8,MAPK9,PRKCA
Enzastaurin	PRKCA,PRKCB,PRKCE,PRKCG	Sunitinib	KIT,FLT3,STK17A,FLT1,CSF1R,BMP2K,CHEK2,AXL,KDR,AAK1
Eribulin		Tamoxifen	
Erlotinib	EGFR,GAK,STK10,BLK,ABL2,ERBB4,LCK,ABL1,EPHA6,LYN	Taurolidine	
Fenretinide		Temsirolimus	MTOR
Fostamatinib		Tozasertib	ABL2,AURKA,AURKC,FLT3,PLK4,ABL1,MLCK,RIPK1,DDR1,RET
GANT61		TrichostatinA	HDAC1,HDAC3,HDAC4,HDAC6,HDAC8
Imatinib	DDR1,ABL2,ABL1,DDR2,CSF1R,LCK,KIT,BLK,LYN,GAK	Valproate	
Irinotecan		Vandetanib	EGFR,FGFR1,FGFR2,FGFR3,FLT1,FLT4,KDR,MERTK,PDGFRB,RET
Itraconazole		Veliparib	PARP1,PARP2
Lapatinib	EGFR,ERBB2,ERBB4	Vemurafenib	BRAF,RAF1
Linsitinib	IGF1R,INSR	VER-155008	HSP70Kd,HSPA
MK-2206	AKT1,AKT2,AKT3	Vincristine	
N-acetyl cysteine		Vismodegib	ABCG2,GLI1
Nicotinamide		Vorinostat	HDAC1,HDAC2,HDAC3,HDAC6,HDAC8
Nilotinib	ABL1	Zibotentan	EDNRA

Table S4: Ensemble Prediction performance: Table shows the performance of drug sensitivity prediction based on mutation information, gene expression, drug target inhibition profiles and combinations of data from these three sources. We have used

Matlab ensemble prediction with 500 regression trees and report the 10 fold cross validation mean absolute errors (MAE). We also report the correlation coefficient between the predicted and experimental sensitivities for 10 fold cross validation case. A hill slope of 1 and concentration of 10,000 nM was used to convert the IC50's to normalized sensitivities. The data was fused as follows: (a) For drug target profile and mutation, only the drug target inhibitions that have mutations are considered (i.e. D*M where D denotes the target inhibition and M is binary 1 or 0 denoting mutation). (b) For drug target profile and gene expression, we have multiplied the 1- drug target inhibition with the normalized gene expression (i.e. (1-D)*G where G denotes the ratio of the tumor gene expression to mean of normal cell line gene expression. The (1-D)*G estimates the gene expression after application of the drug). The table also includes the top targets selected by each approach and their corresponding weights.

Ensemble analysis					
	Mutation	RNA Expression	Drug Target Profile	Drug target Profile, Mutation	Drug target Profile, Gene Expression
10 fold CV CC	0.1536	0.3392	0.5325	0.1623	0.6299
10 fold CV MAE	0.2982	0.2705	0.2174	0.2942	0.183

Method (Target, weight)				
Mutation	RNA Expression	Drug Target Profile	Drug target Profile, Mutation	Drug target Profile, Gene Expression
PAK7 : 0.1749	CHEK2 : 0.1834	CDK2 : 0.1966	HDAC3 : 0.741	HDAC8 : 0.3588
TGFBR2 : 0.164	MDM4 : 0.1606	HDAC3 : 0.1805	GSK3B : 0.2261	MET : 0.1824
TP53 : 0.0861	ADCK4 : 0.157	HDAC1 : 0.1378	AURKB : 0.1819	HDAC3 : 0.153
CSNK2A1 : 0.0446	TSSK1B : 0.1503	HDAC2 : 0.1285	NTRK1 : 0.1568	CDK9 : 0.1382
EDNRA : 0.0407	STK3 : 0.1229	CDK5 : 0.1165	TGFBR2 : 0.1376	PSMB5 : 0.1238
EPHA6 : 0.0397	PKN1 : 0.1206	KDR : 0.0978	CLK2 : 0.1097	MAPK15 : 0.1215
CLK4 : 0.0383	PRKD2 : 0.1157	MET : 0.0838	PDGFRB : 0.0653	KDR : 0.1067
CAMK2A : 0.0377	ERN1 : 0.1132	EHMT1 : 0.072	STK10 : 0.0652	PRKD1 : 0.1035
HDAC3 : 0.035	FGFR1 : 0.0994	HDAC8 : 0.0704	DDR2 : 0.0556	CDK2 : 0.1005
MINK1 : 0.0333	CAMK1D : 0.0905	HDAC6 : 0.0691	NUAK2 : 0.0525	HDAC2 : 0.0996
MDM2 : 0.0328	ACVR2A : 0.09	CDK9 : 0.0668	ABL2 : 0.0523	HDAC5 : 0.0724
ULK2 : 0.0315	AKT2 : 0.0858	PSMB5 : 0.0653	FLT4 : 0.049	HDAC1 : 0.0714
CSNK1G3 : 0.0314	BRAF : 0.0817	EHMT2 : 0.0645	BCL2 : 0.0433	EHMT1 : 0.066
ITK : 0.0312	NEK6 : 0.0804	PSMB8 : 0.0633	MLCK : 0.0413	HDAC6 : 0.0621
RIOK3 : 0.0301	CDC42BPA : 0.0799	MST1R : 0.0604	CSF1R : 0.0383	PSMB8 : 0.0609
CAMKK1 : 0.0286	EPHA2 : 0.0794	GSK3B : 0.0453	LYN : 0.0335	EHMT2 : 0.0541
AURKB : 0.0275	MAPK12 : 0.0754	ERBB2 : 0.0389	EPHA3 : 0.0312	HDAC7 : 0.0507
GRK7 : 0.0269	PAK2 : 0.0739	IGF1R : 0.0262	FGFR2 : 0.0289	FLT4 : 0.0478
GSK3B : 0.0263	PRKD3 : 0.073	FLT4 : 0.0242	FGFR4 : 0.0216	MST1R : 0.0463
MAP2K3 : 0.0262	TEK : 0.0699	AKT1 : 0.0239	CSNK1D : 0.0212	GSK3B : 0.0427
PRKCB : 0.0262	PARP1 : 0.0691	BCL2L2 : 0.0232	PRKCB : 0.0179	TEK : 0.0414
WEE1 : 0.0254	PIK3C2B : 0.0661	BCL2A1 : 0.0217	CLK4 : 0.0141	BCLXL : 0.037
MAPK9 : 0.0251	STK25 : 0.0655	CDK7 : 0.0217	RIPK2 : 0.014	CSNK1D : 0.0309
FLT4 : 0.025	PIK3CA : 0.0645	GSK3A : 0.0213	PRKCA : 0.0115	ALK : 0.0294
TLK2 : 0.0243	TNIK : 0.0645	MCL1 : 0.0199	MAPK7 : 0.0114	JAK3 : 0.029
PSMB5 : 0.0239	CAMK1G : 0.0628	BCL2L10 : 0.0195	PIK3CB : 0.0113	AURKA : 0.0289
PDGFRB : 0.0236	CAMK4 : 0.0609	ALK : 0.0185	TP53 : 0.0107	MDM2 : 0.0288
LYN : 0.0234	EGFR : 0.0578	ABL1 : 0.0177	MDM2 : 0.0097	DYRK1B : 0.0276
FGFR4 : 0.0223	MAPK1 : 0.0573	TEK : 0.0172	ITK : 0.0094	CDK7 : 0.0274
STK10 : 0.0221	ACVR2B : 0.0569	FLT1 : 0.0168	MARK1 : 0.0072	MCL1 : 0.0263
CSNK2A2 : 0.022	GSK3B : 0.0566	AKT2 : 0.0157	EPHB1 : 0.0068	CDK5 : 0.0233
BCL2 : 0.0218	CSNK1E : 0.0542	MTOR : 0.0151	NLK : 0.0064	AURKB : 0.0216
FGFR2 : 0.0213	PAK4 : 0.0506	AKT3 : 0.0149	YES1 : 0.0064	IGF1R : 0.0184
NLK : 0.021	RIOK2 : 0.0484	EGFR : 0.0142	INSRR : 0.0059	EGFR : 0.0182
EPHB1 : 0.0204	LATS1 : 0.0469	KIT : 0.0139	PSMB5 : 0.0055	KIT : 0.0175
MAPK7 : 0.0204	RAF1 : 0.0466	HDAC10 : 0.013	MAP2K4 : 0.0055	BCL2 : 0.0165
RIPK2 : 0.0198	TAOK2 : 0.0445	CDK3 : 0.0123	MAP2K3 : 0.0052	PCTK2 : 0.0163
PRKAA1 : 0.018	EIF2AK2 : 0.0411	HDAC4 : 0.0119	NEK2 : 0.0047	AKT1 : 0.0155
YES1 : 0.0163	STK32B : 0.0383	BCL2 : 0.0106	MAPK11 : 0.0045	FGFR1 : 0.0152
PIK3CB : 0.0154	STK32C : 0.0379	AURKA : 0.0099	PIP5K1A : 0.0045	FGFR3 : 0.0139

Table S5: TIM Prediction performance: Table shows the performance of drug sensitivity prediction based on TIM Analysis. We report three cases: (a) prediction based on drug target profile information with RNA expression data added where available, (b) prediction based on drug screen data exclusively and (c) prediction based only on drug screen data with matched RNA expression data. For the integrated TIM analysis, the RNA expression was used to remove non expressed genes from the TIM analysis. We report the mean absolute error and correlation coefficient between the predicted and experimental sensitivities for 10 fold cross validation. The table also includes the top targets selected by each approach. The targets were sequentially selected by the TIM algorithm until no improvement in prediction accuracy was observed

TIM Analysis			
	TIM: Drug target Profile+RNA Expression	**TIM: Drug target Profile**	**TIM: Drug target Profile+RNAseq (RNAseq data only)**
10 fold CV Correlation Coefficient	**0.834**	**0.842**	**0.754**
10 fold CV MAE	**0.113**	**0.102**	**0.075**

Drug target Profile+RNAseq (All data)	**Drug target Profile**	**Drug target Profile + RNAseq (RNAseq data only)**
AKT1	AKT3	ABL1
AKT2	AURKA	AKT2
AURKA	BCL2	CDK2
BCL2	BCL2L10	CDK3
CDC42BPA	CDK2	CDK5
CDK2	CDK5	EHMT1
CDK3	CDK8	EPHB4
CDK9	EDNRA	GSK3B
CLK2	EHMT1	HDAC1
CTSG	EPHB3	HDAC2
EDNRA	EPHB4	MAPK15
EHMT1	FGFR3	MCL1
EPHA5	GLI1	NTRK1
FGFR2	GSK3B	PDGFRA
GLI1	HDAC1	PDGFRB
GSK3B	HDAC2	PRKCD
HDAC1	HDAC4	PSMB8
HDAC2	HSP90	PSMB5
HDAC4	HSPB	ROCK2
HSP90	MAPK15	TYK2
HSPB	MDM2	ULK1
MCL1	MET	
MDM2	MTOR	
MTOR	NTRK1	
NTRK1	PIK3CA	
PDGFRB	PIK3CG	
PIK3CA	PSMB8	
PSMB8	PSMB5	
PSMB5	STK36	
SRC	ZAP70	
STK36		
ULK1		

Table S6: TIM top performing blocks: Table contains the top performing blocks for TIM analysis with integrated drug target profile and gene expression data. The second row contains the 34 targets selected by the integrated TIM analysis. The first column in each row contains the block score and the targets of that block are listed under the corresponding target column.

Block Scores									
0.901549	AKT1	AURKA	CDK2	CDK9	**0.519803**	CDK3	HDAC1		
0.9	CDK2	CDK9			**0.519803**	CDK9	HDAC1		
0.9	HSP90	HSPB			**0.519803**	CLK2	HDAC1		
0.882353	PSMB8	PSMB5			**0.519803**	CTSG	HDAC1		
0.822639	HDAC1	HDAC2			**0.519803**	EPHA5	HDAC1		
0.715207	CLK2	PDGFRB	ULK1		**0.519803**	GSK3B	HDAC1		
0.711606	FGFR2	PDGFRB			**0.519803**	HDAC1	HSP90		
0.6	MTOR	PIK3CA			**0.519803**	HDAC1	HSPB		
0.595971	EPHA5	PDGFRB			**0.519803**	HDAC1	NTRK1		
0.583749	CLK2	GSK3B	NTRK1		**0.519803**	HDAC1	PSMB5		
0.583749	CDK2	CLK2	NTRK1		**0.519803**	HDAC1	ULK1		
0.579374	CDK3	NTRK1			**0.519803**	CDK2	EHMT1		
0.579374	CDK9	NTRK1			**0.519803**	CDK3	EHMT1		
0.579374	CTSG	NTRK1			**0.511652**	CDK9	EHMT1		
0.579374	EPHA5	NTRK1			**0.511652**	CLK2	EHMT1		
0.579374	HDAC2	NTRK1			**0.511652**	CTSG	EHMT1		
0.579374	HDAC4	NTRK1			**0.511652**	EHMT1	EPHA5		
0.579374	HSP90	NTRK1			**0.511652**	EHMT1	GSK3B		
0.579374	HSPB	NTRK1			**0.511652**	EHMT1	HDAC1		
0.579374	NTRK1	PSMB5			**0.511652**	EHMT1	HDAC2		
0.56926	CDK2	CDK3			**0.511652**	EHMT1	HDAC4		
0.56926	CDK2	GSK3B			**0.511652**	EHMT1	HSP90		
0.56926	CDK3	CDK9			**0.511652**	EHMT1	HSPB		
0.56926	CDK3	GSK3B			**0.511652**	EHMT1	NTRK1		
0.546956	HDAC1	HDAC4			**0.511652**	EHMT1	PSMB5		
0.545827	NTRK1	ULK1			**0.511652**	EHMT1	ULK1		
0.528091	HDAC2	HDAC4			**0.511652**	AURKA	NTRK1	SRC	
0.519803	CDK2	HDAC1			**0.511652**	PDGFRB	SRC		

.

Table S7: TIM targets in Biological Pathways:
Table contains the top (in terms of low p-value)
35 Biological Processes that contains genes belonging to the network in Figure 6. The enrichment was done based on String DB provided GO enrichment analysis feature

p-value sorted			
GO_id	**Term**	**#Genes**	**p-value**
GO:0048017	inositol lipid-mediated signaling	8	2.20E-10
GO:0048015	phosphatidylinositol-mediated signaling	8	2.20E-10
GO:0035556	intracellular signal transduction	18	7.54E-10
GO:0010646	regulation of cell communication	18	6.00E-09
GO:0048583	regulation of response to stimulus	20	7.10E-09
GO:0009966	regulation of signal transduction	18	8.63E-09
GO:0048011	nerve growth factor receptor signaling pathway	10	1.72E-08
GO:0007169	transmembrane RTK signaling pathway	12	1.12E-07
GO:0023051	regulation of signaling	18	1.18E-07
GO:0010648	negative regulation of cell communication	12	1.68E-07
GO:0008543	fibroblast growth factor receptor signaling pathway	8	1.96E-07
GO:0006464	cellular protein modification process	20	2.53E-07
GO:0010962	regulation of glucan biosynthetic process	4	2.95E-07
GO:0005979	regulation of glycogen biosynthetic process	4	2.95E-07
GO:0044344	cellular response to fibroblast growth factor stimulus	8	3.97E-07
GO:0071774	response to fibroblast growth factor stimulus	8	3.97E-07
GO:0043412	macromolecule modification	20	4.50E-07
GO:0048585	negative regulation of response to stimulus	12	4.55E-07
GO:0006468	protein phosphorylation	13	4.80E-07
GO:0070873	regulation of glycogen metabolic process	4	5.60E-07
GO:0009968	negative regulation of signal transduction	11	6.52E-07
GO:0032885	regulation of polysaccharide biosynthetic process	4	9.70E-07
GO:0007167	enzyme linked receptor protein signaling pathway	12	1.14E-06
GO:0007265	Ras protein signal transduction	6	1.23E-06
GO:0051726	regulation of cell cycle	12	1.26E-06
GO:0044267	cellular protein metabolic process	20	1.49E-06
GO:0032881	regulation of polysaccharide metabolic process	4	1.57E-06
GO:0023057	negative regulation of signaling	11	1.58E-06
GO:0016310	phosphorylation	13	2.34E-06
GO:0005524	ATP binding	16	2.71E-06
GO:0021761	limbic system development	5	3.23E-06
GO:0032559	adenyl ribonucleotide binding	16	3.34E-06
GO:0043066	negative regulation of apoptotic process	11	3.42E-06
GO:0030554	adenyl nucleotide binding	16	3.56E-06
GO:0043069	negative regulation of programmed cell death	11	3.78E-06

Table S8: TIM targets in Biological Pathways: Table contains the top (in terms of number of genes in process) 35 Biological Processes that contains genes belonging to the network in Figure 6. The enrichment was done based on String DB provided GO enrichment analysis feature

Gene Count Sorted			
GO_id	**Term**	**#Genes**	**p-value**
):0019538	protein metabolic process	21	4.02E-06
GO:0048583	regulation of response to stimulus	20	7.10E-09
GO:0006464	cellular protein modification process	20	2.53E-07
GO:0043412	macromolecule modification	20	4.50E-07
GO:0044267	cellular protein metabolic process	20	1.49E-06
GO:0035556	intracellular signal transduction	18	7.54E-10
GO:0010646	regulation of cell communication	18	6.00E-09
GO:0009966	regulation of signal transduction	18	8.63E-09
GO:0023051	regulation of signaling	18	1.18E-07
GO:0016043	cellular component organization	18	4.27E-05
GO:0071840	cellular component organization or biogenesis	18	5.82E-05
GO:0005737	cytoplasm	18	4.90E-01
GO:0071842	cellular component organization at cellular level	17	8.79E-06
GO:0071841	cellular component organization or biogenesis at cellular level	17	1.23E-05
GO:0042221	response to chemical stimulus	17	3.22E-04
GO:0007165	signal transduction	17	2.59E-03
GO:0023052	signaling	17	7.93E-03
GO:0043170	macromolecule metabolic process	17	6.67E-02
GO:0005524	ATP binding	16	2.71E-06
GO:0032559	adenyl ribonucleotide binding	16	3.34E-06
GO:0030554	adenyl nucleotide binding	16	3.56E-06
GO:0035639	purine ribonucleoside triphosphate binding	16	1.72E-05
GO:0032555	purine ribonucleotide binding	16	2.07E-05
GO:0032553	ribonucleotide binding	16	2.09E-05
GO:0017076	purine nucleotide binding	16	2.18E-05
GO:0000166	nucleotide binding	16	1.83E-04
GO:1901265	nucleoside phosphate binding	16	1.85E-04
GO:0097159	organic cyclic compound binding	16	1.87E-04
GO:0036094	small molecule binding	16	5.21E-04
GO:0044260	cellular macromolecule metabolic process	16	5.70E-02
GO:0005515	protein binding	16	3.47E-01
GO:0044238	primary metabolic process	16	4.81E-01
GO:0065009	regulation of molecular function	15	5.47E-05
GO:0048519	negative regulation of biological process	15	2.06E-03
GO:0007154	cell communication	15	5.68E-02

DISCUSSION

Ce mémoire de thèse présente nos résultats dans la recherche de cibles thérapeutiques potentielles ou en voie de validation mais aussi des nouvelles stratégies de découverte de thérapies ciblées dans les gliomes infiltrants du tronc cérébral (DIPG).

ACVR1, nouvelle cible thérapeutique dans les DIPG

Le séquençage « génome-entier » de 20 DIPG au diagnostic a permis la découverte de mutations activatrices récurrentes dans le gène *ACVR1/ALK2* qui code pour le récepteur à l'activine de type I, dans 20% des DIPG (cf. **ARTICLE 1**). De manière surprenante, ces mutations somatiques (R206H, Q207E, R258G, G328E/V/W, G356D) n'ont jusque là jamais été identifiées dans aucun autre cancer mais sont identiques à celles décrites dans une maladie congénitale de l'enfant appelée « Fibrodysplasie Ossifiante Progressive » (FOP) et ont pour conséquence d'activer constitutivement la voie des BMP/TGF-β. Ces mutations sont présentes exclusivement dans les tumeurs présentant une mutation dans le gène des histones H3.1.

D'autres résultats supportent également le rôle important d'*ACVR1* dans les DIPG. En effet, les analyses génomiques et transcriptomiques menées au cours du travail de collaboration avec le groupe de Charles Keller révèlent non seulement la présence de mutations dans *ACVR1* mais également un gain récurrent du chromosome 2 contenant ce gène (cf. **ARTICLE 4**). Nos résultats montrent aussi que le gain du chromosome 2 est plus fréquent dans les tumeurs porteuses d'une mutation du gène des histones H3.1 (cf. **ARTICLE 4**). D'autre part, l'analyse transcriptomique en RNA-Seq montre sa surexpression dans les DIPG de manière très significative par rapport au cerveau normal (cf. **ARTICLE 4**). De manière générale, ces données prouvent l'existence de multiples mécanismes de dérégulation d'*ACVR1* dans une large proportion des échantillons analysés, proche probablement de 40-50% des échantillons de DIPG.

Enfin, dans le cadre de l'évaluation préclinique du dasatinib sur nos modèles, *ACVR1* étant une cible secondaire connue de dasatinib, nous montrons que le traitement par des doses élevées (1-10 μM) de cette molécule induit une diminution de la phosphorylation des SMAD1/5/8 qui sont les effecteurs en aval de la voie des BMP/TGF-β, y compris dans des lignées qui ne présentent pas de mutation d'ACVR1 (cf. **ARTICLE 3**).

En outre, une première génération d'inhibiteurs d'ACVR1 est déjà disponible en préclinique (Yu et al. 2008). Nous avons utilisé l'un des inhibiteurs disponibles, le LDN-193189, sur des lignées de gliomes infiltrants du tronc cérébral. Les lignées ayant une mutation d'ACVR1 sont un peu plus sensibles que les lignées sauvages avec une IC_{50} proche de 1μM (cf **ARTICLE 1**). De nombreuses étapes sont encore nécessaires dans le

développement de ces molécules (notamment sur le plan du passage de la barrière hémato-encéphalique) et la dasatinib est pour l'instant une molécule intéressante sur ce point aussi.

Stratégies de découverte de traitements ciblés

Un des objectifs de ce travail était de présenter une stratégie efficace pour proposer un traitement ciblé dans les DIPG. En effet, compte-tenu du large éventail de nouveaux médicaments actuellement en développement, nous rapportons ici différentes approches permettant de définir de nouvelles cibles thérapeutiques. Les succès des thérapeutiques ciblées dans le cancer sont fréquemment limités d'une part, par le manque de connaissance sur les voies de signalisation critiques d'une tumeur chez un patient donné et d'autre part, par l'énorme quantité de données nécessaires pour l'estimation de cette signature génétique. Prédire la réponse à un agent donné est à la fois un enjeu capital et un défi extraordinaire de la médecine personnalisée en oncologie. L'approche actuelle est basée principalement sur la caractérisation génétique de la tumeur.

- Criblage pharmacologique et intégration de données génomiques (cf. **ARTICLE 4**)

La première approche concerne le ciblage de 84 médicaments sur 14 lignées cellulaires de DIPG. Ces évaluations effectuées en monothérapie mettent en évidence un effet antiprolifératif pour un nombre limité de composés. Parmi les composés actifs, seuls ont été retenus (« Hits ») ceux pour lesquels la concentration inhibant 50% de la prolifération cellulaire (IC_{50}) était inférieure à la concentration maximale mesurée dans le sérum (C_{max}), pour 3 ou plus des 14 lignées testées.

D'autre part, des analyses génomiques ont été réalisées conjointement à ce criblage par séquençage de l'exome et du transcriptome de 17 tumeurs primaires et des lignées. Ces données ont ensuite été intégrées aux résultats du criblage afin d'estimer le valeur prédictive des anomalies génétiques à cibler. Nos résultats montrent clairement un faible taux de mutations et d'anomalies du nombre de copies dans nos échantillons, et permettent ainsi de conclure sur le fait que les sensibilités aux médicaments observées ne corrèlent pas avec les rares aberrations génomiques détectées par séquençage de l'exome. De plus, l'absence relative de mutation oriente fortement vers une origine épigénétique de la maladie, ceci étant en cohérence avec la forte incidence des mutations d'histones retrouvée dans ces tumeurs.

En revanche, la combinaison de l'information sur les cibles des médicaments avec celle des gènes surexprimés dans les cellules tumorales permet la meilleure prédiction de la sensibilité d'une lignée à un médicament donné grâce au programme TIM (*Target Inhibition Map)* (Berlow et al. 2013). Ce programme de prédiction est basé sur les données de

perturbations fonctionnelles incluant des informations sur les interactions entre les drogues-protéines (au sens de cibles primaires et secondaires) et les sensibilités à un set d'apprentissage de drogues avec des cibles connues (données expérimentales injectées dans le modèle). Pour notre travail sur les lignées de DIPG, nous avons associé et testé l'apport de données supplémentaires à type de exome-sequencing (inventaire des anomalies génomiques, gains/pertes et mutations) et de RNAseq (utilisé pour définir l'expression des gènes). Comme attendu, les données du séquençage d'exomes n'augmentent pas le pouvoir de prédiction, par contre les données d'expression dans les lignées des gènes codant pour les différentes cibles considérées améliorent le précision de la prédication de la sensibilité aux drogues. Ceci a permis de générer une carte d'inhibition intégrant l'information de plusieurs expériences sur des lignées de DIPG. De cette carte résumée, on peut déduire par exemple que l'inhibition simultanée de CDK2 et de CDK9 devrait être une combinaison très efficace, tout comme l'inhibition combinée de PDGFRB et FGFR2. Ces données du modèle global nécessitent maintenant une validation externe.

L'approche TIM est intéressante pour prédire la réponse à des combinaisons (comme nous avons pu le valider sur certaines lignées de façon individuelle) ce qui peut-être très utile pour développer des combinaisons en clinique. D'autre part, si l'information obtenue sur un échantillon d'apprentissage peut être étendue à un échantillon test, on peut imaginer prédire les combinaisons les plus susceptibles d'être efficaces dans le plus grand nombre de lignées ou de tumeur.

De manière intéressante, parmi les combinaisons potentiellement efficaces dans les DIPG, l'inhibition de plusieurs HDAC semble prometteuse. En effet, cette hypothèse est validée expérimentalement *in vivo* par l'utilisation d'un inhibiteur d'HDAC (HDACi) multi-ciblé. Ces médicaments ne sont pas efficaces sur des lignées de gliome qui n'ont pas de mutation K27M des histones H3. En revanche, l'interprétation de cet effet anti-tumoral ne semble pas évidente compte tenu de la dérégulation épigénétique induite par la mutation de l'histone H3. En effet, les HDACi et la mutation H3 K27M conduisent directement et indirectement à l'acétylation des histones (Lewis et al. 2013) et par suite à l'activation de l'expression génique et ne sont - de ce point de vue, pas antagonistes. Des études sont en cours pour essayer d'expliquer ce phénomène.

On peut néanmoins discuter l'hypothèse suivante, en analysant les modifications transcriptomiques qui sont induites pas les HDACi dans les lignées de DIPG in vitro, nous constatons la disparition des traits phénotypiques importants présents dans ces lignées, à savoir les marqueurs mésenchymateux et les marqueurs des cellules souches embryonnaires. De plus, il existe une perte des marqueurs astrocytaires présents dans les deux lignées testées parallèle à l'apparition de marqueurs oligodendrogliaux sous traitement.

Enfin, sous inhibiteur des HDACi, les lignées surexpriment globalement les gènes des histones. C'est donc un remodelage épigénétique complet qui est induit par les HDACi dans ces lignées. Plusieurs oncogènes importants sont sous-exprimés, probablement indirectement comme *MYC* et *FOXM1* alors que des gènes suppresseurs de tumeurs comme *EPHB6* et *TP53* sont ré-exprimés. Ce n'est donc peut-être pas directement par une interaction avec le mécanisme oncogénique impliqué dans les DIPG au niveau de la triméthylation des histones H3 que les HDACi agissent.

- Signature de sensibilité (**ARTICLE 3**)

La seconde approche rapportée concerne l'évaluation préclinique de dasatinib, qui est un inhibiteur multi-ciblé de l'activité tyrosine-kinase, déjà indiqué dans certaines formes de leucémies et en cours de développement dans de nombreux autres cancers.

Le développement clinique de nouveaux médicaments inclue l'identification de sous-population de patients potentiellement répondeurs. Ceci passe par la recherche de marqueurs moléculaires permettant de prédire la réponse au traitement. Le dasatinib a lui-même fait l'objet de cette stratégie. Une signature d'expression génique liée à la sensibilité à cet inhibiteur a d'abord été établie *in vitro* sur un panel de lignées cellulaires de cancer du sein à partir des données transcriptomiques et de sensibilité, puis validée sur deux panels externes. Les auteurs ont ensuite cherché l'expression de cette signature sur des tumeurs primaires afin d'estimer la proportion de patients potentiellement répondeurs (Huang et al. 2007)

De la même manière, nous nous sommes intéressé de savoir si cette signature était exprimée dans notre cohorte de DIPG. En effet, celle-ci est significativement exprimée dans nos échantillons. Cette observation a constitué une première piste d'investigation. D'autre part, le fait que dasatinib compte parmi ses cibles le PDGFRα, qui représente une des cibles les plus attrayantes dans cette tumeur nous a conforté à persévérer dans cette voie. Nous avons ensuite montré que cette signature de sensibilité au dasatinib était surexprimée également dans nos modèles cellulaires en cohérence avec la grande sensibilité de ces lignées à ce médicament.

De manière générale, notre travail avec le dasatinib montre l'utilisation de signature prédictive publiée dans la littérature y compris dans des contextes cellulaires parfois différents constitue une approche à considérer dans la recherche de thérapie ciblée efficace.

Modèles d'étude préclinique dans les DIPG

- Obtention de nouveaux modèles cellulaires

Dans un premier temps, il a fallu nous affranchir de la première difficulté qui était d'obtenir des modèles expérimentaux pertinents.

Au début de ce travail, seulement quelques études rapportaient l'existence de modèles précliniques de DIPG issus de prélèvements autopsiques et cultivés en neurosphères (Monje et al. 2011) et sont en ces points discutables. Bien que l'autopsie reste un moyen d'obtenir du matériel tumoral en quantité plus importante que par biopsie, il n'en reste pas moins que celui-ci est représentatif de la maladie à un stade avancé. L'analyse en WGS rapporte dans ce sens un taux de mutations significativement plus élevé dans les échantillons de cas autopsiques comparé aux tumeurs non traitées (Taylor et al. 2014). D'autre part, si le prélèvement à l'autopsie permet d'obtenir du tissu tumoral en quantité plus importante, ceci ne garantit pas l'obtention de cellules viables permettant d'établir une lignée cellulaire.

Nous avons donc tenté d'obtenir de nouveaux modèles de DIPG à partir de prélèvements biopsiques.

Grace notre collaboration étroite avec le service de Neurochirurgie de l'Hôpital Necker-Enfants Malades, il a été possible de mettre en place une mise en culture systématique de matériel tumoral recueilli par biopsie stéréotaxique au diagnostic. Nous avons ainsi pu observer l'émergence de cultures avec un taux de succès inespéré dont certaines ont donné lieu à des lignées stables (cf. **ARTICLE 3**).

La mise en place d'une phase d'évaluation préclinique suggère idéalement d'utiliser des modèles stables, multiples et similaires dans leur mode de culture afin de valider la reproductibilité des résultats. De plus, l'établissement de modèles cellulaires adhérents reste plus aisé à la mise en place d'évaluations précliniques *in vitro*.

Un groupe de San Francisco rapporte l'existence d'une lignée de DIPG établie au diagnostic. Cependant, les auteurs ont anticipé le phénomène de sénescence très fréquemment observé lors de l'établissement de culture primaire en immortalisant ces cellules par le gène humain de la reverse transcriptase de la télomérase (hTERT) dès le deuxième passage (Hashizume et al. 2012). Relevons ici que nos modèles n'ont subi aucune transformation génétique.

Enfin, la présence de la mutation H3.3 K27M rajoute à la valeur pertinente de ces lignées.

Néanmoins, nous devons reconnaître quelques limites en lien avec le mode de culture appliqué. D'une part, le fait que ceux-ci aient été développés en milieu contenant du sérum peut apparaître moins fiable que s'ils l'avait été en milieu cellule-souche. En effet, la comparaison de ces deux modes de culture démontre que les modèles dérivés en milieu cellule-souche conservent davantage les caractéristiques génétiques et biologiques de la tumeur d'origine (J. Lee et al. 2006).

D'autre part, la mise en culture en conditions normoxiques reste également discutable. Compte tenu que l'hypoxie tumorale caractérise un des deux sous-groupes de DIPG (Puget et al. 2012) et que la pression en oxygène influence le caractère « cellule-souche » des cellules tumorales *in vitro* et leur comportement *in vivo* (Heddleston et al. 2009), il est aisé d'admettre que les modifications de ce paramètre impactent certainement sur la sélection et l'expansion de populations cellulaires particulières.

- Mise en place d'un modèle *vivo*

Naturellement, le franchissement de cette première étape nous a conduit à tenter de développer un modèle de DIPG *in vivo.* Chacune des 4 lignées établies ont donc été injectées dans le tronc cérébral de souris humanisées de type NSG adultes. Cependant, cette procédure n'a pas permis d'obtenir les modèles attendus. En effet, le suivi au long terme des animaux n'a pas révélé le développement de symptôme sous-jacent à un développement tumoral. Ces observations n'excluent pas une croissance transitoire des cellules tumorales comme cela l'a été démontré via un modèle xénogreffe bioluminescent (Caretti et al. 2012) ou bien une dissémination tumorale non destructive dans le cerveau de la souris (Angel Carbosa, communication personnelle). Seule l'analyse histologique par la recherche de marqueurs humains permettra de conclure quant à ces hypothèses (en cours). De manière évidente, l'absence de développement tumoral peut s'expliquer par le rôle du microenvironnement dans la croissance de cette tumeur. En effet, l'importance du microenvironnement a été mise en évidence par injection de cellules de gliome dans des cerveaux de rats juvéniles et de rats adultes où une différence de comportement dans la croissance tumorale a été observée (Q. Liu et al. 2008). Pour répondre à ce problème, nous devrons envisager d'injecter ces cellules après transfection stable avec un gène rapporteur permettant un suivi de la croissance tumorale par bioluminescence, au sein de cerveaux de souris néonatales aussi.

Enfin, ces lignées ne sont peut-être plus tumorigènes.

Questions clés

En perspectives du travail présenté dans cette thèse et des données actuelles de la littérature, quelques pistes intéressantes de travail ont été formulées pour des développements ultérieurs.

- Quelle est la cellule d'origine des DIPG ?

La différentiation phénotypique des DIPG pouvant être astrocytaire ou oligodendrogliale (Puget et al. 2012) implique que la cellule tumorale initiatrice provient d'une cellule peu différenciée de type cellule-souche ou progéniteurs glial.
D'autre part, nous avons mis en évidence que la mutation H3.3 K27M survient indifféremment dans les gliomes de la ligne médiane alors la mutation H3.1 K27M est spécifique des gliomes localisés dans le tronc cérébral. Cette observation suggère que ces anomalies ne sont capables de transformer qu'un type précis de cellules. Pour répondre à cette question, il conviendrait de les cultiver en milieu cellule-souche et de vérifier leur capacité à se différencier selon les différents types gliaux en les caractérisant par des marqueurs phénotypiques (Thirant et al. 2011).

- Quels sont les obstacles à la chimiothérapie intracérébrale ?

De nombreuses causes sont suspectées quant au manque d'efficacité des chimiothérapies constaté lors des essais cliniques. Outre la nécessité d'avoir un agent actif délivré en concentration suffisante ou encore d'utiliser un inhibiteur pertinent par rapport à l'anomalie ciblée, la question de la diffusion des molécules thérapeutiques au sein de cette tumeur cérébrale n'en demeure pas moins centrale. Cette question est particulièrement bienvenue dans les tumeurs cérébrales compte tenu de la présence de la barrière hémato-encéphalique (BHE). Il existe néanmoins des moyens de la contourner. Le système d'infusion en chambre convective ou *convection-enhanced delivery* (CED) permettant d'injecter des molécules thérapeutiques directement dans la tumeur apporte l'avantage de pouvoir traiter avec des doses plus importantes que par traitement systémique où la dose maximale tolérée est définie. D'autre part, le médicament peut-être connu comme étant le substrat d'un transporteur membranaire, limitant ainsi sa diffusion intracellulaire à l'image de la glycoprotéine P (P-gp), particulièrement présente au niveau de la BHE, l'utilisation concomitante avec un inhibiteur spécifique (tel que l'elacidrar) peut améliorer l'efficacité du médicament.

- Comment appréhender le phénotype invasif et diffus propre à ce gliome ?

La spécificité de ce gliome repose essentiellement sur son caractère invasif. En effet, à la différence des autres gliomes malins, les cellules tumorales prolifèrent et infiltrent le tissu cérébral de manière simultanée en induisant la formation d'une masse tumorale diffuse et par conséquent non opérable. Ce phénotype constitue un critère essentiel afin de pouvoir considérer les futurs modèles et évaluer l'efficacité anti-tumorale de nouveaux médicaments, or la plupart des modèles disponibles ne rendent pas compte de ce phénotype.

- Comment cibler spécifiquement les mutations de l'histone H3 ?

Enfin la forte prévalence des mutations d'histone illustre toute la singularité de ce cancer. Si leur effet a été décrit, leur rôle dans la progression tumorale n'a toujours pas été clairement élucidé et celles-ci représentent une cible thérapeutique à explorer. L'originalité de cette anomalie ne permet pas d'orienter vers une stratégie particulière à *priori* et conduira plutôt vers une approche de ciblage haut-débit telle que des banques de composés ou encore des cribles shRNA.

Conclusion générale

Le gliome infiltrant du tronc cérébral reste à ce jour une tumeur rare et universellement fatale et représente un défi redoutable en neuro-oncologie.

Les particularités cliniques, génétiques et biologiques abordées au cours des chapitres de ce manuscrit nous ont permis d'appréhender cette entité tumorale singulière qui n'a jusqu'ici, jamais répondu à une quelconque approche thérapeutique*. Nous avons maintenant des directions plus claires pour avancer dans le développement thérapeutique pour les DIPG et relever ce défi de l'oncologie pédiatrique en 2014.

ANNEXE

Cancer Cell
Annexe
Article

Reduced H3K27me3 and DNA Hypomethylation Are Major Drivers of Gene Expression in K27M Mutant Pediatric High-Grade Gliomas

Sebastian Bender,[1,2,23] Yujie Tang,[3,4,23] Anders M. Lindroth,[5,23] Volker Hovestadt,[6] David T.W. Jones,[1] Marcel Kool,[1] Marc Zapatka,[6] Paul A. Northcott,[1] Dominik Sturm,[1] Wei Wang,[6] Bernhard Radlwimmer,[6] Jonas W. Højfeldt,[7] Nathalène Truffaux,[8] David Castel,[8] Simone Schubert,[3,4] Marina Ryzhova,[9] Huriye Şeker-Cin,[1] Jan Gronych,[6] Pascal David Johann,[1,2] Sebastian Stark,[1,10] Jochen Meyer,[11,12] Till Milde,[13,14] Martin Schuhmann,[15] Martin Ebinger,[16] Camelia-Maria Monoranu,[17] Anitha Ponnuswami,[3] Spenser Chen,[3] Chris Jones,[18] Olaf Witt,[13,14] V. Peter Collins,[19] Andreas von Deimling,[11,12] Nada Jabado,[20] Stephanie Puget,[21] Jacques Grill,[8] Kristian Helin,[7] Andrey Korshunov,[11,12] Peter Lichter,[6] Michelle Monje,[3,4,22] Christoph Plass,[5,24,*] Yoon-Jae Cho,[3,4,24,*] and Stefan M. Pfister[1,2,24,*]

[1]Division of Pediatric Neurooncology, German Cancer Research Center (DKFZ), 69120 Heidelberg, Germany
[2]Department of Pediatric Oncology, Hematology, and Immunology, Heidelberg University Hospital, 69120 Heidelberg, Germany
[3]Department of Neurology and Neurological Sciences, Stanford University School of Medicine, Stanford, CA 94305, USA
[4]Department of Neurosurgery, Stanford University School of Medicine, Stanford, CA 94305, USA
[5]Division of Epigenomics and Cancer Risk Factors, German Cancer Research Center (DKFZ), 69120 Heidelberg, Germany
[6]Division of Molecular Genetics, German Cancer Research Center (DKFZ), 69120 Heidelberg, Germany
[7]Biotech Research and Innovation Centre (BRIC) and Centre for Epigenetics, University of Copenhagen, 2200 Copenhagen, Denmark
[8]Institut Gustave Roussy, Laboratoire de Vectorologie et Thérapeutiques Anticancéreuses, Unité Miste de Recherche du Centre National de la Recherche Scientifique (CNRS) 8203, Université Paris Sud, Villejuif 94800, France
[9]Department of Neuropathology, NN Burdenko Neurosurgical Institute, Moscow 125047, Russia
[10]Department of General Pediatrics, Heidelberg University Hospital, 69120 Heidelberg, Germany
[11]Department of Neuropathology, Heidelberg University Hospital, 69120 Heidelberg, Germany
[12]Clinical Cooperation Unit Neuropathology, German Cancer Research Center (DKFZ), 69120 Heidelberg, Germany
[13]Clinical Cooperation Unit Pediatric Oncology, German Cancer Research Center (DKFZ), 69120 Heidelberg, Germany
[14]Section of Pediatric Brain Tumors, Department of Pediatric Oncology, Hematology and Immunology, Heidelberg University Hospital, 69120 Heidelberg, Germany
[15]Department of Neurosurgery, University Hospital Tübingen, 72076 Tübingen, Germany
[16]Department of Hematology and Oncology, Children's University Hospital Tübingen, 72076 Tübingen, Germany
[17]Department of Neuropathology, Institute of Pathology, University Würzburg, 97080 Würzburg, Germany
[18]Divisions of Molecular Pathology and Cancer Therapeutics, The Institute of Cancer Research, Sutton, Surrey 5NG, UK
[19]Division of Molecular Histopathology, Department of Pathology, University of Cambridge, Cambridge 0QQ, UK
[20]Departments of Pediatrics and Human Genetics, McGill University and the McGill University Health Center Research Institute, Montreal, QC H3Z 2Z3, Canada
[21]Département de Neurochirurgie Pédiatrique et Unité 845, l'Institut National Recherche Médicale (INSERM), Université Paris V Descartes, Hôpital Necker Enfants Malades, 75743 Paris, France
[22]Department of Pediatrics, Stanford University School of Medicine, Stanford, CA 94305, USA
[23]These authors contributed equally to this work
[24]Co-senior authors
*Correspondence: c.plass@dkfz.de (C.P.), yjcho1@stanford.edu (Y.-J.C.), s.pfister@dkfz.de (S.M.P.)
http://dx.doi.org/10.1016/j.ccr.2013.10.006

SUMMARY

Two recurrent mutations, K27M and G34R/V, within histone variant H3.3 were recently identified in ~50% of pHGGs. Both mutations define clinically and biologically distinct subgroups of pHGGs. Here, we provide further insight about the dominant-negative effect of K27M mutant H3.3, leading to a global reduction of

Significance

Loss of polycomb repression, which is reflected by reduced H3K27me3 levels, is associated with unfavorable prognosis in several cancer entities. Here, we highlight the molecular mechanism of global H3K27me3 loss in pHGGs harboring the K27M mutation of histone H3.3. Additionally, we provide evidence that H3K27me3 occupancy as well as DNA methylation are specifically altered in K27M mutant pHGGs. Both deregulated epigenetic mechanisms cooperate to establish a transcriptional program that is specific for K27M mutant pHGGs. In conclusion, our data shed light on the molecular consequences induced by one of the two histone H3.3 mutations driving tumorigenesis in ~50% of pHGGs.

the repressive histone mark H3K27me3. We demonstrate that this is caused by aberrant recruitment of the PRC2 complex to K27M mutant H3.3 and enzymatic inhibition of the H3K27me3-establishing methyltransferase EZH2. By performing chromatin immunoprecipitation followed by next-generation sequencing and whole-genome bisulfite sequencing in primary pHGGs, we show that reduced H3K27me3 levels and DNA hypomethylation act in concert to activate gene expression in K27M mutant pHGGs.

INTRODUCTION

Pediatric high-grade gliomas (pHGGs), which include glioblastomas and diffuse intrinsic pontine gliomas (DIPGs), represent a highly malignant type of brain tumor in children, which is reflected by a 3-year overall survival rate of only 5%–10% (Louis et al., 2007). Similar to other cancers, comprehensive sequencing studies have revealed a variety of genetic abnormalities in chromatin remodeling factors in pHGGs (Fontebasso et al., 2013). However, unique to HGGs in children and adolescents are two recurrent mutations within the histone H3.3 gene *H3F3A*, which have been identified in ~50% of cases (Schwartzentruber et al., 2012; Wu et al., 2012). These two mutations result in substitutions at residues K27 and G34 on the amino-terminal tail of H3.3. The K27 mutations universally substitute the K27 with a methionine (K27M), whereas the G34 mutations typically replace the G34 with an arginine (G34R), and in some cases with a valine (G34V). Similar mutations have also been reported at a lower frequency in *HIST1H3B*, which encodes the canonical histone H3.1. These *HIST1H3B* mutations have exclusively been identified in DIPGs (Wu et al., 2012). Interestingly, K27M and G34R/V mutations are associated not only with clinical parameters such as patient age or tumor location, but they also exhibit a mutation-specific gene expression and DNA methylation profile (Khuong-Quang et al., 2012; Sturm et al., 2012). Recently, it has been reported that K27M mutant pHGGs display a global decrease of the repressive posttranslational histone modification H3K27me3 (Chan et al., 2013; Lewis et al., 2013; Venneti et al., 2013), which under physiological conditions is mainly established by the H3K27-specific histone methyltransferase enhancer of zeste 2 (EZH2) within the Polycomb Repressive Complex 2 (PRC2) (Margueron and Reinberg, 2011). Mechanistically, reduction of H3K27me3 levels is caused by an inhibitory effect of the K27M mutant H3.3 protein (Lewis et al., 2013).

In this study, we explore the dominant-negative effect of K27M mutant H3.3 and the association of K27M-induced H3K27me3 reduction with DNA methylation and gene expression.

RESULTS

H3K27me3 Is Strongly Reduced in K27M Mutant pHGGs

Recent studies have reported a reduction of H3K27me3 levels in K27M mutant pHGGs by using immunohistochemistry (IHC) on small numbers of patient samples ($n \leq 20$ tumors; Lewis et al., 2013; Venneti et al., 2013). To investigate whether immunohistochemical testing of H3K27me3 abundance in pHGGs might be useful for routine clinical application, we performed IHC for H3K27me3 in a large cohort of pHGGs with known *H3F3A* mutation status (n = 104). Strikingly, all K27M mutant pHGGs (n = 21) showed a strong reduction of overall H3K27me3 levels (Figure 1A), even though the antibody detects H3K27me3 at all H3 variants including canonical histone proteins. H3K27me3-positive endothelial cells lining the blood vessels show that H3K27me3 is specifically lost in the tumor cells (Figure 1B). In contrast, all G34R/V mutant cases (n = 7) and 74 out of 76 pHGGs (97%) without H3.3 mutation (wild-type H3.3 [H3.3-WT]) were strongly positive for H3K27me3. No mutation of canonical H3.1 was found in the two H3K27me3-negative tumors without H3.3 mutation. The average number of H3K27me3 immunopositive cell nuclei in K27M mutant pHGGs did not exceed 8% (average, 5%) compared with at least 71% (average, 95%) of H3K27me3-positive cell nuclei in non-K27M tumor cores (Figure 1C). Moreover, no global differences were observed for several other key histone marks including H3K4me3, H3K9me3, and H3K36me3, which are all known to also substantially influence chromatin structure and gene expression. Immunopositivity for these three histone marks was detected in all analyzed tumor samples (data not shown).

To further confirm the IHC results, we isolated histone extracts from a non-overlapping cohort of additional primary pHGG samples and studied H3K27me3 levels by western blot analysis. Two different H3K27me3-specific antibodies detected significantly lower H3K27me3 levels in all K27M mutant tumors (n = 3) compared with H3.3-WT samples (n = 2) and a G34R mutant tumor (Figure 1D).

We also determined H3K27me3 levels in a set of primary cultures/cell lines, which cover the whole spectrum of H3.3 mutations that have been identified in primary pHGG tumors. We used primary cell lines established from freshly resected K27M mutant pHGGs (NEM157 and NEM165) as well as a G34R mutant tumor (MGBM1) and compared them with the levels in a human embryonal kidney cell line (HEK293T, H3.3-WT), human epithelial carcinoma cells (HeLa-S3, H3.3-WT), and two well-established pediatric glioblastoma cell lines (SF188, H3.3-WT and KNS42, H3.3-G34V). Whereas H3K27me3 levels were found to be subject to fluctuations in non-K27M cell types (very high in HEK293T, low in MGBM1), H3K27me3 was almost completely absent in NEM157 and NEM165 cells, which harbor a heterozygous K27M mutation (Figure 1E).

H3.3-K27M Is a Dominant-Negative Inhibitor of H3K27 Di- and Trimethylation

All described *H3F3A* mutations in primary tumors and cell lines are heterozygous and thus affect only one *H3F3A* allele, indicating a dominant-negative effect of the K27M mutant protein on the wild-type histone H3 protein. Although transgene-induced reduction of H3K27me3 was shown to take place in a cell-type-independent manner in HEK293T, human astrocytes, mouse embryonic fibroblasts, and human neural stem cells (NSCs; Chan et al., 2013; Lewis et al., 2013), we aimed to mimic the genetic background of pHGGs more closely by generating isogenic SF188 glioblastoma cells stably overexpressing ectopic

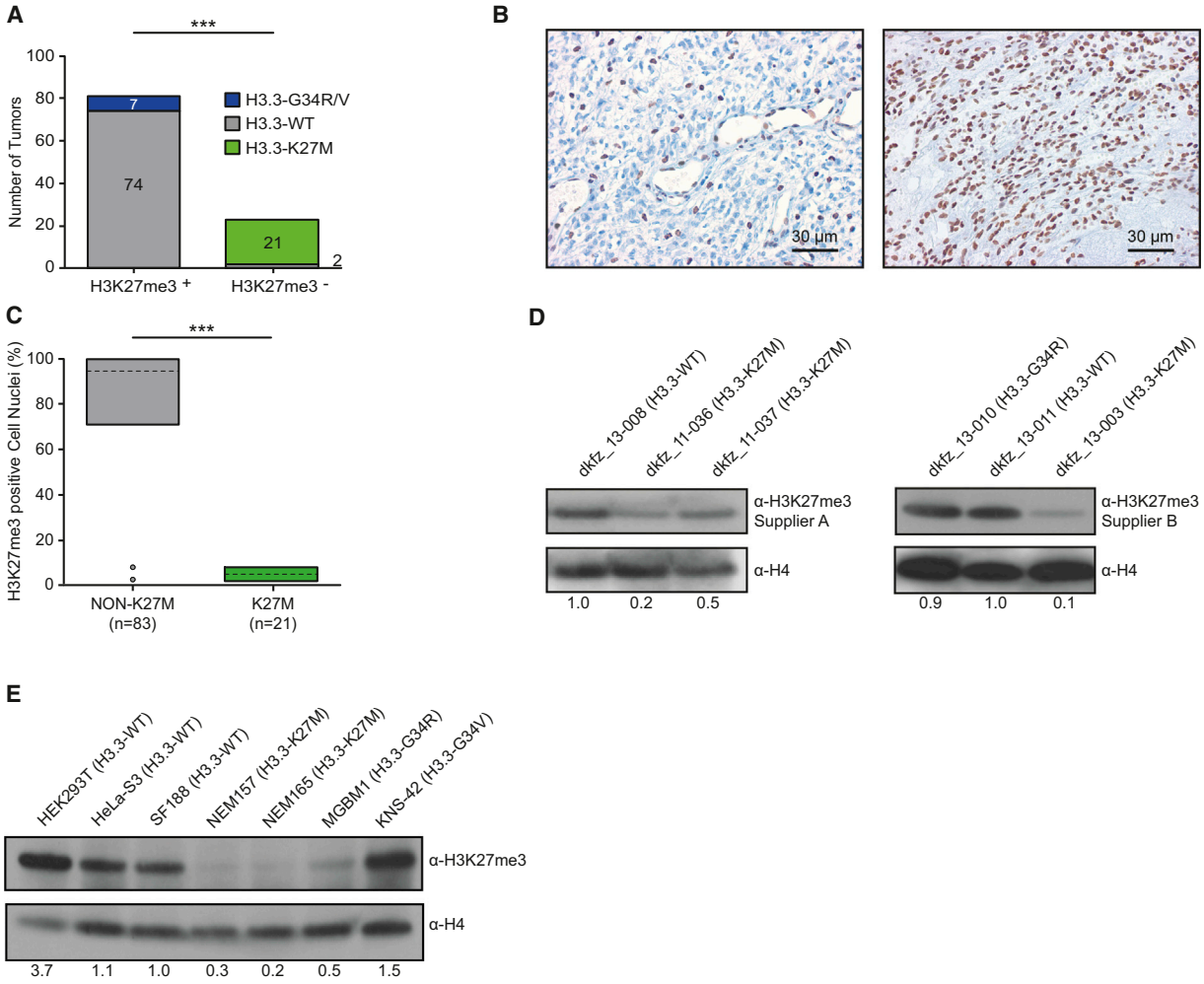

Figure 1. pHGGs Carrying Histone H3.3-K27M Mutations Show a Global Reduction of K27 Trimethylation on Histone H3

(A) Summary of H3K27me3 immunostaining of 104 pHGGs containing wild-type (H3.3-WT), K27M mutant, or G34R/V mutant H3.3 (***$p < 0.001$).

(B) Representative results of immunohistochemistry for H3K27me3 of a K27M mutant (left) and H3.3-WT (right) pHGG.

(C) Quantification of H3K27me3 positive cell nuclei in pHGGs without (non-K27M) or with the K27M mutation (200 cell nuclei/tumor) (***$p < 0.001$). Box plots represent the maximum/minimum number (%) of H3K27me3 positive cell nuclei. The mean is indicated by the dashed line.

(D) Western blot analysis of histone extracts from primary pHGGs using two different H3K27me3-specific antibodies. Numbers below the western blots indicate H3K27me3 band intensity (normalized to total histone H4) measured by using ImageJ.

(E) Evaluation of H3K27me3 expression in patient-derived pHGG cell lines, HEK293T, and HeLa-S3 cells. Numbers below the western blots indicate H3K27me3 band intensity (normalized to total histone H4) measured by using ImageJ.

wild-type, K27M or G34R mutant H3.3. Initially, at 6 days after transduction, K27M-expressing SF188 cells did not show differences in H3K27 trimethylation compared with cells overexpressing H3.3-WT or the G34R variant (Figure S1A available online). However, it was previously reported that reshaping of the epigenome occurs over an extended time period (Turcan et al., 2012). In line with this, Chan et al. (2013) showed that K27M-induced reduction of H3K27me3 is dependent on several cell divisions. Therefore, we re-analyzed transduced SF188 cells maintained in culture for 70 days (25 passages). At this later time point, H3K27me3 levels were significantly reduced in SF188 cells expressing the K27M mutant (Figure 2A). We further verified this regulatory effect of the K27M transgene on global H3K27me3 levels in vitro by using wild-type, K27M-transduced, or G34R-transduced HEK293T, cultured for the same time period (Figure 2A).

To confirm the dominant-negative effect of the K27M mutant on endogenous H3 histones, we immunoprecipitated mononucleosomes using epitope-tagged wild-type or K27M mutant H3.3 expressed in SF188, HEK293T, and HeLa-S3 cells for at least 10 days. As expected, mono-, di-, and trimethylation of H3K27 was absent on exogenous K27M mutant H3.3 (Figure 2B, labeled with *). In addition, reduced di- and trimethylation was also detected at endogenous wild-type H3 proteins within the same nucleosomes (Figure 2B, labeled with **; Table S1) as well as with global endogenous H3 protein (Figure 2B, labeled with ***; Table S1). Notably, H3K27me1 levels were found to be unchanged at wild-type H3 within the same nucleosome, as

well as overall endogenous H3 protein (Figure 2B). Together, our results strongly suggest that K27M mutant H3.3 interferes with PRC2 function, as this complex is responsible for di- and trimethylation (but not monomethylation) of H3K27 through its enzymatic subunit EZH2 (Margueron and Reinberg, 2011).

K27M Mutant H3.3 Aberrantly Binds PRC2 and Interferes with Its Enzymatic Activity

Di- and trimethylation of K27 at histone H3 is mainly mediated by the nonredundant H3K27-specific histone methyltransferase EZH2, which is part of PRC2. Recently, it has been reported that synthetic peptides containing the K27M mutant interact with the catalytic site of EZH2 (Lewis et al., 2013). By performing coimmunoprecipitation (coIP) experiments in SF188, HEK293T, and HeLa-S3 cells ectopically expressing HA-tagged wild-type or K27M mutant H3.3, we found that EZH2 as well as the PRC2 component suppressor of zeste homolog 12 (SUZ12) was dramatically enriched in immunoprecipitated K27M-containing mono-nucleosomes relative to wild-type H3.3 protein in all three cell lines (Figure 2C; Table S1). Conversely, coIP for endogenous EZH2 in all three cell lines led to an enrichment of exogenous K27M mutant H3.3 compared with the exogenous wild-type H3.3 protein (Figure 2D).

Next, we investigated whether PRC2 complexes bound to K27M mutant H3.3 were associated with an altered enzymatic activity of EZH2. Using total chromatin lysate and an immunoprecipitation (IP) fraction bound to anti-HA beads from both wild-type H3.3 and K27M-transduced SF188, HEK293T, or HeLa-S3 cells, we performed in vitro histone methyltransferase (HMT) assays. We observed a significant decrease of HMT activity of 40%–70% with chromatin lysate from all three K27M-transduced cell lines. Even more strikingly, with the IP fraction composed of K27M-containing mono-nucleosomes from each cell line, EZH2 enzymatic activity was decreased by at least 85% (Figure 2E; Figure S1B). To evaluate the inhibitory effect of K27M mutant H3.3 on EZH2 catalytic activity, we determined the IC_{50} value of K27M-containing peptides and compared it with the highly potent and selective small molecule EZH2-inhibitor GSK343 (Verma et al., 2012). Whereas addition of wild-type H3.3 peptide was found to have a stimulatory effect on PRC2 activity (Figure S1C), the IC_{50} value of the K27M-containing peptide (0.067 μM) was in a range similar to that of GSK343 (0.027 μM) (Figure 2F). Instead of using synthetic peptides, we also performed in vitro HMT assays using oligonucleosomes purified directly from K27M mutant NEM157 cells or SF188 cells (H3.3-WT). The addition of oligonucleosomes purified from NEM157 cells led to a significant inhibition of PRC2 enzymatic activity compared with SF188 oligonucleosomes (Figure S1D).

In contrast, the enzymatic activities of the H3K27me3 demethylases JMJD3/UTX were found to remain largely unchanged between wild-type and K27M-containing mono-nucleosomes when tested with the same chromatin lysates and IP-bound fractions (Figure 2G).

Genome-wide Analysis of H3K27me3 in K27M Mutant pHGGs

To generate genome-wide maps of H3K27me3 in primary K27M mutant pHGGs, we performed chromatin IP followed by next-generation sequencing (ChIP-Seq) on fresh-frozen primary tumor tissue from two K27M mutant pHGGs and two pHGGs without H3.3 mutation. In addition, we conducted H3K27me3 ChIP-Seq in the K27M mutant primary cell line NEM165 as well as the established pediatric glioblastoma cell line SF188 (H3.3-WT). As expected, the identified number of H3K27me3 ChIP-Seq peaks in both K27M mutant pHGGs was substantially lower across the entire genome (promoter: transcriptional start site [TSS] ± 3 kb, gene body, intergenic regions) compared with both H3.3-WT tumors (Figure 3A). The proportions of overlapping ChIP-Seq peaks among H3.3-WT pHGGs and among K27M mutant tumors were comparable (37% overlapping H3K27me3 peaks in both groups; Figure 3B). In line with the K27M-induced reduction of H3K27me3, the number of H3K27me3 peaks unique to H3.3-WT tumors was four times of the number of peaks unique to K27M mutant pHGGs (Figure 3B).

Although global H3K27me3 levels detected by western blot are dramatically reduced in K27M mutant NEM165 cells (Figure 1E), there was no clear reduction in peak number in these cells compared with SF188 cells (Figure 3A). Moreover, only 57% of ChIP-Seq Peaks detected in NEM165 cells overlapped with peaks detected in at least one of the K27M mutant primary tumors (Figure 3B). In contrast, we identified a higher concordance between SF188 cells and H3.3-WT primary tumors (92% overlapping ChIP-Seq peaks).

Next, we looked at global differences in H3K27me3 ChIP-Seq peaks (n = 21,217) identified in primary tumors (Figure 4A). In total, 75% of all detected H3K27me3 peaks were found to be reduced or lost in K27M mutant tumors (n = 15,853). However, our analysis also revealed a significant number of H3K27me3 peaks showing increased H3K27me3 occupancy in K27M mutant tumors (n = 5,364). Even more interestingly, peaks with reduced H3K27me3 levels had a significantly different genomic location to peaks with increased H3K27me3 occupancy (χ^2 test; $p < 0.01$). Peaks with reduced and increased H3K27me3 levels in K27M mutant tumors were more frequently associated with gene promoters and intergenic regions, respectively (Figure 4A).

In order to find out to what extent our in vitro cultures recapitulate H3K27me3 occupancy in primary pHGGs, we conducted a similar analysis with global peak distribution for the analyzed cell lines (NEM165 and SF188). This highlighted substantial differences in H3K27me3 distribution between primary tumors and both cell lines (Figures S2A and S2B). Due to these differences, ChIP-Seq data from in vitro cultures were excluded from subsequent analyses.

Alterations in H3K27me3 occupancy in the promoter have been shown to affect gene expression. Therefore, we compared gene expression data of 12 K27M mutant tumors and 10 pHGGs without H3.3 mutations to specifically analyze H3K27me3 occupancy around the TSS of differentially expressed genes. In doing so, we identified a total of 294 genes as being differentially expressed ($p < 0.01$; Student's t test, Benjamini-Hochberg correction; Figure S2C; Table S2). Gene ontology analysis of differentially expressed genes revealed a significant enrichment of genes involved in neuronal differentiation (Table S3). Compared with all other genes, differentially expressed genes were found to be significantly overrepresented within our set of genes showing alterations in H3K27me3 ($p < 0.01$, Fisher's exact test). Remarkably, 66% (95 out of 143) of transcriptionally

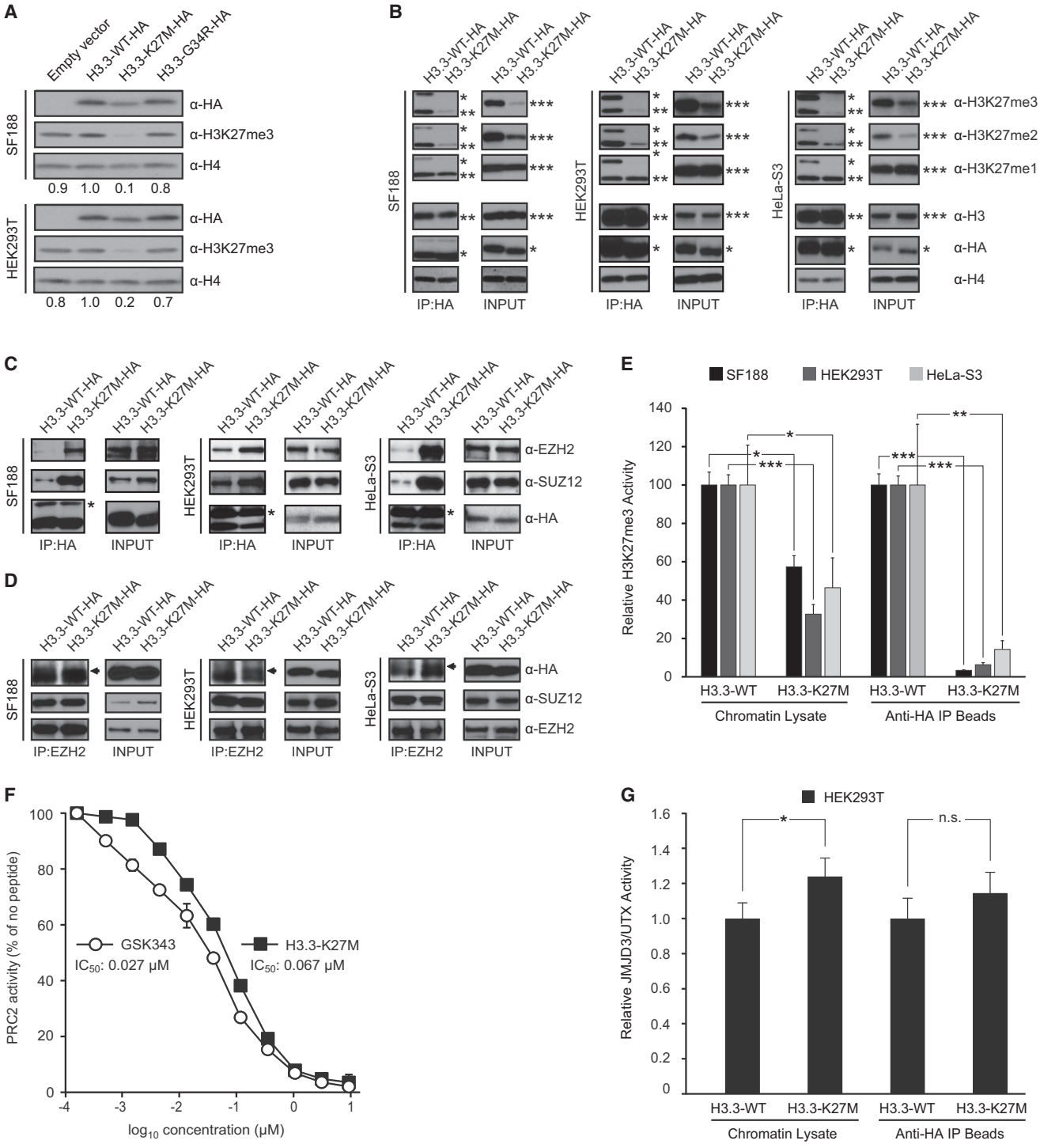

Figure 2. K27M Mutant H3.3 Exerts a Dominant-Negative Effect on the Methylation State of Wild-Type H3K27

(A) Western blot of H3K27me3 in histone extracts from SF188 and HEK293T cells transduced with HA-tagged H3.3 (WT, K27M, or G34R). Numbers below the western blot indicate H3K27me3 band intensity (normalized to total histone H4) measured by using ImageJ.

(B) Western blot analysis of methylated marks on mono-nucleosome immunoprecipitates of HA-tagged histone H3.3 in SF188, HEK293T, and HeLa-S3 cells. The symbols * and ** denote exogenous HA-tagged histone H3.3 and endogenous histone H3 within mono-nucleosomes, respectively; *** denotes total endogenous histone H3. Anti-histone H3, H4, anti-HA, and input protein lysates are shown as controls.

(C) Western blot analysis of EZH2 and SUZ12 in immunorecipitates of exogenous HA-tagged histone H3.3 (WT or K27M) expressed in SF188, HEK293T, or HeLa-S3 cells. Anti-HA is shown as loading control. The * denotes IgG light chain.

(D) Exogenous HA-tagged H3.3 (WT or K27M) coimmunoprecipitated with endogenous EZH2 in SF188, HEK293T, and HeLa-S3 cells was detected by western blot analysis. Anti-EZH2 and anti-SUZ12 are shown as loading controls.

(legend continued on next page)

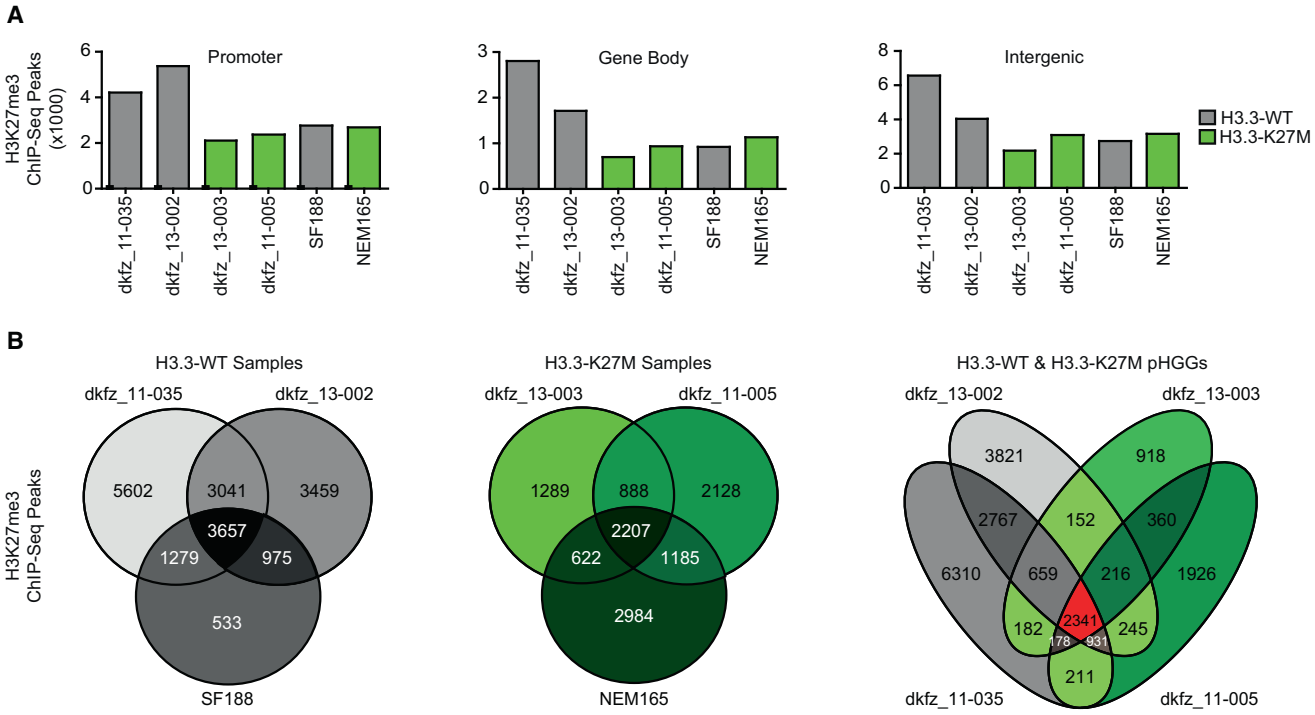

Figure 3. H3K27me3 Occupancy in Primary pHGGs and in Vitro Cultures

(A) Bar chart representing the numbers of overall H3K27me3 ChIP-Seq peaks identified in different genomic regions in four pHGGs and the two patient-derived glioblastoma cell lines, SF188 and NEM165.

(B) Venn diagrams illustrating overlapping H3K27me3 ChIP-Seq peaks in H3.3-WT and/or K27M mutant samples.

upregulated genes in K27M mutant pHGGs were found to hold decreased levels of H3K27me3 compared with H3.3-WT tumors (Figure 4B). Elevated gene expression and decreased H3K27me3 occupancy were found for several genes that are known to be involved in gliomagenesis, such as the platelet-derived growth factor receptor-α (*PDGFRA*) gene (Figure 4B; Table S2) (Verhaak et al., 2010; Zarghooni et al., 2010).

In addition to overall reduction of H3K27me3, we also identified several genes/loci with increased levels of H3K27me3 and concomitant reduction of gene expression specifically in K27M mutant pHGGs (Figures 4A and 4B; Table S2). One example showing reduced expression and a gain of H3K27me3 occupancy in its promoter in K27M mutant pHGGs was the MHC class I polypeptide-related sequence A (*MICA*) gene (Figure 4B). Downregulation of this gene has been suggested as a potential mechanism of immune evasion in malignant gliomas (Eisele et al., 2006). By comparing ChIP-Seq data of a K27M mutant DIPG cell line and NSCs, a recent study also reported on the K27M-specific gain of H3K27me3 at specific genes (Chan et al., 2013). In line with this study, the long isoform of *CDK6* was also found to hold elevated levels of H3K27me3 in both K27M mutant primary pHGGs (Figure S2D).

In keeping with the above findings, among the differentially expressed genes we found a significant ($p < 0.01$, Fisher's exact test) enrichment of genes known to be targeted by H3K27me3 (PRC2 target genes; Bernstein et al., 2006; Lee et al., 2006). Therefore, we subsequently visualized H3K27me3 occupancy around the TSSs of PRC2 target genes (n = 606; Figure 4C). Based on H3K27me3 occupancy, PRC2 target genes were divided into two groups. As expected, the large majority of these genes (n = 461) had lower H3K27me3 levels in K27M mutant pHGGs compared with H3.3-WT tumors (H3K27me3 LOSS in K27M). In line with this, average expression of these genes was significantly higher in K27M mutant pHGGs (n = 12) than in H3.3-WT samples (n = 10; Figure 4C). In contrast, PRC2 target genes holding increased levels of H3K27me3 in K27M mutant tumors (n = 145; H3K27me3 GAIN in K27M) showed reduced average expression in K27M mutant pHGGs (Figure 4C).

Alterations of H3K27me3 and DNA Methylation Establish the K27M-Specific Transcriptional Program

Numerous studies have shown a dynamic interaction between H3K27me3 and DNA methylation (Cedar and Bergman, 2009).

(E) In vitro histone H3K27 methyltransferase enzymatic assay using total chromatin lysate or immunoprecipitated HA-tagged H3.3 complexes (WT or K27M) from SF188, HEK293T, or HeLa-S3 cells (***$p < 0.001$, **$p < 0.01$, *$p < 0.05$).

(F) IC_{50} measurement of K27M peptide (AA16–46) and the EZH2 inhibitor GSK343. Assay was performed in duplicates.

(G) In vitro JMJD3/UTX histone demethylase activity assay with the same samples from HEK293T cells used in (D) (*$p < 0.05$; n.s., not significant). Error bars represent standard deviation. See also Figure S1 and Table S1.

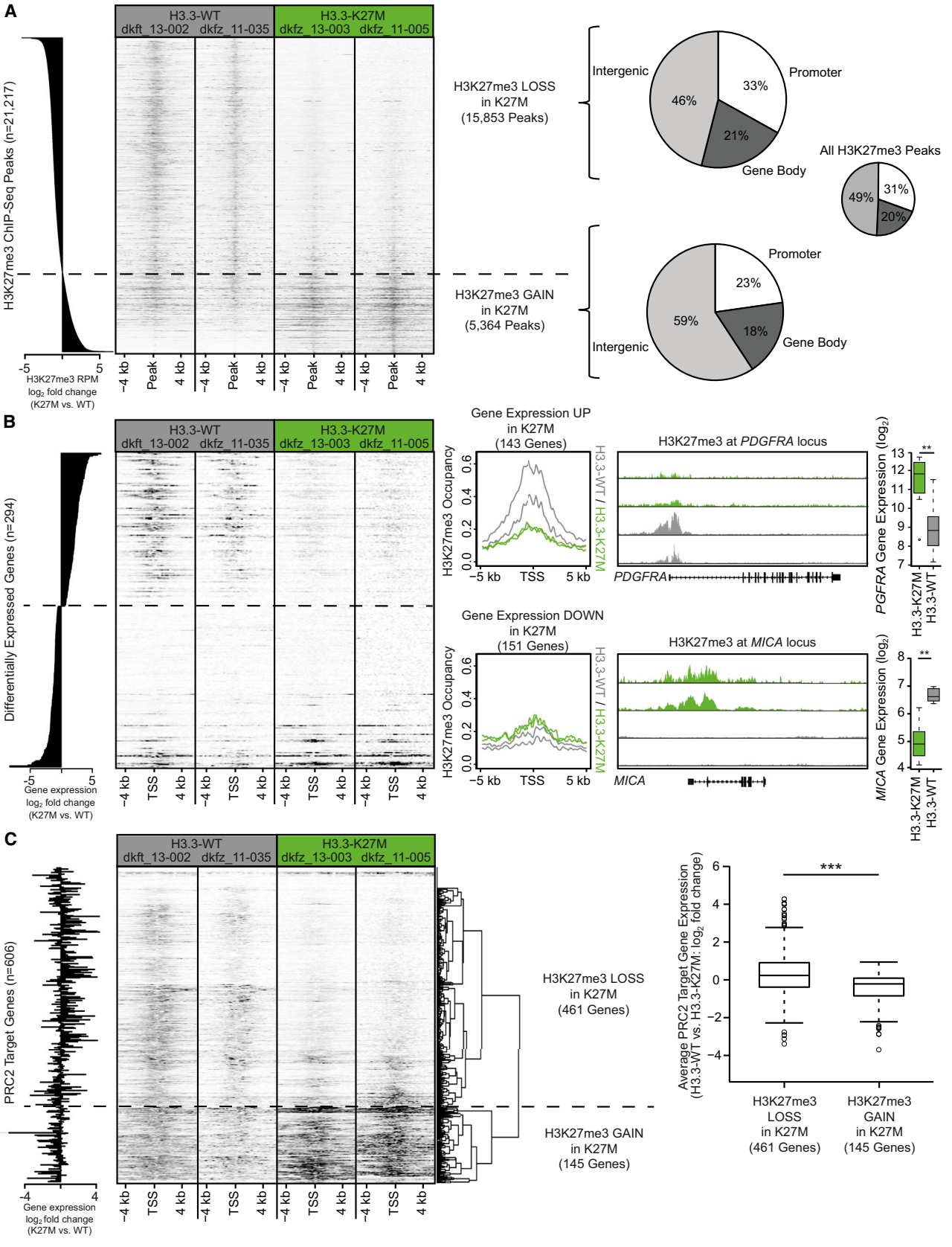

(legend on next page)

Previous work from us and others demonstrated that both of these epigenetic modifications are specifically altered in K27M mutant pHGGs (Lewis et al., 2013; Sturm et al., 2012; Venneti et al., 2013). To study DNA methylation in more detail and to find a potential cross-talk between H3K27me3 and DNA methylation in pHGGs, we subjected 13 primary tumors (six H3.3-WT and seven K27M) to whole-genome bisulfite sequencing (WGBS; see Table S4 for an overview of the WGBS statistics). Globally, K27M mutant tumors have a DNA methylation profile substantially different from that of H3.3-WT pHGGs (Figures 5A and S3A). As indicated in our previous study using DNA methylation arrays (Sturm et al., 2012), WGBS data confirmed an overall reduction in global DNA methylation levels in K27M mutant tumors compared with H3.3-WT pHGGs (Figure 5B). In line with this, we identified a substantially higher number of hypomethylated rather than hypermethylated differentially methylated regions (DMRs) in our data set when comparing K27M mutant tumors versus H3.3-WT pHGGs (Figure 5C).

Next, we analyzed overall DNA methylation patterns in genomic regions flanking the TSSs (± 5 kb) of differentially expressed genes (n = 294). As shown in Figure 5D, we found DNA hypomethylation to be specifically pronounced at genomic regions directly downstream of the TSSs of transcriptionally upregulated genes such as eyes absent homolog 1 (*EYA1*; Figure 5D; Auvergne et al., 2013). In contrast, DNA hypermethylation was found to be centered around the TSSs of transcriptionally downregulated genes such as PDZ and LIM domain 4 (*PDLIM4*; Figure 5D; de Tayrac et al., 2011). While hypomethylated DMRs were found at 54 out of 143 (38%) of transcriptionally upregulated genes, hypermethylated DMRs were identified at only 15% (22 out of 151) of downregulated genes (Table S2). However, DNA hypomethylation as well as hypermethylation were significantly associated with transcriptional activation and repression, respectively ($p < 0.01$; Fisher's exact test).

Subsequently, we aimed to find out whether regions with loss or gain of H3K27me3 were specifically associated with alterations in DNA methylation. In doing so, average DNA methylation at genomic regions flanking H3K27me3 peaks as identified by ChIP-Seq did not show significant changes (Figure S3B). However, H3K27me3 occupancy at hypomethylated gene promoters in K27M mutant pHGGs was found to be substantially lower compared with hypermethylated promoters in these tumors (Figure 5E). Although these results do not support a global link between H3K27me3 and DNA methylation, we identified a substantial number of transcriptionally activated genes such as protocadherin-7 (*PCDH7*) showing loss of H3K27me3 together with DNA hypomethylation (Figure 5E). The PRC2 target gene *PCDH7* has been shown to promote metastasis in breast cancer and is known to be targeted by DNA methylation (Beukers et al., 2013; Li et al., 2013). In total, 30% (43 out of 143) of all upregulated genes in K27M mutant pHGGs were found to hold decreased H3K27me3 levels together with DNA hypomethylation at the promoter. In contrast, only 7% (10 out of 143) of upregulated genes show DNA hypomethylation but no alteration in H3K27me3. Taken together, whereas the majority of downregulated genes in K27M mutant pHGGs (96 out of 151 genes, 64%) showed no difference in H3K27me3 or DNA methylation, the increased expression of 74% (106 out of 143) of upregulated genes might be explained by at least one of these two epigenetic mechanisms, suggesting that increased expression subsequent to a loss of gene silencing is the principle mode of direct epigenetic dysregulation in these tumors.

DISCUSSION

Deregulated H3K27me3 levels have been demonstrated in a variety of human cancers. For most of these entities, H3K27me3 levels are altered due to genetic hits within the machinery responsible for H3K27me3 turnover (Martinez-Garcia and Licht, 2010). Several findings, such as activating mutations of EZH2 (e.g., Y641) in lymphomas or overexpression of *EZH2* in numerous tumor entities, point toward an oncogenic role of *EZH2* and H3K27me3. However, a different set of mutations leading to loss of EZH2 methyltransferase activity and reduced H3K27 trimethylation indicate a dual role of *EZH2* and this histone mark in tumorigenesis, depending on context (Greer and Shi, 2012). Accordingly, reduced H3K27me3 levels are associated with unfavorable prognosis in breast, ovarian, and pancreatic cancers (Greer and Shi, 2012; Wei et al., 2008). Recently, pHGGs harboring the K27M mutation of histone H3.3 were reported to have strongly reduced H3K27me3 levels as a consequence of a dominant-negative effect of the K27M mutant H3.3 protein (Chan et al., 2013; Lewis et al., 2013; Venneti et al., 2013). Interestingly, K27M mutant pHGGs also show a trend toward inferior overall survival compared with their nonmutated counterpart (Khuong-Quang et al., 2012; Sturm et al., 2012). In this study, we demonstrate that immunohistochemical staining of H3K27me3 is a valuable tool to identify K27M mutant pHGGs with an overall accuracy of 98% using a large cohort of 104 pHGGs. This stratification may help to inform future clinical trial design and/or to identify patients who may respond to specific targeted therapy. The identification of 3% of pHGGs without

Figure 4. Alterations in H3K27me3 Occupancy in K27M Mutant pHGGs Are Directly Associated with Differential Gene Expression

(A) Heatmap illustrating H3K27me3 occupancy at 21,217 ChIP-Seq peaks identified in pHGGs. Peaks are sorted according to H3K27me3 occupancy (RPM $\log_2$ fold change: K27M versus H3.3-WT). Pie charts illustrate genomic location of ChIP-Seq peaks.

(B) Heatmap and intensity plots illustrate H3K27me3 occupancy in the genomic region flanking the TSS of differentially expressed genes (n = 294). Gene expression values ($\log_2$ fold change) are given for every differentially expressed gene. H3K27me3 occupancy in the genomic region of *PDGFRA* (chr4: 55,074,548–55,175,548) and *MICA* (chr6: 31,353,339–31,403,976) as well as corresponding gene expression in 12 K27M mutant pHGGs and 10 H3.3-WT tumors are shown as box plots (**$p < 0.01$). Box plots represent the interquartile range (IQR), with the median represented by a solid line. Bars extend to the maximum/minimum (up to 1.5 IQR). Outliers (>1.5 IQR) are plotted as circles. See also Figure S2 and Tables S2 and S3.

(C) Heatmap displaying H3K27me3 occupancy in the genomic region flanking the TSS of known PRC2 target genes (n = 606). Group separation (H3K27me3 LOSS in K27M or K27me3 GAIN in K27M) indicated by the dendrogram was based on H3K27me3 occupancy. Gene expression values ($\log_2$ fold change) determined in a cohort of 12 K27M mutant and 10 H3.3-WT pHGGs are given for each PRC2 target gene. Average gene expression ($\log_2$ fold change) of PRC2 target genes of the respective group is shown as a box plot (***$p < 0.001$). Box plots represent the IQR, with the median represented by a solid line. Bars extend to the maximum/minimum (up to 1.5 IQR). Outliers (>1.5 IQR) are plotted as circles. See also Figure S2 and Tables S2 and S3.

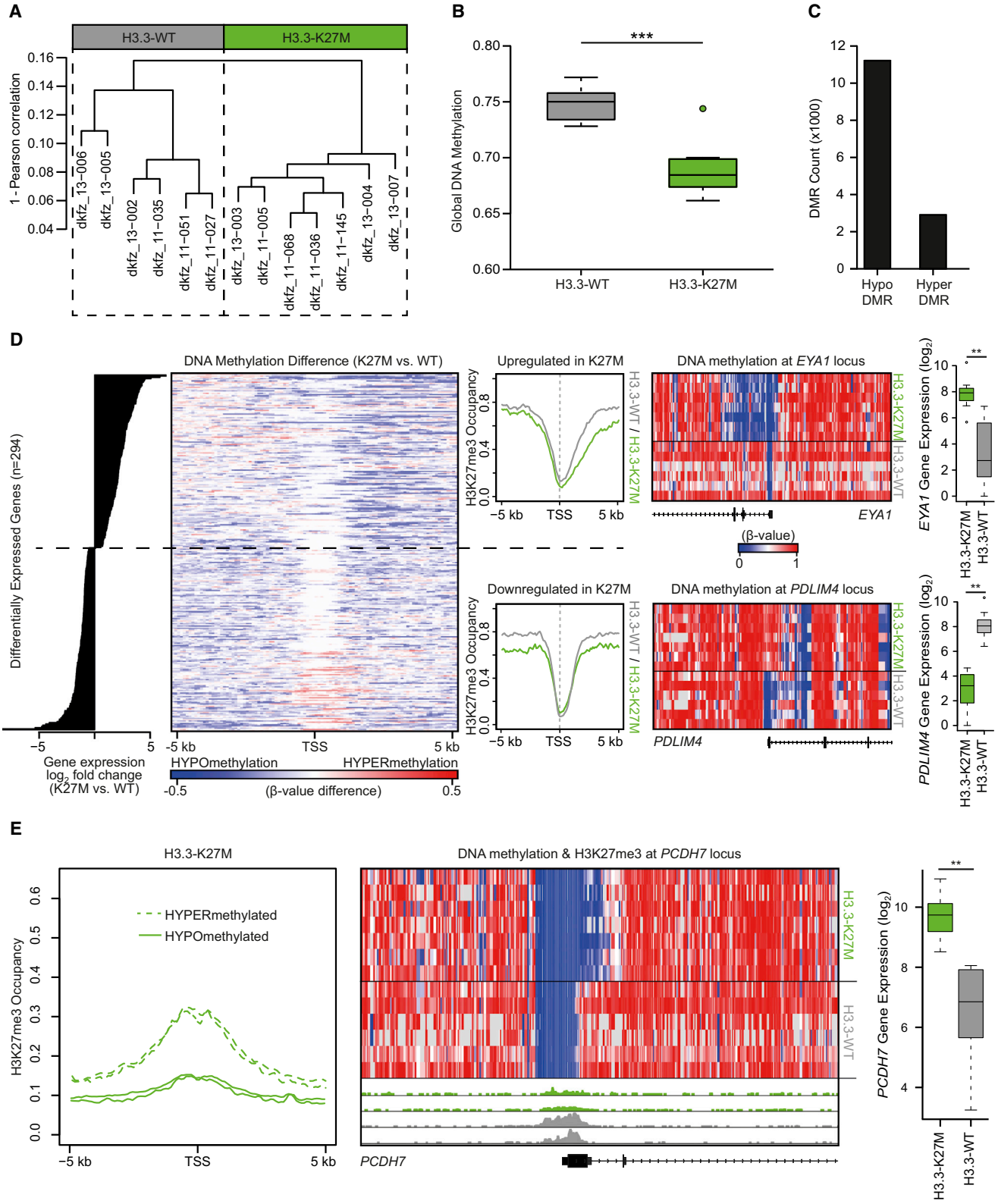

Figure 5. Global DNA Hypomethylation Contributes to Differential Gene Expressions in Concert with Loss of H3K27me3

(A) Cluster analysis of WGBS data in six H3.3-WT pHGGs and seven K27M mutant tumors.

(B) Box plot illustrating global DNA methylation levels in 13 pHGGs analyzed by WGBS (***$p < 0.001$). Box plots represent the IQR with the median represented by a solid line. Bars extend to the maximum/minimum (up to 1.5 IQR). Outliers (>1.5 IQR) are plotted as circles. See also Figure S3 and Table S4.

(legend continued on next page)

H3.3/H3.1 mutation showing similar reduced H3K27me3 levels suggests the existence of other (epi)genetic alterations affecting H3K27me3 establishment or maintenance.

Although there are conflicting data, several lines of evidence point to PRC2-mediated establishment of H3K27me3 and DNA methylation acting in parallel to modulate gene expression (Gal-Yam et al., 2008; Schlesinger et al., 2007; Viré et al., 2006; Widschwendter et al., 2007). In this study, we describe concerted alterations in H3K27me3 occupancy and DNA methylation in K27M mutant pHGGs. Both of these epigenetic mechanisms, involved in regulation of gene expression, are found to be specifically impaired in pHGGs harboring the K27M mutation of H3.3. Whereas the main focus of our study deals with the K27M-induced reduction of the repressive histone mark H3K27me3, our data also provide evidence that K27M mutant pHGGs are characterized by global DNA hypomethylation, a feature which has recently been described as being even more strongly prevalent in G34R mutant pHGGs (Sturm et al., 2012). As expected, reduced H3K27me3 and DNA hypomethylation were both found to be significantly associated with activated gene expression. Strikingly, reduced H3K27me3 alone or in combination with DNA hypomethylation was found at 74% of all transcriptionally upregulated genes in K27M mutant tumors, indicating that these are the two main mechanisms conferring the highly characteristic gene expression program.

Loss of PRC2 activity (e.g., due to depletion of EZH2 or EED) has been shown to induce changes in DNA methylation, including DNA hypomethylation (Reddington et al., 2013; Wu et al., 2008). In line with this, overexpression of K27R mutant canonical H3 was reported to lead to a significant reduction of global DNA methylation levels in human ovarian cancer cells (Abbosh et al., 2006). The high percentage (45%) of transcriptionally upregulated genes with reduced H3K27me3 levels in K27M mutant pHGGs that also showed a loss of DNA methylation suggests that K27M-induced reduction of H3K27me3 might indeed prime for DNA hypomethylation.

In addition, we aimed to find out whether K27M-induced reduction of H3K27me3 primes for DNA hypomethylation by using modified isogenic cell lines. Although these cells show a strong reduction of H3K27me3 after lentiviral overexpression of K27M mutant H3.3, we did not detect any consistent alteration in gene expression or DNA methylation in these cell lines (data not shown). In line with this, our study revealed substantial differences in H3K27me3 occupancy between primary tumor samples and pHGG cell lines. Therefore, caution is needed when attempting to extrapolate from cell models to disease pathology of different cancer entities including pHGGs in vivo (Houshdaran et al., 2010). Although our H3K27me3 ChIP-Seq data of primary pHGGs are in line with most of the recently described K27M-induced changes found by comparing a K27M mutant cell line with neural stem cells (global H3K27me3 reduction and focal gain of H3K27me3 at some loci/genes such as *CDK6*), not all conclusions generated out of a comparison of cell lines will reflect the situation in primary tumors (e.g., there are no differences in H3K27me3 peak widths between K27M mutant and H3.3-WT pHGGs; Chan et al., 2013).

Promoter hypermethylation was reported to be a general mechanism to silence known PRC2 target genes in several human cancer entities (Avissar-Whiting et al., 2011; Bennett et al., 2009; Schlesinger et al., 2007; Widschwendter et al., 2007). Interestingly, gain of H3K27me3 at the TSSs of several genes in K27M mutant pHGGs was not associated with DNA hypermethylation. This is consistent with other studies reporting on PRC2-mediated gene silencing independent of DNA hypermethylation (Kondo et al., 2008). However, the identification of specific loci with gain of H3K27me3 in the context of overall reduction of this epigenetic mark (in K27M mutant tumors) raises interesting questions about the molecular mechanisms behind PRC2 targeting, which is still a field of intense research (Simon and Kingston, 2013). A recently described model, which is based on the fact that DNA methylation attenuates PRC2 binding, might explain increased H3K27me3 levels at specific loci in K27M mutant pHGGs (Reddington et al., 2013). Global DNA hypomethylation may allow for increased binding of PRC2 and establishment of H3K27me3 at genomic sites that are normally protected by the DNA methylation mark. As a consequence, this may also enhance the reduction of H3K27me3 at normal PRC2 targets due to dilution of PRC2 molecules.

In conclusion, our study provides intriguing evidence that reduced H3K27me3 and/or DNA hypomethylation are the major driving forces of activated gene expression in K27M mutant pHGGs. Although our data suggest a potential link between K27M-induced loss of PRC2 repression and DNA hypomethylation, further work will be required to elucidate how these changes are targeted to specific genomic loci.

EXPERIMENTAL PROCEDURES

Patient and Tumor Samples

All primary tumor samples used in this study were collected at the German Cancer Research Center (DKFZ) and the Burdenko Neurosurgical Institute in accordance with the respective research ethics boards. Informed consent was obtained from all patients included in this study. An ethical vote was obtained from the ethics committee of the Medical Faculty of Heidelberg. The majority of primary tumor samples for gene expression analysis were part of a previously described study cohort (n = 17; Sturm et al., 2012). Five

(C) Overall number of DMRs in 13 pHGGs detected by WGBS.

(D) Heatmap illustrating averaged difference in DNA methylation detected by WGBS in genomic regions flanking the TSS of 294 differentially expressed genes. In addition, averaged DNA methylation levels in H3.3-WT (gray) and K27M mutant pHGGs (green) are given as intensity plots for transcriptionally upregulated and downregulated genes, respectively. DNA methylation the genomic regions flanking the TSS of *EYA1* (chr8: 72,249,222–72,300,222) and *PDLIM4* (chr5: 131,583,226–131,604,226) are shown as examples together with gene expression (log_2) in 12 K27M mutant pHGGs and 10 H3.3-WT tumors illustrated by box blots (**$p < 0.01$). Box plots represent the IQR with the median represented by a solid line. Bars extend to the maximum/minimum (up to 1.5 IQR). Outliers (>1.5 IQR) are plotted as circles.

(E) Intensity plot illustrating H3K27me3 occupancy around the TSS of genes found to be hypo- or hypermethylated in K27M mutant pHGGs. DNA methylation as well as H3K27me3 occupancy at the genomic region of *PCDH7* (chr4: 30,687,866–30,768,866) is shown as an example together with corresponding gene expression data (log_2) in 12 K27M mutant pHGGs and 10 H3.3-WT tumors illustrated by box blots (**$p < 0.01$). Box plots represent the IQR with the median represented by a solid line. Bars extend to the maximum/minimum (up to 1.5 IQR). Outliers (>1.5 IQR) are plotted as circles. See also Figure S3 and Table S4.

additional tumor samples were analyzed on the Affymetrix GeneChip Human GenomeU133 Plus 2.0 Array. A list of all used primary tumor samples and their use in the study of Sturm et al. (2012) is provided in Supplemental Experimental Procedures.

Immunohistochemistry

Tumor cores or whole tumor sections of 104 pHGGs with known *H3F3A* mutation status were stained for H3K27me3 by using the following antibody: H3K27me3 (Millipore 07-449).

Western Blot Analysis

The Histone Purification Mini Kit (Active Motif) was used to isolate and purify histone proteins followed by electrophoretic separation and transfer to a polyvinylidene fluoride membrane. Antibodies against the following antigens were applied: H3K27me3 (Millipore 07-449), H3K27me3 (Abcam ab6002), H3K27me2 (Abcam ab24684), H3K27me1 (Abcam 07-448), HA-tag (Abcam ab9110), histone H4 (Abcam ab10158), H3 (Abcam ab1791), SUZ12 (Active Motif 39357), and EZH2 (Active Motif 39933).

Generation of H3.3-Overexpressing Cell Lines

SF188 glioblastoma cells (University of California, San Francisco), HEK293T cells (ATCC), or HeLa-S3 cells (ATCC) were lentivirally transduced (multiplicity of infection of 5) using the open reading frame of H3.3 cloned into pLVX-Puro (Clontech) or pCDH1-CMV-MCS-EF1-copGFP backbone (System Bio). Both H3.3 mutants were generated by using the QuikChange II Site-Directed Mutagenesis Kit (Agilent).

Cell Culture

HEK293T, HeLa-S3, SF188, MGBM1, and KNS42 cells were cultured in high glucose Dulbecco's modified Eagle's medium (Life Technologies) supplemented with 10% fetal calf serium (GIBCO) at 37°C and 5% CO_2. NEM157 and NEM165 primary pHGG cells were cultured in AmniomaxC100 + 10% AmniomaxC100 supplement (GIBCO). Upon reaching a confluency of 80%, cells were trypsinized and used for protein extraction.

Coimmunoprecipitation

To compare the binding of PRC2 complex components with H3.3-WT or K27M mutant protein, mono-nucleosome IP was performed with EZview Red Anti-HA Affinity Gel or anti-EZH2 antibody (Active Motif 39901) using HA-tagged H3.3 (WT or K27M)-transduced HEK293T, HeLa-S3, or SF188 cells. The precipitates were analyzed by western blot using antibodies against EZH2, SUZ12, and HA, as indicated.

Chromatin Lysate Preparation and Mono-Nucleosome IP

Cells were harvested by centrifugation and washed in PBS before cell lysis. Cell nuclei were pelleted and lysed to collect insoluble chromatin followed by MNase digestion. For mono-nucleosome IP, EZview Red Anti-HA Affinity Gel (Sigma E6779) was added into the chromatin lysate. After incubation at 4°C overnight, samples were analyzed by western blot using the indicated antibodies.

In Vitro Histone Methyltransferase/Demethylase Assay

In vitro HMT assays were performed using the EpiQuik Histone Methyltransferase Activity/Inhibition Assay Kit (H3K27; Epigentek; P-3005-96). In vitro histone demethylase assays were performed using the Epigenase JMJD3/UTX Demethylase Activity/Inhibition Assay Kit (Fluorometric; Epigentek; P-3085-48). The assays were performed using either chromatin lysate or anti-HA beads after mono-nucleosome IP, as per the manufacturer's instructions.

H3K27me3 ChIP-Seq Sequencing and Data Processing

H3K27me3 ChIP-Seq of primary pHGG samples and cell lines has been performed at Active Motif according to proprietary methods. Libraries were sequenced on the Illumina HiSeq 2000 platform. To make the number of detected peaks comparable between samples, we first applied Picard DownsampleSam to equalize the number properly paired reads per sample.

Whole-Genome Bisulfite Sequencing and Data Processing

Strand-specific MethylC-seq libraries were prepared using a previously described approach with modifications (Lister et al., 2011). Adaptor-ligated DNA fragments with insert lengths of 200–250 bp were isolated and bisulfite converted using the EZ DNA Methylation kit (Zymo Research). After PCR amplification, libraries were sequenced on the Illumina HiSeq 2000 platform. An overview of generated WGBS data is provided in Table S4. Differentially methylated regions (DMRs) were identified using the bsseq Bioconductor package, version 0.6.2 (Hansen et al., 2012).

Integrative Genomic Analysis

Downstream analyses were performed in R, version 2.15.2 (R Development Core Team, 2012). Genes were termed differentially expressed between K27M-mutatnt and H3.3-WT tumors when displaying an adjusted p value < 0.01 (Student's t test, Benjamini-Hochberg correction for multiple testing). Overlapping H3K27me3 ChIP-Seq peaks in the four clinical samples were merged and mean reads per million (RPM) values for all samples were extracted from the whole-genome coverage tracks. Merged peaks within ±3 kb of the TSS were associated with annotated RefSeq genes. For heatmap representations of H3K27me3 occupancy surrounding merged peaks or TSSs, RPM values were extracted from the whole-genome coverage tracks with a window size of 100, effectively separating the depicted 10-kb region into 100 equally sized bins. Heatmaps were vertically ordered by mean RPMs in the combined peak region. Hierarchical clustering in Figure 4C was performed using Euclidean distance and complete linkage.

All DMRs associated with a RefSeq gene annotation (within ±3 kb of the TSS [hyper DMRs] and −3/+20 kb of the TSS [hypo DMRs]) were combined per gene, independently for hypo- and hypermethylated DMRs. Heatmap representations of DNA methylation were generated by separating the depicted 10-kb region into 100 equally sized bins.

ACCESSION NUMBERS

Microarray expression data of 22 tumor samples are available in National Center for Biotechnology Information's Gene Expression Omnibus (GEO; http://www.ncbi.nlm.nih.gov/geo) through GEO Series accession numbers GSE36245, GSE34824, and GSE49822. H3K27me3 ChIP-Seq and WGBS data are available through European Genome-phenome Archive accession number EGAS00001000578.

SUPPLEMENTAL INFORMATION

Supplemental Information includes Supplemental Experimental Procedures, three figures, and four tables and can be found with this article online at http://dx.doi.org/10.1016/j.ccr.2013.10.006.

ACKNOWLEDGMENTS

We would like to thank Laura Sieber and Andrea Wittmann from the Division of Pediatric Neurooncology at the DKFZ for excellent technical support. The project was supported by grants from the German Cancer Aid (109252 and 108456) and the Federal Ministry of Education and Research (to P.L. and S.M.P.; International Cancer Genome Consortium PedBrain, NGFNPlus #01GS0883); St. Baldrick's Foundation (to Y.J.C), National Institutes of Health K08NS070926 (to M.M.); and National Health Service funding to the National Institute for Health Research Biomedical Research Centre (to C.J.). This work was also supported by funds from the Center for Children's Brain Tumors at Stanford (to Y.J.C. and M.M.), a Beirne Faculty Scholar endowment at Stanford (to Y.J.C. and M.M.), Alex's Lemonade Stand Foundation (to M.M.), the McKenna Claire Foundation (to M.M.), The Cure Starts Now (to M.M.), the Lyla Nsouli Foundation (to M.M.), the Connor Johnson Memorial Fund (to M.M.), the Dylan Jewett Memorial Fund (to M.M.), the Dylan Frick Memorial Fund (to M.M.), the Abigail Jensen Memorial Fund (to M.M.), the Zoey Ganesh Memorial Fund (to M.M.), and "L'Etoile de Martin" (to N.T., D.C., and J.G.). The authors would like to thank Joanna Wysocka for helpful discussions.

Received: March 29, 2013
Revised: August 9, 2013
Accepted: October 4, 2013
Published: October 31, 2013

REFERENCES

Abbosh, P.H., Montgomery, J.S., Starkey, J.A., Novotny, M., Zuhowski, E.G., Egorin, M.J., Moseman, A.P., Golas, A., Brannon, K.M., Balch, C., et al. (2006). Dominant-negative histone H3 lysine 27 mutant derepresses silenced tumor suppressor genes and reverses the drug-resistant phenotype in cancer cells. Cancer Res. *66*, 5582–5591.

Auvergne, R.M., Sim, F.J., Wang, S., Chandler-Militello, D., Burch, J., Al Fanek, Y., Davis, D., Benraiss, A., Walter, K., Achanta, P., et al. (2013). Transcriptional differences between normal and glioma-derived glial progenitor cells identify a core set of dysregulated genes. Cell Rep. *3*, 2127–2141.

Avissar-Whiting, M., Koestler, D.C., Houseman, E.A., Christensen, B.C., Kelsey, K.T., and Marsit, C.J. (2011). Polycomb group genes are targets of aberrant DNA methylation in renal cell carcinoma. Epigenetics *6*, 703–709.

Bennett, L.B., Schnabel, J.L., Kelchen, J.M., Taylor, K.H., Guo, J., Arthur, G.L., Papageorgio, C.N., Shi, H., and Caldwell, C.W. (2009). DNA hypermethylation accompanied by transcriptional repression in follicular lymphoma. Genes Chromosomes Cancer *48*, 828–841.

Bernstein, B.E., Mikkelsen, T.S., Xie, X., Kamal, M., Huebert, D.J., Cuff, J., Fry, B., Meissner, A., Wernig, M., Plath, K., et al. (2006). A bivalent chromatin structure marks key developmental genes in embryonic stem cells. Cell *125*, 315–326.

Beukers, W., Hercegovac, A., Vermeij, M., Kandimalla, R., Blok, A.C., van der Aa, M.M., Zwarthoff, E.C., and Zuiverloon, T.C. (2013). Hypermethylation of the polycomb group target gene PCDH7 in bladder tumors from patients of all ages. J. Urol. *190*, 311–316.

Cedar, H., and Bergman, Y. (2009). Linking DNA methylation and histone modification: patterns and paradigms. Nat. Rev. Genet. *10*, 295–304.

Chan, K.M., Fang, D., Gan, H., Hashizume, R., Yu, C., Schroeder, M., Gupta, N., Mueller, S., James, C.D., Jenkins, R., et al. (2013). The histone H3.3K27M mutation in pediatric glioma reprograms H3K27 methylation and gene expression. Genes Dev. *27*, 985–990.

de Tayrac, M., Aubry, M., Saikali, S., Etcheverry, A., Surbled, C., Guenot, F., Galibert, M.D., Hamlat, A., Lesimple, T., Quillien, V., et al. (2011). A 4-gene signature associated with clinical outcome in high-grade gliomas. Clin. Cancer Res. *17*, 317–327.

Eisele, G., Wischhusen, J., Mittelbronn, M., Meyermann, R., Waldhauer, I., Steinle, A., Weller, M., and Friese, M.A. (2006). TGF-β and metalloproteinases differentially suppress NKG2D ligand surface expression on malignant glioma cells. Brain *129*, 2416–2425.

Fontebasso, A.M., Schwartzentruber, J., Khuong-Quang, D.A., Liu, X.Y., Sturm, D., Korshunov, A., Jones, D.T., Witt, H., Kool, M., Albrecht, S., et al. (2013). Mutations in SETD2 and genes affecting histone H3K36 methylation target hemispheric high-grade gliomas. Acta Neuropathol. *125*, 659–669.

Gal-Yam, E.N., Egger, G., Iniguez, L., Holster, H., Einarsson, S., Zhang, X., Lin, J.C., Liang, G., Jones, P.A., and Tanay, A. (2008). Frequent switching of Polycomb repressive marks and DNA hypermethylation in the PC3 prostate cancer cell line. Proc. Natl. Acad. Sci. USA *105*, 12979–12984.

Greer, E.L., and Shi, Y. (2012). Histone methylation: a dynamic mark in health, disease and inheritance. Nat. Rev. Genet. *13*, 343–357.

Hansen, K.D., Langmead, B., and Irizarry, R.A. (2012). BSmooth: from whole genome bisulfite sequencing reads to differentially methylated regions. Genome Biol. *13*, R83.

Houshdaran, S., Hawley, S., Palmer, C., Campan, M., Olsen, M.N., Ventura, A.P., Knudsen, B.S., Drescher, C.W., Urban, N.D., Brown, P.O., and Laird, P.W. (2010). DNA methylation profiles of ovarian epithelial carcinoma tumors and cell lines. PLoS ONE *5*, e9359.

Khuong-Quang, D.A., Buczkowicz, P., Rakopoulos, P., Liu, X.Y., Fontebasso, A.M., Bouffet, E., Bartels, U., Albrecht, S., Schwartzentruber, J., Letourneau, L., et al. (2012). K27M mutation in histone H3.3 defines clinically and biologically distinct subgroups of pediatric diffuse intrinsic pontine gliomas. Acta Neuropathol. *124*, 439–447.

Kondo, Y., Shen, L., Cheng, A.S., Ahmed, S., Boumber, Y., Charo, C., Yamochi, T., Urano, T., Furukawa, K., Kwabi-Addo, B., et al. (2008). Gene silencing in cancer by histone H3 lysine 27 trimethylation independent of promoter DNA methylation. Nat. Genet. *40*, 741–750.

Lee, T.I., Jenner, R.G., Boyer, L.A., Guenther, M.G., Levine, S.S., Kumar, R.M., Chevalier, B., Johnstone, S.E., Cole, M.F., Isono, K., et al. (2006). Control of developmental regulators by Polycomb in human embryonic stem cells. Cell *125*, 301–313.

Lewis, P.W., Müller, M.M., Koletsky, M.S., Cordero, F., Lin, S., Banaszynski, L.A., Garcia, B.A., Muir, T.W., Becher, O.J., and Allis, C.D. (2013). Inhibition of PRC2 activity by a gain-of-function H3 mutation found in pediatric glioblastoma. Science *340*, 857–861.

Li, A.M., Tian, A.X., Zhang, R.X., Ge, J., Sun, X., and Cao, X.C. (2013). Protocadherin-7 induces bone metastasis of breast cancer. Biochem. Biophys. Res. Commun. *436*, 486–490.

Lister, R., Pelizzola, M., Kida, Y.S., Hawkins, R.D., Nery, J.R., Hon, G., Antosiewicz-Bourget, J., O'Malley, R., Castanon, R., Klugman, S., et al. (2011). Hotspots of aberrant epigenomic reprogramming in human induced pluripotent stem cells. Nature *471*, 68–73.

Louis, D.N., Ohgaki, H., Wiestler, O.D., Cavenee, W.K., Burger, P.C., Jouvet, A., Scheithauer, B.W., and Kleihues, P. (2007). The 2007 WHO classification of tumours of the central nervous system. Acta Neuropathol. *114*, 97–109.

Margueron, R., and Reinberg, D. (2011). The Polycomb complex PRC2 and its mark in life. Nature *469*, 343–349.

Martinez-Garcia, E., and Licht, J.D. (2010). Deregulation of H3K27 methylation in cancer. Nat. Genet. *42*, 100–101.

R Development Core Team (2012). R: A language and environment for statistical computing. R Foundation for Statistical Computing, Vienna. ISBN 3-900051-07-0, http://www.R-project.org.

Reddington, J.P., Perricone, S.M., Nestor, C.E., Reichmann, J., Youngson, N.A., Suzuki, M., Reinhardt, D., Dunican, D.S., Prendergast, J.G., Mjoseng, H., et al. (2013). Redistribution of H3K27me3 upon DNA hypomethylation results in de-repression of Polycomb target genes. Genome Biol. *14*, R25.

Schlesinger, Y., Straussman, R., Keshet, I., Farkash, S., Hecht, M., Zimmerman, J., Eden, E., Yakhini, Z., Ben-Shushan, E., Reubinoff, B.E., et al. (2007). Polycomb-mediated methylation on Lys27 of histone H3 pre-marks genes for de novo methylation in cancer. Nat. Genet. *39*, 232–236.

Schwartzentruber, J., Korshunov, A., Liu, X.Y., Jones, D.T., Pfaff, E., Jacob, K., Sturm, D., Fontebasso, A.M., Quang, D.A., Tönjes, M., et al. (2012). Driver mutations in histone H3.3 and chromatin remodelling genes in paediatric glioblastoma. Nature *482*, 226–231.

Simon, J.A., and Kingston, R.E. (2013). Occupying chromatin: Polycomb mechanisms for getting to genomic targets, stopping transcriptional traffic, and staying put. Mol. Cell *49*, 808–824.

Sturm, D., Witt, H., Hovestadt, V., Khuong-Quang, D.A., Jones, D.T., Konermann, C., Pfaff, E., Tönjes, M., Sill, M., Bender, S., et al. (2012). Hotspot mutations in H3F3A and IDH1 define distinct epigenetic and biological subgroups of glioblastoma. Cancer Cell *22*, 425–437.

Turcan, S., Rohle, D., Goenka, A., Walsh, L.A., Fang, F., Yilmaz, E., Campos, C., Fabius, A.W., Lu, C., Ward, P.S., et al. (2012). IDH1 mutation is sufficient to establish the glioma hypermethylator phenotype. Nature *483*, 479–483.

Venneti, S., Garimella, M.T., Sullivan, L.M., Martinez, D., Huse, J.T., Heguy, A., Santi, M., Thompson, C.B., and Judkins, A.R. (2013). Evaluation of histone 3 lysine 27 trimethylation (H3K27me3) and enhancer of zest 2 (EZH2) in pediatric glial and glioneuronal tumors shows decreased H3K27me3 in H3F3A K27M mutant glioblastomas. Brain Pathol. *23*, 558–564.

Verhaak, R.G., Hoadley, K.A., Purdom, E., Wang, V., Qi, Y., Wilkerson, M.D., Miller, C.R., Ding, L., Golub, T., Mesirov, J.P., et al.; Cancer Genome Atlas Research Network. (2010). Integrated genomic analysis identifies clinically

relevant subtypes of glioblastoma characterized by abnormalities in PDGFRA, IDH1, EGFR, and NF1. Cancer Cell *17*, 98–110.

Verma, S.K., Tian, X., LaFrance, L.V., Duquenne, C., Suarez, D.P., Newlander, K.A., Romeril, S.P., Burgess, J.L., Grant, S.W., Brackley, J.A., et al. (2012). Identification of potent, selective, cell-active inhibitors of the histone lysine methyltransferase EZH2. ACS Med. Chem. Lett. *3*, 1091–1096.

Viré, E., Brenner, C., Deplus, R., Blanchon, L., Fraga, M., Didelot, C., Morey, L., Van Eynde, A., Bernard, D., Vanderwinden, J.M., et al. (2006). The Polycomb group protein EZH2 directly controls DNA methylation. Nature *439*, 871–874.

Wei, Y., Xia, W., Zhang, Z., Liu, J., Wang, H., Adsay, N.V., Albarracin, C., Yu, D., Abbruzzese, J.L., Mills, G.B., et al. (2008). Loss of trimethylation at lysine 27 of histone H3 is a predictor of poor outcome in breast, ovarian, and pancreatic cancers. Mol. Carcinog. *47*, 701–706.

Widschwendter, M., Fiegl, H., Egle, D., Mueller-Holzner, E., Spizzo, G., Marth, C., Weisenberger, D.J., Campan, M., Young, J., Jacobs, I., and Laird, P.W. (2007). Epigenetic stem cell signature in cancer. Nat. Genet. *39*, 157–158.

Wu, X., Gong, Y., Yue, J., Qiang, B., Yuan, J., and Peng, X. (2008). Cooperation between EZH2, NSPc1-mediated histone H2A ubiquitination and Dnmt1 in HOX gene silencing. Nucleic Acids Res. *36*, 3590–3599.

Wu, G., Broniscer, A., McEachron, T.A., Lu, C., Paugh, B.S., Becksfort, J., Qu, C., Ding, L., Huether, R., Parker, M., et al.; St. Jude Children's Research Hospital–Washington University Pediatric Cancer Genome Project. (2012). Somatic histone H3 alterations in pediatric diffuse intrinsic pontine gliomas and non-brainstem glioblastomas. Nat. Genet. *44*, 251–253.

Zarghooni, M., Bartels, U., Lee, E., Buczkowicz, P., Morrison, A., Huang, A., Bouffet, E., and Hawkins, C. (2010). Whole-genome profiling of pediatric diffuse intrinsic pontine gliomas highlights platelet-derived growth factor receptor alpha and poly (ADP-ribose) polymerase as potential therapeutic targets. J. Clin. Oncol. *28*, 1337–1344.

REFERENCES BIBLIOGRAPHIQUES

Agarwal, Sagar, Rajendar K Mittapalli, David M Zellmer, Jose L Gallardo, Randy Donelson, Charlie Seiler, Stacy A Decker, et al. 2012. « Active efflux of dasatinib from the brain limits efficacy against murine glioblastoma: broad implications for the clinical use of molecularly-targeted agents ». *Molecular cancer therapeutics*, août. doi:10.1158/1535-7163.MCT-12-0552. http://www.ncbi.nlm.nih.gov/pubmed/22891038.

Ahluwalia, Manmeet S., John de Groot, Wei (Michael) Liu, et Candece L Gladson. 2010. « Targeting SRC in glioblastoma tumors and brain metastases: Rationale and preclinical studies ». *Cancer Letters* 298 (2): 139-149. doi:10.1016/j.canlet.2010.08.014.

Ahn, Sohyun, et Alexandra L. Joyner. 2005. « In Vivo Analysis of Quiescent Adult Neural Stem Cells Responding to Sonic Hedgehog ». *Nature* 437 (7060): 894-897. doi:10.1038/nature03994.

Albright, A L, R J Packer, R Zimmerman, L B Rorke, J Boyett, et G D Hammond. 1993. « Magnetic Resonance Scans Should Replace Biopsies for the Diagnosis of Diffuse Brain Stem Gliomas: A Report from the Children's Cancer Group ». *Neurosurgery* 33 (6): 1026-1029; discussion 1029-1030.

Andrae, Johanna, Radiosa Gallini, et Christer Betsholtz. 2008. « Role of Platelet-Derived Growth Factors in Physiology and Medicine ». *Genes & Development* 22 (10): 1276-1312. doi:10.1101/gad.1653708.

Antonelli, Manila, Francesca Romana Buttarelli, Antonietta Arcella, Sumihito Nobusawa, Vittoria Donofrio, Hiroko Oghaki, et Felice Giangaspero. 2010. « Prognostic significance of histological grading, p53 status, YKL-40 expression, and IDH1 mutations in pediatric high-grade gliomas ». *Journal of Neuro-Oncology* 99 (2): 209-215. doi:10.1007/s11060-010-0129-5.

Aoki, Yasuyuki, Rintaro Hashizume, Tomoko Ozawa, Anu Banerjee, Michael Prados, C. David James, et Nalin Gupta. 2012. « An experimental xenograft mouse model of diffuse pontine glioma designed for therapeutic testing ». *Journal of Neuro-Oncology*, janvier. doi:10.1007/s11060-011-0796-x. http://www.springerlink.com.gate2.inist.fr/content/l6884m1064lm46x0/.

Aquino-Parsons, C, J Hukin, et A Green. 2008. « Concurrent Carbogen and Radiation Therapy in Children with High-Risk Brainstem Gliomas ». *Pediatric Blood & Cancer* 50 (2): 397-399. doi:10.1002/pbc.21057.

Balss, Jörg, Jochen Meyer, Wolf Mueller, Andrey Korshunov, Christian Hartmann, et Andreas von Deimling. 2008. « Analysis of the IDH1 Codon 132 Mutation in Brain Tumors ». *Acta Neuropathologica* 116 (6): 597-602. doi:10.1007/s00401-008-0455-2.

Barkovich, A J, J Krischer, L E Kun, R Packer, R A Zimmerman, C R Freeman, W M Wara, L Albright, J C Allen, et H J Hoffman. 1990. « Brain Stem Gliomas: A Classification System Based on Magnetic Resonance Imaging ». *Pediatric Neurosurgery* 16 (2): 73-83.

Barrow, Jennifer, Martyna Adamowicz-Brice, Maria Cartmill, Donald MacArthur, James Lowe, Keith Robson, Marie-Anne Brundler, David A Walker, Beth Coyle, et Richard Grundy. 2011. « Homozygous Loss of ADAM3A Revealed by Genome-Wide Analysis of Pediatric High-Grade Glioma and Diffuse Intrinsic Pontine Gliomas ». *Neuro-Oncology* 13 (2): 212-222. doi:10.1093/neuonc/noq158.

Bartek, Jiri, Kimberly Ng, Jiri Bartek, Walter Fischer, Bob Carter, et Clark C. Chen. 2012. « Key Concepts in Glioblastoma Therapy ». *Journal of Neurology, Neurosurgery & Psychiatry* 83 (7): 753-760. doi:10.1136/jnnp-2011-300709.

Bax, Dorine A, Alan Mackay, Suzanne E Little, Diana Carvalho, Marta Viana-Pereira, Narinder Tamber, Anita E Grigoriadis, et al. 2010. « A Distinct Spectrum of Copy Number Aberrations in Pediatric High-Grade Gliomas ». *Clinical Cancer Research: An Official Journal of the American Association for Cancer Research* 16 (13): 3368-3377. doi:10.1158/1078-0432.CCR-10-0438.

Bax, Dorine A., Suzanne E. Little, Nathalie Gaspar, Lara Perryman, Lynley Marshall, Marta Viana-Pereira, Tania A. Jones, et al. 2009. « Molecular and Phenotypic Characterisation of Paediatric Glioma Cell Lines as Models for Preclinical Drug Development ». *PLoS ONE* 4 (4): e5209. doi:10.1371/journal.pone.0005209.

Becher, Oren J, Dolores Hambardzumyan, Talia R Walker, Karim Helmy, Javad Nazarian, Steffen Albrecht, Rebecca L Hiner, et al. 2010. « Preclinical Evaluation of Radiation and Perifosine in a Genetically and Histologically Accurate Model of Brainstem Glioma ». *Cancer Research* 70 (6): 2548-2557. doi:10.1158/0008-5472.CAN-09-2503.

Bender, Sebastian, Yujie Tang, Anders M Lindroth, Volker Hovestadt, David T W Jones, Marcel Kool, Marc

Zapatka, et al. 2013. « Reduced H3K27me3 and DNA Hypomethylation Are Major Drivers of Gene Expression in K27M Mutant Pediatric High-Grade Gliomas ». *Cancer Cell* 24 (5): 660-672. doi:10.1016/j.ccr.2013.10.006.

Benezra, Miriam, Dolores Hambardzumyan, Oula Penate-Medina, Darren R. Veach, Nagavarakishore Pillarsetty, Peter Smith-Jones, Evan Phillips, et al. 2012. « Fluorine-Labeled Dasatinib Nanoformulations as Targeted Molecular Imaging Probes in a PDGFB-Driven Murine Glioblastoma Model ». *Neoplasia (New York, N.Y.)* 14 (12): 1132.

Berger, M S, M S Edwards, D LaMasters, R L Davis, et C B Wilson. 1983. « Pediatric Brain Stem Tumors: Radiographic, Pathological, and Clinical Correlations ». *Neurosurgery* 12 (3): 298-302.

Berlow, Noah, Lara E Davis, Emma L Cantor, Bernard Séguin, Charles Keller, et Ranadip Pal. 2013. « A New Approach for Prediction of Tumor Sensitivity to Targeted Drugs Based on Functional Data ». *BMC Bioinformatics* 14: 239. doi:10.1186/1471-2105-14-239.

Blüml, Stefan, Ashok Panigrahy, Mikhail Laskov, Girish Dhall, Mark D Krieger, Marvin D Nelson, Jonathan L Finlay, et Floyd H Gilles. 2011. « Elevated Citrate in Pediatric Astrocytomas with Malignant Progression ». *Neuro-Oncology* 13 (10): 1107-1117. doi:10.1093/neuonc/nor087.

Bradley, Kristin A, Tianni Zhou, Rene Y McNall-Knapp, Regina I Jakacki, Adam S Levy, Gilbert Vezina, et Ian F Pollack. 2013. « Motexafin-Gadolinium and Involved Field Radiation Therapy for Intrinsic Pontine Glioma of Childhood: A Children's Oncology Group Phase 2 Study ». *International Journal of Radiation Oncology, Biology, Physics* 85 (1): e55-60. doi:10.1016/j.ijrobp.2012.09.004.

Bredel, M, I F Pollack, R L Hamilton, et C D James. 1999. « Epidermal Growth Factor Receptor Expression and Gene Amplification in High-Grade Non-Brainstem Gliomas of Childhood ». *Clinical Cancer Research: An Official Journal of the American Association for Cancer Research* 5 (7): 1786-1792.

Brennan, Cameron W., Roel G. W. Verhaak, Aaron McKenna, Benito Campos, Houtan Noushmehr, Sofie R. Salama, Siyuan Zheng, et al. 2013. « The Somatic Genomic Landscape of Glioblastoma ». *Cell* 155 (2): 462-477. doi:10.1016/j.cell.2013.09.034.

Broniscer, Alberto, Justin N Baker, Suzanne J Baker, Susan N Chi, J Russell Geyer, E Brannon Morris, et Amar Gajjar. 2010. « Prospective Collection of Tissue Samples at Autopsy in Children with Diffuse Intrinsic Pontine Glioma ». *Cancer* 116 (19): 4632-4637. doi:10.1002/cncr.25405.

Broniscer, Alberto, Sharyn D. Baker, Cynthia Wetmore, Atmaram S. Pai Panandiker, Jie Huang, Andrew M. Davidoff, Arzu Onar-Thomas, et al. 2013. « Phase I Trial, Pharmacokinetics, and Pharmacodynamics of Vandetanib and Dasatinib in Children with Newly Diagnosed Diffuse Intrinsic Pontine Glioma ». *Clinical Cancer Research* 19 (11): 3050-3058. doi:10.1158/1078-0432.CCR-13-0306.

Cairncross, J G, K Ueki, M C Zlatescu, D K Lisle, D M Finkelstein, R R Hammond, J S Silver, et al. 1998. « Specific Genetic Predictors of Chemotherapeutic Response and Survival in Patients with Anaplastic Oligodendrogliomas ». *Journal of the National Cancer Institute* 90 (19): 1473-1479.

Calver, A R, A C Hall, W P Yu, F S Walsh, J K Heath, C Betsholtz, et W D Richardson. 1998. « Oligodendrocyte Population Dynamics and the Role of PDGF in Vivo ». *Neuron* 20 (5): 869-882.

Cancer Genome Atlas Research Network. 2008. « Comprehensive Genomic Characterization Defines Human Glioblastoma Genes and Core Pathways ». *Nature* 455 (7216): 1061-1068. doi:10.1038/nature07385.

Caretti, V, M H A Jansen, D G van Vuurden, T Lagerweij, M Bugiani, I Horsman, H Wessels, et al. 2012. « Implementation of a Multi-Institutional Diffuse Intrinsic Pontine Glioma Autopsy Protocol and Characterization of a Primary Cell Culture ». *Neuropathology and applied neurobiology*, juillet. doi:10.1111/j.1365-2990.2012.01294.x.

Carro, Maria Stella, Wei Keat Lim, Mariano Javier Alvarez, Robert J Bollo, Xudong Zhao, Evan Y Snyder, Erik P Sulman, et al. 2010. « The Transcriptional Network for Mesenchymal Transformation of Brain Tumours ». *Nature* 463 (7279): 318-325. doi:10.1038/nature08712.

Chan, Kui-Ming, Haiyun Gan, Rintaro Hashizume, Chuanhe Yu, Mark Schroeder, Nalin Gupta, Sabine Mueller, et al. 2013. « The Histone H3.3K27M Mutation in Pediatric Glioma Reprograms H3K27 Methylation and Gene Expression ». *Genes & Development*, avril. doi:10.1101/gad.217778.113. http://genesdev.cshlp.org.gate2.inist.fr/content/early/2013/04/18/gad.217778.113.

Chassot, Andrea, Sandra Canale, Pascale Varlet, Stephanie Puget, Thomas Roujeau, Laura Negretti, Frederic Dhermain, et al. 2012. « Radiotherapy with Concurrent and Adjuvant Temozolomide in Children with Newly Diagnosed Diffuse Intrinsic Pontine Glioma ». *Journal of Neuro-Oncology* 106 (2): 399-407. doi:10.1007/s11060-011-0681-7.

Chowdhury, Rasheduzzaman, Kar Kheng Yeoh, Ya-Min Tian, Lars Hillringhaus, Eleanor A Bagg, Nathan R Rose, Ivanhoe K H Leung, et al. 2011. « The oncometabolite 2-hydroxyglutarate inhibits histone lysine demethylases ». *EMBO reports* 12 (5): 463-469. doi:10.1038/embor.2011.43.

Cohen, Kenneth J, Ian F Pollack, Tianni Zhou, Allen Buxton, Emiko J Holmes, Peter C Burger, Daniel J Brat, et al. 2011. « Temozolomide in the Treatment of High-Grade Gliomas in Children: A Report from the Children's Oncology Group ». *Neuro-Oncology* 13 (3): 317-323. doi:10.1093/neuonc/noq191.

Coutel, Y. 1959. « [Infiltrating glioblastoma of the brain stem in an 8-year-old child; normalization of the pneumoencephalogram after radiotherapy] ». *Revue d'oto-neuro-ophtalmologie* 31: 119-123.

Dang, Lenny, David W White, Stefan Gross, Bryson D Bennett, Mark A Bittinger, Edward M Driggers, Valeria R Fantin, et al. 2009. « Cancer-Associated IDH1 Mutations Produce 2-Hydroxyglutarate ». *Nature* 462 (7274): 739-744. doi:10.1038/nature08617.

Davis, Mindy I, Jeremy P Hunt, Sanna Herrgard, Pietro Ciceri, Lisa M Wodicka, Gabriel Pallares, Michael Hocker, Daniel K Treiber, et Patrick P Zarrinkar. 2011. « Comprehensive Analysis of Kinase Inhibitor Selectivity ». *Nature Biotechnology* 29 (11): 1046-1051. doi:10.1038/nbt.1990.

De Carli, Emilie, Xiaowei Wang, et Stéphanie Puget. 2009. « IDH1 and IDH2 Mutations in Gliomas ». *The New England Journal of Medicine* 360 (21): 2248; author reply 2249. doi:10.1056/NEJMc090593.

Desandes, Emmanuel, Brigitte Lacour, Danièle Sommelet, Antoine Buemi, Arlette Danzon, Patricia Delafosse, Pascale Grosclaude, et al. 2004. « Cancer Incidence among Adolescents in France ». *Pediatric Blood & Cancer* 43 (7): 742-748. doi:10.1002/pbc.20106.

Di Sapio, Alessia, Isabella Morra, Luca Pradotto, Marilena Guido, Davide Schiffer, et Alessandro Mauro. 2002. « Molecular Genetic Changes in a Series of Neuroepithelial Tumors of Childhood ». *Journal of Neuro-Oncology* 59 (2): 117-122.

Donson, Andrew M, Steven O Addo-Yobo, Michael H Handler, Lia Gore, et Nicholas K Foreman. 2007. « MGMT Promoter Methylation Correlates with Survival Benefit and Sensitivity to Temozolomide in Pediatric Glioblastoma ». *Pediatric Blood & Cancer* 48 (4): 403-407. doi:10.1002/pbc.20803.

Du, Jinyan, Paula Bernasconi, Karl R Clauser, D R Mani, Stephen P Finn, Rameen Beroukhim, Melissa Burns, et al. 2009. « Bead-Based Profiling of Tyrosine Kinase Phosphorylation Identifies SRC as a Potential Target for Glioblastoma Therapy ». *Nature Biotechnology* 27 (1): 77-83. doi:10.1038/nbt.1513.

Epstein, F, et E L McCleary. 1986. « Intrinsic Brain-Stem Tumors of Childhood: Surgical Indications ». *Journal of Neurosurgery* 64 (1): 11-15. doi:10.3171/jns.1986.64.1.0011.

Faury, Damien, André Nantel, Sandra E Dunn, Marie-Christine Guiot, Takrima Haque, Péter Hauser, Miklós Garami, et al. 2007. « Molecular Profiling Identifies Prognostic Subgroups of Pediatric Glioblastoma and Shows Increased YB-1 Expression in Tumors ». *Journal of Clinical Oncology: Official Journal of the American Society of Clinical Oncology* 25 (10): 1196-1208. doi:10.1200/JCO.2006.07.8626.

Fischbein, N J, M D Prados, W Wara, C Russo, M S Edwards, et A J Barkovich. 1996. « Radiologic Classification of Brain Stem Tumors: Correlation of Magnetic Resonance Imaging Appearance with Clinical Outcome ». *Pediatric Neurosurgery* 24 (1): 9-23.

Franzini, A, A Allegranza, A Melcarne, C Giorgi, S Ferraresi, et G Broggi. 1988. « Serial Stereotactic Biopsy of Brain Stem Expanding Lesions. Considerations on 45 Consecutive Cases ». *Acta Neurochirurgica. Supplementum* 42: 170-176.

Frappaz, Didier, Matthias Schell, Philippe Thiesse, Perrine Marec-Bérard, Carmine Mottolese, David Perol, Christophe Bergeron, et al. 2008. « Preradiation Chemotherapy May Improve Survival in Pediatric Diffuse Intrinsic Brainstem Gliomas: Final Results of BSG 98 Prospective Trial ». *Neuro-Oncology* 10 (4): 599-607. doi:10.1215/15228517-2008-029.

Freeman, C R, J P Krischer, R A Sanford, M E Cohen, P C Burger, R del Carpio, E C Halperin, L Munoz, H S Friedman, et L E Kun. 1993. « Final Results of a Study of Escalating Doses of Hyperfractionated

Radiotherapy in Brain Stem Tumors in Children: A Pediatric Oncology Group Study ». *International Journal of Radiation Oncology, Biology, Physics* 27 (2): 197-206.

Fried, Iris, Cynthia Hawkins, Katrin Scheinemann, Elena Tsangaris, Leila Hesselson, Ute Bartels, Annie Huang, et al. 2012. « Favorable Outcome with Conservative Treatment for Children with Low Grade Brainstem Tumors ». *Pediatric Blood & Cancer* 58 (4): 556-560. doi:10.1002/pbc.23200.

Geoerger, Birgit, Darren Hargrave, Fabienne Thomas, Anna Ndiaye, Didier Frappaz, Felipe Andreiuolo, Pascale Varlet, et al. 2011. « Innovative Therapies for Children with Cancer Pediatric Phase I Study of Erlotinib in Brainstem Glioma and Relapsing/refractory Brain Tumors ». *Neuro-Oncology* 13 (1): 109-118. doi:10.1093/neuonc/noq141.

Geoerger, Birgit, Bruce Morland, Anna Ndiaye, Francois Doz, Gabriel Kalifa, Anne Geoffray, Fabienne Pichon, et al. 2009. « Target-Driven Exploratory Study of Imatinib Mesylate in Children with Solid Malignancies by the Innovative Therapies for Children with Cancer (ITCC) European Consortium ». *European Journal of Cancer (Oxford, England: 1990)* 45 (13): 2342-2351. doi:10.1016/j.ejca.2009.03.007.

Gilbertson, Richard J, D Ashley Hill, Roberto Hernan, Mehmet Kocak, Russell Geyer, Jim Olson, Amar Gajjar, et al. 2003. « ERBB1 Is Amplified and Overexpressed in High-Grade Diffusely Infiltrative Pediatric Brain Stem Glioma ». *Clinical Cancer Research: An Official Journal of the American Association for Cancer Research* 9 (10 Pt 1): 3620-3624.

Gilles, Floyd H., William D. Brown, Alan Leviton, C. Jane Tavaré, Lester Adelman, Lucy B. Rorke, Richard L. Davis, Tessa E. Hedley-Whyte, et for the Childhood Brain Tumor Consortium. 2000. « Limitations of the World Health Organization Classification of Childhood Supratentorial Astrocytic Tumors ». *Cancer* 88 (6): 1477-83. doi:10.1002/(SICI)1097-0142(20000315)88:6<1477::AID-CNCR28>3.0.CO;2-8.

Grill, Jacques, Stephanie Puget, Felipe Andreiuolo, Cathy Philippe, et Laura MacConaill. 2012. « Critical Oncogenic Mutations in Newly Diagnosed Pediatric Diffuse Intrinsic Pontine Glioma ». *Pediatric Blood & Cancer* 58 (4): 489-491. doi:10.1002/pbc.24060.

Grill, Jacques, Stephanie Puget, Felipe Andreiuolo, Cathy Philippe, Laura MacConaill, et Mark W. Kieran. 2012. « Critical Oncogenic Mutations in Newly Diagnosed Pediatric Diffuse Intrinsic Pontine Glioma ». *Pediatric Blood & Cancer* 58 (4): 489-91. doi:10.1002/pbc.24060.

Gurney, James G., Malcolm A Smith, et Greta R Buni. 2013. « CNS AND MISCELLANEOUS INTRACRANIAL AND INTRASPINAL NEOPLASMS ». Consulté le avril 27. http://seer.cancer.gov/publications/childhood/cns.pdf.

Gururangan, Sridharan, Susan N. Chi, Tina Young Poussaint, Arzu Onar-Thomas, Richard J. Gilbertson, Sridhar Vajapeyam, Henry S. Friedman, et al. 2010. « Lack of Efficacy of Bevacizumab Plus Irinotecan in Children With Recurrent Malignant Glioma and Diffuse Brainstem Glioma: A Pediatric Brain Tumor Consortium Study ». *Journal of Clinical Oncology* 28 (18): 3069-3075. doi:10.1200/JCO.2009.26.8789.

Hamiche, Ali, et Muhammad Shuaib. 2012. « Chaperoning the Histone H3 Family ». *Biochimica et Biophysica Acta* 1819 (3-4): 230-237. doi:10.1016/j.bbagrm.2011.08.009.

Hankinson, Todd C, Elizabeth J Campagna, Nicholas K Foreman, et Michael H Handler. 2011. « Interpretation of Magnetic Resonance Images in Diffuse Intrinsic Pontine Glioma: A Survey of Pediatric Neurosurgeons ». *Journal of Neurosurgery. Pediatrics* 8 (1): 97-102. doi:10.3171/2011.4.PEDS1180.

Haque, Takrima, Damien Faury, Steffen Albrecht, Enrique Lopez-Aguilar, Péter Hauser, Miklós Garami, Zoltán Hanzély, et al. 2007. « Gene Expression Profiling from Formalin-Fixed Paraffin-Embedded Tumors of Pediatric Glioblastoma ». *Clinical Cancer Research: An Official Journal of the American Association for Cancer Research* 13 (21): 6284-6292. doi:10.1158/1078-0432.CCR-07-0525.

Hargrave, Darren, Ute Bartels, et Eric Bouffet. 2006. « Diffuse brainstem glioma in children: critical review of clinical trials ». *The Lancet Oncology* 7 (3): 241-248. doi:10.1016/S1470-2045(06)70615-5.

Hartmann, Christian, Jochen Meyer, Jörg Balss, David Capper, Wolf Mueller, Arne Christians, Jörg Felsberg, et al. 2009. « Type and Frequency of IDH1 and IDH2 Mutations Are Related to Astrocytic and Oligodendroglial Differentiation and Age: A Study of 1,010 Diffuse Gliomas ». *Acta Neuropathologica* 118 (4): 469-474. doi:10.1007/s00401-009-0561-9.

Hashizume, Rintaro, Tomoko Ozawa, Eduard B Dinca, Anuradha Banerjee, Michael D Prados, Charles D James, et Nalin Gupta. 2010. « A Human Brainstem Glioma Xenograft Model Enabled for Bioluminescence Imaging ». *Journal of Neuro-Oncology* 96 (2): 151-159. doi:10.1007/s11060-009-9954-9.

Hashizume, Rintaro, Ivan Smirnov, Sharon Liu, Joanna J Phillips, Jeanette Hyer, Tracy R McKnight, Michael Wendland, et al. 2012. « Characterization of a Diffuse Intrinsic Pontine Glioma Cell Line: Implications for Future Investigations and Treatment ». *Journal of Neuro-Oncology* 110 (3): 305-313. doi:10.1007/s11060-012-0973-6.

Heddleston, John M, Zhizhong Li, Roger E McLendon, Anita B Hjelmeland, et Jeremy N Rich. 2009. « The Hypoxic Microenvironment Maintains Glioblastoma Stem Cells and Promotes Reprogramming towards a Cancer Stem Cell Phenotype ». *Cell Cycle (Georgetown, Tex.)* 8 (20): 3274-3284.

Hegi, Monika E, Annie-Claire Diserens, Thierry Gorlia, Marie-France Hamou, Nicolas de Tribolet, Michael Weller, Johan M Kros, et al. 2005. « MGMT Gene Silencing and Benefit from Temozolomide in Glioblastoma ». *The New England Journal of Medicine* 352 (10): 997-1003. doi:10.1056/NEJMoa043331.

Huang, Fei, Karen Reeves, Xia Han, Craig Fairchild, Suso Platero, Tai W. Wong, Francis Lee, Peter Shaw, et Edwin Clark. 2007. « Identification of candidate molecular markers predicting sensitivity in solid tumors to dasatinib: rationale for patient selection ». *Cancer Research* 67 (5): 2226-38.

Huveldt, Deborah, Laura J Lewis-Tuffin, Brett L Carlson, Mark A Schroeder, Fausto Rodriguez, Caterina Giannini, Evanthia Galanis, Jann N Sarkaria, et Panos Z Anastasiadis. 2013. « Targeting Src Family Kinases Inhibits Bevacizumab-Induced Glioma Cell Invasion ». *PloS One* 8 (2): e56505. doi:10.1371/journal.pone.0056505.

Ichimura, Koichi, Danita M Pearson, Sylvia Kocialkowski, L Magnus Bäcklund, Raymond Chan, David T W Jones, et V Peter Collins. 2009. « IDH1 Mutations Are Present in the Majority of Common Adult Gliomas but Rare in Primary Glioblastomas ». *Neuro-Oncology* 11 (4): 341-347. doi:10.1215/15228517-2009-025.

Jalali, Rakesh, Nirmal Raut, Brijesh Arora, Tejpal Gupta, Debnarayan Dutta, Anusheel Munshi, Rajiv Sarin, et Purna Kurkure. 2010. « Prospective Evaluation of Radiotherapy with Concurrent and Adjuvant Temozolomide in Children with Newly Diagnosed Diffuse Intrinsic Pontine Glioma ». *International Journal of Radiation Oncology, Biology, Physics* 77 (1): 113-118. doi:10.1016/j.ijrobp.2009.04.031.

Janssens, Geert O., Marc H. Jansen, Selmer J. Lauwers, Peter J. Nowak, Foppe R. Oldenburger, Eric Bouffet, Frank Saran, et al. 2013. « Hypofractionation vs Conventional Radiation Therapy for Newly Diagnosed Diffuse Intrinsic Pontine Glioma: A Matched-Cohort Analysis ». *International Journal of Radiation Oncology*Biology*Physics* 85 (2): 315-320. doi:10.1016/j.ijrobp.2012.04.006.

Jennings, Mark T, Richard Sposto, James M Boyett, L Gilbert Vezina, Emi Holmes, Mitchell S Berger, Carol S Bruggers, et al. 2002. « Preradiation Chemotherapy in Primary High-Risk Brainstem Tumors: Phase II Study CCG-9941 of the Children's Cancer Group ». *Journal of Clinical Oncology: Official Journal of the American Society of Clinical Oncology* 20 (16): 3431-3437.

Kaplan, Frederick S, Meiqi Xu, Petra Seemann, J Michael Connor, David L Glaser, Liam Carroll, Patricia Delai, et al. 2009. « Classic and Atypical Fibrodysplasia Ossificans Progressiva (FOP) Phenotypes Are Caused by Mutations in the Bone Morphogenetic Protein (BMP) Type I Receptor ACVR1 ». *Human Mutation* 30 (3): 379-390. doi:10.1002/humu.20868.

Kebudi, Rejin, et Fatma Betul Cakir. 2013. « Management of Diffuse Pontine Gliomas in Children: Recent Developments ». *Paediatric Drugs*, mai. doi:10.1007/s40272-013-0033-5.

Kim, Chae-Yong, Seung-Ki Kim, Ji Hoon Phi, Min Mi Lee, In Ah Kim, Il Han Kim, Kyu-Chang Wang, Hye-Lim Jung, Mee Jeong Lee, et Byung-Kyu Cho. 2010. « A Prospective Study of Temozolomide plus Thalidomide during and after Radiation Therapy for Pediatric Diffuse Pontine Gliomas: Preliminary Results of the Korean Society for Pediatric Neuro-Oncology Study ». *Journal of Neuro-Oncology* 100 (2): 193-198. doi:10.1007/s11060-010-0157-1.

Kim, T H, H W Chin, S Pollan, J H Hazel, et J H Webster. 1980. « Radiotherapy of Primary Brain Stem Tumors ». *International Journal of Radiation Oncology, Biology, Physics* 6 (1): 51-57.

Kivivuori, Sanna-Maria, Pekka Riikonen, Leena Valanne, Tuula Lönnqvist, et Ulla M Saarinen-Pihkala. 2011. « Antiangiogenic combination therapy after local radiotherapy with topotecan

radiosensitizer improved quality of life for children with inoperable brainstem gliomas: Antiangiogenic therapy for brainstem tumors ». *Acta Paediatrica* 100 (1): 134-138. doi:10.1111/j.1651-2227.2010.01961.x.

Kondo, Yutaka, Lanlan Shen, Alfred S Cheng, Saira Ahmed, Yanis Boumber, Chantale Charo, Tadanori Yamochi, et al. 2008. « Gene Silencing in Cancer by Histone H3 Lysine 27 Trimethylation Independent of Promoter DNA Methylation ». *Nature Genetics* 40 (6): 741-750. doi:10.1038/ng.159.

Korshunov, Andrey, Regina Sycheva, Sergey Gorelyshev, et Andrey Golanov. 2005. « Clinical Utility of Fluorescence in Situ Hybridization (FISH) in Nonbrainstem Glioblastomas of Childhood ». *Modern Pathology: An Official Journal of the United States and Canadian Academy of Pathology, Inc* 18 (9): 1258-1263. doi:10.1038/modpathol.3800415.

Langmoen, I A, T Lundar, I Storm-Mathisen, S O Lie, et K H Hovind. 1991. « Management of Pediatric Pontine Gliomas ». *Child's Nervous System: ChNS: Official Journal of the International Society for Pediatric Neurosurgery* 7 (1): 13-15.

Leach, P A, E J Estlin, D J Coope, J A Thorne, et I D Kamaly-Asl. 2008. « Diffuse Brainstem Gliomas in Children: Should We or Shouldn't We Biopsy? » *British Journal of Neurosurgery* 22 (5): 619-624. doi:10.1080/02688690802366198.

Lee, F. 1975. « Radiation of Infratentorial and Supratentorial Brain-Stem Tumors ». *Journal of Neurosurgery* 43 (1): 65-68. doi:10.3171/jns.1975.43.1.0065.

Lee, Jeongwu, Svetlana Kotliarova, Yuri Kotliarov, Aiguo Li, Qin Su, Nicholas M. Donin, Sandra Pastorino, et al. 2006. « Tumor stem cells derived from glioblastomas cultured in bFGF and EGF more closely mirror the phenotype and genotype of primary tumors than do serum-cultured cell lines ». *Cancer Cell* 9 (5): 391-403. doi:10.1016/j.ccr.2006.03.030.

Lewis, Peter W., Manuel M. Müller, Matthew S. Koletsky, Francisco Cordero, Shu Lin, Laura A. Banaszynski, Benjamin A. Garcia, Tom W. Muir, Oren J. Becher, et C. David Allis. 2013. « Inhibition of PRC2 Activity by a Gain-of-Function H3 Mutation Found in Pediatric Glioblastoma ». *Science* 340 (6134): 857-861. doi:10.1126/science.1232245.

Li, Gordon, Siddhartha S Mitra, Michelle Monje, Kristy N Henrich, C Dana Bangs, Ryan T Nitta, et Albert J Wong. 2012. « Expression of epidermal growth factor variant III (EGFRvIII) in pediatric diffuse intrinsic pontine gliomas ». *Journal of Neuro-Oncology*, mars. doi:10.1007/s11060-012-0842-3. http://www.ncbi.nlm.nih.gov/pubmed/22382786.

Liang, Muh-Lii, Jing Ma, Michael Ho, Lauren Solomon, Eric Bouffet, James T. Rutka, et Cynthia Hawkins. 2008. « Tyrosine Kinase Expression in Pediatric High Grade Astrocytoma ». *Journal of Neuro-Oncology* 87 (3): 247-253. doi:10.1007/s11060-007-9513-1.

Little, Suzanne E, Sergey Popov, Alexa Jury, Dorine A Bax, Lawrence Doey, Safa Al-Sarraj, Juliane M Jurgensmeier, et Chris Jones. 2012. « Receptor Tyrosine Kinase Genes Amplified in Glioblastoma Exhibit a Mutual Exclusivity in Variable Proportions Reflective of Individual Tumor Heterogeneity ». *Cancer Research* 72 (7): 1614-1620. doi:10.1158/0008-5472.CAN-11-4069.

Littman, P, P Jarrett, L T Bilaniuk, L B Rorke, R A Zimmerman, D A Bruce, S C Carabell, et L Schut. 1980. « Pediatric Brain Stem Gliomas ». *Cancer* 45 (11): 2787-2792.

Liu, Lu, L Magnus Bäcklund, Bo R Nilsson, Dan Grandér, Koichi Ichimura, Helena M Goike, et V Peter Collins. 2005. « Clinical Significance of EGFR Amplification and the Aberrant EGFRvIII Transcript in Conventionally Treated Astrocytic Gliomas ». *Journal of Molecular Medicine (Berlin, Germany)* 83 (11): 917-926. doi:10.1007/s00109-005-0700-2.

Liu, Qing, Ran Liu, Meghana V Kashyap, Rajnee Agarwal, Xiang'en Shi, Chung-cheng Wang, et Shao-Hua Yang. 2008. « Brainstem Glioma Progression in Juvenile and Adult Rats ». *Journal of Neurosurgery* 109 (5): 849-855. doi:10.3171/JNS/2008/109/11/0849.

Lokker, Nathalie A., Carol M. Sullivan, Stanley J. Hollenbach, Mark A. Israel, et Neill A. Giese. 2002. « Platelet-Derived Growth Factor (PDGF) Autocrine Signaling Regulates Survival and Mitogenic Pathways in Glioblastoma Cells Evidence That the Novel PDGF-C and PDGF-D Ligands May Play a Role in the Development of Brain Tumors ». *Cancer Research* 62 (13): 3729-3735.

Louis, David N., Hiroko Ohgaki, Otmar D. Wiestler, Webster K. Cavenee, Peter C. Burger, Anne Jouvet,

Bernd W. Scheithauer, et Paul Kleihues. 2007. « The 2007 WHO Classification of Tumours of the Central Nervous System ». *Acta Neuropathologica* 114 (2): 97-109. doi:10.1007/s00401-007-0243-4.

Lu, Kan V, Shaojun Zhu, Anna Cvrljevic, Tiffany T Huang, Shawn Sarkaria, David Ahkavan, Julie Dang, et al. 2009. « Fyn and SRC Are Effectors of Oncogenic Epidermal Growth Factor Receptor Signaling in Glioblastoma Patients ». *Cancer Research* 69 (17): 6889-6898. doi:10.1158/0008-5472.CAN-09-0347.

Lu, Q R, D Yuk, J A Alberta, Z Zhu, I Pawlitzky, J Chan, A P McMahon, C D Stiles, et D H Rowitch. 2000. « Sonic Hedgehog--Regulated Oligodendrocyte Lineage Genes Encoding bHLH Proteins in the Mammalian Central Nervous System ». *Neuron* 25 (2): 317-329.

Mandell, L R, R Kadota, C Freeman, E C Douglass, J Fontanesi, M E Cohen, E Kovnar, et al. 1999. « There Is No Role for Hyperfractionated Radiotherapy in the Management of Children with Newly Diagnosed Diffuse Intrinsic Brainstem Tumors: Results of a Pediatric Oncology Group Phase III Trial Comparing Conventional vs. Hyperfractionated Radiotherapy ». *International Journal of Radiation Oncology, Biology, Physics* 43 (5): 959-964.

Masui, Kenta, Satoshi O Suzuki, Rina Torisu, James E Goldman, Peter Canoll, et Toru Iwaki. 2010. « Glial Progenitors in the Brainstem Give Rise to Malignant Gliomas by Platelet-Derived Growth Factor Stimulation ». *Glia* 58 (9): 1050-1065. doi:10.1002/glia.20986.

Mellinghoff, Ingo K, Tim F Cloughesy, et Paul S Mischel. 2007. « PTEN-Mediated Resistance to Epidermal Growth Factor Receptor Kinase Inhibitors ». *Clinical Cancer Research: An Official Journal of the American Association for Cancer Research* 13 (2 Pt 1): 378-381. doi:10.1158/1078-0432.CCR-06-1992.

Milano, Vanessa, Yuji Piao, Tiffany LaFortune, et John de Groot. 2009. « Dasatinib-induced autophagy is enhanced in combination with temozolomide in glioma ». *Molecular Cancer Therapeutics* 8 (2): 394 -406. doi:10.1158/1535-7163.MCT-08-0669.

Monje, M., S. S. Mitra, M. E. Freret, T. B. Raveh, J. Kim, M. Masek, J. L. Attema, et al. 2011. « Hedgehog-responsive candidate cell of origin for diffuse intrinsic pontine glioma ». *Proceedings of the National Academy of Sciences* 108 (11): 4453-4458. doi:10.1073/pnas.1101657108.

Morgan, Marc Alard, et Ali Shilatifard. 2013. « (Poly)Combing the Pediatric Cancer Genome for Answers ». *Science* 340 (6134): 823-824. doi:10.1126/science.1239223.

Mueller, Sabine, Rintaro Hashizume, Xiaodong Yang, Ilan Kolkowitz, Aleksandra K Olow, Joanna Phillips, Ivan Smirnov, et al. 2014. « Targeting Wee1 for the Treatment of Pediatric High-Grade Gliomas ». *Neuro-Oncology* 16 (3): 352-360. doi:10.1093/neuonc/not220.

Mueller, Sabine, Joanna Phillips, Arzu Onar-Thomas, Eloy Romero, Shichun Zheng, John K Wiencke, Sean M McBride, et al. 2012. « PTEN Promoter Methylation and Activation of the PI3K/Akt/mTOR Pathway in Pediatric Gliomas and Influence on Clinical Outcome ». *Neuro-Oncology* 14 (9): 1146-1152. doi:10.1093/neuonc/nos140.

Negretti, Laura, Karim Bouchireb, Christine Levy-Piedbois, Jean Louis Habrand, Frederic Dhermain, Chantal Kalifa, Jacques Grill, et Christelle Dufour. 2011. « Hypofractionated Radiotherapy in the Treatment of Diffuse Intrinsic Pontine Glioma in Children: A Single Institution's Experience ». *Journal of Neuro-Oncology* 104 (3): 773-777. doi:10.1007/s11060-011-0542-4.

Nobusawa, Sumihito, Takuya Watanabe, Paul Kleihues, et Hiroko Ohgaki. 2009. « IDH1 Mutations as Molecular Signature and Predictive Factor of Secondary Glioblastomas ». *Clinical Cancer Research: An Official Journal of the American Association for Cancer Research* 15 (19): 6002-6007. doi:10.1158/1078-0432.CCR-09-0715.

Ozawa, Tatsuya, Cameron W Brennan, Lu Wang, Massimo Squatrito, Takashi Sasayama, Mitsutoshi Nakada, Jason T Huse, et al. 2010. « PDGFRA Gene Rearrangements Are Frequent Genetic Events in PDGFRA-Amplified Glioblastomas ». *Genes & Development* 24 (19): 2205-2218. doi:10.1101/gad.1972310.

Packer, R J, J M Boyett, R A Zimmerman, A L Albright, A M Kaplan, L B Rorke, M T Selch, J M Cherlow, J L Finlay, et W M Wara. 1994. « Outcome of Children with Brain Stem Gliomas after Treatment with 7800 cGy of Hyperfractionated Radiotherapy. A Childrens Cancer Group Phase I/II Trial ». *Cancer* 74 (6): 1827-1834.

Parsons, D Williams, Siân Jones, Xiaosong Zhang, Jimmy Cheng-Ho Lin, Rebecca J Leary, Philipp Angenendt, Parminder Mankoo, et al. 2008. « An Integrated Genomic Analysis of Human Glioblastoma Multiforme ». *Science (New York, N.Y.)* 321 (5897): 1807-1812. doi:10.1126/science.1164382.

Paugh, Barbara S, Chunxu Qu, Chris Jones, Zhaoli Liu, Martyna Adamowicz-Brice, Junyuan Zhang, Dorine A Bax, et al. 2010. « Integrated Molecular Genetic Profiling of Pediatric High-Grade Gliomas Reveals Key Differences with the Adult Disease ». *Journal of Clinical Oncology: Official Journal of the American Society of Clinical Oncology* 28 (18): 3061-3068. doi:10.1200/JCO.2009.26.7252.

Paugh, Barbara S., Alberto Broniscer, Chunxu Qu, Claudia P. Miller, Junyuan Zhang, Ruth G. Tatevossian, James M. Olson, et al. 2011. « Genome-Wide Analyses Identify Recurrent Amplifications of Receptor Tyrosine Kinases and Cell-Cycle Regulatory Genes in Diffuse Intrinsic Pontine Glioma ». *Journal of Clinical Oncology* 29 (30): 3999-4006. doi:10.1200/JCO.2011.35.5677.

Paugh, Barbara S., Xiaoyan Zhu, Chunxu Qu, Raelene Endersby, Alexander K. Diaz, Junyuan Zhang, Dorine A. Bax, et al. 2013. « Novel Oncogenic PDGFRA Mutations in Pediatric High-Grade Gliomas ». *Cancer Research*, août, canres.1491.2013. doi:10.1158/0008-5472.CAN-13-1491.

Pincus, David W, Erich O Richter, Anthony T Yachnis, Jeffrey Bennett, M Tariq Bhatti, et Amy Smith. 2006. « Brainstem Stereotactic Biopsy Sampling in Children ». *Journal of Neurosurgery* 104 (2 Suppl): 108-114. doi:10.3171/ped.2006.104.2.108.

Pollack, Ian F, Ronald L Hamilton, C David James, Sydney D Finkelstein, Judith Burnham, Allan J Yates, Emiko J Holmes, Tianni Zhou, Jonathan L Finlay, et Children's Oncology Group. 2006. « Rarity of PTEN Deletions and EGFR Amplification in Malignant Gliomas of Childhood: Results from the Children's Cancer Group 945 Cohort ». *Journal of Neurosurgery* 105 (5 Suppl): 418-424. doi:10.3171/ped.2006.105.5.418.

Pollack, Ian F, Ronald L Hamilton, Robert W Sobol, Judith Burnham, Allan J Yates, Emiko J Holmes, Tianni Zhou, et Jonathan L Finlay. 2006. « O6-Methylguanine-DNA Methyltransferase Expression Strongly Correlates with Outcome in Childhood Malignant Gliomas: Results from the CCG-945 Cohort ». *Journal of Clinical Oncology: Official Journal of the American Society of Clinical Oncology* 24 (21): 3431-3437. doi:10.1200/JCO.2006.05.7265.

Pollack, Ian F, Ronald L Hamilton, Robert W Sobol, Marina N Nikiforova, Maureen A Lyons-Weiler, William A LaFramboise, Peter C Burger, et al. 2011. « IDH1 Mutations Are Common in Malignant Gliomas Arising in Adolescents: A Report from the Children's Oncology Group ». *Child's Nervous System: ChNS: Official Journal of the International Society for Pediatric Neurosurgery* 27 (1): 87-94. doi:10.1007/s00381-010-1264-1.

Pollack, Ian F., Regina I. Jakacki, Susan M. Blaney, Michael L. Hancock, Mark W. Kieran, Peter Phillips, Larry E. Kun, et al. 2007. « Phase I trial of imatinib in children with newly diagnosed brainstem and recurrent malignant gliomas: A Pediatric Brain Tumor Consortium report ». *Neuro-Oncology* 9 (2): 145-160. doi:10.1215/15228517-2006-031.

Pollack, IanF, DanielR Premkumar, EstherP Jane, NaomiR Agostino, et JosephL Scialabba. 2010. « Dasatinib synergizes with JSI-124 to inhibit growth and migration and induce apoptosis of malignant human glioma cells ». *Journal of Carcinogenesis* 9 (1): 7. doi:10.4103/1477-3163.65448.

Puget, Stephanie, T. Blauwblome, et Jacques Grill. 2012. « Is Biopsy Safe in Children with Newly Diagnosed Diffuse Intrinsic Pontine Glioma ». *ASCO 2012 Educational Book*, 629-33.

Puget, Stephanie, Cathy Philippe, Dorine A. Bax, Bastien Job, Pascale Varlet, Marie-Pierre Junier, Felipe Andreiuolo, et al. 2012. « Mesenchymal Transition and PDGFRA Amplification/Mutation Are Key Distinct Oncogenic Events in Pediatric Diffuse Intrinsic Pontine Gliomas ». *PLoS ONE* 7 (2). doi:10.1371/journal.pone.0030313. http://www.ncbi.nlm.nih.gov/pmc/articles/PMC3289615/.

Qaddoumi, Ibrahim, Iyad Sultan, et Amar Gajjar. 2009. « Outcome and prognostic features in pediatric gliomas ». *Cancer* 115 (24): 5761-5770. doi:10.1002/cncr.24663.

Qu, Hui-Qi, Karine Jacob, Sarah Fatet, Bing Ge, David Barnett, Olivier Delattre, Damien Faury, et al. 2010. « Genome-Wide Profiling Using Single-Nucleotide Polymorphism Arrays Identifies Novel Chromosomal Imbalances in Pediatric Glioblastomas ». *Neuro-Oncology* 12 (2): 153-163. doi:10.1093/neuonc/nop001.

Raffel, C, L Frederick, J R O'Fallon, P Atherton-Skaff, A Perry, R B Jenkins, et C D James. 1999. « Analysis of Oncogene and Tumor Suppressor Gene Alterations in Pediatric Malignant Astrocytomas Reveals

Reduced Survival for Patients with PTEN Mutations ». *Clinical Cancer Research: An Official Journal of the American Association for Cancer Research* 5 (12): 4085-4090.

Raghavan, Ravi, Jyoti Balani, Arie Perry, Linda Margraf, Mary B Vono, Dan X Cai, Robert E Wyatt, et al. 2003. « Pediatric Oligodendrogliomas: A Study of Molecular Alterations on 1p and 19q Using Fluorescence in Situ Hybridization ». *Journal of Neuropathology and Experimental Neurology* 62 (5): 530-537.

Rao, Shailaja K, Jennifer Edwards, Avadhut D Joshi, I-Mei Siu, et Gregory J Riggins. 2010. « A Survey of Glioblastoma Genomic Amplifications and Deletions ». *Journal of Neuro-Oncology* 96 (2): 169-179. doi:10.1007/s11060-009-9959-4.

Rickert, C H, R Sträter, P Kaatsch, H Wassmann, H Jürgens, B Dockhorn-Dworniczak, et W Paulus. 2001. « Pediatric High-Grade Astrocytomas Show Chromosomal Imbalances Distinct from Adult Cases ». *The American Journal of Pathology* 158 (4): 1525-1532. doi:10.1016/S0002-9440(10)64103-X.

Roujeau, Thomas, Guilherme Machado, Matthew R Garnett, Catherine Miquel, Stephanie Puget, Birgit Geoerger, Jacques Grill, et al. 2007. « Stereotactic Biopsy of Diffuse Pontine Lesions in Children ». *Journal of Neurosurgery* 107 (1 Suppl): 1-4. doi:10.3171/PED-07/07/001.

Samadani, Uzma, Sherman Stein, Gul Moonis, Seema S Sonnad, Pia Bonura, et Kevin D Judy. 2006. « Stereotactic Biopsy of Brain Stem Masses: Decision Analysis and Literature Review ». *Surgical Neurology* 66 (5): 484-490; discussion 491. doi:10.1016/j.surneu.2006.05.056.

Samuels, Yardena, Zhenghe Wang, Alberto Bardelli, Natalie Silliman, Janine Ptak, Steve Szabo, Hai Yan, et al. 2004. « High Frequency of Mutations of the PIK3CA Gene in Human Cancers ». *Science* 304 (5670): 554-554. doi:10.1126/science.1096502.

Schiffman, Joshua D, J Graeme Hodgson, Scott R VandenBerg, Patrick Flaherty, Mei-Yin C Polley, Mamie Yu, Paul G Fisher, et al. 2010. « Oncogenic BRAF Mutation with CDKN2A Inactivation Is Characteristic of a Subset of Pediatric Malignant Astrocytomas ». *Cancer Research* 70 (2): 512-519. doi:10.1158/0008-5472.CAN-09-1851.

Schwartzentruber, Jeremy, Andrey Korshunov, Xiao-Yang Liu, David T W Jones, Elke Pfaff, Karine Jacob, Dominik Sturm, et al. 2012. « Driver Mutations in Histone H3.3 and Chromatin Remodelling Genes in Paediatric Glioblastoma ». *Nature* 482 (7384): 226-231. doi:10.1038/nature10833.

Sedlacik, J, A Winchell, M Kocak, R B Loeffler, A Broniscer, et C M Hillenbrand. 2013. « MR Imaging Assessment of Tumor Perfusion and 3D Segmented Volume at Baseline, during Treatment, and at Tumor Progression in Children with Newly Diagnosed Diffuse Intrinsic Pontine Glioma ». *AJNR. American Journal of Neuroradiology* 34 (7): 1450-1455. doi:10.3174/ajnr.A3421.

Sethi, Rajni, Jeffrey Allen, Bernadine Donahue, Matthias Karajannis, Sharon Gardner, Jeffrey Wisoff, Saroj Kunnakkat, et al. 2010. « Prospective neuraxis MRI surveillance reveals a high risk of leptomeningeal dissemination in diffuse intrinsic pontine glioma ». *Journal of Neuro-Oncology* 102 (1): 121-127. doi:10.1007/s11060-010-0301-y.

Setty, Prashanth, Jennifer Hammes, Thomas Rothämel, Valentina Vladimirova, Christof M Kramm, Torsten Pietsch, et Andreas Waha. 2010. « A Pyrosequencing-Based Assay for the Rapid Detection of IDH1 Mutations in Clinical Samples ». *The Journal of Molecular Diagnostics: JMD* 12 (6): 750-756. doi:10.2353/jmoldx.2010.090237.

Seymour, Z A, A Panigrahy, J L Finlay, M D Nelson Jr, et S Blüml. 2008. « Citrate in Pediatric CNS Tumors? » *AJNR. American Journal of Neuroradiology* 29 (5): 1006-1011. doi:10.3174/ajnr.A1018.

Sharp, Julia R, Eric Bouffet, Diana Stempak, Janet Gammon, Derek Stephens, Donna L Johnston, David Eisenstat, et al. 2010. « A Multi-Centre Canadian Pilot Study of Metronomic Temozolomide Combined with Radiotherapy for Newly Diagnosed Paediatric Brainstem Glioma ». *European Journal of Cancer (Oxford, England: 1990)* 46 (18): 3271-3279. doi:10.1016/j.ejca.2010.06.115.

Shore, Eileen M, Meiqi Xu, George J Feldman, David A Fenstermacher, Tae-Joon Cho, In Ho Choi, J Michael Connor, et al. 2006. « A Recurrent Mutation in the BMP Type I Receptor ACVR1 Causes Inherited and Sporadic Fibrodysplasia Ossificans Progressiva ». *Nature Genetics* 38 (5): 525-527. doi:10.1038/ng1783.

Sirachainan, Nongnuch, Samart Pakakasama, Anannit Visudithbhan, Surang Chiamchanya, Lojana Tuntiyatorn, Mantana Dhanachai, Jiraporn Laothamatas, et Suradej Hongeng. 2008. « Concurrent

Radiotherapy with Temozolomide Followed by Adjuvant Temozolomide and Cis-Retinoic Acid in Children with Diffuse Intrinsic Pontine Glioma ». *Neuro-Oncology* 10 (4): 577-582. doi:10.1215/15228517-2008-025.

Siu, I-Mei, Betty M Tyler, James X Chen, Charles G Eberhart, Ulrich-Wilhelm Thomale, Alessandro Olivi, George I Jallo, Gregory J Riggins, et Gary L Gallia. 2010. « Establishment of a Human Glioblastoma Stemlike Brainstem Rodent Tumor Model ». *Journal of Neurosurgery. Pediatrics* 6 (1): 92-97. doi:10.3171/2010.3.PEDS09366.

Smith, Justin S., Issei Tachibana, Sandra M. Passe, Brenda K. Huntley, Thomas J. Borell, Nancy Iturria, Judith R. O'Fallon, et al. 2001. « PTEN Mutation, EGFR Amplification, and Outcome in Patients With Anaplastic Astrocytoma and Glioblastoma Multiforme ». *Journal of the National Cancer Institute* 93 (16): 1246-1256. doi:10.1093/jnci/93.16.1246.

Stroink, A R, H J Hoffman, E B Hendrick, R P Humphreys, et G Davidson. 1987. « Transependymal Benign Dorsally Exophytic Brain Stem Gliomas in Childhood: Diagnosis and Treatment Recommendations ». *Neurosurgery* 20 (3): 439-444.

Stupp, R., et F. Roila. 2008. « Malignant Glioma: ESMO Clinical Recommendations for Diagnosis, Treatment and Follow-Up ». *Annals of Oncology* 19 (suppl 2): ii83-ii85. doi:10.1093/annonc/mdn099.

Sturm, Dominik, Sebastian Bender, David T W Jones, Peter Lichter, Jacques Grill, Oren Becher, Cynthia Hawkins, et al. 2014. « Paediatric and Adult Glioblastoma: Multiform (epi)genomic Culprits Emerge ». *Nature Reviews. Cancer* 14 (2): 92-107. doi:10.1038/nrc3655.

Sturm, Dominik, Hendrik Witt, Volker Hovestadt, Dong-Anh Khuong-Quang, David T.W. Jones, Carolin Konermann, Elke Pfaff, et al. 2012. « Hotspot Mutations in H3F3A and IDH1 Define Distinct Epigenetic and Biological Subgroups of Glioblastoma ». *Cancer Cell* 22 (4): 425-437. doi:10.1016/j.ccr.2012.08.024.

Sufit, Alexandra, Andrew M Donson, Diane K Birks, Jeffrey A Knipstein, Laura Z Fenton, Paul Jedlicka, Todd C Hankinson, Michael H Handler, et Nicholas K Foreman. 2012. « Diffuse Intrinsic Pontine Tumors: A Study of Primitive Neuroectodermal Tumors versus the More Common Diffuse Intrinsic Pontine Gliomas ». *Journal of Neurosurgery. Pediatrics* 10 (2): 81-88. doi:10.3171/2012.3.PEDS11316.

Szenker, Emmanuelle. 2012. « Etude des variants de l'histoire H3 : H3.2 et H3.3, au cours du développement embryonnaire d'un vertébré, Xenopus laevis ». Université Pierre et Marie Curie - Paris VI. http://tel.archives-ouvertes.fr/tel-00836233.

Tang, Jing, Leena Karhinen, Tao Xu, Agnieszka Szwajda, Bhagwan Yadav, Krister Wennerberg, et Tero Aittokallio. 2013. « Target Inhibition Networks: Predicting Selective Combinations of Druggable Targets to Block Cancer Survival Pathways ». *PLoS Comput Biol* 9 (9): e1003226. doi:10.1371/journal.pcbi.1003226.

Tau, Gregory Z, et Bradley S Peterson. 2010. « Normal Development of Brain Circuits ». *Neuropsychopharmacology: Official Publication of the American College of Neuropsychopharmacology* 35 (1): 147-168. doi:10.1038/npp.2009.115.

Taylor, Kathryn R, Alan Mackay, Nathalène Truffaux, Yaron S Butterfield, Olena Morozova, Cathy Philippe, David Castel, et al. 2014. « Recurrent Activating ACVR1 Mutations in Diffuse Intrinsic Pontine Glioma ». *Nature Genetics*, avril. doi:10.1038/ng.2925.

Thirant, Cécile, Barbara Bessette, Pascale Varlet, Stéphanie Puget, Josette Cadusseau, Silvina Dos Reis Tavares, Jeanne-Marie Studler, et al. 2011. « Clinical relevance of tumor cells with stem-like properties in pediatric brain tumors ». *PloS one* 6 (1): e16375. doi:10.1371/journal.pone.0016375.

Thorarinsdottir, H. K., M. Santi, R. McCarter, E. J. Rushing, R. Cornelison, A. Jales, et T. J. MacDonald. 2008. « Protein Expression of Platelet-Derived Growth Factor Receptor Correlates with Malignant Histology and PTEN with Survival in Childhood Gliomas ». *Clinical Cancer Research* 14 (11): 3386-3394. doi:10.1158/1078-0432.CCR-07-1616.

Uhrbom, L, G Hesselager, M Nistér, et B Westermark. 1998. « Induction of Brain Tumors in Mice Using a Recombinant Platelet-Derived Growth Factor B-Chain Retrovirus ». *Cancer Research* 58 (23): 5275-5279.

Uhrbom, L, G Hesselager, A Ostman, M Nistér, et B Westermark. 2000. « Dependence of Autocrine Growth Factor Stimulation in Platelet-Derived Growth Factor-B-Induced Mouse Brain Tumor Cells ». *International Journal of Cancer. Journal International Du Cancer* 85 (3): 398-406.

Verhaak, Roel G.W., Katherine A. Hoadley, Elizabeth Purdom, Victoria Wang, Yuan Qi, Matthew D. Wilkerson, C. Ryan Miller, et al. 2010. « Integrated Genomic Analysis Identifies Clinically Relevant Subtypes of Glioblastoma Characterized by Abnormalities in PDGFRA, IDH1, EGFR, and NF1 ». *Cancer Cell* 17 (1): 98-110. doi:10.1016/j.ccr.2009.12.020.

Wagner, S, M Benesch, F Berthold, A K Gnekow, S Rutkowski, R Sträter, M Warmuth-Metz, R-D Kortmann, T Pietsch, et J E A Wolff. 2006. « Secondary Dissemination in Children with High-Grade Malignant Gliomas and Diffuse Intrinsic Pontine Gliomas ». *British Journal of Cancer* 95 (8): 991-997. doi:10.1038/sj.bjc.6603402.

Warren, Katherine E., Sri Gururangan, J. Russell Geyer, Roger E. McLendon, Tina Young Poussaint, Dana Wallace, Frank M. Balis, et al. 2012. « A Phase II Study of O6-Benzylguanine and Temozolomide in Pediatric Patients with Recurrent or Progressive High Grade Gliomas and Brainstem Gliomas: A Pediatric Brain Tumor Consortium Study ». *Journal of neuro-oncology* 106 (3): 643-649. doi:10.1007/s11060-011-0709-z.

Wolff, Johannes E A, Carl Friedrich Classen, Sabine Wagner, Rolf-Dieter Kortmann, Shana L Palla, Torsten Pietsch, Joachim Kühl, Astrid Gnekow, et Christof M Kramm. 2008. « Subpopulations of Malignant Gliomas in Pediatric Patients: Analysis of the HIT-GBM Database ». *Journal of Neuro-Oncology* 87 (2): 155-164. doi:10.1007/s11060-007-9495-z.

Wong, Kwong-Kwok, Yvonne T M Tsang, Yi-Mieng Chang, Jack Su, Angela M Di Francesco, Daniela Meco, Riccardo Riccardi, et al. 2006. « Genome-Wide Allelic Imbalance Analysis of Pediatric Gliomas by Single Nucleotide Polymorphic Allele Array ». *Cancer Research* 66 (23): 11172-11178. doi:10.1158/0008-5472.CAN-06-2438.

Wu, Gang, Alberto Broniscer, Troy A McEachron, Charles Lu, Barbara S Paugh, Jared Becksfort, Chunxu Qu, et al. 2012. « Somatic histone H3 alterations in pediatric diffuse intrinsic pontine gliomas and non-brainstem glioblastomas ». *Nature genetics* 44 (3): 251-253. doi:10.1038/ng.1102.

Xu, Wei, Hui Yang, Ying Liu, Ying Yang, Ping Wang, Se-Hee Kim, Shinsuke Ito, Chen Yang, Pu Wang, et Meng-Tao Xiao. 2011. « Oncometabolite 2-Hydroxyglutarate Is a Competitive Inhibitor of α-Ketoglutarate-Dependent Dioxygenases ». *Cancer Cell* 19 (1): 17-30. doi:10.1016/j.ccr.2010.12.014.

Yan, Hai, D Williams Parsons, Genglin Jin, Roger McLendon, B Ahmed Rasheed, Weishi Yuan, Ivan Kos, et al. 2009. « IDH1 and IDH2 Mutations in Gliomas ». *The New England Journal of Medicine* 360 (8): 765-773. doi:10.1056/NEJMoa0808710.

Yoshimura, Junichi, Kiyoshi Onda, Ryuichi Tanaka, et Hitoshi Takahashi. 2003. « Clinicopathological Study of Diffuse Type Brainstem Gliomas: Analysis of 40 Autopsy Cases ». *Neurologia Medico-Chirurgica* 43 (8): 375-382; discussion 382.

Yu, Paul B, Donna Y Deng, Carol S Lai, Charles C Hong, Gregory D Cuny, Mary L Bouxsein, Deborah W Hong, et al. 2008. « BMP Type I Receptor Inhibition Reduces Heterotopic [corrected] Ossification ». *Nature Medicine* 14 (12): 1363-1369. doi:10.1038/nm.1888.

Zagzag, D, D C Miller, E Knopp, J P Farmer, M Lee, S Biria, A Pellicer, F J Epstein, et J C Allen. 2000. « Primitive Neuroectodermal Tumors of the Brainstem: Investigation of Seven Cases ». *Pediatrics* 106 (5): 1045-1053.

Zarghooni, Maryam, Ute Bartels, Eric Lee, Pawel Buczkowicz, Andrew Morrison, Annie Huang, Eric Bouffet, et Cynthia Hawkins. 2010. « Whole-genome profiling of pediatric diffuse intrinsic pontine gliomas highlights platelet-derived growth factor receptor alpha and poly (ADP-ribose) polymerase as potential therapeutic targets ». *Journal of clinical oncology: official journal of the American Society of Clinical Oncology* 28 (8): 1337-1344. doi:10.1200/JCO.2009.25.5463.

RESUME

Le gliome infiltrant du tronc cérébral est une tumeur rare, non opérable et inéluctablement fatale. En raison du manque de ressource biologique disponible, aucun progrès dans la compréhension de la biologie de ces tumeurs n'a été fait jusqu'à ces dernières années, laissant la radiothérapie pour seul traitement efficace (mais seulement transitoirement). Ces deux dernières années, grâce à la mise en place de collecte d'échantillons de gliomes infiltrants du tronc cérébral au diagnostic ou à l'autopsie, un nombre sans précédent d'analyses biologiques et génomiques a pu être mené et améliorer la connaissance de ces tumeurs. Si ces études ont montré que ces gliomes pédiatriques étaient bien différents de ceux de l'adulte, elles ont aussi fait apparaître la présence d'anomalies génétiques récurrentes spécifiques de ces tumeurs sous-tentorielles. Ainsi le *Platelet-Derived Growth Factor Receptor Alpha* (PDGFRα) est apparu comme cible prédominante dans ces tumeurs compte tenu des nombreuses anomalies génétiques constatées. La recherche d'un médicament efficace pouvant inhiber cette voie nous a conduit à évaluer l'effet du dasatinib qui est un inhibiteur multi-ciblé. Nous en rapportons ici l'efficacité *in vitro* sur de nouvelles lignées cellulaires de gliome infiltrant du tronc cérébral établies à partir de biopsies stéréotaxiques réalisées au diagnostic. Sachant néanmoins que les thérapies ciblées restent peu efficaces en clinique quand elles sont utilisées seules, nous mettons en évidence l'intérêt de combiner le dasatinib avec un inhibiteur de MET, 2ème oncogène fréquemment amplifié dans ces tumeurs. D'autre part, une stratégie originale de criblage médicamenteux a été mise en œuvre. Celle-ci a permis de définir de manière fonctionnelle de nouveaux médicaments potentiellement efficaces dans les gliomes infiltrants du tronc cérébral, incluant les inhibiteurs d'*Histone deacetylases* (HDAC), les inhibiteurs des *Cyclin-Dependent Kinases* (CDK) ou encore les inhibiteurs du protéasome.
Enfin par la technique de séquençage génome-entier, de nouvelles anomalies génétiques jamais rencontrées dans aucun autre cancer ont été détectées. Parmi celles-ci se trouvent des mutations de histone H3K27M dont la fréquence élevée (80%) suggère leur rôle fondamental dans la genèse de ces tumeurs. Des mutations activatrices d'ACVR1/ALK2 ont été également mises en évidence. Celles-ci représentent désormais de nouvelles cibles à explorer.
Ce travail de thèse rapporte la recherche de nouvelles cibles thérapeutiques d'une part, *via* une approche exploratoire par criblage médicamenteux et recherche d'anomalies génétiques par séquençage « génome-entier », et d'autre part, via une approche de validation préclinique sur le plan des thérapies ciblées de type inhibiteurs de tyrosine-kinases.

Mots clés : Gliome infiltrant du tronc cérébral, thérapie ciblée, criblage fonctionnel, dasatinib, séquençage « génome-entier », *ACVR1*

Frais de reprographie pris en charge par la taxe d'apprentissage de l'IGR